



Università degli Studi dell'Insubria
Dipartimento di Scienza e Alta Tecnologia - Como

**STRUCTURAL, THERMAL AND FUNCTIONAL
CHARACTERIZATION OF
METAL-ORGANIC FRAMEWORKS CONTAINING
POLY(PYRAZOLATE)-BASED LIGANDS
FOR CARBON DIOXIDE ADSORPTION**

Rebecca Vismara

XXXII Ph. D. Cycle in Chemistry and Environmental Sciences

Supervisor:
Prof. Simona Galli

List of Abbreviations and Acronyms.....	i
CHAPTER I.....	1
1. Facing Global Warming: Gas Adsorption Technologies.....	1
1.1. Global Warming and Greenhouse Gases.....	3
1.2. CO ₂ Capture: Post-Combustion Technologies.....	6
1.3. Solid Adsorbents.....	8
1.4. Inorganic Compounds.....	10
1.5. Metal-organic Frameworks (MOFs).....	11
1.6. Metal-organic Frameworks as CO ₂ Adsorbents	15
1.7. Primary CO ₂ Adsorption Sites in MOFs.....	16
1.8. Conclusions	23
1.9. References	24
CHAPTER II	35
2. The Family of Bis(pyrazolate) MOFs.....	35
2.1. N-donor Organic Ligands	37
2.2. Pyrazolate and Poly(pyrazolate) Ligands	38
2.3. Synthesis and Spectroscopic Characterization of the M-BPZX MOFs	41
2.3.1. M-Me ₂ BPZ [M = Co(II), Zn(II)]	42
2.3.2. M-BPZNO ₂ [M = Co(II), Cu(II), Zn(II)].....	42
2.3.3. M-BPZNH ₂ [M = Ni(II), Cu(II), Zn(II)]	43
2.3.4. Zn-BPZ(NH ₂) ₂	43
2.4. Conclusions	43
2.5. References	44
CHAPTER III.....	47
3. Structural and Thermal Characterization of the M-BPZX MOFs	47
3.1. Structural Characterization of the M-BPZX MOFs.....	49
3.1.1. M-Me ₂ BPZ	50
3.1.2. M-BPZNO ₂	53
3.1.3. M-BPZNH ₂	58
3.1.4. M-BPZ(NH ₂) ₂	61
3.2. Thermal characterization of the M-BPZX MOFs.....	63

3.2.1. M-Me ₂ BPZ·S.....	63
3.2.2. M-BPZNO ₂ ·S	65
3.2.3. M-BPZNH ₂ ·S	68
3.2.4. M-BPZ(NH ₂) ₂ ·S.....	70
3.3. Water vapor stability.....	71
3.4. Conclusions	71
3.5. References	73
CHAPTER IV	75
4. CO ₂ Adsorption Properties of the M-BPZX MOFs.....	75
4.1. Adsorption Properties of the M-BPZX MOFs.....	77
4.2. M-Me ₂ BPZ	77
4.3. M-BPZNO ₂	82
4.4. M-BPZNH ₂	92
4.5. Zn-BPZ(NH ₂) ₂	97
4.5.1. C ₆ H ₁₄ Isomers Separation.....	98
4.5.2. Variable-temperature Pulse Gas Chromatography	99
4.5.3. Molecular Simulations.....	102
4.6. Conclusions	104
4.7. References	106
CHAPTER V.....	113
5. Zn(II) MIXMOFs: Synthesis, Crystal Structure and Adsorption Properties	113
5.1. Zn(II) Mixed-ligand Bis(pyrazolate) MOFs	115
5.2. Synthesis and Preliminary Characterization of the MIXMOFs.....	116
5.3. Structural and Thermal Characterization of the MIXMOFs.....	118
5.4. Thermal Behaviour of the MIXMOFs	127
5.5. Solid-state ¹³ C and ¹⁵ N CPMAS NMR Analysis of the MIXMOFs	132
5.6. Water Vapour Stability	135
5.7. Textural Properties and CO ₂ Adsorption Ability of the MIXMOFs.....	136
5.8. Conclusions	142
5.9. References	143
CHAPTER VI.....	147

6. Conclusions	147
6.1. Conclusions	149
Annex I	153
7. Materials and Methods	153
7.1. M-Me ₂ BPZ	155
7.1.1. Synthesis and Preliminary Characterization.....	155
7.1.2. Powder X-ray Diffraction Structural Characterization.....	156
7.1.3. Variable-temperature Powder X-ray Diffraction (VT-PXRD).....	157
7.1.4. Textural Characterization	157
7.1.5. Theoretical Calculations.....	158
7.2. M-BPZNO ₂	159
7.2.1. Synthesis and Preliminary Characterization.....	160
7.2.2. Powder X-ray Diffraction Structural Characterization.....	162
7.2.3. Variable-temperature Powder X-ray Diffraction (VT-PXRD).....	162
7.2.4. Textural Characterization	163
7.2.5. High-resolution Powder X-ray Diffraction.....	164
7.2.6. Computational Details.....	164
7.3. M-BPZNH ₂	165
7.3.1. Synthesis and Preliminary Characterization.....	166
7.3.2. Powder X-ray Diffraction Structural Characterization.....	168
7.3.3. Water Vapour Stability.....	168
7.3.4. Textural Characterization	169
7.3.5. Catalytic CO ₂ Epoxidation with Zn-BPZNH ₂	169
7.4. Zn-BPZ(NH ₂) ₂	170
7.4.1. Synthesis and Preliminary Characterization.....	170
7.4.2. Powder X-ray Diffraction Structural Characterization.....	171
7.4.3. Variable-temperature Powder X-ray Diffraction.....	171
7.4.4. Gas-chromatography	171
7.4.5. Molecular Simulations.....	173
7.5. Zn-MIXMOFs	173
7.5.1. Synthesis and Preliminary Characterization.....	174

7.5.2. Powder X-ray Diffraction Structural Characterization.....	176
7.5.3. Solid-state NMR Characterization	176
7.5.4. Variable-temperature Powder X-ray Diffraction.....	177
7.5.5. Water Vapor Stability.....	177
7.5.6. Textural Characterization	178
7.6. References	179
List of Publications.....	183
Acknowledgements.....	185

LIST OF ABBREVIATIONS AND ACRONIMS

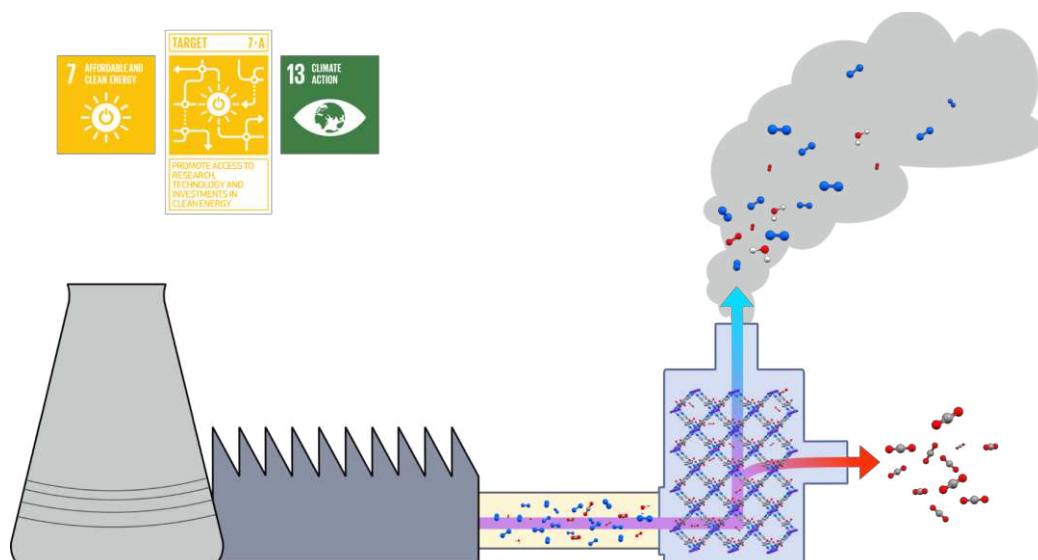
2MP	2-methylpentane
3MP	3-methylpentane
22DMB	2,2-dimethylbutane
2,3DMB	2,3-dimethylbutane
2-mIm	2-methylimidazolate
AC	Activated carbon
bbIm	5(6)-bromo-benzimidazolate
BET	Brunauer-Emmett-Teller surface area
H₂BPZ	4,4'-bipyrazole
BU	Building unit
cbIm	5(6)-chlorobenzimidazolate
CCS	Carbon capture and sequestration
CCU	Carbon capture and utilization
COP21	2015 Paris Climate Conference
CP	Coordination polymer
DMF	Dimethylformamide
DSC	Differential Scanning Calorimetry
GHG	Greenhouse gas
HEX	<i>n</i> -hexane
HR-PXRD	High-resolution powder X-ray diffraction
IRMOF	Isorecticular metal-organic framework
mbIm	5(6)-methyl-benzimidazolate
MEA	Monoethanolamine
MIL-100(Fe)	Fe ₃ O(H ₂ O) ₂ F {C ₆ H ₃ (CO ₂) ₃ } ₂ · <i>n</i> H ₂ O (<i>n</i> ~14.5)
MIL-101	Cr ₃ F(H ₂ O) ₂ O(BDC) ₃ · <i>n</i> H ₂ O (<i>n</i> ~25)
MIL-125	[Ti ₈ O ₈ (OH) ₄ (BDC) ₆]
MIL-53	[Al(OH)(BDC)] _{<i>n</i>}
MOF	Metal-organic framework
MOF-5	[Zn ₄ O(BDC) ₃]
M-MOF-74	[M ₂ (dobdc)(H ₂ O) ₂] (M = Mg ²⁺ , Ni ²⁺ , Co ²⁺ , Zn ²⁺)
NU-1000	[Zr ₆ (μ ₃ -O) ₄ (μ ₃ -OH) ₄] ₂ (TBAPy) ₆
OMS	Open metal site
PCP	Porous coordination polymer
PSP	Pore space partition
PXRD	Powder X-ray diffraction

Q_{st}	Isosteric heat of adsorption
SBU	Secondary building unit
SPC	Soft porous crystal
SSA	Specific surface area
STA	Simultaneous thermal analysis
TGA	Thermogravimetric analysis
UiO-66	$[\text{Zr}_6\text{O}_4(\text{OH})_4(\text{BDC})_6]_n$
VT-PXRD	Variable temperature powder X-ray diffraction
ZIF	Zeolitic imidazolate framework

CHAPTER I

1. FACING GLOBAL WARMING: GAS ADSORPTION TECHNOLOGIES

The aim of this chapter is to introduce the readers to the Ph. D. thesis work, providing them with the motivations and the collocation of the research topic in the state of art. First, an overview on the global warming concerns and on the actual policies to face it is proposed. The following paragraph briefly illustrates the essential properties an adsorbent should have, and the different classes of materials commonly used, or studied, for carbon dioxide sequestration. The focus is then moved to a relatively new class of materials: metal-organic frameworks, which have been the topic of the candidate's thesis. The conclusion paragraph illustrates the advantages of this class of materials and the challenges not yet overcome.



1.1. Global Warming and Greenhouse Gases

In September 2015, the United Nation General Assembly adopted “17 Sustainable Goals” to be achieved before 2030.¹ Among them, “Goal 13: Climate Action” expresses the necessity of facing global warming to limit and gradually overcome its sometimes hidden effects on food and water security, public health, migration and peace. After COP21, the Paris Climate Conference held in December 2015, 195 countries signed an agreement to keep the temperature rise under 2 K in the current century,^{2,3} limit further lowered down to 1.5 K in 2018.⁴ To this aim, two different but complementary paths have to be followed: *i*) investments and research on green energies and *ii*) development of more efficient technologies for greenhouse gases (GHGs) capture and sequestration or capture and utilization.⁵⁻⁷ “Goal 7: Affordable and clean energy”, especially its target 7.4, promotes the access to research, technology and investments in clean energy and sets as goal: “By 2030, enhance international cooperation to facilitate access to clean energy research and technology, including renewable energy, energy efficiency and advanced and cleaner fossil-fuel technology, and promote investment in energy infrastructure and clean energy technology”.

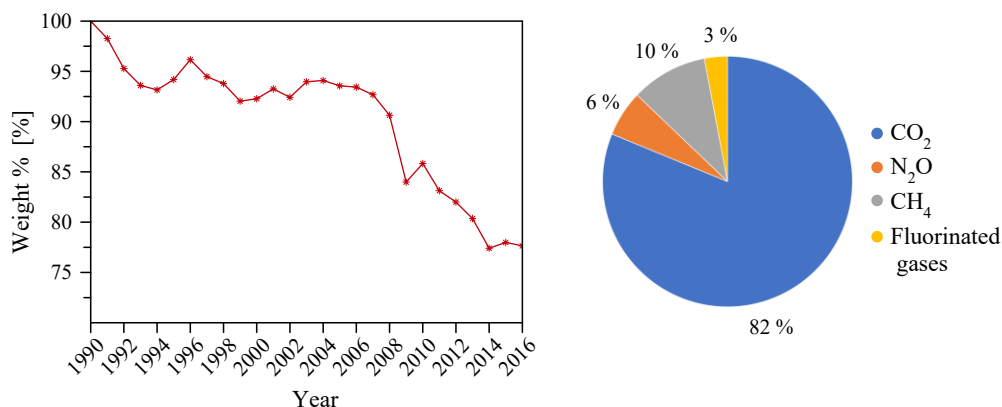


Figure 1.1 *Left*: Emission of GHGs in Europe in the period 1990-2016; the data are normalized with respect to the values of 1990 (graph adapted from 8). *Right*: GHGs emissions by gas type in CO₂-equivalents in the United States in 2017.⁹

GHGs, especially those ascribable to human activities (namely: carbon dioxide, methane, nitrogen oxides and fluorinated gases), contribute to global warming confining

heat in the atmosphere. Their role is definitely recognized, and some climate policies have already been actuated. As a representative result, Europe total emissions of GHGs have decreased more than 20% since 1990⁸ (Figure 1.1 left).

Among GHGs, carbon dioxide is that of major anthropogenic origin (Figure 1.1 right), with a release in the atmosphere of ~ 32 Gt *per year*.^{4,9} As demonstrated by paleoclimatic studies,¹⁰ the concentration of CO₂ in the atmosphere follows a natural cyclic behaviour, passing from 170 ppm up to 300 ppm during glacial-interglacial events (Figure 1.2). Nevertheless, since 1958, the natural maximum limit has been overcome, reaching a new maximum of 410 ppm in February 2019 (Figure 1.2).⁹ The CO₂ increase in emissions by $\sim 45\%$ with respect to the pre-industrial era is related to human activities and has to be considered a problem to face.

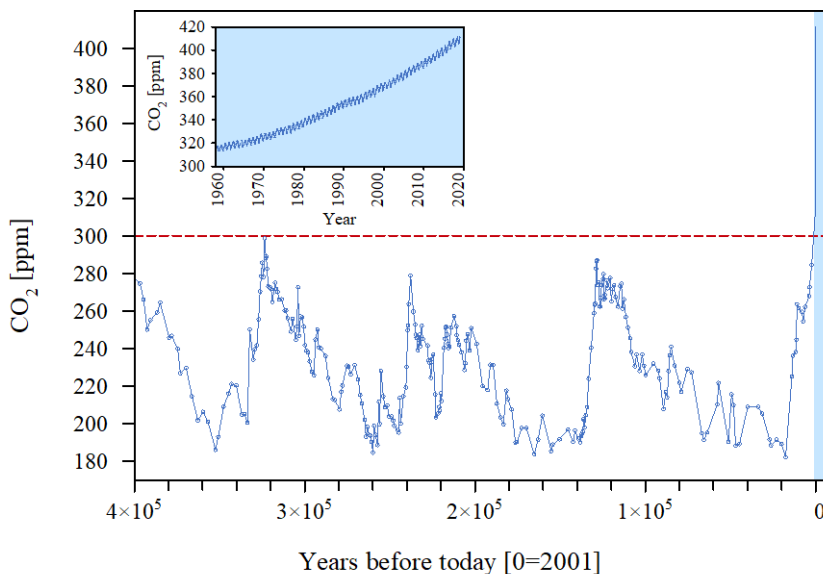


Figure 1.2 Variation of CO₂ concentration during the past centuries as estimated from Vostok ice cores, Antarctica (index: 0 = 2001);¹⁰ in the inset, the amount of CO₂ retraceable to human activities. Measurements carried out at Mauna Loa, Hawaii, United States.¹¹

Since the sources of anthropogenic CO₂ are several and differentiated,¹² in terms of both amounts of gas released and spatial distribution (Figure 1.3), CO₂ capture from large point sources could be a promising strategy to reduce its emission in the atmosphere.

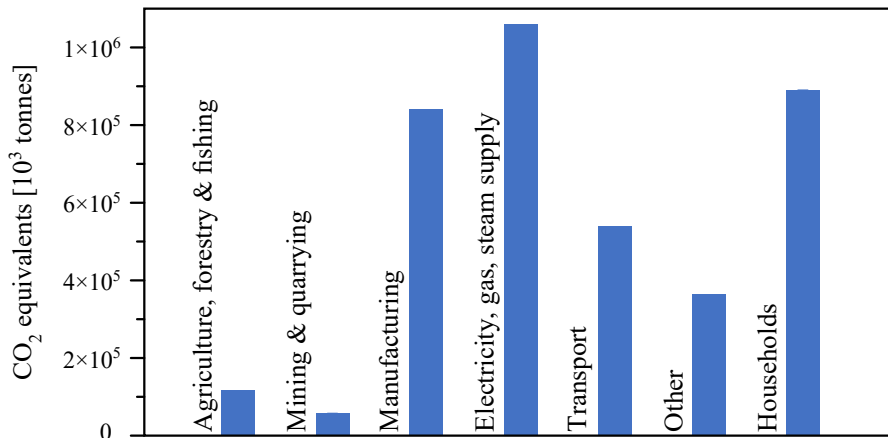


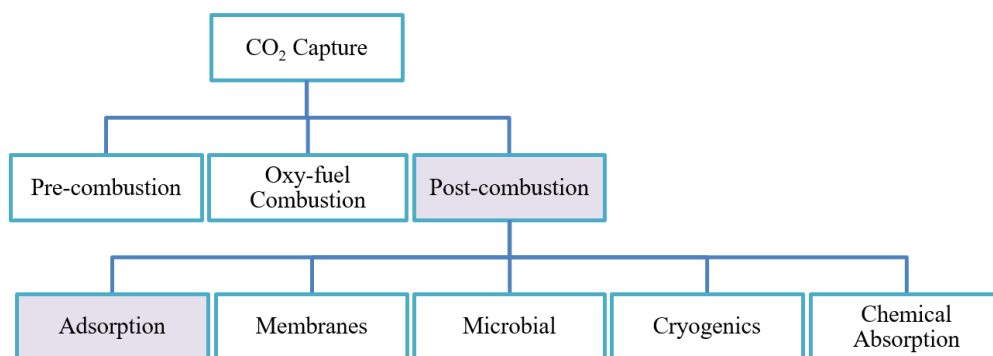
Figure 1.3 CO₂ emissions by economic activity in Europe in 2017 (graph adapted from 8).

The economic sector of energy supply is one of the most relevant in GHGs emissions (Figure 1.3). Moreover, it is constituted by a limited number of sources if compared, for example, to transport or household. This is the reason why power plants, especially the coal-fired ones, have been receiving the attention of the researchers community to limit and control their exhaust gases.^{5,13–16}

Three different policies, associated to three different steps of the power production, have been proposed to reduce CO₂ emissions (Scheme 1.1): *i*) pre-combustion, *ii*) oxy-fuel combustion and *iii*) post-combustion.^{17–21} In *i*), the *pre-combustion* process, carbon is removed before combustion in order to avoid CO₂ in the power plant emissions. Fossil fuels are converted into a mixture of carbon dioxide and hydrogen; then, CO₂ at moderately high content (15-40%) and pressure (up to 40 bar) is removed and the remaining hydrogen can be used as fuel. The *ii*) *oxy-combustion* process is based on the combustion of fuel and pure oxygen instead of air, to have a more complete combustion and, consequently, a flow highly enriched in CO₂ (~90%) and containing water vapour. In this case, the higher CO₂ concentration results in an easier separation process. Unfortunately, separating oxygen from air requires a lot of energy and associated costs. *iii*) *Post-combustion* technologies have the advantage that they can be inserted in pre-existing plants without a radical and expensive reorganization. They are based on the sequestration of CO₂ from flue gases after a prior removal of fly ashes and sulphur-

containing compounds. Then, the sorbent can be regenerated and reused for multiple cycles of adsorption-desorption. The outgoing CO₂ will be either used as chemical reagent (carbon capture and utilization, CCU), or stored (carbon capture and sequestration, CCS) *via* mineralization or injection in geological formations.

The aim of the present thesis work is a systematic study on new materials as CO₂ solid adsorbents for post-combustion CCS/CCU. As a consequence, points *i*) and *ii*) will not be discussed anymore in this manuscript: for further information the readers are referred to pertinent bibliography.^{19,20,22}



Scheme 1.1 Simplified scheme of CO₂ capture technologies and processes. Highlighted in violet the topic of this thesis work.

1.2. CO₂ Capture: Post-Combustion Technologies

Power plants emissions are constituted by a mixture of components, namely: N₂ ~70-75%, CO₂ ~12-15%, H₂O_{vap} ~4-6%, O₂ ~3-4%, together with a minor amount of SO₂ (~800 ppm), NO_x (~500 ppm) and trace metals (Hg ~1 ppb).^{12,23,24} The huge volume of gases is emitted at medium-high temperatures (T = 310-400 K) and at atmospheric pressure, resulting in a low partial pressure of CO₂: only ~0.13 bar.²⁵ Furthermore, as shown in Table 1.1, the physical parameters of the flue gas components, relevant for carbon capture processes, are similar at the operating conditions. A useful tool for carbon dioxide separation can be identified in its chemical nature, as it is a Lewis acid and can selectively interact with Lewis bases.

Taking into account the complexity of exhausted flue gases and the operating conditions, a suitable technology for post-combustion capture should fulfil the following requirements: on the one hand, *i*) a good selectivity and *ii*) a high affinity for CO₂; on the other hand, *iii*) water and *iv*) thermal stability. Besides, from an economic point of view also the production and implementation costs, together with: *v*) high capacity, *vi*) reusability and *vii*) low regeneration costs must be considered.¹⁴ All these factors make finding efficient and cheap materials for CCS or CCU still challenging.

Table 1.1 Physical parameters of the components of a typical flue gas emitted by coal-fired power plants.

	N ₂	CO ₂	H ₂ O	O ₂
Kinetic diameter [Å]	3.68	3.30	2.65	3.46
Boiling point [K]	77	195	373	90
Dipole moment [10 ⁻¹⁹ esu ⁻¹ cm ⁻¹]	0	0	19	0
Polarizability [10 ⁻²⁵ cm ⁻³]	17	29	15	16
Quadrupole moment [10 ⁻²⁶ esu ⁻¹ cm ⁻²]	1.5	4.3	-	0.4

In the past years, different approaches have been investigated to implement post-combustion technologies, namely: absorption, cryogenic separation, membrane separation, microbial fixation and adsorption (Scheme 1.1). Today, the liquid-phase chemisorption technology, through aqueous alkanolamine solutions, is the most used one in industry.²⁶ This approach is based on a patent issued in 1930,²⁷ in which the so-called amine process was recognized to separate acid gases. Due to their low cost of production and good performance, aqueous amine solutions gained a large diffusion in industry. The strong affinity between amines and CO₂ is associated with a high heat of adsorption (Q_{st}) of ~ 75 kJ mol⁻¹. While the presence of strong binding between CO₂ and amines results in high selectivity and high removal of carbon dioxide [$\sim 90\%$ at $T = 313$ K and $P_{CO_2} = 0.10$ - 0.13 bar for a 30% aqueous solution of monoethanolamine (MEA)], the main limit of these materials is the elevated cost in regeneration, which reaches 30% of the total energy produced by the power plant.²⁸ The costs are mainly related to the high temperature required for regeneration ($T > 393$ K). Furthermore, alkanolamines undergo a partial

thermal and oxidative degradation at each use, in association to a low working capacity of ~2%.²⁹⁻³¹

In order to overcome the drawbacks of amine aqueous solutions, from the early 1990's solid adsorbents were taken into consideration as a valid alternative for carbon capture processes.¹⁴ The development of new adsorbents with higher working capacity, better stability and selectivity towards carbon dioxide as well as tolerance to impurities are the main goals of these studies.

1.3. Solid Adsorbents

The use of a solid adsorbent for CCS/CCU could lead to many advantages vs. amine aqueous solutions, such as sorbent easy handling, higher stability, tuneable chemistry and easier regeneration by thermal or pressure modulation, as well as fast gas diffusion. However, solid adsorbents are usually associated to drawbacks such as high costs of production and/or limited selectivity. In order to have an efficient and competitive carbon dioxide adsorbent for physisorption, some additional properties^{22,28,29,32} must be searched for in addition to those listed in section 1.2, namely (the limit values reported below are referred to a typical MEA aqueous solution used in industry for CO₂ capture):

- *Low energy for reactivation*, which is strictly related to a Q_{st} comprised in the range 35-50 kJ mol⁻¹. Values lower than 35 kJ mol⁻¹ are related to weak binding and, consequently, low capacity of adsorption. By contrast, higher Q_{st} values are associated to a high affinity between CO₂ and the adsorbent and a higher regeneration temperature. 30% aqueous solutions of MEA show a Q_{st} of ~75 kJ mol⁻¹, hence the necessity of finding other options to be used in industry.
- *System and working capacity* - the identified material should adsorb more than 2 mmol g⁻¹ and have a higher working capacity than amine solutions (~2%).
- *Selectivity* - as already pointed out, flue gases are a mixture of components. In solid adsorbents, selectivity can be achieved kinetically, taking advantage of the difference in guests diffusivity and size, or thermodynamically, modulating the strength of the host-guest interactions.

- *High porosity* - it is strictly related to the system capacity. The ideal porosity could be very similar to the dynamic radius of CO₂ to act as a physical sieve (in the range of 0.3-0.4 nm) or, by contrast, the adsorbent could be macroporous and functionalized with proper adsorption sites, that can selectively interact with carbon dioxide molecules. Usually the second choice is preferred, since adsorbents with pore size able to discriminate the kinetic diameter of gases make the diffusivity of the gases themselves rather difficult.

Classical inorganic adsorbents, such as zeolites and activated carbons, were initially favoured because of their availability on the large scale, low cost of production and high stability. Then, also metal-organic frameworks (MOFs), hydrotalcites, amine supported materials (*e.g.* mesoporous silica), polymers and metal oxides were evaluated as carbon dioxide adsorbents (Figure 1.4).

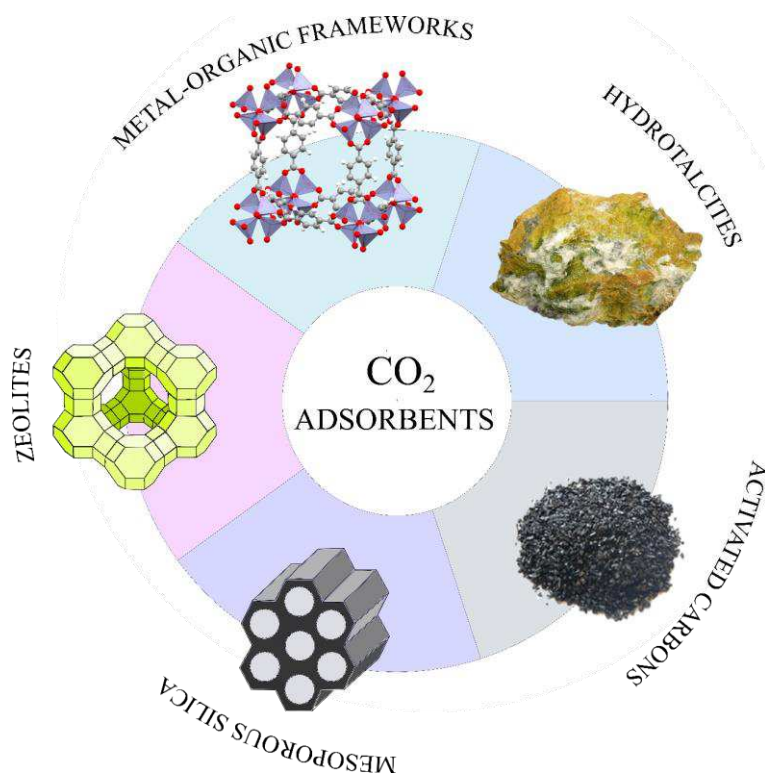


Figure 1.4 Classes of inorganic and hybrid organic/inorganic materials used as carbon dioxide solid adsorbents.

1.4. Inorganic Compounds

Activated carbons (ACs) are a well-known class of inorganic porous materials, which have been studied for a large number of applications in gas separation and storage technologies.^{7,33} Their appeal is strictly correlated to large specific surface area, high thermal stability, high availability and good chemical resistance.^{34,35} Moreover, if considered as post-combustion carbon dioxide adsorbents, ACs are hydrophobic, stable over multiple adsorption-desorption cycles at low temperature ($T < 373$ K),³⁴ tailorable via pre- or post-modification methods, and with low production cost. The interactions between ACs and carbon dioxide are based on weak intermolecular interactions ($Q_{st} \sim 30$ kJ mol⁻¹), such as dispersion interactions, leading to low desorption temperature but also low selectivity and capacity (despite the high specific surface area). Besides, ACs adsorption capacity is also highly affected at the operating temperatures of power plants emissions.³⁶⁻³⁸

On the other hand, *zeolites* show a CO₂/N₂ selectivity 5 to 10 times higher than ACs and an associated Q_{st} of ~ 36 - 37 kJ mol⁻¹.³⁹ Their framework type, in terms of size and shape of the channels/cages, can differ a lot, and offers the possibility of tuning parameters such as: pore size, Si/Al ratio or extra-framework cations. In particular, the Si/Al ratio is inversely proportional to framework basicity, leading, in a proper proportion, to a high carbon dioxide uptake.⁴⁰ Taking all the different parameters and combinations into account, zeolites of A and X type, especially zeolites 5A and 13X, have arisen as the most suitable ones for carbon dioxide capture.⁴¹⁻⁴³ In particular, zeolite 13X shows a relatively high uptake of CO₂ at low pressure (2-3 mmol g⁻¹ of CO₂ adsorbed at 0.1 bar in the range of temperatures 288-308 K), together with a good selectivity over N₂ and a good working capacity.^{18,44-46} However, zeolites suffer from a substantial drawback correlated to their high hydrophilicity (their moisture content can reach 20% of the total weight).⁴⁷ The presence of water, which is one of the components of flue gases, alters the electric field of cationic zeolites, favours the formation of bicarbonate-like species and reduces the interactions with CO₂, thus lowering the total carbon dioxide uptake and making the activation process difficult.^{18,43,48}

Mesoporous silicas show different pore sizes/geometries and high porosity. Mesoporous silicas themselves are not ideal materials for carbon dioxide adsorption, due to their acidic pores surface and relatively large pores. Nonetheless, their pore surface can be decorated with amines or other functional groups enhancing their affinity towards CO₂.⁴⁹⁻⁵² The main limits of mesoporous silicas remain the higher energy required for their regeneration vs. ACs or zeolites and the high affinity with water molecules. Besides, the post-synthetic modifications necessary for CO₂ uptake significantly raise their cost.

In the following section the readers' attention will be focused on metal-organic frameworks and their application as CCS/CCU materials.

1.5. Metal-organic Frameworks (MOFs)

The term "metal-organic frameworks" (MOFs) was coined in 1995 by O. M. Yaghi and coworkers,⁵³ describing the dual composition (metal ion/cluster and organic ligand) of the reported coordination polymer, namely [Cu(BIPY)_{1.5}](NO₃) (BIPY = 4,4'-bipyridine). Only later, thanks to the spreading interest in studying MOFs, the specific structural features and properties (porosity) of MOFs became part of their definition, as defined by IUPAC: "*A metal-organic framework, abbreviated to MOF, is a coordination network with organic ligands containing potential voids*" (cited from 54).

MOFs, also named porous coordination polymers (PCPs), are auto-assembled hybrid materials constituted by an organic linker and an inorganic moiety, or secondary building unit (SBU), specifically a metal ion or an oxo-metallic cluster. The resulting 1-, 2- or 3-dimensional frameworks are characterized by tuneable topology and structural features strictly dependent on the pristine building units (BUs) (Figure 1.5).

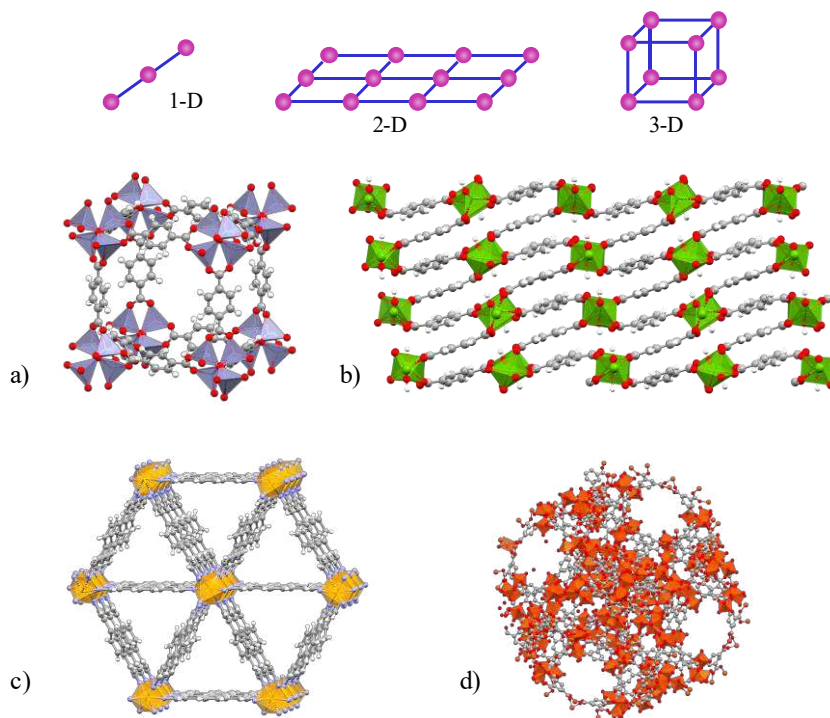


Figure 1.5 *Top*: Schematic examples of 1-, 2- and 3-dimensional coordination polymers; *bottom*: crystal structures of some prototypical MOFs: a) MOF-5,⁵⁵ b) MIL-53,⁵⁶ c) Fe₂(BDP)₃,⁵⁷ and d) MIL-100.⁵⁸

The stereochemistry of the metal ion/cluster together with the shape, size and functionalization of the ligand can lead to many different crystal structures and functional properties feasible for different applications. The chemical nature of the metal ion/cluster can enhance thermal and mechanical robustness and impart key chemical/physical properties (*e.g.* catalytic, magnetic or optical properties) as well as direct the connectivity of the final structure.⁵⁹ On the other hand, the shape and size of the ligand, together with its electronic properties, can be tuned via substitution (*e.g.* a CH group with a N atom), influencing the coordination angles, or *via* modification of the bonding type (*e.g.* from single to double or triple bond), determining shrinkage or expansion. The linker can be modified not only by varying its length, but also by adding different functional groups. The latter can induce preferential host-guest interactions, impart hydrophilicity or hydrophobicity to the pores, as well as modulate their perviousness and electronic and steric properties.^{60–62} The solids resulting from these ligand changes are a family of

isorecticular frameworks as soon as the connectivity between the organic moiety and the inorganic one is preserved and the topology does not change. However, within an isorecticular family, porosity can be largely influenced in terms of surface area, pore volume, pore size and shape, being directly connected to the length and steric hindrance of the organic backbone. An explicative example can be found in the family of the so-called IRMOFs,^{55,63} as highlighted by Figure 1.6, where the topology of the pristine MOF-5 is maintained despite the multiple ligand modifications. The massive library of possible compounds can be further grown by mixing different ligands and/or metal ions in the same structure.^{64–70}

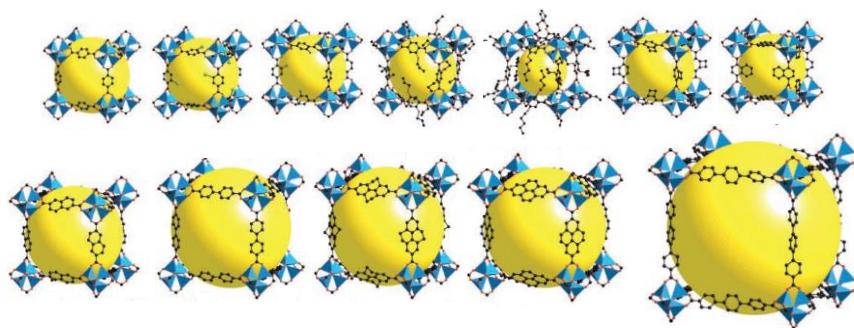


Figure 1.6 Ordered models of the components of the isorecticular family of IRMOF-n, from ref. 58. Color code: zinc (blue polyhedron), oxygen (red), carbon (black), Br (green), amino-group (blue sphere). Hydrogen atoms have been omitted. The large yellow spheres are the largest van der Waals spheres that would fit in the pores.

An additional peculiar feature of MOFs is the possibility of having a flexible framework, which can “breathe” in response to external stimuli, such as pressure, temperature or loss of the clathrate solvent (the so-called activation process). Starting from this observation, in early 1997 Prof. Kitagawa proposed to classify PCPs in three different categories, called “generations” (Figure 1.7).⁷¹ Those MOFs which collapse after solvent removal belong to the first generation, while the second one is formed by MOFs being rigid and showing permanent porosity after activation. The third one refers to flexible PCPs, which show permanent porosity and can change their pore aperture in relation to external stimuli. In 2009, the PCPs of the third generation were named “soft porous crystals” (SPCs) and defined “*as porous solids that possess both a highly ordered network and structural transformability. They are bistable or multistable crystalline*

materials with long range structural ordering, a reversible transformability between states, and permanent porosity. The term porosity means that at least one crystal phase possesses space that can be occupied by guest molecules, so that the framework exhibits reproducible guest adsorption” (cited from S. Horike *et al.*,⁷²). In particular SPCs have a higher appeal in separation processes, since, theoretically, a multiple step separation can be performed by a single material modulating an external stimulus, like pressure or temperature.⁷³

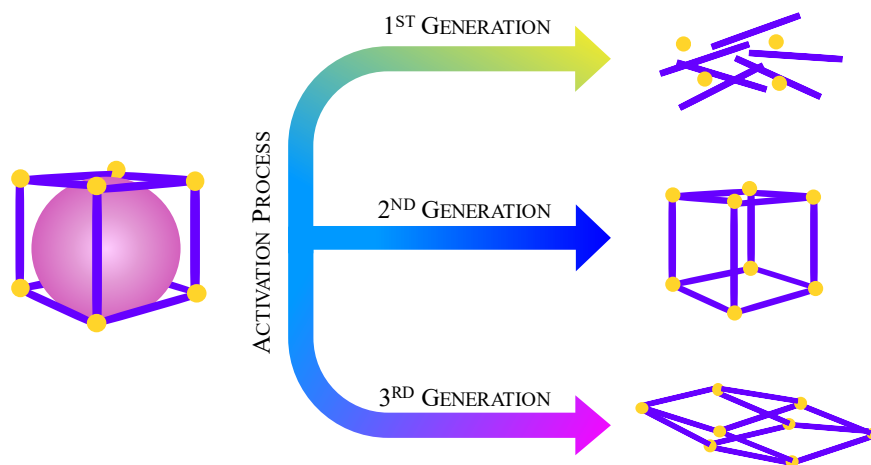


Figure 1.7 Schematic representation of Kitagawa’s classification of PCPs according to their different behaviour. Colour code: purple stick, organic linker; yellow sphere, SBU; pink sphere, clathrate solvent.

The different topologies, the multiple possibilities of tuning the chemical and physical properties and the high porosity of MOFs led to several application fields (*e.g.* gas separation/storage,^{74–78} drug-delivery,^{79,80} sensing,^{81,82} heterogeneous catalysis^{83–85}) and an increasing interest in both chemistry and material science, as demonstrated by the exponentially increasing number of publications in the past 30 years (Figure 1.8).⁸⁶ Furthermore, the interest in this class of materials is not exclusive of the academic world. Indeed, some MOFs are currently produced on an industrial scale. As an example, BASF SE produces zeolitic imidazolate frameworks (ZIFs) on ton scale commercialized by Aldrich.⁸⁷

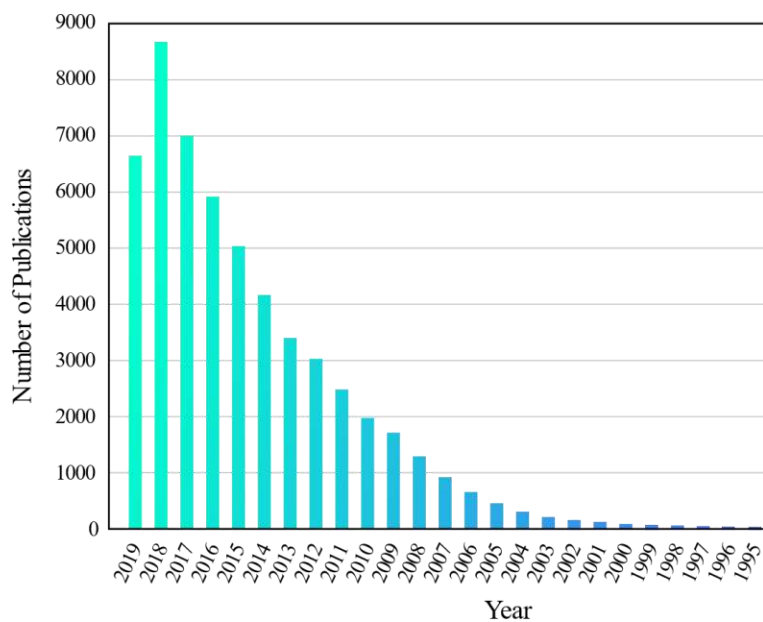


Figure 1.8 Analysis of a bibliographic research in the Web of Science based on the “*Metal-organic framework*” keyword (webofknowledge.com, accessed September 10th, 2019). *Top*: Representation of the number of publications *per* year from 1995 up to September 2019. *Bottom*: Representation of the publication fields according to the Web of Science categories.

1.6. Metal-organic Frameworks as CO₂ Adsorbents

Looking back to the specific characteristics a solid adsorbent should have (Section 1.2.1), MOFs appear as highly appealing competitors in carbon dioxide capture and separation. Indeed, they combine the “power” of a highly porous material with finely tuned porosity in terms of chemical and physical properties, thus enabling accessibility,

selectivity and reactivity of the framework towards the guest molecules. Hence, the resulting performances are expected to overpass those of their classic counterparts (zeolites, ACs, silicas, *etc.*) in terms of both capture and decomposition of the guest molecules.⁸⁸⁻⁹⁰ Besides, MOFs offer the advantage, *via* reticular chemistry,⁶² of predictable crystal structures, which can be further optimized *via* pre- or post-synthetic modifications.^{62,77} The knowledge and tuneability of their crystal structures have also the relevant advantage of allowing the understanding of the mechanisms underneath carbon dioxide capture or catalysis.^{74,91,92}

Initially, the researchers' attention was focused on the possibility of having ultrahigh porosity, paving the way to gas storage and allowing to compact large amounts of gases in a confined space for a long time. In 2005, Yaghi reported of a MOF, namely MOF-177 [$Zn_4O(BTB)_2$; BTB = 4,4',4''-benzene-1,3,5-triyl-tribenzoate; Brunauer-Emmett-Teller (BET) surface area $\sim 4500 \text{ m}^2 \text{ g}^{-1}$], which can capture and store nine times the amount of CO_2 that can fit in a gas cylinder at ambient temperature and pressure of 35 bar, showing a better capacity than zeolite 13X and activated carbons.⁷⁶ Then, the attention moved on the tunability of MOFs pore surface in order to enhance the framework affinity towards selective CO_2 capture in the condition typical of flue gases emissions, meaning mixed gas systems at low pressures.

MOFs, as other traditional adsorbents, interact with carbon dioxide through weak forces in specific binding sites of the pores. The adsorption process can thus be promoted by inserting in the framework smart sites, which can take advantage of the quadrupole moment of carbon dioxide (Table 1.1). Based on this, some efforts were made in studying possible adsorption sites, namely: *i*) open metal sites, *ii*) Lewis basic sites or *iii*) polar functional groups, together with a proper *iv*) pore size, *v*) flexibility and *vi*) hydrophobicity of the framework. Needless to say, in MOFs multiple functional groups can coexist.

1.7. Primary CO_2 Adsorption Sites in MOFs

In the following paragraphs a list of the recognized adsorption sites, together with some explicative examples, is proposed to the readers. The adsorption process cannot be

obviously explained by a single phenomenon. However, understanding the impact of the different components of a MOF can improve the design of advanced and better performing materials.

The introduction of *i) open metal sites* (OMSs) in SBUs was one of the most used strategies to improve carbon dioxide uptake, since they give a partial positive charge to the pore surface. The associated Q_{st} are high at low pressure, ensuring good uptake of CO_2 , thanks to end-on interactions between the metal ion and the gas,⁹³ and selectivity over molecules with weak dipole or quadrupole moment. The first results on the beneficial effects of OMSs on CO_2 adsorption were reported in 1998.⁹⁴ In 2005, HKUST-1 was found to adsorb up to 10 mmol g^{-1} of CO_2 at 42 bar and ambient temperature.⁷⁶ Following this impressive result, a lot of efforts were made in studying metal-organic frameworks with OMSs, among which: MIL-101, M-MOF-74 and NU-1000.⁹⁵⁻⁹⁷ As an example, the well-studied M-MOF-74 ($M = Mg^{2+}, Co^{2+}, Ni^{2+}, Zn^{2+}$) series adsorbs large amounts of CO_2 at low pressure with a maximum of 5.4 mmol g^{-1} at 0.1 bar and a $Q_{st} = 47 \text{ kJ mol}^{-1}$ for Mg-MOF-74 (Figure 1.9).^{96,98} However, MOFs with OMSs show a high affinity towards all the molecules with high polarity or quadrupole moment. Therefore, the water molecules present in flue gases terribly affect the CO_2 uptake through competitive binding with the OMSs.

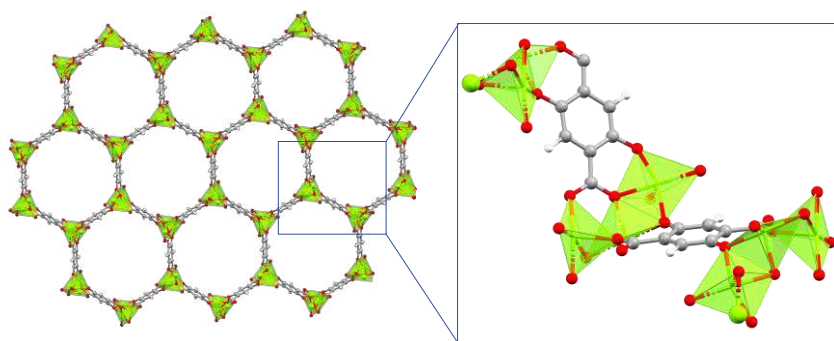


Figure 1.9 Representation of the crystal structure of Mg-MOF-74.⁸⁶ In the highlight, the magnification of the OMSs decorating the 1-dimensional hexagonal pores.

The incorporation of *ii) Lewis basic sites* took inspiration from the outstanding properties in adsorption and selectivity of MEA aqueous solutions and can be achieved

modifying either the SBU or the organic linker. Moreover, it can reduce the interactions with water molecules with respect to OMSs. A pioneer work was published by Professor Long's group,⁹⁹ where ethylenediamine was coordinated to the unsaturated metal centre of Cu-BTTri [$H_3BTTri = 1,3,5\text{-tris}(1H\text{-}1,2,3\text{-triazol-}5\text{-yl})\text{benzene}$] *via* post-synthetic modification (Figure 1.10 a). Unluckily, both the pristine and the modified MOF did not equate the amount of CO_2 adsorbed by Mg-MOF-74 at 298 K and 1 bar. However, after the incorporation of *N,N'*-dimethylethylenediamine, a better selectivity over N_2 and a higher amount of CO_2 adsorbed at low pressure were observed. The chemisorption process, associated to the high $Q_{st} = 90 \text{ kJ mol}^{-1}$ of the modified MOF, led to the formation of carbamates. The functionalization of the SBUs with diamine through post-synthetic modifications was found beneficial in adsorption; however, a partial loss of amines and consequent exchange with water molecules was observed over multiple cycles.^{100–102}

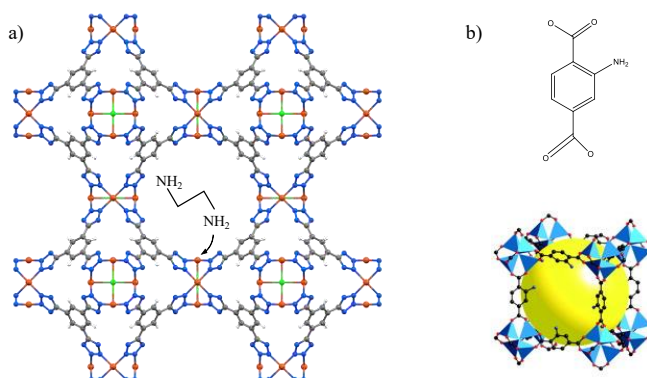


Figure 1.10 a) Schematic representation of the functionalization of Cu-BTTri through post-synthetic modification in correspondence of the OMSs.⁹⁹ b) *Top*: amine functionalized ligand used in the synthesis of IRMOF-3. *Bottom*: portion of the crystal structure of IRMOF-3.⁷⁶

As mentioned before, appending amine groups on the organic linker is an alternative approach to take advantage of Lewis bases. Representative examples can be found in both the previously mentioned isorecticular family of IRMOFs, where 2-amino-terephthalic acid ($NH_2\text{-}H_2BDC$) was used to synthesize IRMOF-3 (Figure 1.10 b),⁷⁶ and many other isorecticular MOFs, such as $NH_2\text{-}UiO\text{-}66$,¹⁰³ $NH_2\text{-}MIL\text{-}125$ ¹⁰⁴ or $NH_2\text{-}MIL\text{-}53$.¹⁰⁵ In the case of IRMOF-3, the presence of amines enhanced CO_2 uptake at 298 K and a pressure of 12.3 bar, passing from the 14.0 mmol/g of MOF-5 up to 14.7 mmol/g. A further example of the beneficial effect of appending amines on the ligand skeleton is

(Mg)IRMOF-74-III(CH₂NH₂).^{106,107} Indeed, even if its performance is not comparable to that of the non-functionalized parents, the presence of water during the adsorption process does not affect the total CO₂ uptake.

Nitrogen-containing linkers, as well, give to the resulting MOF Lewis basic sites. This is the reason why ligands including triazines, azoles and pyrimidines have been used as building unit for MOFs with Lewis basic sites.^{101,108–112} Among them, Cu-TDPAT, a *rht*-type MOF, was reported to adsorb 5.9 mmol g⁻¹ of CO₂ at 298 K and 1 bar (10.1 mmol g⁻¹ at 273 K and 1 bar) with an associated Q_{st} = 42 kJ mol⁻¹.¹⁰⁸

Last but not least, as anticipated before, the introduction of *iii*) *polar functional groups* on the organic linker can improve carbon dioxide adsorption capacity. The dipole moment of polar functionalities like -F, -Cl, -Br, -OH, -COOH, NO₂ and SO₃ can interact with the quadrupole moment of CO₂.^{113–116} The polar “tag” can be inserted directly during the synthesis of the MOF, using a functionalized organic ligand, or at a second stage through post-synthesis modification.

A different approach to make stronger host-guest interactions and improve CO₂ selectivity is *iv*) *pore size control*. Carbon dioxide has a small kinetic diameter (3.3 Å), thus microporous MOFs can be used as molecular sieves. Moreover, reduced pores favour the total uptake increasing the binding energies. To get a favourable pore size two different methods can be followed: firstly, modulating the pore size using organic linkers with a proper length. Secondly, searching for self-interpenetrated frameworks or for “pore space partition” (PSP).¹¹⁷ When PSP occurs, the original pores can be segmented in a designed fashion by inserting additional organic spacers or guest molecules. As an example, the case of study of SNU-70 ([Zn₄O-(CVB)₃]₃·13DEF·2H₂O) and SNU-71 ([Zn₄O-(CEB)₃]₃·6DEF·H₂O) (CVB = (*E*)-4-(2-carboxylatovinyl)benzoate, CEB = 4-(2-carboxylatoethyl)benzoate, DEF = *N,N*-diethylformamide) can be considered.¹¹⁸ The two MOFs have a very similar framework, the main difference is the length of the C-C bond on the organic linker. SNU-71, which has an interpenetrated framework, adsorb a larger amount of CO₂ at low pressure with respect to SNU-70 due to the smaller pore size.

Pore size can also be tuned taking advantage of *v*) *flexible* PCPs. Soft porous crystals can show a dynamic response - the so called “breathing” - sometimes associated to phase transitions, during the CO₂ adsorption process. SPCs adsorption isotherms are characterized by one or multiple steps at definite relative pressure(s) (Figure 1.11, left). Different guest molecules lead to different pore disclosure in terms of both relative pressure and pore opening. As a consequence, since the “gate opening” effect is strictly related to the guest molecule, it can be used for gas separation and purification, as recently reported by Long and co-workers.¹¹⁹ The mentioned work reports of near-perfect CO₂/CH₄ selectivity through the flexibility of Co(bdp) [H₂bdp = 1,4-bis(pyrazol-4-yl)benzene]. Co(bdp) changes the relative pressure of pore opening depending on the guest molecules, as shown in Figure 1.11, allowing a good selectivity for carbon dioxide.

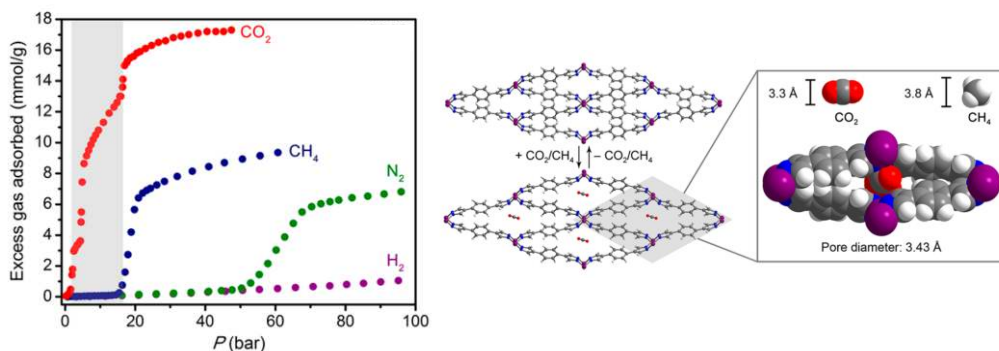


Figure 1.11 *Left*: single-component adsorption isotherms of Co(bdp) for CO₂, CH₄, N₂, and H₂ at 298 K as reported in 119. *Right*: interpretation of the selective adsorption of CO₂ over CH₄. Figures from Taylor *et al.*¹¹⁹

However, one of the main challenges in post-combustion capture is the working capacity of the adsorbent in wet conditions. In order to limit this drawback, the possibility of using *vi*) *hydrophobic* PCPs was also explored.⁷⁴ An example can be found in the hydrophobic series of zeolite imidazolate frameworks (ZIFs), specifically ZIF-300 [Zn(2-mIm)_{0.86}(bbIm)_{1.14}], ZIF-301 [Zn(2-mIm)_{0.94}(cbIm)_{1.06}], ZIF-302 [Zn(2-mIm)_{0.67}(mbIm)_{1.33}] (2-mIm = 2-methylimidazolate; bbIm = 5(6)-bromobenzimidazolate; cbIm = 5(6)-chlorobenzimidazolate; mbIm = 5(6)-methylbenzimidazolate), which show a comparable carbon dioxide adsorption capacity both under dry conditions and in the presence of 80% humidity.¹²⁰ Thanks to their hydrophobic behaviour, these ZIFs show a

good CO₂/H₂O selectivity and a reusability without losing performance for at least three cycles. Nonetheless, due to their low affinity for carbon dioxide they suffer from poor uptake. Post-synthetic modification of the pore walls with hydrophobic functionalities was also studied. An example can be found in MOF-5, whose pores were loaded with 1,2-diethynylbenzene monomers to form polynaphthylene (PN). The resulting PN-MOF-5 showed a doubled capacity for CO₂ adsorption and a better CO₂/N₂ selectivity vs. MOF-5 and maintained a 90% adsorption capacity even under humid conditions.^{121,122}

It should be clear that the efficiency of an adsorbent is strictly related to its selectivity and capacity. All the variables and examples listed above are the expression of the efforts made for enhancing the interactions between adsorbate and adsorbent, *i.e.* thermodynamic affinity (*i.e.* Q_{st}) between them.

Table 1.2 collects a non-exhaustive list of PCPs studied as CO₂ adsorbents in terms of capacity, selectivity and isosteric heat of adsorption, together with the type of primary adsorption site. It is important to note that the values reported are at low pressure and ambient temperature to simulate the conditions of post-combustion adsorption from flue gases.

Comparing the different performances related to different primary adsorption sites some observations can be done:

- The insertion of adsorption sites enhances the performance with respect to the non-functionalized parent;
- PCPs containing open-metal sites show a higher affinity, selectivity and capacity; however, they lose their selectivity in presence of water;
- The presence of Lewis basic functionalities results in high affinity and selectivity, but also in this case the selectivity decreases under wet conditions if the amines are appended to the OMSs;

A successful strategy under real conditions could be the use of heteroatomic frameworks with tailored pore metrics and hydrophobicity in order to exclude the competition of other guest molecules during adsorption. The combination of different tags, as well, could lead to a positive effect in gas adsorption combining selectivity and host-guest interactions, enhancing the desired properties and limiting the intrinsic drawbacks.

Table 1.2 Summary of MOFs studied as carbon dioxide adsorbents and corresponding capacity, affinity and selectivity over N₂.

	Pressure [bar]	Temperature [K]	Capacity [mmol g ⁻¹]	Q _{st} [kJ mol ⁻¹]	Selectivity
OMS					
CuBTTri ⁹⁹	1	298	3.2	-	10
FeBTT ¹²³	1	298	3.1	-	-
Mg-MOF-74 ⁹⁸	1	298	8.0	47	44
Zn-MOF-74 ⁹⁸	1	296	5.8	-	-
Ni-MOF-74 ⁹⁸	1	296	5.8	41	30
Co-MOF-74 ⁹⁸	1	296	7.0	37	-
MIL-101(Cr) ⁹⁵	-	-	-	62	-
H-KUST-1 ⁷⁶	1	298	4.1	35	100
Mg ₂ (dobpdc) ¹²⁴	1	298	6.4	-	-
LBS					
NH ₂ -MIL125 ¹⁰⁴	1	298	2.2	-	-
IRMOF-74-III-(CH ₂ NH ₂) ₂ ¹⁰⁷	1	298	3.0	-	-
IRMOF-74-III-CH ₂ NH ₂ ¹⁰⁶	1	298	3.3	-	-
CuBTTri-en ⁹⁹	1	298	1.27	90	44
Bio-MOF-11 ¹²⁵	1	298	4.1	-	-
Cu-TDPAT ¹⁰⁸	1	298	5.9	42	-
IFMC-1 ¹²⁶	1	298	2.7	-	-
PFG					
TMOF-1 ¹¹⁵	1	298	1.4	-	-
Zn(BPZNO ₂) ¹¹⁶	1	298	4.4	20.5	15
USTC-53 ¹²⁷	1	298	2.1	-	-

Gravimetric weight uptake, Q_{st} and selectivity are given at low pressure and room temperature, in order to mimic the operating conditions of post-combustion capture. OMS: open-metal site; LBS: Lewis basic site; PFG: polar functional group.

1.8. Conclusions

Carbon capture and storage, together with the negative emissions technologies (NETs), are key to limiting global warming up to 1.5 K with respect to the pre-industrial era. Post-combustion capture can be a practical strategy to face GHGs emissions before other greener energies will be viable.

An overview on the currently used technologies in power plants for post-combustion carbon capture has been proposed. MEA aqueous solutions show a high affinity for carbon dioxide and have a very competitive cost of production; nonetheless, the reactivation process is energy consuming due to the high temperatures required. Solid adsorbents are a potential category of materials to be used in CCS instead of amine solutions; however, they suffer from some drawbacks such as cost of production, selectivity and capacity. The properties and limits of traditional inorganic solid adsorbents, namely: activated carbons, zeolites and mesoporous silica, as CO₂ adsorbents were outlined.

Metal-organic frameworks have raised as an alternative to satisfy the CO₂ cycle. A lot of progress and studies have been done in this field, as demonstrated by the high number of publications from 1990 up to date. After an initial interest in the fundamental aspects of the interactions between CO₂ and the host framework, today the attention is moving towards real operating conditions, that are still challenging. The main features influencing carbon dioxide adsorption and selectivity have been listed above. Selective adsorption in presence of water or contaminants, high temperatures stability, low costs of production and regeneration and long-term use are still challenging and far to be reached.

1.9. References

- (1) Sustainable Development Goals. <https://www.un.org/sustainabledevelopment/> (accessed Sep 9, 2019).
- (2) COP21. <http://www.cop21paris.org/>.
- (3) *Intergovernmental Panel on Climate Change 2014 (IPCC 2014)*; Geneva, Switzerland, 2014.
- (4) *Intergovernmental Panel on Climate Change 2018 (IPCC 2018)*; Geneva, Switzerland, 2018.
- (5) Davis, S. J.; Caldeira, K.; Matthews, H. D. Future CO₂ Emissions and Climate Change from Existing Energy Infrastructure. *Science* **2010**, *329* (September), 1330–1334.
- (6) Thonemann, N.; Pizzol, M. Consequential Life Cycle Assessment of Carbon Capture and Utilization Technologies within the Chemical Industry. *Energy Environ. Sci.* **2019**, No. 12, 2253–2263.
- (7) Shi, X.; Xiao, H.; Azarabadi, H.; Song, J.; Wu, X.; Chen, X.; Lackner, K. S. Sorbents for Direct Capture of CO₂ from Ambient Air. *Angew. Chem., Int. Ed* **2019**.
- (8) <https://www.eea.europa.eu/data-and-maps/data/data-viewers/greenhouse-gases-viewer> (accessed Apr 30, 2019).
- (9) <https://www.epa.gov/ghgemissions/inventory-us-greenhouse-gas-emissions-and-sinks> (accessed Apr 30, 2019).
- (10) Petit, J.-R.; Jouzel, J.; Raynaud, D.; Barkov, N. I.; Barnola, J.-M.; Basile, I.; Bender, M.; Chappellaz, J.; Davis, M.; Delaygue, G.; et al. Climate and Atmospheric History of the Past 420,000 Years from the Vostok Ice Core, Antarctica. *Nature* **1999**, *399* (6735), 429–436.
- (11) <https://www.esrl.noaa.gov/gmd/dv/iadv/graph.php?code=MLO&program=ccgg&type=ts> (accessed Apr 30, 2019)
- (12) CO₂ Emissions from Fuel Combustion. International Energy Agency: Paris, France 2018, pp 1–51.
- (13) Koytoumpa, E. I.; Bergins, C.; Kakaras, E. The CO₂ Economy: Review of CO₂ Capture and Reuse Technologies. *J. Supercrit. Fluids* **2018**, *132* (July 2017), 3–16.
- (14) Bui, M.; Adjiman, C. S.; Bardow, A.; Anthony, E. J.; Boston, A.; Brown, S.; Fennell, P. S.; Fuss, S.; Galindo, A.; Hackett, L. A.; et al. Carbon Capture and Storage (CCS): The Way Forward. *Energy Environ. Sci.* **2018**, *11* (5), 1062–1176.
- (15) Walters, M. S.; Edgar, T. F.; Rochelle, G. T. Regulatory Control of Amine Scrubbing for CO₂ Capture from Power Plants. *Ind. Eng. Chem. Res.* **2016**, *55* (16), 4646–4657.

- (16) Yang, H.; Xu, Z.; Fan, M.; Slimane, R. B.; Bland, A. E.; Wright, I. Progress in Carbon Dioxide Separation and Capture: A Review. *J. Environ. Sci.* **2008**, *20*, 14–27.
- (17) Hinkov, I.; Lamari, F. D.; Langlois, P.; Dicko, M.; Chilev, C.; Pentchev, I. Carbon Dioxide Capture by Adsorption (Review). *J. Chem. Technol. Metall.* **2016**, *51* (6), 609–626.
- (18) Younas, M.; Sohail, M.; Kong, L. L.; Bashir, M. J. K.; Sethupathi, S. Feasibility of CO₂ Adsorption by Solid Adsorbents: A Review on Low-Temperature Systems. *Int. J. Environ. Sci. Technol.* **2016**, *13* (7), 1839–1860.
- (19) MacDowell, N.; Florin, N.; Buchard, A.; Hallett, J.; Galindo, A.; Jackson, G.; Adjiman, C. S.; Williams, C. K.; Shah, N.; Fennell, P. An Overview of CO₂ Capture Technologies. *Energy Environ. Sci.* **2010**, *3* (11), 1645–1669.
- (20) Boot-Handford, M. E.; Abanades, J. C.; Anthony, E. J.; Blunt, M. J.; Brandani, S.; Mac Dowell, N.; Fernández, J. R.; Ferrari, M. C.; Gross, R.; Hallett, J. P.; et al. Carbon Capture and Storage Update. *Energy Environ. Sci.* **2014**, *7* (1), 130–189.
- (21) Stauffer, P. H.; Keating, G. N.; Middleton, R. S.; Viswanathan, H. S.; Berchtold, K. A.; Singh, R. P.; Pawar, R. J.; Mancino, A. Greening Coal: Breakthroughs and Challenges in Carbon Capture and Storage. *Environ. Sci. Technol.* **2011**, *45* (20), 8597–8604.
- (22) Wang, Q.; Luo, J.; Zhong, Z.; Borgna, A. CO₂ Capture by Solid Adsorbents and Their Applications: Current Status and New Trends. *Energy Environ. Sci.* **2011**, *4* (1), 42–55.
- (23) 20 Years of Carbon Capture and Storage. International Energy Agency: Paris, France 2016.
- (24) Vaccarelli, M.; Carapellucci, R.; Giordano, L. Energy and Economic Analysis of the CO₂ capture from Flue Gas of Combined Cycle Power Plants. *Energy Procedia* **2014**, *45*, 1165–1174.
- (25) Feron, P. H. M. Exploring the Potential for Improvement of the Energy Performance of Pulverized Coal Fired Power Stations with Post-Combustion Capture of Carbon Dioxide. *Int. J. Greenh. Gas Control* **2010**, 152–160.
- (26) Kohl, A. L.; Nielsen, R. *Gas Separation*, 5th ed.; Gulf Publishing Company: Houston, Texas, 1997.
- (27) Bottoms, R. R. Process for Separating Acidic Gases, United States Patent Office. 1783901, 1930.
- (28) Cheng-hsiu, Y.; Chih-hung, H.; Chung-sung, T. A Review of CO₂ Capture by Absorption and Adsorption. *Aerosol Air Qual. Res.* **2012**, *12* (5), 745–769.
- (29) Patel, H. A.; Byun, J.; Yavuz, C. T. Carbon Dioxide Capture Adsorbents: Chemistry and Methods. *ChemSusChem* **2017**, *10* (7), 1303–1317.

- (30) Mazari, S. A.; Si Ali, B.; Jan, B. M.; Saeed, I. M.; Nizamuddin, S. An Overview of Solvent Management and Emissions of Amine-Based CO₂ Capture Technology. *Int. J. Greenh. Gas Control* **2015**, *34*, 129–140.
- (31) Rubin, E. S.; Davison, J. E.; Herzog, H. J. The Cost of CO₂ Capture and Storage. *Int. J. Greenh. Gas Control* **2015**, *40*, 378–400.
- (32) Chen, S.; Lucier, B. E. G.; Boyle, P. D.; Huang, Y. Understanding the Fascinating Origins of CO₂ Adsorption and Dynamics in MOFs. *Chem. Mater.* **2016**, *28* (16), 5829–5846.
- (33) Siriwardane, R. V.; Shen, M. S.; Fisher, E. P.; Poston, J. A. Adsorption of CO₂ on Molecular Sieves and Activated Carbon. *Energy and Fuels* **2001**, *15* (2), 279–284.
- (34) Mukherjee, A.; Okolie, J. A.; Abdelrasoul, A.; Niu, C.; Dalai, A. K. Review of Post-Combustion Carbon Dioxide Capture Technologies Using Activated Carbon. *J. Environ. Sci.* **2019**, *83*, 46–63.
- (35) Dodevski, V.; Janković, B.; Stojmenović, M.; Krstić, S.; Popović, J.; Pagnacco, M. C.; Popović, M.; Pašalić, S. Plane Tree Seed Biomass Used for Preparation of Activated Carbons (AC) Derived from Pyrolysis. Modeling the Activation Process. *Colloids Surfaces A Physicochem. Eng. Asp.* **2017**, *522*, 83–96.
- (36) Zhao, Y.; Liu, X.; Han, Y. Microporous Carbonaceous Adsorbents for CO₂ Separation via Selective Adsorption. *RSC Adv.* **2015**, *5* (38), 30310–30330.
- (37) Hao, G. P.; Jin, Z. Y.; Sun, Q.; Zhang, X. Q.; Zhang, J. T.; Lu, A. H. Porous Carbon Nanosheets with Precisely Tunable Thickness and Selective CO₂ Adsorption Properties. *Energy Environ. Sci.* **2013**, *6* (12), 3740–3747.
- (38) Alabadi, A.; Razzaque, S.; Yang, Y.; Chen, S.; Tan, B. Highly Porous Activated Carbon Materials from Carbonized Biomass with High CO₂ Capturing Capacity. *Chem. Eng. J.* **2015**, *281*, 606–612.
- (39) Herzog, H.; Hatton, A. Advanced Post-Combustion CO₂ Capture *Clean Air Task Force*, **2009**, *1*, 39.
- (40) Bonenfant, D.; Kharoune, M.; Niquette, P.; Mimeault, M.; Hausler, R. Advances in Principal Factors Influencing Carbon Dioxide Adsorption on Zeolites. *Sci. Technol. Adv. Mater.* **2008**, *9* (1).
- (41) Nugent, P.; Giannopoulou, E. G.; Burd, S. D.; Elemento, O.; Giannopoulou, E. G.; Forrest, K.; Pham, T.; Ma, S.; Space, B.; Wojtas, L.; et al. Porous Materials with Optimal Adsorption Thermodynamics and Kinetics for CO₂ separation. *Nature* **2013**, *495* (7439), 80–84.
- (42) Riboldi, L.; Bolland, O. Overview on Pressure Swing Adsorption (PSA) as CO₂ Capture Technology: State-of-the-Art, Limits and Potentials. *Energy Procedia* **2017**, *114* (1876), 2390–2400.
- (43) Montanari, T.; Finocchio, E.; Salvatore, E.; Garuti, G.; Giordano, A.; Pistarino, C.; Busca, G. CO₂ Separation And Landfill Biogas Upgrading: A Comparison Of

- 4A And 13X Zeolite Adsorbents. *Energy* **2011**, *36* (1), 314–319.
- (44) Deng, H.; Yi, H.; Tang, X.; Yu, Q.; Ning, P.; Yang, L. Adsorption Equilibrium For Sulfur Dioxide, Nitric Oxide, Carbon Dioxide, Nitrogen on 13X and 5A Zeolites. *Chem. Eng. J.* **2012**, *188*, 77–85.
- (45) Yi, H.; Deng, H.; Tang, X.; Yu, Q.; Zhou, X.; Liu, H. Adsorption Equilibrium And Kinetics For SO₂, NO, CO₂ On Zeolites FAU and LTA. *J. Hazard. Mater.* **2012**, *203–204*, 111–117.
- (46) Aprea, P.; Caputo, D.; Gargiulo, N.; Iucolano, F.; Pepe, F. Modeling Carbon Dioxide Adsorption On Microporous Substrates: Comparison Between Cu-BTC Metal-Organic Framework and 13X Zeolitic Molecular Sieve. *J. Chem. Eng. Data* **2010**, *55* (9), 3655–3661.
- (47) Brandani, F.; Ruthven, D. M. The effect of water on the adsorption of CO₂ and C₃H₈ on type X zeolites. *Ind. Eng. Chem. Res.* **2004**, *43*, 8339–8344.
- (48) Martin-Calvo, A.; Parra, J. B.; Ania, C. O.; Calero, S. Insights On The Anomalous Adsorption Of Carbon Dioxide In LTA Zeolites. *J. Phys. Chem. C* **2014**, *118* (44), 25460–25467.
- (49) Brühwiler, D. Postsynthetic Functionalization Of Mesoporous Silica. *Nanoscale* **2010**, *2* (6).
- (50) Oschatz, M.; Antonietti, M. A Search For Selectivity To Enable CO₂ Capture with porous Adsorbents. *Energy Environ. Sci.* **2018**, *11* (1), 57–70.
- (51) Gargiulo, N.; Pepe, F.; Caputo, D. Adsorption By Functionalized Nanoporous Materials: A Review. *J. Nanosci. Nanotechnol.* **2014**, *14* (2), 1811–1822.
- (52) Jiao, J.; Cao, J.; Xia, Y.; Zhao, L. Improvement of Adsorbent Materials for CO₂ Capture by Amine Functionalized Mesoporous Silica with Worm-Hole Framework Structure. *Chem. Eng. J.* **2016**, *306*, 9–16.
- (53) Yaghi, O. M.; Li, H. Hydrothermal Synthesis of a Metal-Organic Framework Containing Large Rectangular Channels. *J. Am. Chem. Soc.* **1995**, *117* (41), 10401–10402.
- (54) Batten, S. R.; Champness, N. R.; Chen, X.; Garcia-martinez, J.; Kitagawa, S.; Öhrström, L.; O’Keeffe, M.; Suh, M. P.; Reedijk, J. Terminology of Metal–Organic Frameworks and Coordination Polymers (IUPAC Recommendations 2013). *Pure Appl. Chem.* **2013**, *85* (8), 1715–1724.
- (55) Li, H.; Eddaoudi, M.; O’Keeffe, M.; Yaghi, O. M. Design and Synthesis of an Exceptionally Stable and Highly Porous Metal-Organic Framework. *Nature* **1999**, *402* (November), 276–279.
- (56) Chen, L.; Mowat, J. P. S.; Fairen-Jimenez, D.; Morrison, C. A.; Thompson, S. P.; Wright, P. A.; Düren, T. Elucidating the Breathing of the Metal-Organic Framework MIL-53(Sc) with Ab Initio Molecular Dynamics Simulations and in Situ X-Ray Powder Diffraction Experiments. *J. Am. Chem. Soc.* **2013**, *135* (42), 15763–15773.

- (57) Herm, Z. R.; Wiers, B. M.; Mason, J. A.; van Baten, J. M.; Hudson, M. R.; Zajdel, P.; Brown, C. M.; Masciocchi, N.; Krishna, R.; Long, J. R. Separation of Hexane Isomers in a Metal-Organic Framework with Triangular Channels. *Science* **2013**, *340* (May), 960–964.
- (58) Horcajada, P.; Surblé, S.; Serre, C.; Hong, D. Y.; Seo, Y. K.; Chang, J. S.; Grenèche, J. M.; Margiolaki, I.; Férey, G. Synthesis and Catalytic Properties of MIL-100(Fe), an Iron(III) Carboxylate with Large Pores. *Chem. Commun.* **2007**, *100* (27), 2820–2822.
- (59) Férey, G. Hybrid Porous Solids: Past, Present, Future. *Chem. Soc. Rev.* **2008**, *37* (1), 191–214.
- (60) Kandiah, M.; Nilsen, M. H.; Usseglio, S.; Jakobsen, S.; Olsbye, U.; Tilset, M.; Larabi, C.; Quadrelli, E. A.; Bonino, F.; Lillerud, K. P. Synthesis and Stability of Tagged UiO-66 Zr-MOFs. *Chem. Mater.* **2010**.
- (61) Eddaoudi, M.; Kim, J.; Rosi, N.; Vodak, D.; Wachter, J.; O’Keeffe, M.; Yaghi, O. M. Systematic Design of Pore Size and Functionality in Isoreticular MOFs and Their Application in Methane Storage. *Science* **2002**, *295* (5554), 469–472.
- (62) Yaghi, O. M.; Kalmutzki, M. J.; Diercks, C. S. *Introduction to Reticular Chemistry: Metal-Organic Frameworks and Covalent Organic Frameworks.*; Wiley-VCH: Weinheim, Germany, 2019.
- (63) Eddaoudi, M.; Kim, J.; Rosi, N.; Vodak, D.; Wachter, J.; Keffe, M. O.; Yaghi, O. M.; Eddaoudi, M.; Kimrn, J.; Rosi, N.; et al. Systematic Design of Pore Size and Functionality in Isoreticular MOFs and Their Application in Methane Storage. *American Association for the Advancement of Science* **2002**, *295* (5554), 469–472.
- (64) Castillo-Blas, C.; López-Salas, N.; Gutiérrez, M. C.; Puente-Orench, I.; Gutiérrez-Puebla, E.; Ferrer, M. L.; Monge, M. Á.; Gándara, F. Encoding Metal-Cation Arrangements in Metal-Organic Frameworks for Programming the Composition of Electrocatalytically Active Multimetal Oxides. *J. Am. Chem. Soc.* **2019**, *141* (4), 1766–1774.
- (65) Rada, Z. H.; Abid, H. R.; Sun, H.; Shang, J.; Li, J.; He, Y.; Liu, S.; Wang, S. Effects of -NO₂ and -NH₂ functional Groups in Mixed-Linker Zr-Based MOFs on Gas Adsorption of CO₂ and CH₄. *Prog. Nat. Sci. Mater. Int.* **2018**, *28* (2), 160–167.
- (66) Reinsch, H.; Waitschat, S.; Stock, N. Mixed-Linker MOFs with CAU-10 Structure: Synthesis and Gas Sorption Characteristics. *Dalt. Trans.* **2013**, *42* (14), 4840.
- (67) Eum, K.; Jayachandrababu, K. C.; Rashidi, F.; Zhang, K.; Leisen, J.; Graham, S.; Lively, R. P.; Chance, R. R.; Sholl, D. S.; Jones, C. W.; et al. Highly Tunable Molecular Sieving and Adsorption Properties of Mixed-Linker Zeolitic Imidazolate Frameworks. *J. Am. Chem. Soc.* **2015**, *137* (12), 4191–4197.
- (68) Bunck, D. N.; Dichtel, W. R. Mixed Linker Strategies for Organic Framework

- Functionalization. *Chem. - A Eur. J.* **2013**, *19* (3), 818–827. h
- (69) Masoomi, M. Y.; Morsali, A.; Dhakshinamoorthy, A.; Garcia, H. Mixed-Metal MOFs: Unique Opportunities in Metal-Organic Framework (MOF) Functionality and Design. *Angew. Chem., Int. Ed* **2019**, 2–20.
- (70) Szécsényi, A.; Li, G.; Gascon, J.; Pidko, E. A. Unraveling Reaction Networks behind the Catalytic Oxidation of Methane with H₂O₂ over a Mixed-Metal MIL-53(Al,Fe) MOF Catalyst. *Chem. Sci.* **2018**, *9* (33), 6765–6773.
- (71) Kondo, M.; Yoshitomi, T.; Seki, K.; Matsuzaka, H.; Kitagawa, S. Three-Dimensional Framework with Channeling Cavities for Small Molecules: {[M₂(4,4'-Bpy)₃(NO₃)₄]·XH₂O}_n (M = Co, Ni, Zn). *Angew. Chem. Int. Ed.* **1997**, *36* (16), 1725–1727.
- (72) Horike, S.; Shimomura, S.; Kitagawa, S. Soft Porous Crystals. *Nat. Chem.* **2009**, *1* (9), 695–704.
- (73) Schneemann, A.; Bon, V.; Schwedler, I.; Senkovska, I.; Kaskel, S.; Fischer, R. A. Flexible Metal-Organic Frameworks. *Chem. Soc. Rev.* **2014**, *43* (16), 6062–6096.
- (74) Trickett, C. A.; Helal, A.; Al-Maythaly, B. A.; Yamani, Z. H.; Cordova, K. E.; Yaghi, O. M. The Chemistry of Metal-Organic Frameworks for CO₂ Capture, Regeneration and Conversion. *Nat. Rev. Mater.* **2017**, *2* (8), 1–16.
- (75) Nandasiri, M. I.; Jambovane, S. R.; McGrail, B. P.; Schaef, H. T.; Nune, S. K. Adsorption, Separation, and Catalytic Properties of Densified Metal-Organic Frameworks. *Coordination Chemistry Reviews.* **2016**.
- (76) Millward, A. R.; Yaghi, O. M. Metal-Organic Frameworks with Exceptionally High Capacity for Storage of Carbon Dioxide at Room Temperature. *J. Am. Chem. Soc.* **2005**, *127* (51), 17998–17999.
- (77) Mon, M.; Tiburcio, E.; Ferrando-Soria, J.; Gil San Millán, R.; Navarro, J. A. R.; Armentano, D.; Pardo, E. A Post-Synthetic Approach Triggers Selective and Reversible Sulphur Dioxide Adsorption on a Metal-Organic Framework. *Chem. Commun.* **2018**, *54* (65), 9063–9066.
- (78) Giménez-Marqués, M.; Calvo Galve, N.; Palomino, M.; Valencia, S.; Rey, F.; Sastre, G.; Vitorica-Yrezábal, I. J.; Jiménez-Ruiz, M.; Rodríguez-Velamazán, J. A.; González, M. A.; et al. Gas Confinement in Compartmentalized Coordination Polymers for Highly Selective Sorption. *Chem. Sci.* **2017**, *8* (4), 3109–3120.
- (79) Giménez-Marqués, M.; Hidalgo, T.; Serre, C.; Horcajada, P. Nanostructured Metal-Organic Frameworks and Their Bio-Related Applications. *Coord. Chem. Rev.* **2016**, *307*, 342–360.
- (80) Rojas, S.; Carmona, F. J.; Maldonado, C. R.; Horcajada, P.; Hidalgo, T.; Serre, C.; Navarro, J. A. R.; Barea, E. Nanoscaled Zinc Pyrazolate Metal-Organic Frameworks as Drug-Delivery Systems. *Inorg. Chem.* **2016**, *55* (5), 2650–2663.
- (81) Müller-Buschbaum, K.; Beuerle, F.; Feldmann, C. MOF Based Luminescence Tuning and Chemical/Physical Sensing. *Microporous Mesoporous Mater.* **2015**,

- 216, 171–199.
- (82) Yi, F. Y.; Chen, D.; Wu, M. K.; Han, L.; Jiang, H. L. Chemical Sensors Based on Metal–Organic Frameworks. *Chempluschem* **2016**, *81* (8), 675–690.
- (83) Blandez, J. F.; Santiago-Portillo, A.; Navalón, S.; Giménez-Marqués, M.; Álvaro, M.; Horcajada, P.; García, H. Influence of Functionalization of Terephthalate Linker on the Catalytic Activity of UiO-66 for Epoxide Ring Opening. *J. Mol. Catal. A Chem.* **2016**, *425*, 332–339.
- (84) Majewski, M. B.; Noh, H.; Islamoglu, T.; Farha, O. K. NanoMOFs: Little Crystallites for Substantial Applications. *J. Mater. Chem. A* **2018**, *6* (17), 7338–7350.
- (85) Aguado, S.; Canivet, J.; Farrusseng, D. Engineering Structured MOF at Nano and Macroscales for Catalysis and Separation. *J. Mater. Chem.* **2011**, *21* (21), 7582–7588.
- (86) <http://apps.webofknowledge.com/> (accessed Sep 10, 2019).
- (87) BASOLITE MOF www.sigma-aldrich.com or at www.mof.basf.com.
- (88) Kuppler, R. J.; Timmons, D. J.; Fang, Q.-R.; Li, J.-R.; Makal, T. A.; Young, M. D.; Yuan, D.; Zhao, D.; Zhuang, W.; Zhou, H.-C. Potential Applications of Metal–Organic Frameworks. *Coord. Chem. Rev.* **2009**.
- (89) Li, J. R.; Kuppler, R. J.; Zhou, H. C. Selective Gas Adsorption and Separation in Metal–Organic Frameworks. *Chem. Soc. Rev.* **2009**, *38* (5), 1477–1504.
- (90) Morris, R. E.; Wheatley, P. S. Gas Storage in Nanoporous Materials. *Angew. Chem., Int. Ed* **2008**, *47* (27), 4966–4981.
- (91) Ding, M.; Flaig, R. W.; Jiang, H.-L.; Yaghi, O. M. Carbon Capture and Conversion Using Metal–Organic Frameworks and MOF-Based Materials. *Chem. Soc. Rev.* **2019**, *48* (10), 2783–2828.
- (92) Liu, J.; Wei, Y.; Zhao, Y. Trace Carbon Dioxide Capture by Metal–Organic Frameworks. *ACS Sustain. Chem. Eng.* **2019**, *7* (1), 82–93.
- (93) Kong, X.; Scott, E.; Ding, W.; Mason, J. A.; Long, J. R.; Reimer, J. A. CO₂ Dynamics in a Metal–Organic Framework with Open Metal Sites. *J. Am. Chem. Soc.* **2012**, *134* (35), 14341–14344.
- (94) Li, H.; Davis, C. E.; Groy, T. L.; Kelley, D. G.; Yaghi, O. M. Coordinatively Unsaturated Metal Centers in the Extended Porous Framework of Zn₃(BDC)₃·6CH₃OH (BDC = 1,4-Benzenedicarboxylate). *J. Am. Chem. Soc.* **1998**, *120* (9), 2186–2187.
- (95) Llewellyn, P. L.; Bourrelly, S.; Serre, C.; Vimont, A.; Daturi, M.; Hamon, L.; Weireld, G. De; Chang, J.; Hong, D.; Hwang, Y. K.; et al. High Uptakes of CO₂ and CH₄ in Mesoporous Metal s Organic Frameworks MIL-100 and MIL-101. *Langmuir* **2008**, *24*, 7245–7250.
- (96) Queen, W. L.; Hudson, M. R.; Bloch, E. D.; Mason, J. A.; Gonzalez, M. I.; Lee,

- J. S.; Gygi, D.; Howe, J. D.; Lee, K.; Darwish, T. A.; et al. Comprehensive Study of Carbon Dioxide Adsorption in the Metal–Organic Frameworks $M^2(\text{Dobdc})$ ($M = \text{Mg, Mn, Fe, Co, Ni, Cu, Zn}$). *Chem. Sci.* **2014**, *5* (12), 4569–4581.
- (97) Farha, O. K.; Özgür Yazaydın, A.; Eryazici, I.; Malliakas, C. D.; Hauser, B. G.; Kanatzidis, M. G.; Nguyen, S. T.; Snurr, R. Q.; Hupp, J. T. De Novo Synthesis of a Metal–Organic Framework Material Featuring Ultrahigh Surface Area and Gas Storage Capacities. *Nat. Chem.* **2010**, *2* (11), 944–948.
- (98) Caskey, S. R.; Wong-Foy, A. G.; Matzger, A. J. Dramatic Tuning of Carbon Dioxide Uptake via Metal Substitution in a Coordination Polymer with Cylindrical Pores. *J. Am. Chem. Soc.* **2008**, *130* (33), 10870–10871.
- (99) Demessence, A.; D’Alessandro, D. M.; Foo, M. L.; Long, J. R. Strong CO₂ Binding in a Water-Stable, Triazolate-Bridged Metal–Organic Framework Functionalized with Ethylenediamine. *J. Am. Chem. Soc.* **2009**, *131* (25), 8784–8786.
- (100) Jo, H.; Lee, W. R.; Kim, N. W.; Jung, H.; Lim, K. S.; Kim, J. E.; Kang, D. W.; Lee, H.; Hiremath, V.; Seo, J. G.; et al. Fine-Tuning of the Carbon Dioxide Capture Capability of Diamine-Grafted Metal–Organic Framework Adsorbents Through Amine Functionalization. *ChemSusChem* **2017**, *9*, 1–11.
- (101) McDonald, T. M.; D’Alessandro, D. M.; Krishna, R.; Long, J. R. Enhanced Carbon Dioxide Capture upon Incorporation of N,N'- Dimethylethylenediamine in the Metal–Organic Framework CuBTri. *Chem. Sci.* **2011**, *2*, 2022–2028.
- (102) Milner, P. J.; Siegelman, R. L.; Forse, A. C.; Gonzalez, M. I.; Runčevski, T.; Martell, J. D.; Reimer, J. A.; Long, J. R. A Diaminopropane-Appended Metal–Organic Framework Enabling Efficient CO₂ Capture from Coal Flue Gas via a Mixed Adsorption Mechanism. *J. Am. Chem. Soc.* **2017**, *139* (38), 13541–13553.
- (103) Yang, Q.; Wiersum, A. D.; Llewellyn, P. L.; Guillerm, V.; Serre, C.; Maurin, G. Functionalizing Porous Zirconium Terephthalate UiO-66(Zr) for Natural Gas Upgrading: A Computational Exploration. *Chem. Commun.* **2011**, *47*, 9603–9605.
- (104) Kim, S. N.; Kim, J.; Kim, H. Y.; Cho, H. Y.; Ahn, W. S. Adsorption/Catalytic Properties of MIL-125 and NH₂-MIL-125. *Catal. Today* **2013**, *204*, 85–93.
- (105) Couck, S.; Denayer, J. F. M.; Baron, G. V.; Rémy, T.; Gascon, J.; Kapteijn, F. An Amine-Functionalized MIL-53 Metal–Organic Framework with Large Separation Power for CO₂ and CH₄. *J. Am. Chem. Soc.* **2009**, *131*, 6326–6327.
- (106) Fracaroli, A. M.; Furukawa, H.; Suzuki, M.; Dodd, M.; Okajima, S.; Gándara, F.; Reimer, J. A.; Yaghi, O. M. Metal–Organic Frameworks with Precisely Designed Interior for Carbon Dioxide Capture in the Presence of Water. *J. Am. Chem. Soc.* **2014**, *136*, 8863–8866.
- (107) Flaig, R. W.; Osborn Popp, T. M.; Fracaroli, A. M.; Kapustin, E. A.; Kalmutzki, M. J.; Altamimi, R. M.; Fathieh, F.; Reimer, J. A.; Yaghi, O. M. The Chemistry of CO₂ Capture in an Amine-Functionalized Metal–Organic Framework under Dry and Humid Conditions. *J. Am. Chem. Soc.* **2017**, *139*, 12125–12128.

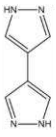

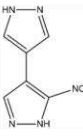
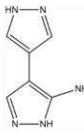
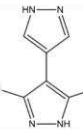
























- (108) Li, B.; Zhang, Z.; Li, Y.; Yao, K.; Zhu, Y.; Deng, Z.; Yang, F.; Zhou, X.; Li, G.; Wu, H.; et al. Enhanced Binding Affinity, Remarkable Selectivity, and High Capacity of CO₂ by Dual Functionalization of a Rht-Type Metal-Organic Framework. *Angew. Chem., Int. Ed* **2012**, *51* (6), 1412–1415.
- (109) Vaidhyanathan, R.; Iremonger, S. S.; Shimizu, G. K. H.; Boyd, P. G.; Alavi, S.; Woo, T. K. Direct Observation and Quantification of CO₂ Binding within an Amine-Functionalized Nanoporous Solid. *Science* **2010**, *330* (6004), 650–653.
- (110) Colombo, V.; Montoro, C.; Maspero, A.; Palmisano, G.; Masciocchi, N.; Galli, S.; Barea, E.; Navarro, J. A. R. Tuning the Adsorption Properties of Isorecticular Pyrazolate-Based Metal-Organic Frameworks through Ligand Modification. *J. Am. Chem. Soc.* **2012**.
- (111) Giacobbe, C.; Lavigna, E.; Maspero, A.; Galli, S. Elucidating the CO₂ Adsorption Mechanisms in the Triangular Channels of the Bis(Pyrazolate) MOF Fe₂(BPEB)₃ by in Situ Synchrotron X-Ray Diffraction and Molecular Dynamics Simulations. *J. Mater. Chem. A* **2017**, *5* (32), 16964–16975.
- (112) Pettinari, C.; Tăbăcaru, A.; Boldog, I.; Domasevitch, K. V.; Galli, S.; Masciocchi, N. Novel Coordination Frameworks Incorporating the 4,4'-Bipyrazolyl Ditopic Ligand. *Inorg. Chem.* **2012**.
- (113) Debatin, F.; Thomas, A.; Kelling, A.; Hedin, N.; Bacsik, Z.; Senkovska, I.; Kaskel, S.; Junginger, M.; Müller, H.; Schilde, U.; et al. In Situ Synthesis of an Imidazolate-4-Amide-5-Imidate Ligand and Formation of a Microporous Zinc-Organic Framework with H₂- and CO₂-Storage Ability. *Angew. Chem., Int. Ed* **2010**, *49* (7), 1258–1262.
- (114) Gassensmith, J. J.; Furukawa, H.; Smaldone, R. A.; Forgan, R. S.; Botros, Y. Y.; Yaghi, O. M.; Stoddart, J. F. Strong and Reversible Binding of Carbon Dioxide in a Green Metal-Organic Framework. *J. Am. Chem. Soc.* **2011**, *133*, 15312–15315.
- (115) Zhang, G.; Wei, G.; Liu, Z.; Oliver, S. R. J.; Fei, H. A Robust Sulfonate-Based Metal-Organic Framework with Permanent Porosity for Efficient CO₂ Capture and Conversion. *Chem. Mater.* **2016**, *28* (17), 6276–6281.
- (116) Mosca, N.; Vismara, R.; Fernandes, J. A.; Tuci, G.; Di Nicola, C.; Domasevitch, K. V.; Giacobbe, C.; Giambastiani, G.; Pettinari, C.; Aragones-Anglada, M.; et al. NO₂-Functionalized Bis(Pyrazolate) MOFs as CO₂ Capture Materials at Ambient Conditions. *Chem. - A Eur. J.* **2018**.
- (117) Liang, W.; Bhatt, P. M.; Shkurenko, A.; Adil, K.; Mouchaham, G.; Aggarwal, H.; Mallick, A.; Jamal, A.; Belmabkhout, Y.; Eddaoudi, M. A Tailor-Made Interpenetrated MOF with Exceptional Carbon-Capture Performance from Flue Gas. *Chem* **2019**, *5* (4), 950–963.
- (118) Prasad, T. K.; Suh, M. P. Control of Interpenetration and Gas-Sorption Properties of Metal-Organic Frameworks by a Simple Change in Ligand Design. *Chem. - A Eur. J.* **2012**, *18* (28), 8673–8680.

- (119) Taylor, M. K.; Runčevski, T.; Oktawiec, J.; Bachman, J. E.; Siegelman, R. L.; Jiang, H.; Mason, J. A.; Tarver, J. D.; Long, J. R. Near-Perfect CO₂/CH₄ Selectivity Achieved through Reversible Guest Templating in the Flexible Metal-Organic Framework Co(Bdp). *J. Am. Chem. Soc.* **2018**, *140* (32), 10324–10331.
- (120) Nguyen, N. T. T.; Furukawa, H.; Gándara, F.; Nguyen, H. T.; Cordova, K. E.; Yaghi, O. M. Selective Capture of Carbon Dioxide under Humid Conditions by Hydrophobic Chabazite-Type Zeolitic Imidazolate Frameworks. *Angew. Chem., Int. Ed* **2014**, *53* (40), 10645–10648.
- (121) Ding, N.; Li, H.; Feng, X.; Wang, Q.; Wang, S.; Ma, L.; Zhou, J.; Wang, B. Partitioning MOF-5 into Confined and Hydrophobic Compartments for Carbon Capture under Humid Conditions. *J. Am. Chem. Soc.* **2016**, *138* (32), 10100–10103.
- (122) Zhang, Z.; Nguyen, H. T. H.; Miller, S. A.; Ploskonka, A. M.; Decoste, J. B.; Cohen, S. M. Polymer-Metal-Organic Frameworks (PolyMOFs) as Water Tolerant Materials for Selective Carbon Dioxide Separations. *J. Am. Chem. Soc.* **2016**, *138* (3), 920–925.
- (123) Sumida, K.; Horike, S.; Kaye, S. S.; Herm, Z. R.; Queen, W. L.; Brown, C. M.; Grandjean, F.; Long, G. J.; Dailly, A.; Long, J. R. Hydrogen Storage and Carbon Dioxide Capture in an Iron-Based Sodalite-Type Metal-Organic Framework (Fe-BTT) Discovered via High-Throughput Methods. *Chem. Sci.* **2010**, *1* (2), 184–191.
- (124) McDonald, T. M.; Lee, W. R.; Mason, J. A.; Wiers, B. M.; Hong, C. S.; Long, J. R. Capture of Carbon Dioxide from Air and Flue Gas in the Alkylamine-Appended Metal-Organic Framework Mmen-Mg₂(Dobpdc). *J. Am. Chem. Soc.* **2012**, *134* (16), 7056–
- (125) Fracaroli, A. M.; Furukawa, H.; Suzuki, M.; Dodd, M.; Okajima, S.; Gándara, F.; Reimer, J. A.; Yaghi, O. M. Metal-Organic Frameworks with Precisely Designed Interior for Carbon Dioxide Capture in the Presence of Water. *J. Am. Chem. Soc.* **2014**, *136* (25), 8863–8866.
- (126) An, J.; Rosi, N. L. Tuning MOF CO₂ Adsorption Properties via Cation Exchange. *J. Am. Chem. Soc.* **2010**, *132* (16), 5578–5579.
- (127) Qin, J. S.; Du, D. Y.; Li, W. L.; Zhang, J. P.; Li, S. L.; Su, Z. M.; Wang, X. L.; Xu, Q.; Shao, K. Z.; Lan, Y. Q. N-Rich Zeolite-like Metal-Organic Framework with Sodalite Topology: High CO₂ Uptake, Selective Gas Adsorption and Efficient Drug Delivery. *Chem. Sci.* **2012**, *3* (6), 2114–2118.
- (128) Jiang, Z. R.; Wang, H.; Hu, Y.; Lu, J.; Jiang, H. L. Polar Group and Defect Engineering in a Metal-Organic Framework: Synergistic Promotion of Carbon Dioxide Sorption and Conversion. *ChemSusChem* **2015**, *8* (5), 878–885

CHAPTER II

2. THE FAMILY OF BIS(PYRAZOLATE) MOFs

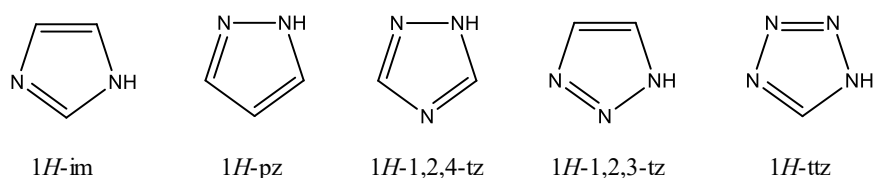
In this chapter the readers will be firstly made familiar with N-donor ligand PCPs, particularly to the families of bis(pyrazolate) MOFs. Then, they will be introduced to the bis(pyrazolate) MOFs studied by the Ph. D. candidate, providing a brief description of their synthesis and preliminary analytical characterization. A more detailed description of the experimental methods can be found in Annex I.

	 H ₂ BPZ	 H ₂ Me ₂ BPZ	 H ₂ BPZNO ₂	 H ₂ BPZNH ₂	 H ₂ BPZ(NH ₂) ₂
 27 Co					
 28 Ni					
 29 Cu					
 30 Zn					

2.1. N-donor Organic Ligands

As written in the previous chapter, MOFs feature infinitely extending networks built up by coordination bonds and characterized by potential porosity. Together with *d* and *f* transition metal ions, alkali-earth metal ions [*e.g.* Mg(II)] or post-transition metal ions [*e.g.* Al(III), In(III)], a vast library of organic molecules containing donor atoms - oxygen, nitrogen,^{1,2} and phosphorous^{3,4} among them - can be used to build MOFs. Initially, the investigation of porous architectures based on poly(carboxylate) linkers flourished, followed, at a later stage, by that on poly(azolate) ones. This occurrence could be ascribed to the high variability of crystal structures that can be obtained due to the versatility of the O-donor atom, that can bind from one up to three metal ions. Moreover, a not negligible number of poly(carboxylate) ligands are commercially available, allowing cheaper and easier MOFs syntheses.

Azoles are heterocycles composed by five-membered rings in which there is at least one nitrogen atom (Scheme 2.1) and, possibly, another heteroatom between oxygen or sulphur. The aromatic behaviour of azoles is due to one of the heteroatoms, which shares two of its valence electrons with the system. Azoles are neutral ligands characterized by *n*-1 coordination sites, where *n* is the number of nitrogen atoms in the ring. When deprotonated, in the form of azolate anions, not only all the nitrogen atoms can coordinate metal ions, but also the basicity of the donor sites increases.



Scheme 2.1 Azole heterocyclic rings, from left to right: 1H-imidazole (1H-im); 1H-pyrazole (1H-pz); 1H-1,2,4-triazole (1H-1,2,4-tz); 1H-1,2,3-triazole (1H-1,2,3-tz) and 1H-tetrazole (1H-ttz).

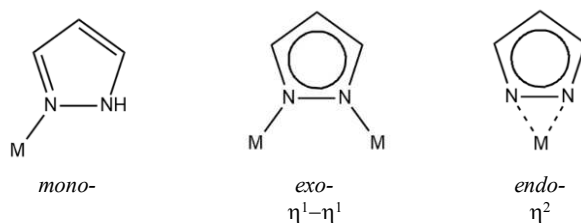
The N atom has an electron-withdrawing effect; as a consequence, the higher the number of N atoms in the ring, the higher the acidity of the azole/azolate ring is. Pyrazole has a higher pK_a compared to imidazole and tetrazole ($pK_{a_pyrazole} = 19.8$, $pK_{a_imidazole} = 18.6$, $pK_{a_tetrazole} = 8.2$),⁵ this occurrence resulting in stronger metal-nitrogen bonds after deprotonation. The number and position of the nitrogen atoms influences as well the

coordination mode and geometry of the final coordination polymer: the pyrazolate anion imposes a nitrogen-metal-nitrogen angle of 70° , vs. that of imidazolate, amounting to 140° . The majority of azolates reacts with first row transition metal ions [*e.g.* Ni(II), Co(II), Cu(II), Zn(II)] or univalent coinage metals [Cu(I) and Ag(I)]. The resulting coordination polymer^{6,7} typically shows short and strong M-N (M = metal) bonds and, potentially, a high thermal and chemical stability. Azolate coordination polymers can be charged or, more frequently, neutral. Among azolate-based MOFs two different scenarios appear, namely: the possibility of growing single crystals, as in imidazolate based MOFs, *i.e.* ZIFs,⁸ and the fast precipitation of highly insoluble microcrystalline powders, such as in pyrazolate containing CPs, preventing single crystal X-ray diffraction studies.

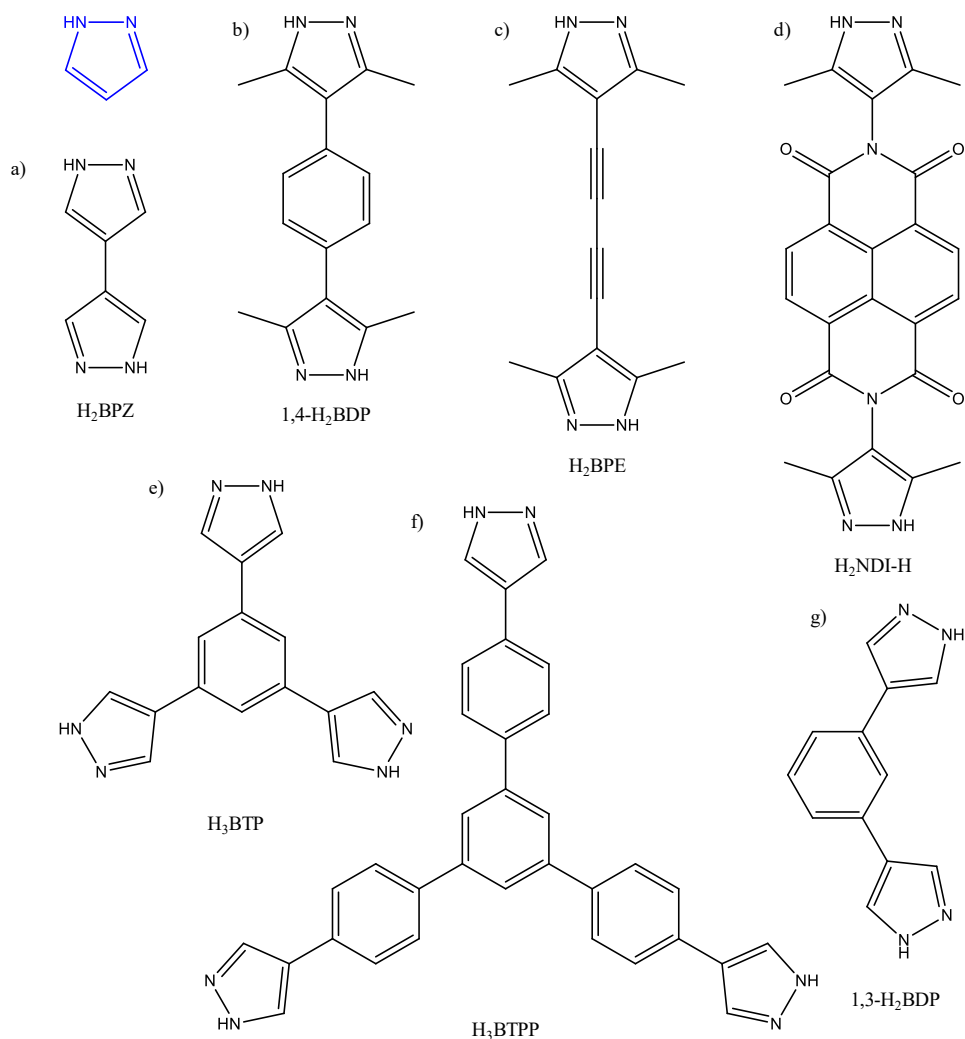
The following sections of this chapter will focus the attention on pyrazolate and poly(pyrazolate) ligands, since the latter are one of the building blocks of the MOFs reported in this Ph. D. thesis.

2.2. Pyrazolate and Poly(pyrazolate) Ligands

Pyrazole, itself or as building unit of polydentate linkers, has been largely studied as heterocyclic compound in coordination chemistry.^{1,9-11} Upon deprotonation, pyrazole passes from being a monodentate to an *exo/endo*-bidentate ligand (Scheme 2.2), allowing the bridging of two metal ions at a rather short distance (3.5-4.7 Å).¹ However, only a limited number of possible structural motifs can be reached using pyrazoles or pyrazolates as linkers, namely monomers, clusters or low dimensionality polymers.¹²⁻¹⁴ This library can be extended due to the insurgence of hydrogen bond interactions between the N-H site and an adjacent (anionic) Lewis basic group.



Scheme 2.2 Common coordination modes for pyrazole and the pyrazolate anion.



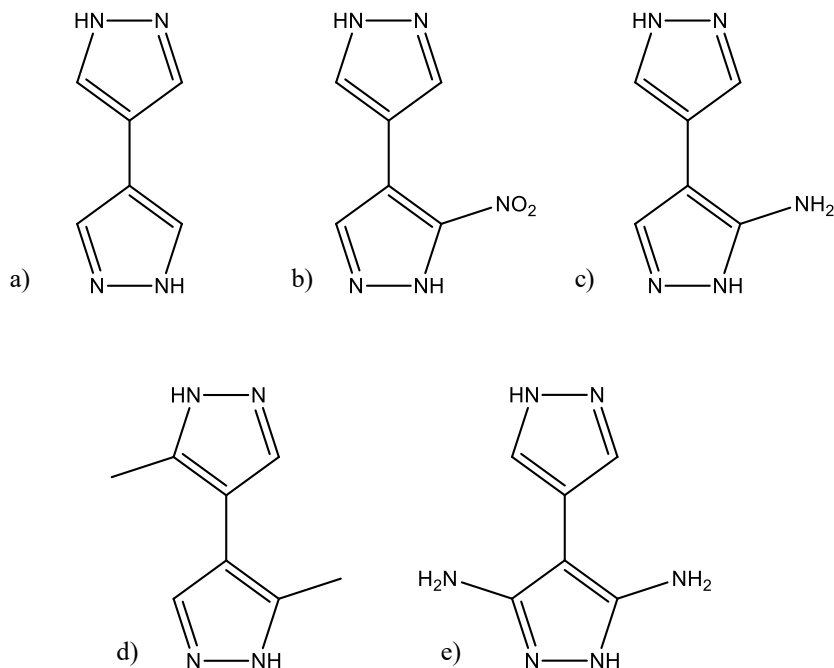
Scheme 2.3 Some examples of *exo*-polydentate poly(pyrazole) ligands reported in the literature compared to pyrazole (in blue). Starting from top left: a) H₂BPZ,¹⁵ b) 1,4-H₂BDP,¹⁶ c) H₂BPE,¹⁷ d) H₂NDI-H,¹⁸ e) H₃BTP,¹⁹ f) H₃BTPP,²⁰ g) 1,3-H₂BDP.²¹

An additional *facile* route to augment the dimensions and functionality of CPs is the use of *exo*-polydentate linkers as highlighted in Scheme 2.3. Some examples of *exo*-polydentate poly(pyrazole) ligands reported in the literature compared to pyrazole (in blue). As an example, starting from a pyrazole ring, the introduction of a second pyrazole in position 4 through appropriate organic synthesis can lead to the bitopic ligand 4,4'-bis(pyrazole) (H₂BPZ).¹⁵ The length of the linker can be modulated by adding a supplementary ring between the two pyrazoles, as a phenyl ring in 1,4-bis(pyrazol-4-

yl)benzene (1,4-H₂BDP)¹⁹ and 1,3-bis(pyrazol-4-yl)benzene (1,3-H₂BDP),²¹ or a more complex organic fragment, as in bis(N-(3,5-dimethyl-1*H*-pyrazol-4-yl))naphthalenetetracarboxylic-dianhydride (H₂NDI-H).¹⁸ The insertion of a central ring not only helps in modulating the length of the ligand, and consequently the pore aperture, but can also accommodate a higher number of pyrazole rings, as in 1,3,5-tris((1*H*-pyrazol-4-yl)phenyl)benzene (H₃BTPP),²⁰ and 1,3,5-tris(1*H*-pyrazol-4-yl)benzene (H₃BTP)¹⁹ where three pyrazole-containing moieties are connected to the central phenyl ring in 1,3,5 positions. Other properties like flexibility or functionalization can be added to the organic skeleton using proper central or peripheral groups.

In the past years, in collaboration with other research groups, the Structural Chemistry Group at the University of Insubria, Como, synthesised and characterized in the solid state a series of poly(pyrazolate) MOFs for different applications, ranging from heterogeneous catalysis to gases separation or capture of volatile organic compounds. In 2012, Pettinari *et al.*¹⁵ reported a series of bis(pyrazolate) MOFs, namely M-BPZ [M(BPZ), M = Co, Ni, Cu, Zn, Cd; H₂BPZ = 4,4'-bis(pyrazole)], characterized by a good thermal and chemical stability. The Co(II), Ni(II), Cu(II) and Zn(II) MOFs, showing a BET specific surface area in the range 300-1000 m² g⁻¹, are characterized by a 3-D open framework with 1-D channels. Their pore aperture, that falls in the range of 5–7 Å, together with the azolate nature of the ligand, which potentially imparts the high thermal and chemical stability required in operating conditions, open the possibility of their use as CO₂ adsorbents.²² Starting from this observation, in order to modulate CO₂ adsorption and unveil the role of different functional groups on the H₂BPZ skeleton, four different bis(pyrazole) linkers were synthesised,ⁱ namely: 3,3'-dimethyl-4,4'-bis(pyrazole), 3-nitro-4,4'-bis(pyrazole), 3-amino-4,4'-bis(pyrazole) and 3,5-diamino-4,4'-bis(pyrazole) [H₂Me₂BPZ, H₂BPZNO₂, H₂BPZNH₂ and H₂BPZ(NH₂)₂, respectively; Scheme 2.4]. The systematic study of the four families of M-BPZX [M(BPZX), M = Co, Ni, Cu, Zn; X = Me₂, NO₂, NH₂, (NH₂)₂] MOFs as CO₂ adsorbents will be discussed in the following chapter.

ⁱ The syntheses of the organic ligands were carried out by Prof. K. V. Domasevitch, University of Kyiv, Ukraine.



Scheme 2.4 Molecular structure of: a) H_2BPZ ,¹⁵ b), H_2BPZNO_2 ,²³ c) H_2BPZNH_2 ,²⁴ d) $\text{H}_2\text{Me}_2\text{BPZ}$,²⁵ e) $\text{H}_2\text{BPZ}(\text{NH}_2)_2$.

2.3. Synthesis and Spectroscopic Characterization of the M-BPZX MOFs

In order to modulate the carbon dioxide uptake and selectivity of the M-BPZX metal-organic frameworks, three different functional groups, namely: -Me, NO_2 and NH_2 , were added to the ligand skeleton (Scheme 2.4 b-e) to yield:

- 3,3'-dimethyl-4,4'-bis(pyrazole) ($\text{H}_2\text{Me}_2\text{BPZ}$);
- 3-nitro-4,4'-bis(pyrazole) (H_2BPZNO_2);
- 3-amino-4,4'-bis(pyrazole) (H_2BPZNH_2);
- 3,5-diamino-4,4'-bis(pyrazole) [$\text{H}_2\text{BPZ}(\text{NH}_2)_2$];

These new ligands were then used, together with a number of transition metal ions of the first series, *i.e.* Co(II), Ni(II), Cu(II), and Zn(II), as building units for MOFs. The following section collects the isolated and studied MOFs, subdivided according to the spacer functional group. The reader must be aware that only the compounds with a good

purity and crystallinity to allow for a structural and functional characterization are reported, hence the number of compounds in each series could vary. In all the cases, the products are microcrystalline powders, given the difficulty of growing single crystals from N-donor ligands coordination polymers. The exhaustive synthetic methodology and preliminary analytical characterization (IR spectroscopy, elemental analysis) can be found in Annex I.ⁱⁱ

2.3.1. M-Me₂BPZ [M = Co(II), Zn(II)]

H₂Me₂BPZ was synthesised following the procedure already reported by Sharko *et al.*²⁶ **Zn-Me₂BPZ·S** and **Co-Me₂BPZ·S** (S = solvent, *i.e.* dimethylformamide, DMF) can be isolated in good yields (80-86%) through conventional or solvothermal synthetic routes,²⁵ as white and brownish violet microcrystalline powders, respectively. The absence of the N-H stretching band in the IR spectra of the as-synthesized materials confirms the complete deprotonation of the ligand. DMF, when present as clathrated solvent, can be identified thanks to the C=O stretching band centred around 1670 cm⁻¹. Despite the multiple attempts, it was not possible to isolate the Ni(II) and Cu(II) compounds.

2.3.2. M-BPZNO₂ [M = Co(II), Cu(II), Zn(II)]

H₂BPZNO₂ was obtained through a classical nitration protocol starting from 4,4'-bis(pyrazole). **Co-BPZNO₂·S**, **Cu-BPZNO₂·S** and **Zn-BPZNO₂·S** (S = DMF), respectively as violet, brown and yellow microcrystalline powders, were isolated through solvothermal conditions with good yields (68-80%). The presence of the NO₂ symmetric stretching band centred in the range 1333-1345 cm⁻¹, together with the absence of the N-H stretching band confirmed the presence of the ligand and its complete deprotonation. The presence of DMF was highlighted by the C=O stretching band centred at 1651-1672 cm⁻¹.

ⁱⁱ The syntheses and preliminary characterization of the M-BPZX MOFs were performed by Prof. C. Pettinari's group, University of Camerino, Italy.

2.3.3. M-BPZNH₂ [M = Ni(II), Cu(II), Zn(II)]

H₂BPZNH₂ was obtained in high yield by reducing the parent H₂BPZNO₂ ligand. **Ni-BPZNH₂·S**, **Cu-BPZNH₂·S** and **Zn-BPZNH₂·S** (S = DMF) could be isolated through conventional [Ni(II) and Zn(II)] or solvothermal [Ni(II), Cu(II), Zn(II)] synthetic routes with yields in the range of 78-86%, as brown (M = Ni, Cu) or white (M = Zn) microcrystalline powders. The vibrational stretching bands of the NH₂ group in the range 3208-3330 cm⁻¹ of the IR spectra confirmed the presence of the ligand. The carbonyl group of DMF was found in the IR spectra of all the compounds in the range 1647-1662 cm⁻¹.

2.3.4. Zn-BPZ(NH₂)₂

Zn-BPZ(NH₂)₂·S (S = DMF) was synthesized following a conventional synthetic path with a good yield amounting to 83%. The presence of the ligand was confirmed by N-H the stretching band of the amino group. IR spectroscopy revealed the presence of clathrated solvent, as highlighted by the band centred at 1657 cm⁻¹, which could be ascribed to the stretching mode of the carbonyl group in DMF.

2.4. Conclusions

As highlighted at the beginning of this chapter, azoles are very versatile linkers in coordination chemistry. Hence, when deprotonated and coupled to metal ions, they can generate many different and robust crystal structures. The use of polytopic ligands can enlarge the variety of N-donor based MOFs, not only in terms of structural motif, but also of properties of the final MOFs. Among azoles, pyrazole potentially imparts the highest thermal and chemical stability to the final compound, thanks to the stronger metal-nitrogen bonds it gives. The series of bis(pyrazolate) MOFs, the M-BPZX was introduced and their syntheses reported. In the following chapters, a complete solid-state characterization of the M-BPZX MOFs will be reported.

2.5. References

- (1) Pettinari, C.; Tăbăcaru, A.; Galli, S. Coordination Polymers and Metal-Organic Frameworks Based on Poly(Pyrazole)-Containing Ligands. *Coord. Chem. Rev.* **2016**, 307, 1–31.
- (2) Desai, A. V.; Sharma, S.; Let, S.; Ghosh, S. K. N-Donor Linker Based Metal-Organic Frameworks (MOFs): Advancement and Prospects as Functional Materials. *Coord. Chem. Rev.* **2019**, 395, 146–192.
- (3) Firmino, A. D. G.; Figueira, F.; Tomé, J. P. C.; Paz, F. A. A.; Rocha, J. Metal–Organic Frameworks Assembled from Tetrakisphosphonic Ligands and Lanthanides. *Coord. Chem. Rev.* **2018**, 355, 133–149.
- (4) Gagnon, K. J.; Perry, H. P.; Clearfield, A. Conventional and Unconventional Metal-Organic Frameworks Based on Phosphonate Ligands: MOFs and UMOFs. *Chem. Rev.* **2012**, 112 (2), 1034–1054.
- (5) Bordwell, F. G. Equilibrium Acidities in Dimethyl Sulfoxide Solution. *Acc. Chem. Res.* **1988**, 21 (12), 456–463.
- (6) La Monica, G.; Attilio Ardizzoia, G. The Role of the Pyrazolate Ligand in Building Polynuclear Transition Metal Systems. *Prog. Inorg. Chem.* **1997**, 46, 151–238.
- (7) Zhang, J.-P.; Zhang, Y.-B.; Lin, J.-B.; Chen, X.-M. Metal Azolate Frameworks: From Crystal Engineering to Functional Materials. *Chem. Rev.* **2011**, 112 (2), 1001–1033.
- (8) Hayashi, H.; Cote, A. P.; Furukawa, H.; O’Keeffe, M.; Yaghi, O. M. Zeolite A imidazolate frameworks. *Nature materials*, **2007**, 6 (7), 501-506.
- (9) Trofimenko, S. Scorpionates, *Imperial C.*; **1999**.
- (10) Trofimenko, S. The Coordination Chemistry of Pyrazole-Derived Ligands. *Chem. Rev.* **1972**, 72 (5), 497–509.
- (11) Rodríguez-Albelo, L. M.; López-Maya, E.; Hamad, S.; Ruiz-Salvador, A. R.; Calero, S.; Navarro, J. A. R. Selective Sulfur Dioxide Adsorption on Crystal Defect Sites on an Isoreticular Metal Organic Framework Series. *Nat. Commun.* **2017**, 8.
- (12) Xu, J. Y.; Qiao, X.; Song, H. Bin; Yan, S. P.; Liao, D. Z.; Gao, S.; Journaux, Y.; Cano, J. The Self-Assembly and Magnetic Properties of a Ni(II)₈(μ₄-Hydroxo)₆ Cube with μ₂-Pyrazolate as an Exogeneous Ancillary Ligand. *Chem. Commun.* **2008**, 8 (47), 6414–6416.
- (13) Mezei, G.; Baran, P.; Raptis, R. G. Anion Encapsulation by Neutral Supramolecular Assemblies of Cyclic Cu^{II} Complexes: A Series of Five Polymerization Isomers, [*cis*-Cu^{II}(μ-OH)(μ-Pz)]_n, n = 6, 8, 9, 12, and 14. *Angew. Chemie - Int. Ed.* **2004**, 43 (5), 574–577.
- (14) Pettinari, C.; Masciocchi, N.; Pandolfo, L.; Pucci, D. Tuning the Functional

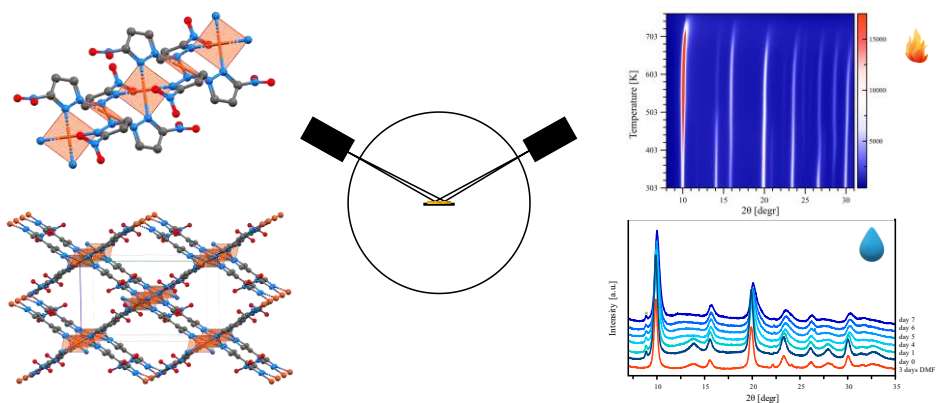
- Properties of Metal Complexes Containing Polytopic Heteroaromatic Nitrogen Ligands. *Chem. - A Eur. J.* **2010**, 16 (4), 1106–1123.
- (15) Pettinari, C.; Tăbăcaru, A.; Boldog, I.; Domasevitch, K. V.; Galli, S.; Masciocchi, N. Novel Coordination Frameworks Incorporating the 4,4'-Bipyrazolyl Ditopic Ligand. *Inorg. Chem.* **2012**, 51, 5235–5245.
- (16) Tonigold, M.; Lu, Y.; Mavrandonakis, A.; Puls, A.; Staudt, R.; Möllmer, J.; Sauer, J.; Volkmer, D. Pyrazolate-Based Cobalt(II)-Containing Metal-Organic Frameworks in Heterogeneous Catalytic Oxidation Reactions: Elucidating the Role of Entatic States for Biomimetic Oxidation Processes. *Chem. - A Eur. J.* **2011**, 17 (31), 8671–8695.
- (17) Padial, N. M.; Quartapelle Procopio, E.; Montoro, C.; López, E.; Oltra, J. E.; Colombo, V.; Maspero, A.; Masciocchi, N.; Galli, S.; Senkowska, I.; et al. Highly Hydrophobic Isorecticular Porous Metal-Organic Frameworks for the Capture of Harmful Volatile Organic Compounds. *Angew. Chemie - Int. Ed.* **2013**, 52 (32), 8290–8294.
- (18) Wade, C. R.; Corrales-Sanchez, T.; Narayan, T. C.; Dincă, M. Postsynthetic Tuning of Hydrophilicity in Pyrazolate MOFs to Modulate Water Adsorption Properties. *Energy Environ. Sci.* **2013**, 6 (7), 2172–2177.
- (19) Galli, S.; Masciocchi, N.; Colombo, V.; Maspero, A.; Palmisano, G.; López-Garzón, F. J.; Domingo-García, M.; Fernández-Morales, I.; Barea, E.; Navarro, J. A. R. Adsorption of Harmful Organic Vapors by Flexible Hydrophobic Bis-Pyrazolate Based MOFs. *Chem. Mater.* **2010**, 22 (5), 1664–1672.
- (20) Tăbăcaru, A.; Galli, S.; Pettinari, C.; Masciocchi, N.; McDonald, T. M.; Long, J. R. Nickel(II) and Copper(I,II)-Based Metal-Organic Frameworks Incorporating an Extended Tris-Pyrazolate Linker. *CrystEngComm* **2015**, 17 (27), 4992–5001.
- (21) Choi, H. J.; Dincă, M.; Dailly, A.; Long, J. R. Hydrogen Storage in Water-Stable Metal-Organic Frameworks Incorporating 1,3- and 1,4-Benzenedipyrazolate. *Energy Environ. Sci.* **2010**, 3 (1), 117–123.
- (22) Oschatz, M.; Antonietti, M. A Search for Selectivity to Enable CO₂ Capture with Porous Adsorbents. *Energy Environ. Sci.* **2018**, 11 (1), 57–70.
- (23) Mosca, N.; Vismara, R.; Fernandes, J. A.; Tuci, G.; Di Nicola, C.; Domasevitch, K. V.; Giacobbe, C.; Giambastiani, G.; Pettinari, C.; Aragoñes-Anglada, M.; et al. NO₂-Functionalized Bis(Pyrazolate) MOFs as CO₂ Capture Materials at Ambient Conditions. *Chem. - A Eur. J.* **2018**, 24 (50), 13170–13180.
- (24) Vismara, R.; Tuci, G.; Mosca, N.; Domasevitch, K. V.; Di Nicola, C.; Pettinari, C.; Giambastiani, G.; Galli, S.; Rossin, A. Amino-Decorated Bis(Pyrazolate) Metal-Organic Frameworks for Carbon Dioxide Capture and Green Conversion into Cyclic Carbonates. *Inorg. Chem. Front.* **2019**, 6 (2), 533–545.
- (25) Mosca, N.; Vismara, R.; Fernandes, J. A.; Casassa, S.; Domasevitch, K. V.; Bailón-García, E.; Maldonado-Hódar, F. J.; Pettinari, C.; Galli, S. CH₃-Tagged Bis(Pyrazolato)-Based Coordination Polymers and Metal-Organic Frameworks:

- An Experimental and Theoretical Insight. *Cryst. Growth Des.* **2017**, 17 (7), 3854–3867.
- (26) Sharko, A. V.; Senchyk, G. A.; Rusanov, E. B.; Domasevitch, K. V. Preparative Synthesis of 3(5),3'(5')-Dimethyl-4,4'-Bipyrazole. *Tetrahedron Lett.* **2015**, 56 (44), 6089–6092.

CHAPTER III

3. STRUCTURAL AND THERMAL CHARACTERIZATION OF THE M-BPZX MOFs

The topic of the first part of this chapter is an exhaustive description of the structural features of the M-BPZX MOFs [$M = \text{Co}, \text{Ni}, \text{Cu}, \text{Zn}$; $X = \text{Me}_2, \text{NO}_2, \text{NH}_2, (\text{NH}_2)_2$]. Then, in the second part, the attention is focused on their thermal behaviour. A more detailed description of the experimental methods used for the structural and thermal characterization can be found in Annex I.



3.1. Structural Characterization of the M-BPZX MOFs

After the syntheses, preliminary powder X-ray diffraction (PXRD) qualitative analyses were performed with a laboratory diffractometer (see Annex I for the instrument specifics), acquiring data in the 4–35° 2 θ range at room temperature, with steps of 0.02°, and time *per* step of 1 s on a Si zero background sample-holder (supplied by Assing Srl, Monterotondo, Italy). Together with elemental analysis and IR spectroscopy, PXRD assessed the nature and purity of all the batches employed for the structural, thermal and functional characterization. A longer diffraction data set for full structure characterization was then collected, in the 2 θ range 5–105° and with time *per* step of 10 s. The software TOPAS-Academic V6¹ was used for all the structure characterization steps, namely: indexing, whole powder pattern refinement, structure solution and structure refinement.

Initially, the PXRD patterns of the new MOFs were visually compared with those of the untagged parents M-BPZ. Nonetheless, an independent indexing procedure starting from the low-to-medium angle maximum peak positions was performed. The approximative unit cell parameters of each compound were derived through the Singular Value Decomposition algorithm.² The correct space group was identified thanks to the observed systematic absences. When the M-BPZX MOFs appeared to be isostructural to the parent M-BPZ, the structural model of the latter was used as starting point for the structure refinement by the Rietveld method.³ Otherwise, the structure was solved by localizing the ligand and metal ion positions using a combined Monte Carlo/Simulated annealing approach⁴ as implemented in Topas-Academic V6. In all cases, the crystallographically independent portion of the ligand was described as a rigid body with the z-matrix formalism, assigning average values to the bond lengths and angles.ⁱⁱⁱ Orientation, rotations and torsions of the rigid body were let free to vary if allowed by crystallographic symmetry. The clathrated solvent as well, *i.e.* DMF, was described as a

ⁱⁱⁱ Average bond distances and angles of the rigid body used to describe the ligands: for all the BPZX²⁻: C-N and C-C of the pyrazole (PZ) ring 1.36 Å, exocyclic C-C 1.40 Å, C-H of the PZ ring 0.95 Å; PZ ring bond angles 108° (internal) and 126° (external). For Me₂BPZ²⁻: C_{CH₃}-H 1.10 Å, C-C_{CH₃} 1.40 Å; angles at the C of the CH₃ group 109.5°. For BPZNO₂²⁻: N-O 1.23 Å, C-N_{NO₂} 1.40 Å; angles at the N of the NO₂ moiety 120°. For BPZNH₂²⁻ and BPZ(NH₂)₂²⁻: N-H 0.95 Å, C-N_{NH₂} 1.40 Å; angles at the N of the NH₂ 120°.

rigid body using fixed bond lengths and angles^{iv} and was localized through a combined Monte Carlo/Simulated annealing approach⁴ allowing its centre of mass position and its orientation to vary. A refined isotropic thermal parameter was assigned to the metal ions and to lighter atoms (increased by 2 Å² with respect to the metal ion one). The Fundamental Parameters Approach² was used to model the peak profile. The background was described with a polynomial Chebyshev function, except for M-BPZNO₂ [M = Co, Zn], whose complexity required a user-defined sequence of segments.^v As final refinement step the ligand bond distances, except for the C/N-H ones, were let vary in restrained ranges.^{vi} The final Crystallographic Information Files (CIFs) were deposited in the Cambridge Crystallographic Data Centre (CCDC) database. The assigned entry codes are reported in the following sections.

3.1.1. M-Me₂BPZ

Among the M-Me₂BPZ coordination polymers, only **Co-Me₂BPZ·S** and **Zn-Me₂BPZ·S** (S = DMF) show a (crystalline) porous framework.⁵ The comparison of the powder diffraction data of **Co-Me₂BPZ·S** and **Zn-Me₂BPZ·S** with that of Zn-BPZ,⁶ together with indexing, suggested a tetragonal unit cell (**Co-Me₂BPZ·S**: $a = 8.91$ Å, $c = 7.45$ Å, $V = 591.9$ Å³; **Zn-Me₂BPZ·S**: $a = 8.92$ Å, $c = 7.44$ Å, $V = 591.5$ Å³). However, no tetragonal *P* space group was found adequate to describe all the observed Bragg reflections. Lowering the symmetry to the isomorphic *Cccm* orthorhombic subgroup, as well, was found unsatisfactory. A further lowering in symmetry down to the *C2/c* monoclinic symmetry allowed the structure determination. A model considering positional disorder of the methyl groups (position 3 vs. 5) of the pyrazole ring was tentatively adopted during Rietveld refinement, and the occupancy factors of the two methyl groups were refined. However, this assumption was not beneficial for the refinement quality. Only one of the two possible positions is fully occupied, so that in the final structural model the functional groups were left ordered. To properly describe the

^{iv} Bond distances and angles of the rigid body used to describe DMF: C-N 1.45 Å, C-H 0.95 Å, C=O 1.25 Å; angles at the N and amidic C atoms 120°, angles at the C atoms of the CH₃ groups 109.5°.

^v See: http://topas.dur.ac.uk/topaswiki/doku.php?id=background_straight_line_segments for the macro used during Rietveld refinement.

^{vi} Ranges of the refined bond distances in Rietveld refinement: C-C 1.40-1.45 Å, C-C and C-N of the PZ ring 1.32-1.38 Å. The ranges were identified after a preliminary bibliographic search in the CCDC database.

anisotropic peak profile, $1/\cos(\theta)$ -dependent fourth order spherical harmonics were used for both compounds. The solvent was found disordered inside the channels. The reader is addressed to Figure 3.1 for the final graphical output of the Rietveld refinement.

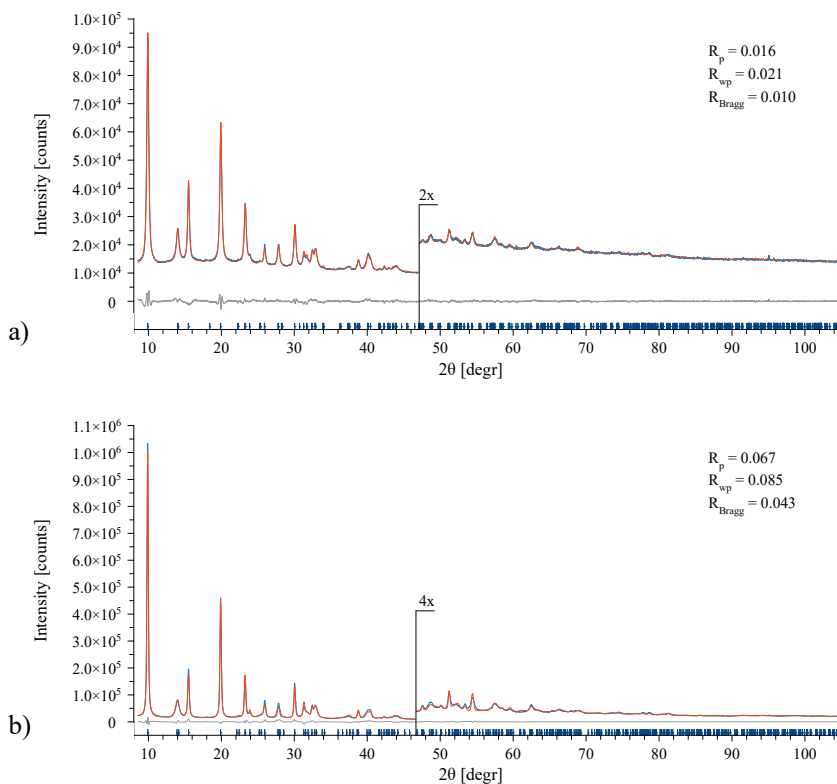


Figure 3.1 Graphical output of the final step of the Rietveld refinement for a) Co-Me₂BPZ and b) Zn-Me₂BPZ. Colour code: observed intensity, blue trace; calculated intensity, red trace; difference, grey trace; Bragg reflections, blue markers. The portion above $\sim 45^\circ$ has been magnified for clarity.

The two compounds are isostructural, crystallizing in the monoclinic space group $C2/c$ and are isorecticular to both the parent Zn-BPZ MOF,⁶ and the M-Me₄BPZ (M = Co, Zn; H₂Me₄BPZ = 3,3',5,5'-tetramethyl-1*H*,1'*H*-4,4'-bipyrazole) series.⁷ The asymmetric unit is composed by one M(II) ion (M = Co, Zn) and half Me₂BPZ²⁻ dianion, laying on special positions ($2/m$ and a centre of inversion, respectively). Each metal ion is tetra-coordinated, in tetrahedral stereochemistry, to four different ligands through their N atoms (Figure 3.2, to which caption the reader is referred for the main bond distances and angles). Each Me₂BPZ²⁻ ligand acts as *exo*-tetradentate spacer: the N atoms of the same

pyrazolate ring connect two metal ions creating 1-D chains parallel to the [001] crystallographic direction (Figure 3.2 left); concomitantly, the whole ligand bridges two different chains. The resulting 3-D porous framework is characterized by 1-D rhombic channels [Figure 3.2; M = Co, diagonals of 12.581(2) and 12.632(1) Å; M = Zn, 12.608(3) and 12.615(3) Å] running parallel to the crystallographic *c*-axis. The walls of the channels are decorated by the functional groups of the linkers.

The channels accessible aperture, calculated taking into account the van der Waals radii of the atoms decorating the channels, are $7.6 \times 5.8 \text{ \AA}^2$ for Co(II), and $7.2 \times 5.8 \text{ \AA}^2$ for Zn(II). At ambient conditions, the two MOFs show an empty volume of $\sim 38\%$,⁸ lower than that of Zn-BPZ ($\sim 42\%$), but higher than that of the tetra-methylated counterparts [Co(II), $\sim 16\%$; Zn(II), $\sim 15\%$].⁷

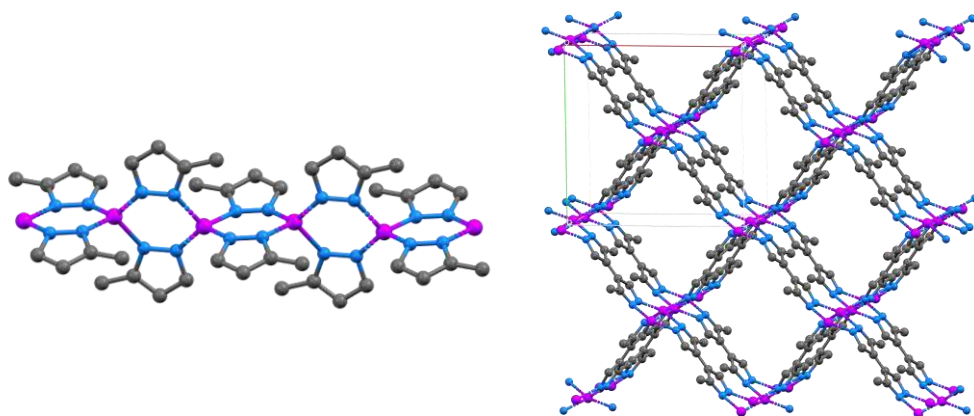


Figure 3.2 Representation of the crystal structure of **Zn-Me₂BPZ·S**. *Left*: Portion of the 1-D chain parallel to the [001] crystallographic direction. *Right*: Portion of the crystal packing viewed, in perspective, down the [001] direction. Atom colour code: carbon, grey; nitrogen, blue; zinc, violet. The DMF molecules and hydrogen atoms have been omitted for clarity. Except for the metal ion, *i.e.* Co(II), at the drawing level the structural features of **Co-Me₂BPZ·S** are similar to those shown in this figure. **Zn-Me₂BPZ·S** main bond distances and angles: Zn-N, 2.042(4) and 2.212(4) Å; Zn···Zn 3.733(3), 8.918(7) and 12.615(3) Å; N-Zn-N, 88.0(3)-112.05(8)°. **Co-Me₂BPZ·S** main bond distances and angles: Co-N, 2.004(7) and 2.149(7) Å; Co···Co 3.727(2), 8.914(9) and 12.632(1) Å; N-Co-N, 96.6(4)-120.9(7)°.

The structural parameters are reproduced with permission from: “Mosca, N.; Vismara, R.; Fernandes, J. A.; Casassa, S.; Domasevitch, K. V.; Bailón-García, E.; Maldonado-Hódar, F. J.; Pettinari, C. and Galli, S. (2017). CH₃-Tagged Bis(pyrazolato)-Based Coordination Polymers and

Metal–Organic Frameworks: An Experimental and Theoretical Insight. Crystal Growth & Design, 17(7), 3854–3867". Copyright © (2017) American Chemical Society.

Crystallographic data for **Co-Me₂BPZ·S**: C₈H₈CoN₄·0.5DMF, Formula weight: 255.65 g mol⁻¹, monoclinic, C2/c, $a = 12.581(2)$ Å, $b = 12.632(1)$ Å, $c = 7.4473(5)$ Å, $\beta = 90.081(9)^\circ$, $V = 1183.5(2)$ Å³, $Z = 8$, $Z' = 4$, $F(000) = 524$, $\rho = 1.441$ g cm⁻³, $R_{wp} = 0.021$, $R_p = 0.016$ and $R_{Bragg} = 0.010$, 2θ range = 8.5–105° for 4826 data and 44 parameters. CCDC No. 1526565.

Crystallographic data for **Zn-Me₂BPZ·S**: C₈H₈N₄Zn·0.3DMF, Formula weight: 247.48 g mol⁻¹, monoclinic, C2/c, $a = 12.608(3)$ Å, $b = 12.615(3)$ Å, $c = 7.4412(4)$ Å, $\beta = 89.805(9)^\circ$, $V = 1183.5(4)$ Å³, $Z = 8$, $Z' = 4$, $F(000) = 507.2$, $\rho = 1.266$ g cm⁻³, $R_{wp} = 0.085$, $R_p = 0.067$ and $R_{Bragg} = 0.043$, 2θ range = 8.5–105° for 4826 data and 37 parameters. CCDC No. 1526569.

3.1.2. M-BPZNO₂

Three nitro functionalized bis(pyrazolate) compounds⁹ were successfully synthesised, namely: **Co-BPZNO₂**, **Cu-BPZNO₂** and **Zn-BPZNO₂**. Unfortunately, except for the Zn(II) compound, which is indefinitely stable in air, the Co(II) and Cu(II) counterparts start losing their crystallinity after two weeks. Nonetheless, the pristine degree of crystallinity can be recovered after suspension in DMF at ambient conditions.

A visual comparison of the PXRD pattern of the M-BPZNO₂·S [Co(II), Zn(II)] MOFs with that of Zn-BPZ⁶ and of **Cu-BPZNO₂** with its unfunctionalized parent Cu-BPZ⁶ suggested that the compounds are isostructural, hypothesis confirmed by the indexing process. **Co-BPZNO₂·S** and **Zn-BPZNO₂·S** are isostructural, showing a tetragonal symmetry, whereas the Cu(II) compound shows an orthorhombic one. The structural model of the untagged parents was used as starting point for the structure refinements through the Rietveld method. In all the cases, the asymmetric unit is composed by one metal ion and a quarter of BPZNO₂²⁻ ligand, both laying on symmetry elements (4_2 and $2/m$, for Co/Zn and Cu, respectively; $2/m$ for the ligand). Since the entire ligand is generated by the crystallographically independent portion, the nitro group can occupy

each of the four equivalent positions with a probability of 25%. The vicariant hydrogen atom can occupy the same positions with a probability of 75%. During the refinement, the orientation of the nitro group with respect to the ligand plane was let free to vary. In both **Zn-BPZNO₂·S** and **Co-BPZNO₂·S**, the sharper $[h00]$ and broader $[0kl]$ Bragg reflections could not be described by employing Lorentzian or Gaussian functions (alone or in combination), or with spherical harmonics. For **Co-BPZNO₂·S**, the $[h00]$ class of Bragg reflections was described by convoluting separate size $[\cos(\theta)^{-1}$ -dependent] and strain $[\tan(\theta)$ -dependent] contributions to the Lorentzian function; a Gaussian contribution modelled the broadening of the $[hk0]$ reflections. For **Zn-BPZNO₂·S**, a Lorentzian function convoluted with a four-leaf clover implicit function well described the anisotropic broadening in the $(0kl)$ plane. Finally, the anisotropic peak profile of **Cu-BPZNO₂·S** was modelled convoluting fourth-order spherical harmonics to a Lorentzian function. Figure 3.3 collects the final Rietveld refinement plots of the M-BPZNO₂ MOFs.

Co-BPZNO₂ and **Zn-BPZNO₂** crystallize in the tetragonal $P4_2/mmc$ space group. Their 3-D open framework is characterized by 1-D square channels decorated by the nitro groups which protrude inside the channels with angles of 49° and 64°, respectively, vs. the plane containing the ligand (Figure 3.4). As previously described for the M-Me₂BPZ MOFs, the metal ion [Co(II) or Zn(II)] shows a tetragonal stereochemistry, defined by four BPZNO₂²⁻ linkers. The reader is referred to the caption of Figure 3.4 for the main bond distances and angles.

On the other hand, **Cu-BPZNO₂** has an orthorhombic $Imma$ symmetry and a 3-D framework similar to that of the Co(II) and Zn(II) derivatives, but the Cu(II) ions show a square planar geometry, defined by the N atoms of four different ligands (Figure 3.5, to which caption the reader is referred for the main bond distances and angles). The resulting 1-D rhombic channels are decorated by the NO₂ groups, whose torsion angle, with respect to the ligand plane, is ~66°, see Figure 3.5. The occurrence of a deviation from coplanarity between the nitro group and the ligand skeleton in the **M-BPZNO₂** MOFs is in contrast with the difficulty in isolating MOFs in which the NO₂ group protrude inside the channels, as claimed by Maity *et al.*¹⁰

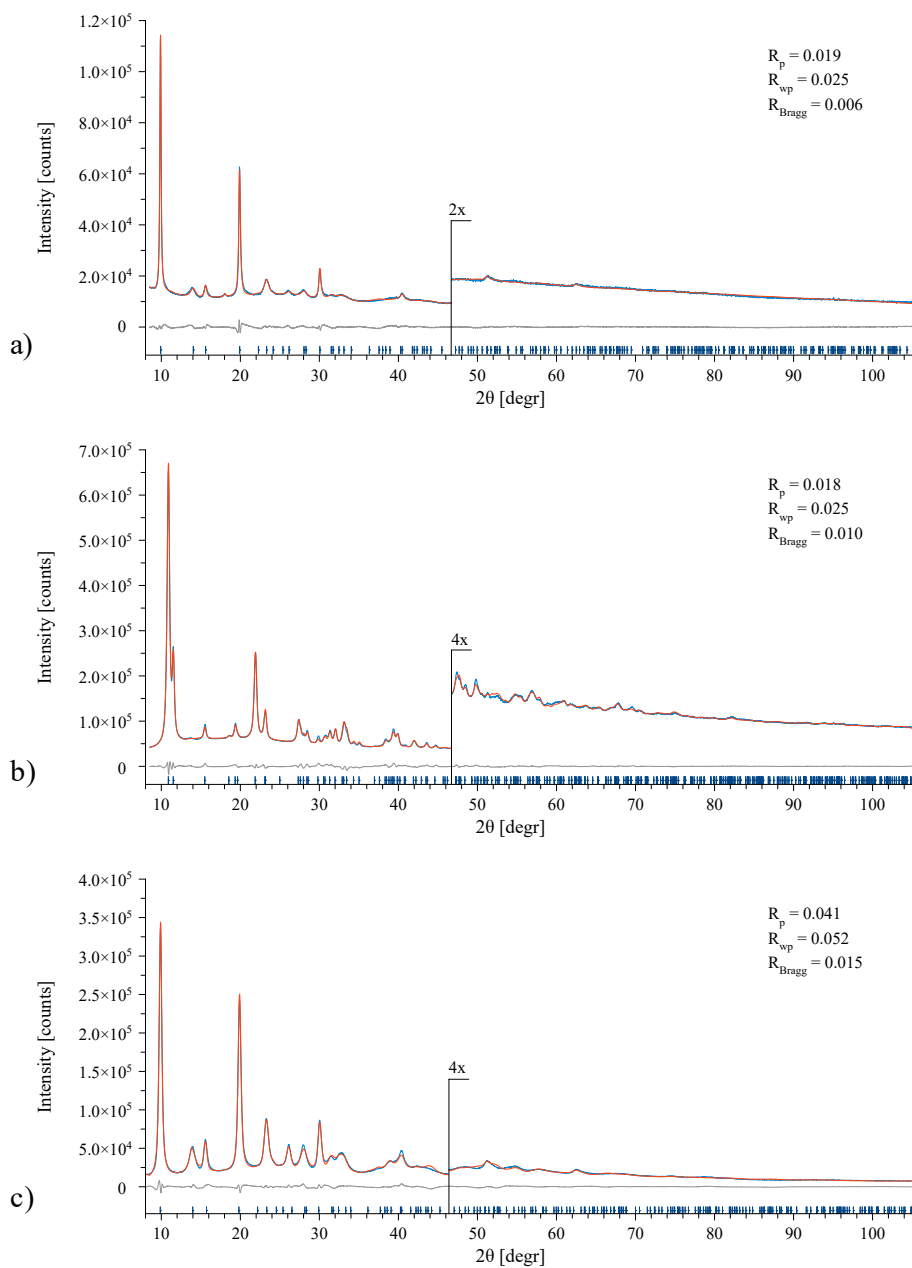


Figure 3.3 Graphical output of the final step of the Rietveld refinement for a) Co-BPZNO₂, b) Cu BPZNO₂ and c) Zn-BPZNO₂. Colour code: observed intensity, blue trace; calculated intensity, red trace; difference, grey trace; Bragg reflections, blue markers. The portion above $\sim 45^\circ$ has been magnified for clarity.

The three presented MOFs, namely: **Co-BPZNO₂**, **Cu-BPZNO₂** and **Zn-BPZNO₂**, belong to the **sra** network type.¹⁰ They show an empty volume^{vii} of ~39.2(40.4), ~35.6(41.4)% and ~39.0(40.3)%, respectively, at room conditions. In all the cases, DMF molecules are found disordered within the channels.

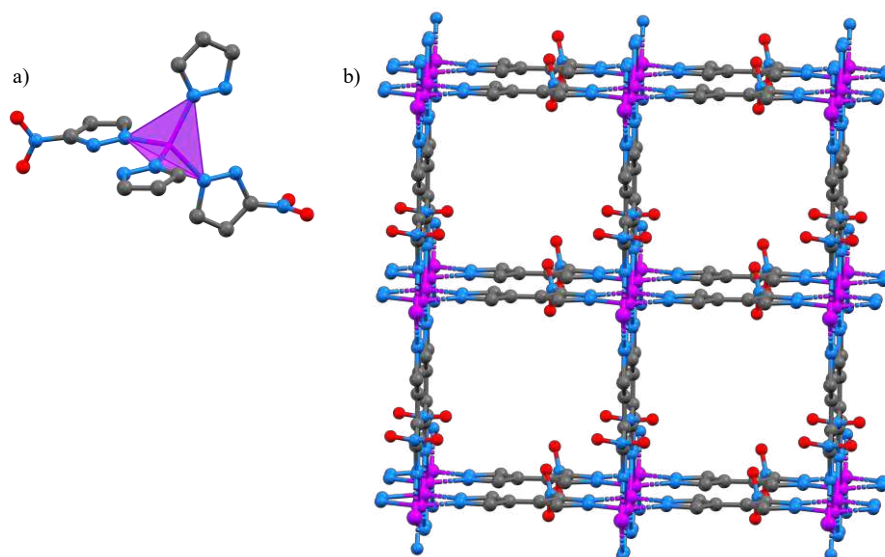


Figure 3.4 Representation of the crystal structure of **Zn-BPZNO₂·S**. a) The Zn(II) coordination sphere. b) Portion of the crystal packing, viewed, in perspective, along the [001] crystallographic direction. Atom colour code: carbon, grey; nitrogen, blue; oxygen, red; zinc, violet. The DMF molecules and hydrogen atoms have been omitted for clarity. An ordered model, obtained by decreasing the symmetry down to *C2/c*, has been used for clarity. The two figures are descriptive also for **Co-BPzNO₂·S** except for the metal ion and the orientation of the NO₂ group. **Zn-BPZNO₂·S** main bond distances and angles: Zn-N, 2.052(11) Å; Zn···Zn, 3.6912(6) and 8.9214(9) Å; N-Zn-N, 108.5(2)-111.5(4)°; **Co-BPzNO₂·S** main bond distances and angles: Co-N, 2.003(14) Å; Co···Co, 3.681(1) and 8.9093(6) Å; N-Co-N, 109.2(5)-110.0(11)°.

^{vii} The empty volume was estimated with the software PLATON⁸ on an ordered model (in *C2/c* for **Co-BPZNO₂·S** and **Zn-BPZNO₂·S** and in *P2/m* for **Cu-BPZNO₂·S**) after removal of DMF. In parenthesis, the empty volume calculated assuming that the nitro group is coplanar to the ligand.

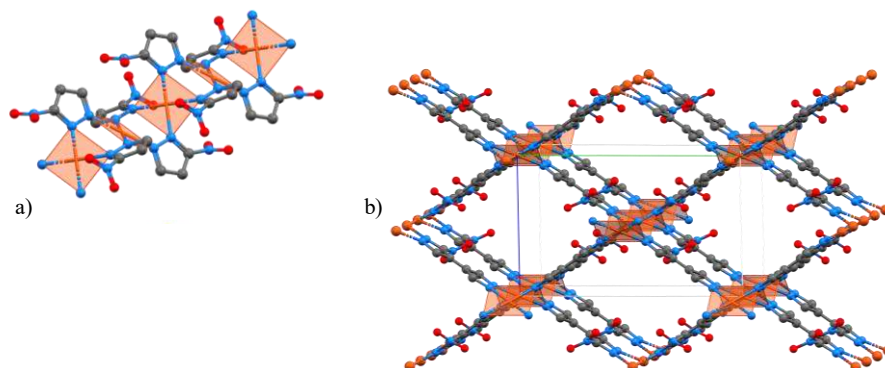


Figure 3.5 Representation of the crystal structure of **Cu-BPZNO₂·S**. a) Portion of the 1-D chain parallel to the [100] crystallographic direction. b) Portion of the crystal packing, viewed, in perspective, along the [100] direction. Atom colour code: carbon, grey; copper, orange; nitrogen, blue; oxygen, red. The DMF molecules and hydrogen atoms have been omitted for clarity. An ordered model obtained by decreasing the symmetry down to $P2/m$, has been used for clarity. **Cu-BPZNO₂·S** main bond distances and angles: Cu-N, 2.068(4) Å; Cu···Cu 3.5614(3), 9.5645(6) and 15.3623(13) Å; N-Cu-N, 82.9(2)-97.1(2)°.

*The structural parameters are reproduced with permission from: Mosca, N.; Vismara, R.; Fernandes, J. A.; Tuci, G.; Di Nicola, C.; Domasevitch, K. V.; Giacobbe, C.; Giambastiani, G.; Pettinari, C.; Aragoñes-Anglada, M.; Moghadam, P. Z.; Fairen-Jimenez, D.; Rossin, A. and Galli, S. (2018). NO₂-Functionalized Bis(Pyrazolate) MOFs as CO₂ Capture Materials at Ambient Conditions. *Chemistry - A European Journal*. 24(50), 13170-13180." Copyright © 2018 Wiley-CH Verlag GmbH & Co. KGaA, Weinheim.*

Crystal data for **Co-BPZNO₂·S**: C₆H₃CoN₅O₂·0.7DMF, Formula weight: 287.23 g mol⁻¹, tetragonal, $P4_2/mmc$, $a = 8.9093(6)$ Å, $c = 7.362(2)$ Å, $V = 584.4(2)$ Å³, $Z = 16$, $Z' = 2$, $F(000) = 290$, $\rho = 1.632$ g cm⁻³, $R_{wp} = 0.025$, $R_p = 0.019$ and $R_{Bragg} = 0.006$, 2θ range = 8.5-105° for 4826 data and 36 parameters. CCDC No. 1578114.

Crystal data for **Cu-BPZNO₂·S**: C₆H₃CuN₅O₂·0.9DMF, Formula weight: 306.44 g mol⁻¹, orthorhombic, $Imma$, $a = 15.3623(13)$ Å, $b = 7.1227(5)$ Å, $c = 9.5645(6)$ Å, $V = 1046.56(13)$ Å³, $Z = 16$, $Z' = 4$, $F(000) = 620$, $\rho = 1.945$ g cm⁻³, $R_{wp} = 0.025$, $R_p = 0.018$ and $R_{Bragg} = 0.010$, 2θ range = 8.5-105° for 4826 data and 44 parameters. CCDC No. 1578115.

Crystal data for **Zn-BPZNO₂·S**: C₆H₃N₅O₂Zn·0.8DMF, Formula weight = 300.98 g mol⁻¹, tetragonal, *P4₂/mmc*, *a* = 8.9214(9) Å, *c* = 7.3824(12) Å, *V* = 587.58(13) Å³, *Z* = 16, *Z'* = 2, *F*(000) = 304, *ρ* = 1.701 g cm⁻³, *R*_{wp} = 0.052, *R*_p = 0.041 and *R*_{Bragg} = 0.015, 2θ range = 8.5-105° for 4851 data and 40 parameters. CCDC No. 1578116.

3.1.3. M-BPZNH₂

Ni-BPZNH₂·S and **Cu-BPZNH₂·S** are isostructural to Cu-BPZ, while **Zn-BPZNH₂·S** is isostructural to Zn-BPZ. For both the orthorhombic *Imma* phases, **Ni-BPZNH₂·S** and **Cu-BPZNH₂·S**, and the tetragonal *P4₂/mmc* one, the asymmetric unit is constituted by one metal ion and a quarter of a ligand, laying on special positions (*4₂* and *2/m*, for Zn and Ni/Cu respectively; *2/m* for the ligand). Hence, as already seen in the **M-BPZNO₂** MOFs, the NH₂ functional group and H atom formally coexists with different probability of occupancy in the same four equivalent positions. Given the difficulty in localizing the hydrogen atoms by X-ray diffraction, the NH₂ group was fixed coplanar to the ligand plane. The different broadening of the [*hkh*] reflections, in **M-BPZNH₂·S** [*M* = Ni, Cu], and the [*hhl*] ones, in **Zn-BPZNH₂·S**, was modelled through the convolution of two different, *hkl*-dependent spherical harmonics. DMF was found disordered inside the channels in all the three compounds. The final plots of the Rietveld refinements are collected in Figure 3.6.

M-BPZNH₂ [*M* = Ni, Cu and Zn] shows a reticular open framework with one-dimensional rhombic (*M* = Ni, Cu) or square (*M* = Zn) channels, see Figure 3.7, where the metal ions are tetraordinated to the linkers in square planar (*M* = Ni, Cu) or tetrahedral (*M* = Zn) stereochemistry. At ambient conditions **Zn-BPZNH₂** shows an empty volume of ~45.7% which translates in a pore volume, *per* cell, of ~0.38 cm³ g⁻¹. On the other hand, **Ni-BPZNH₂** and **Cu-BPZNH₂** show an empty volume of ~44.5 and ~45.4%, respectively, which translate in a pore volume, *per* cell, of ~0.32 and ~0.35 cm³ g⁻¹. All the compounds belong to the **sra** net topology.⁹

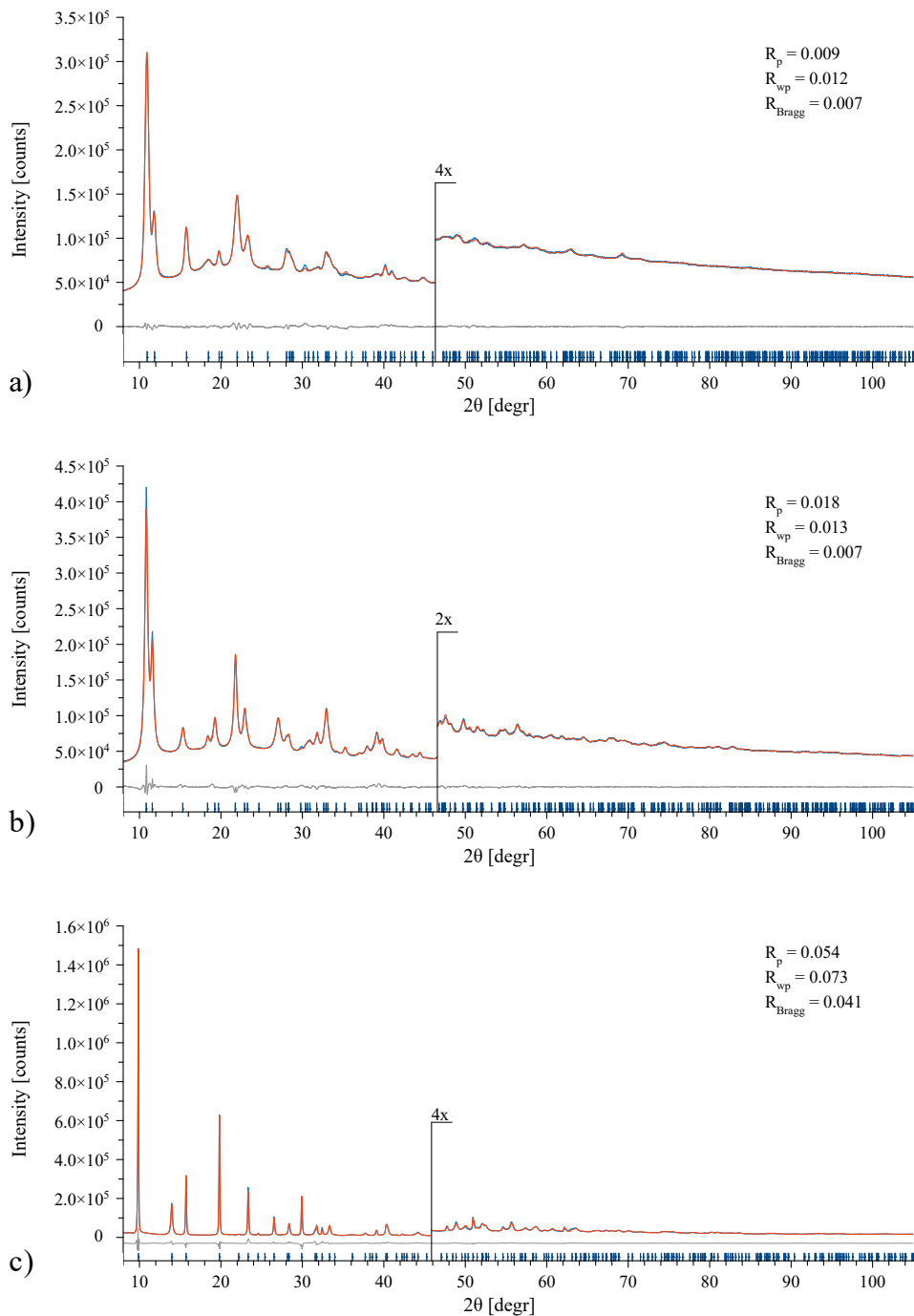


Figure 3.6 Graphical output of the final step of the Rietveld refinement for a) Ni-BPZNH₂·S, b) Cu-BPZNH₂·S and c) Zn-BPZNH₂·S. Colour code: observed intensity, blue trace; calculated intensity, red trace; difference, grey trace; Bragg reflections, blue markers. The portion above ~45° has been magnified for clarity.

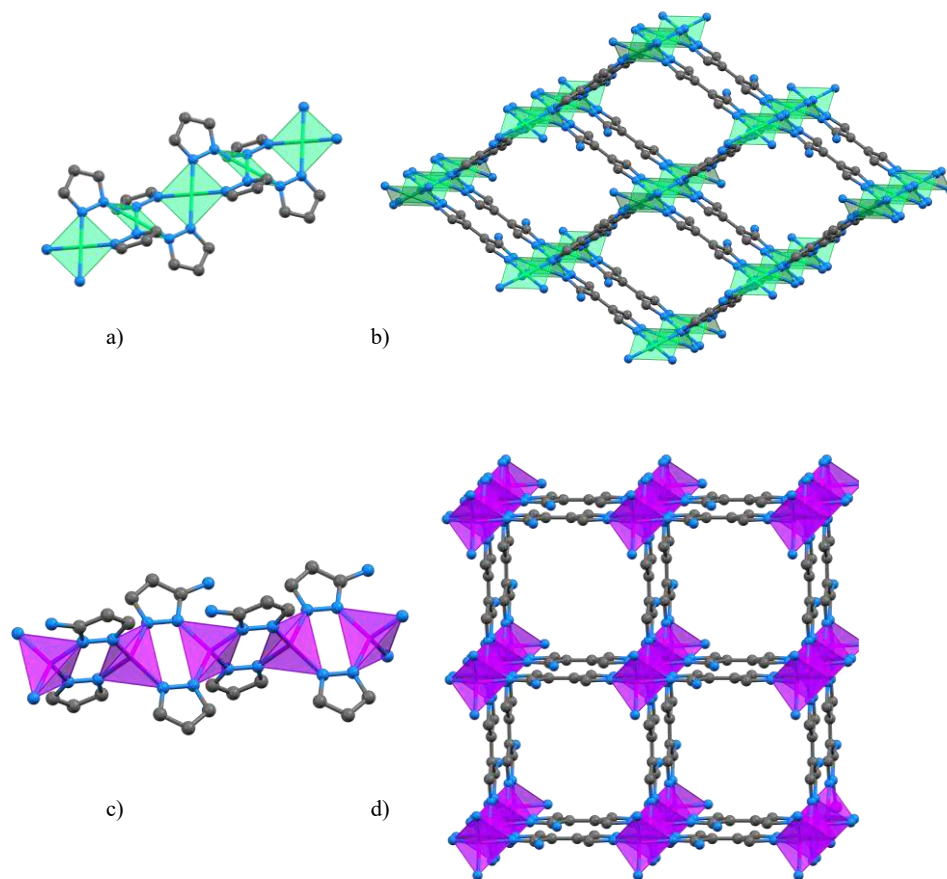


Figure 3.7 Representation of the crystal structure of 1) **Ni-BPZNH₂·S**: a) Portion of the 1-D chain parallel to the [100] crystallographic direction. b) Portion of the crystal packing viewed, in perspective, along the [100] direction; 2) **Zn-BPZNH₂·S**: c) Portion of the 1-D chain parallel to the [001] crystallographic direction. b) Portion of the crystal packing viewed, in perspective, along the [001] direction. Atom colour code: carbon, grey; nickel, green; nitrogen, blue; oxygen, red; zinc, violet. The DMF molecules and hydrogen atoms have been omitted for clarity. An ordered model has been used for clarity. **Cu-BPZNH₂·S**, from a graphical point of view, can be associated to **Ni-BPZNH₂·S**. Main bond distances and angles of **Ni-BPZNH₂·S**: Ni–N, 1.9154(52) Å; Ni···Ni 3.4571(5), 9.6033(14) and 14.928(2) Å; N–Cu–N, 85.4(2) and 94.6(2)°. Main bond distances and angles of **Cu-BPZNH₂·S**: Cu–N, 2.0185(47) Å; Cu···Cu 3.6049(3), 9.6527(7) and 15.2776(11) Å; N–Cu–N, 85.7(2) and 94.6(1)°. Main bond distances and angles of **Zn-BPZNH₂·S**: Zn–N, 2.0086(2)Å; Zn···Zn, 3.6221(2) and 8.9535(2) Å; N–Zn–N, 108.50(2)–111.44(2)°.

The structural parameters are reproduced with permission from: “R. Vismara, G. Tuci, N. Mosca, K. V. Domasevitch, C. Di Nicola, C. Pettinari, G. Giambastiani, S. Galli and A. Rossin, Inorg. Chem. Front., 2019, 6, 533”. - Reproduced by permission of The Royal Society of Chemistry.

Crystallographic data for **Ni-BPZNH₂·S**. C₆H₅NiN₅·0.8DMF, Formula weight: 264.32 g mol⁻¹, orthorhombic, *Imma*, $a = 14.9281(19)$ Å, $b = 6.9141(10)$ Å, $c = 9.6033(13)$ Å, $V = 991.2(2)$ Å³, $Z = 16$, $Z' = 4$, $F(000) = 544$, $\rho = 1.730$ g cm⁻³, $R_{wp} = 0.012$, $R_p = 0.009$ and $R_{Bragg} = 0.003$, 2θ range = 8–105° for 4851 data and 39 parameters. CCDC No. 1866303.

Crystallographic data for **Cu-BPZNH₂·S**. C₆H₅CuN₅·0.9DMF, Formula weight: 276.46 g mol⁻¹, orthorhombic, *Imma*, $a = 15.2776(10)$ Å, $b = 7.2097(5)$ Å, $c = 9.6527(6)$ Å, $V = 1063.2(1)$ Å³, $Z = 16$, $Z' = 4$, $F(000) = 564$, $\rho = 1.750$ g cm⁻³, $R_{wp} = 0.018$, $R_p = 0.013$ and $R_{Bragg} = 0.007$, 2θ range = 8–105° for 4851 data and 40 parameters. CCDC No. 1866301.

Crystallographic data for **Zn-BPZNH₂·S**. C₆H₅N₅Zn·0.9DMF, Formula weight: 278.31 g mol⁻¹, tetragonal, *P4₂/mmc*, $a = 8.9535(2)$ Å, $c = 7.2440(2)$ Å, $V = 580.72(3)$ Å³, $Z = 16$, $Z' = 2$, $F(000) = 284$, $\rho = 1.594$ g cm⁻³, $R_{wp} = 0.073$, $R_p = 0.054$ and $R_{Bragg} = 0.041$, 2θ range = 8–105° for 4851 data and 40 parameters. CCDC No. 1866304.

3.1.4. M-BPZ(NH₂)₂

Zn-BPZ(NH₂)₂·S is isostructural to Zn-BPZ.⁶ Hence, the structure refinement was carried out starting from the crystal structure of Zn-BPZ. As done for the M-BPZNH₂ MOFs, during the structure refinement the NH₂ groups were forced to be coplanar to the ligand, because of the difficult localization of hydrogens *via* X-ray diffraction. Two tan(θ)-dependent spherical harmonics were convoluted to a Lorentzian function in order to describe the different anisotropic peak broadening of the sharper $[h0l]$ Bragg reflections with respect to the other ones, a Gaussian contribution further lowered the R_{wp} figure of merit. The final Rietveld refinement plot is shown in Figure 3.8.

Zn-BPZ(NH₂)₂ crystallizes in the tetragonal space group *P4₂/mmc*, where tetrahedral Zn(II) nodes are connected by exo-tetradentate ligands creating a 3-D framework with 1-D square channels parallel to the $[001]$ crystallographic direction (Figure 3.8; see the caption to this Figure for the main bond distances and angles at the metal ions). At

ambient conditions, **Zn-BPZ(NH₂)₂** shows an empty volume of ~43.8%,^{viii} which translates into a pore volume *per* cell of ~0.32^{ix} cm³ g⁻¹. DMF was found disordered within the channels.

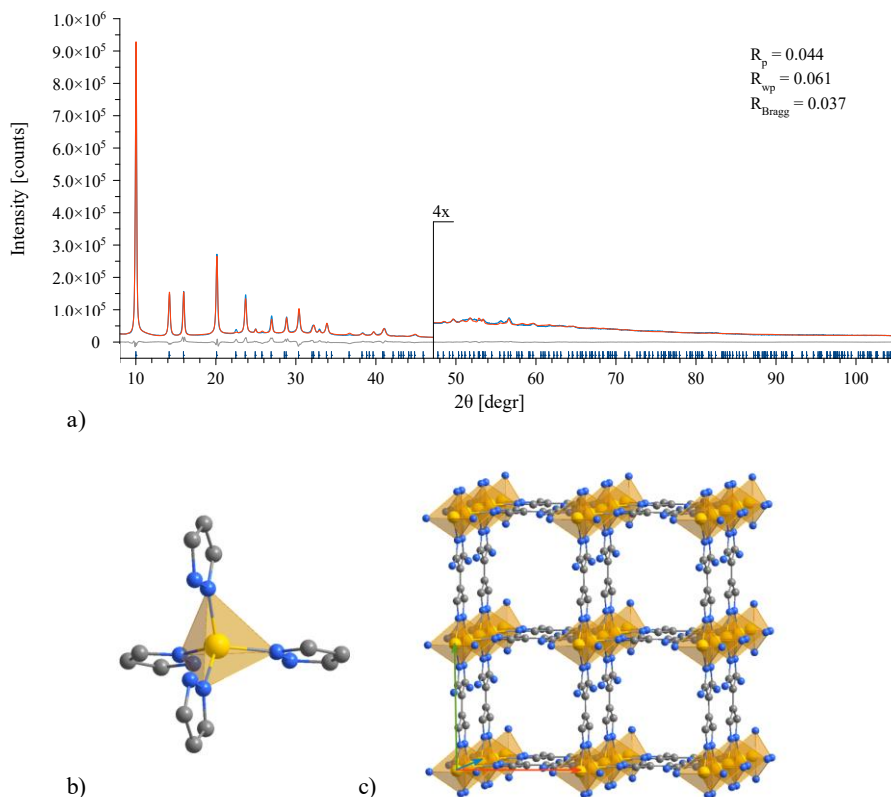


Figure 3.8 a) Graphical output of the final step of the Rietveld refinement for **Zn-BPZ(NH₂)₂**. Colour code: observed intensity, blue trace; calculated intensity, red trace; difference, grey trace; Bragg reflections, blue markers. The portion above ~45° has been magnified for clarity. Representation of the crystal structure of **Zn-BPZ(NH₂)₂·S**: b) The tetrahedral node. c) Portion of the crystal packing viewed, in perspective, along the [001] direction. Atom colour code: carbon, grey; nitrogen, blue; zinc, yellow. The solvent molecules and hydrogen atoms have been omitted for clarity. An ordered model in *P1* has been adopted for the position of the NH₂ groups, for the sake of clarity. Main bond distances and angles: Zn-N, 2.024(12) Å; Zn···Zn, 3.5699(2) and 8.8328(5) Å; N-Zn-N, 108.00(19)-112.5(4)°.

^{viii} The empty volume was estimated with the software PLATON⁸ on an ordered model in *P1* after removal of the clathrated solvent.

^{ix} The pore volume was calculated from the ambient conditions empty volume, supposing that the amino groups are coplanar to the 4,4'-bis(pyrazolate) skeleton.

Crystal data for **Zn-BPZ(NH₂)₂·S**: C₆H₆N₆Zn·1.6DMF, Formula weight: 344.49 g mol⁻¹, tetragonal, *P4₂/mmc*, *a* = 8.8328(5) Å, *c* = 7.1397(4) Å, *V* = 557.03(5) Å³, *Z* = 16, *Z'* = 2, *F*(000) = 356, *ρ* = 2.054 g cm⁻³, *R*_{wp} = 0.061, *R*_p = 0.044 and *R*_{Bragg} = 0.037, 2θ range = 8-105° for 4851 data and 40 parameters.

3.2. Thermal characterization of the M-BPZX MOFs

The thermal behaviour of the M-BPZX MOFs was studied by means of two different techniques - on the one hand thermogravimetric analysis (TGA), on the other hand *in situ* variable-temperature PXRD (VT-PXRD). The thermogravimetric analyses were performed under a N₂ flow in the temperature range 303-1173 K. *In situ* variable-temperature powder X-ray diffraction was performed plugging a custom-made sample heater (Officina Elettrotecnica di Tenno, Ponte Arche, Italy) in the diffractometer described in Annex I, and heating in air the compounds from 303 K up to decomposition (or to 713 K, the highest temperature reached by the apparatus), with steps of 20 K. At each step a PXRD pattern was acquired and treated *via* a whole powder pattern (Le Bail) parametric refinement in order to quantify the variation of the unit cell parameters as a function of temperature. The readers must be aware that the thermocouple of the VT-XRPD apparatus is not in direct contact with the sample; therefore, the same event could be observed at slightly different temperatures in VT-PXRD and TGA. The latter should be considered more reliable. For instrument specification the readers are addressed to Annex I.

3.2.1. M-Me₂BPZ·S

According to TGA, under N₂ **Co-Me₂BPZ·S** and **Zn-Me₂BPZ·S** are stable up to ~613 and ~733 K, respectively, see Figure 3.9. The initial weight losses of ~24% [Co(II)] and ~23% [Zn(II)] below 473 K can be attributed to the loss of clathrated DMF^x [~1(25.0%) and ~ 0.9(24.4%) mol of DMF *per* formula unit (f.u.) for **Co-Me₂BPZ·S**

^x The discrepancy in the solvent content detected by elemental analysis, PXRD structure determination and TGA can be attributed to the use of different samples of the same material. Inside the brackets the calculated percentage of DMF.

and **Zn-Me₂BPZ·S**, respectively]. The two compounds are stable upon and after desolvation, as highlighted by VT-PXRD (Figure 3.10).

During desolvation the unit cell parameters of the two compounds decrease (Figure 3.10), though with different behaviour: **Zn-Me₂BPZ** has a step-like contraction of the volume (\sim -0.8%) and of the *c*-axis between 403 and 483 K. At variance, **Co-Me₂BPZ** shows a smooth and larger decrease of \sim -1.3% in volume from 303 K up to 603 K. Both compounds start losing crystallinity from 623 K.

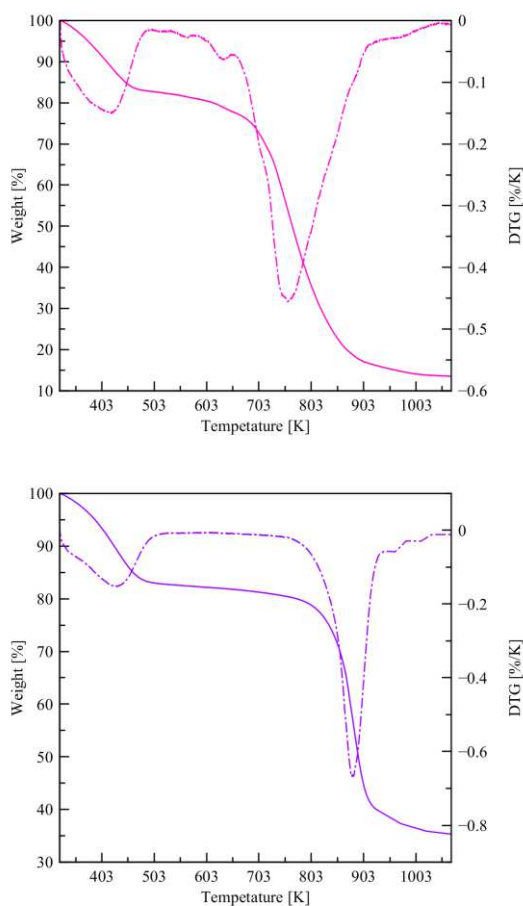


Figure 3.9 *Top*: Thermogravimetric analysis on **Co-Me₂BPZ·S** (pink trace), DTG in dash-dotted pink trace; *bottom*: Thermogravimetric analysis on **Zn-Me₂BPZ·S** (violet trace), DTG in dash-dotted violet trace.

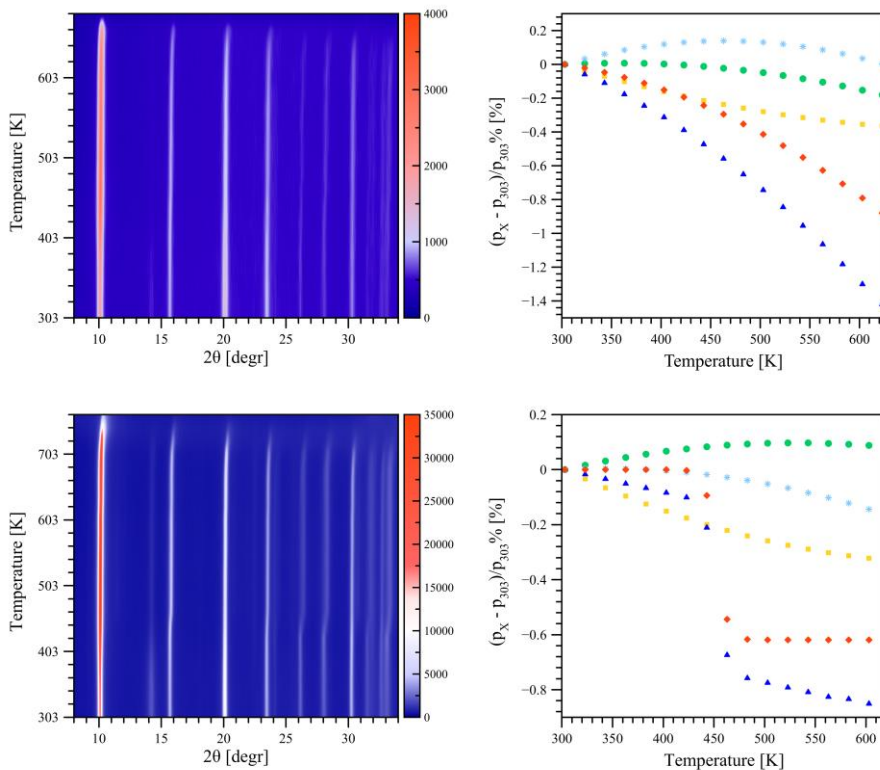


Figure 3.10 *Top*: on the left, the VT-PXRD 2-D plot of **Co-Me₂BPZ·S**; on the right, the result of the whole powder pattern parametric refinement. *Bottom*: on the left, the VT-PXRD 2-D plot of **Zn-Me₂BPZ·S**; on the right, the whole powder pattern parametric refinement. Colour code: *a*-axis, green circle; *b*-axis, yellow square; *c*-axis, red diamond; β , cyan star; volume, blue triangle.

3.2.2. M-BPZNO₂·S

The **M-BPZNO₂·S** [M = Co, Cu, Zn] compounds are stable, under N₂, respectively up to ~623, ~583 K and ~663 K (Figure 3.11). The loss of the clathrated solvent is highlighted by the loss of weight below 513 K:

- ~18%, corresponding to ~0.7(18.0%) mol^x of DMF per f.u. in the Co(II) compound;
- ~25%, corresponding to ~1.0(25.0%) mol^x of DMF per f.u. in the Cu(II) compound;

- ~17%, corresponding to ~0.7(17.5%) mol^x of DMF per f.u. in the Zn(II) compound;

For the **M-BPZNO₂·S** [M = Co, Zn] MOFs, activation is not accompanied by crystallinity loss or phase transitions. The two compounds start suffering from loss of crystallinity from 663 K. On the contrary, the loss of solvent is immediately followed by loss of crystallinity in the case of **Cu-BPZNO₂·S**.

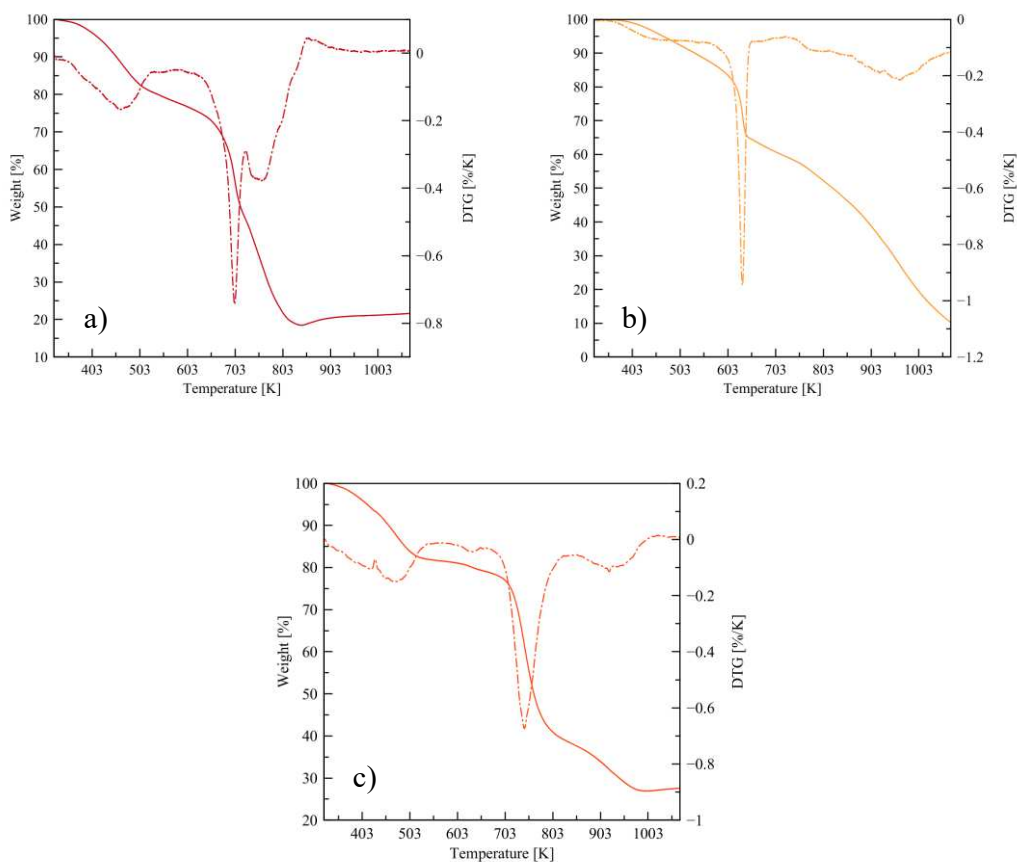


Figure 3.11 Thermogravimetric analysis on a) **Co-BPZNO₂·S** (dark red trace), DTG in dash-dotted dark red trace; b) **Cu-BPZNO₂·S** (orange trace), DTG in dash-dotted orange trace; c) **Zn-BPZNO₂·S** (red trace), DTG in dash-dotted red trace.

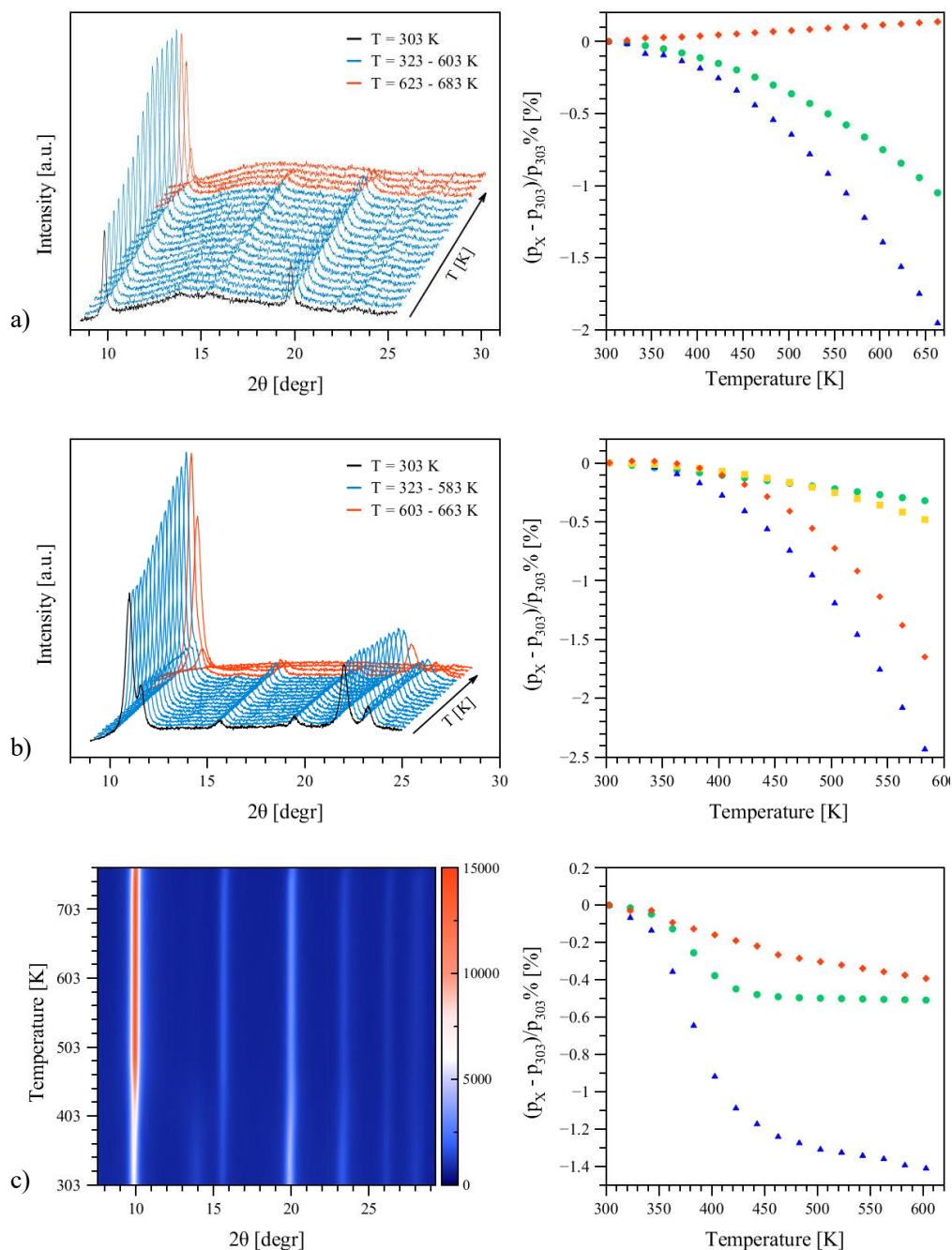


Figure 3.12 a) On the left, the VT-PXRD patterns of **Co-BPZNO₂·S**; on the right, the result of the whole powder pattern parametric refinement. b) On the left, the VT-PXRD patterns of **Cu-BPZNO₂·S**; on the right, the result of the whole powder pattern parametric refinement. c) On the left, the VT-PXRD 2-D plot of **Zn-BPZNO₂·S**; on the right, the whole powder pattern parametric refinement. Colour code: *a*-axis, green circle; *b*-axis, yellow square; *c*-axis, red diamond; volume, blue triangle.

3.2.3. M-BPZNH₂·S

Zn-BPZNH₂·S is stable, under N₂, up to ~703 K (Figure 3.13). The weight loss of ~22.0% below 540 K is related to the loss of ~0.9(23.6%) mol of DMF^x *per* mol of MOF. The VT-PXRD experiment shows that **Zn-BPZNH₂·S** maintains its crystallinity until decomposition, Figure 3.14.

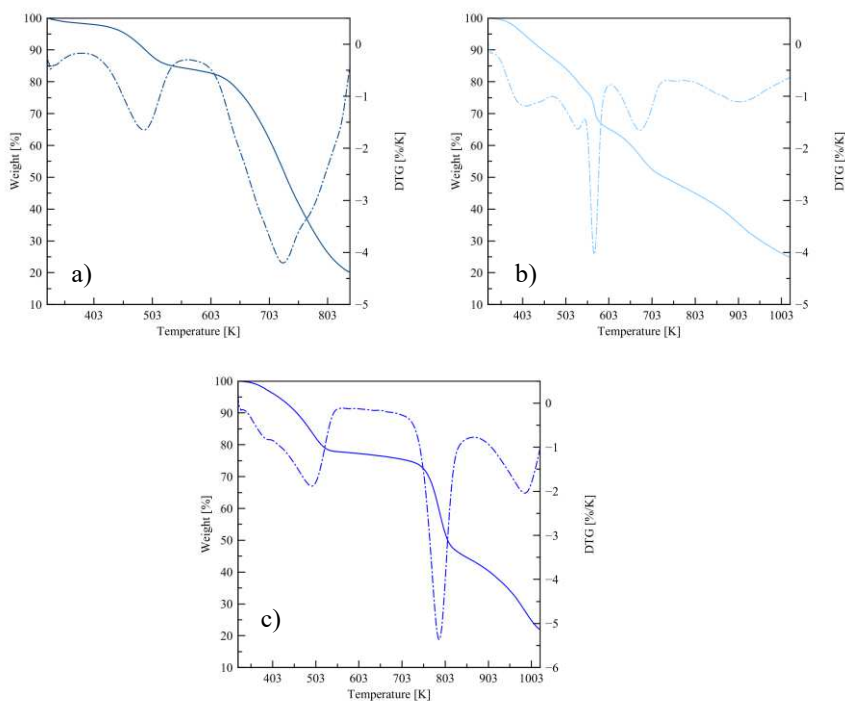


Figure 3.13 Thermogravimetric analyses on a) **Ni-BPZNH₂·S** (dark blue trace), DTG in dash-dotted dark blue trace; b) **Cu-BPZNH₂·S** (cyan trace), DTG in dash-dotted cyan trace; c) **Zn-BPZNH₂·S** (blue trace), DTG in dash-dotted blue trace.

Looking at the unit cell parameters, the desolvation process leads to a modest, step-like decrease of the unit cell volume (~-0.2% in the range 303-483 K), mainly related to the shrinkage of the *a*- and *b*-axes, *i.e.* a reduction of only ~0.3% of the pores section. Overall, in the range of temperatures between activation and decomposition the MOF is rigid, with a negligible decrease in volume of only ~-0.05%. Above 703 K it starts suffering from loss of crystallinity. **Cu-BPZNH₂·S** is stable up to ~563 K, according to TGA, and the solvent loss is immediately followed by decomposition, Figures 3.13-3.14. Finally, **Ni-BPZNH₂** is stable under N₂ up to ~663 K. Between 368 and 483 K a loss of

weight of 15% is observed and can be attributed to the loss of ~ 0.5 (15.1%) mol^x of DMF *per* f.u. with a modest volume expansion of $\sim 0.6\%$. From ~ 583 K, the compound suffers loss of crystallinity.

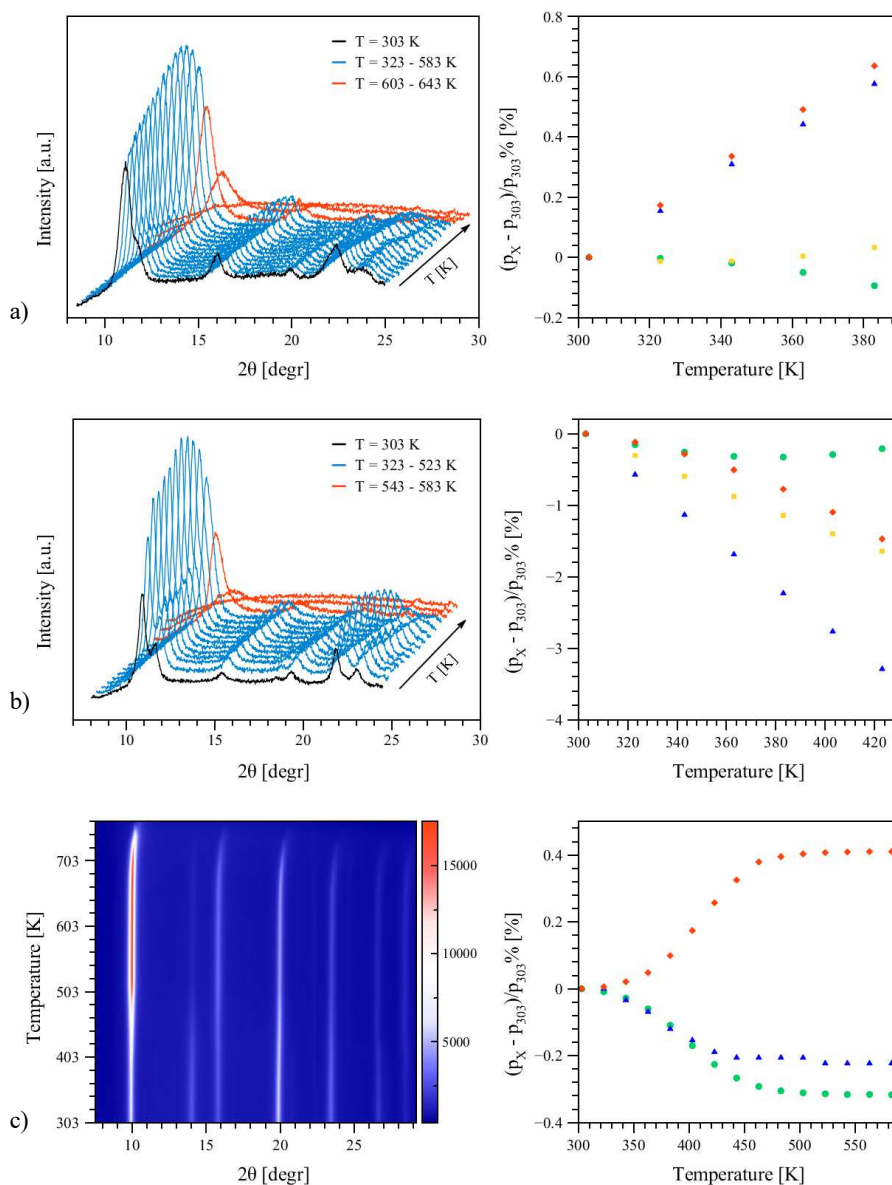


Figure 3.14 a) On the left, the VT-PXRD patterns of Co-BPZNH₂S; on the right, the result of the whole powder pattern parametric refinement. b) On the left, the VT-PXRD patterns of Cu-BPZNH₂S; on the right, the result of the whole powder pattern parametric refinement. c) On the left, the VT-PXRD 2-D plot of Zn-BPZNH₂S; on the right, the result of the whole powder pattern parametric refinement. Colour code: *a*-axis, green circle; *b*-axis, yellow square; *c*-axis, red diamond; volume, blue triangle.

3.2.4. M-BPZ(NH₂)₂·S

Zn-BPZ(NH₂)₂·S shows a good thermal stability both in air and under nitrogen ($T_{\text{dec}} \sim 723$ K, Figure 3.15). Loss of clathrated solvent is denounced, below 610 K, by a weight loss of $\sim 24\%$, corresponding to $\sim 1.0(24.3\%)$ mol^x of DMF per f.u. Neither loss of crystallinity nor phase transition occurs during the desolvation process, as assessed by *in situ* VT-PXRD (Figure 3.15). As highlighted by a whole powder pattern parametric treatment of the data with the Le Bail approach, the decrease of *a*- and *c*-axes, respectively by $\sim 1\%$ and $\sim 0.7\%$, leads to a unit cell volume shrinkage of $\sim 2.8\%$. Above 703 K, **Zn-BPZ(NH₂)₂·S** starts suffering loss of crystallinity.

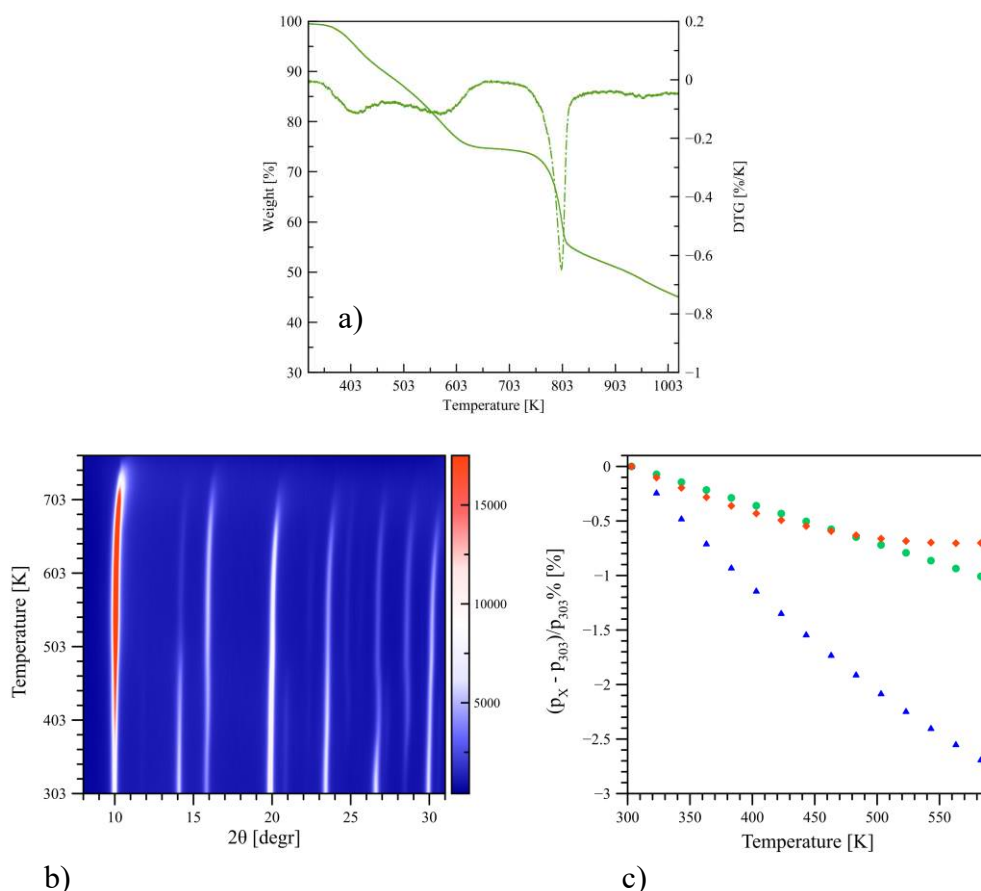


Figure 3.15 a) Thermogravimetric analysis on **Zn-BPZ(NH₂)₂·S** (green trace), DTG in dash-dotted green trace; b) VT-PXRD 2-D plot of **Zn-BPZ(NH₂)₂·S**; c) result of the whole powder pattern parametric refinement. Colour code: *a*-axis, green circle; *c*-axis, red diamond; volume, blue triangle.

3.3. Water vapor stability

To monitor the stability of the M-BPZX compounds with respect to water vapour (one of the components of flue gases, see section 1.2), the samples were introduced in an air-tight water-vapor saturated cell. Powder X-ray diffraction patterns were collected at different times and compared with a preliminary acquisition. None of the compounds show loss of the pristine crystallinity after one week of exposure. As a representative example, Figure 3.16 shows the PXRD patterns of **Zn-BPZNO₂**.

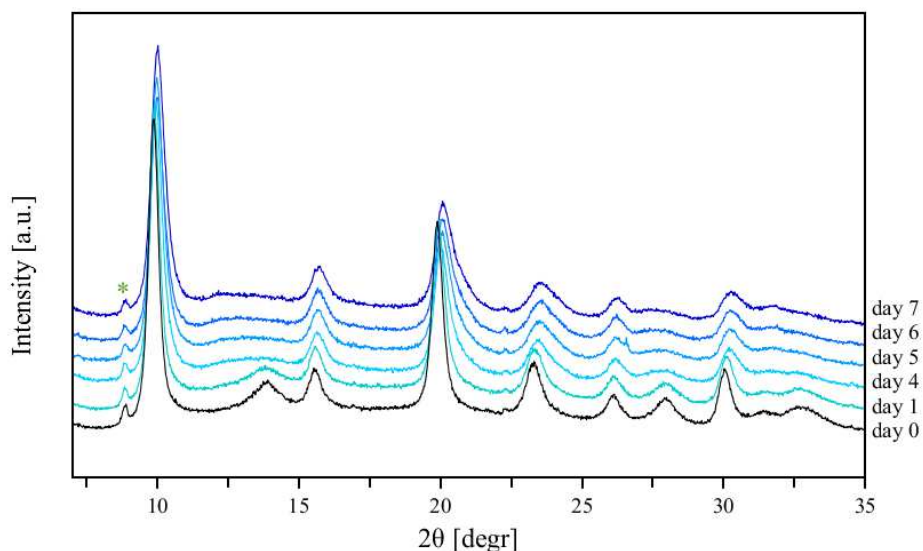


Figure 3.16 Powder X-ray diffraction patterns of **Zn-BPZNO₂** before exposure to an atmosphere saturated of water vapour (black trace) and at different exposure times (blue traces). The asterisk indicates an impurity of the sample.

3.4. Conclusions

The crystal structures of the as-synthesized M-BPZX·S MOFs were determined and refined *via* powder X-ray diffraction, as described in the previous paragraphs. The M-BPZX [M = Co, Zn; X = Me₂, NH₂, NO₂, (NH₂)₂] are isorecticular to a series of bis(pyrazolate) MOFs, as M-BPZ, M-Me₄BPZ (M = Co, Zn) or M(BDP) (M = Co, Zn). Tetrahedral MN₄ nodes and tetradentate linkers build up a three-dimensional open framework in which one-dimensional square channels run along the [001]

crystallographic direction. The different functional groups protrude inside the channels decorating the walls. The Ni(II) and Cu(II) compounds, as well, are isorecticular to already published MOFs, as MIL-53(M) (M = Al, Cr, Fe),¹² showing a 3-D framework with 1-D rhombic channels. At ambient conditions the empty volume ranges between ~36 and ~46%. Except for M-BPZNO₂ [M = Co, Cu], which start losing their crystallinity after two weeks of exposure in air, the other compounds are indefinitely stable at ambient conditions.

The thermal behaviour of the studied MOFs was monitored by the combined use of TGA and VT-PXRD. The bis(pyrazolate) MOFs are stable up to medium-high temperature (563-733 K). The higher stability of azolate-based linkers with respect to carboxylate-based ones is exemplified by the NO₂-functionalized MOFs. Even if the decomposition temperature of **Zn-BPZNO₂·S** is lower than that of the untagged parent Zn-BPZ by ~60 K, the difference in decomposition temperature is lower than that reported for UiO-66-NO₂ and UiO-66,¹³ *i.e.* 190 K. None of the studied MOFs shows any phase transition in response to heating, and, except for **Ni-BPZNH₂**, the desolvation process lead to a shrinkage of the unit cell parameters. The presented MOFs show a rigid behaviour in response to heating with a variation in the unit cell volume ranging from ~0.8 to ~3%. In particular the zinc(II) derivatives – except the dimethylated compound - show a volume variation of only 0.05-0.2% between desolvation and decomposition. Comparing the different metal ions among the same ligand family, Zn(II)-based MOFs show the highest thermal stability. Otherwise, considering Zn(II) MOFs with different functionalization, the trend $T_{\text{dec}}(\text{BPZNH}_2) = T_{\text{dec}}[\text{BPZ}(\text{NH}_2)_2] > T_{\text{dec}}(\text{BPZNO}_2) > T_{\text{dec}}(\text{Me}_2\text{BPZ})$ has been observed.

3.5. References

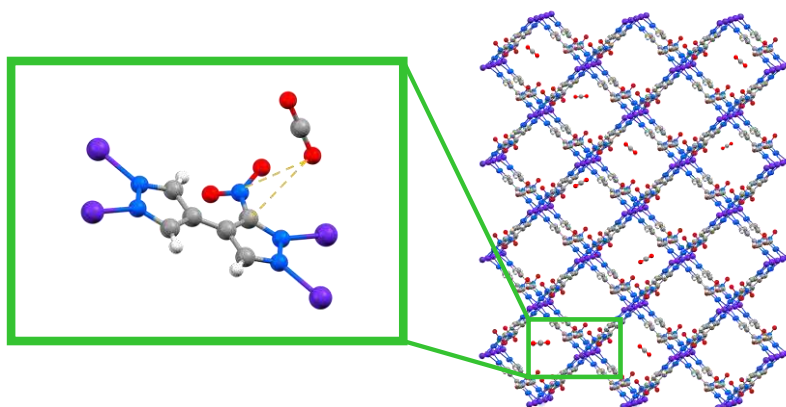
- (1) Coelho, A. A. TOPAS-Academic V6. <http://www.topas-academic.net> 2016.
- (2) Coelho, A. A. Indexing of Powder Diffraction Patterns by Iterative Use of Singular Value Decomposition. *J. Appl. Crystallogr.* **2003**, 36 (1), 86–95.
- (3) Rietveld, H. M. A Profile Refinement Method for Nuclear and Magnetic Structures. *J. Appl. Crystallogr.* **1969**, 2 (2), 65–71.
- (4) Coelho, A. A. Whole-Profile Structure Solution from Powder Diffraction Data Using Simulated Annealing. *J. Appl. Crystallogr.* **2000**, 33, 899–908.
- (5) Mosca, N.; Vismara, R.; Fernandes, J. A.; Casassa, S.; Domasevitch, K. V.; Bailón-García, E.; Maldonado-Hódar, F. J.; Pettinari, C.; Galli, S. CH₃-Tagged Bis(Pyrazolato)-Based Coordination Polymers and Metal-Organic Frameworks: An Experimental and Theoretical Insight. *Cryst. Growth Des.* **2017**, 17 (7), 3854–3867.
- (6) Pettinari, C.; Tăbăcaru, A.; Boldog, I.; Domasevitch, K. V.; Galli, S.; Masciocchi, N. Novel Coordination Frameworks Incorporating the 4,4'-Bipyrazolyl Ditopic Ligand. *Inorg. Chem.* **2012**, 51, 5235–5245.
- (7) Tăbăcaru, A.; Pettinari, C.; Timokhin, I.; Marchetti, F.; Carrasco-Marín, F.; Maldonado-Hódar, F. J.; Galli, S.; Masciocchi, N. Enlarging an Isorecticular Family: 3,3',5,5'-Tetramethyl-4,4'-Bipyrazolato-Based Porous Coordination Polymers. *Cryst. Growth Des.* **2013**, 13 (7), 3087–3097.
- (8) Spek, A. L. *Acta Crystallogr. Sect. D* **2009**, 65, 148-155.
- (9) Mosca, N.; Vismara, R.; Fernandes, J. A.; Tuci, G.; Di Nicola, C.; Domasevitch, K. V.; Giacobbe, C.; Giambastiani, G.; Pettinari, C.; Aragonés-Anglada, M.; et al. NO₂-Functionalized Bis(Pyrazolate) MOFs as CO₂ Capture Materials at Ambient Conditions. *Chem. - A Eur. J.* **2018**, 24 (50), 13170-13180.
- (10) Maity, D. K.; Halder, A.; Bhattacharya, B.; Das, A.; Ghoshal, D. Selective CO₂ Adsorption by Nitro Functionalized Metal Organic Frameworks. *Cryst. Growth Des.* **2016**, 16 (3), 1162-1167.
- (11) Schoedel, A., Li, M., Li, D., O'Keeffe, M., Yaghi, O. M. Structures of metal–organic frameworks with rod secondary building units. *Chem. Rev.*, **2016**, 116(19), 12466-12535.
- (12) Millange, F.; Serre, C.; Férey, G. Synthesis, Structure Determination and Properties of MIL-53as and MIL-53ht: The First Cr^{III} Hybrid Inorganic–Organic Microporous Solids: Cr^{III}(OH)·{O₂C–C₆H₄–CO₂}·{HO₂C–C₆H₄–CO₂H}_x. *Chem. Commun.* **2002**, 822–823.
- (13) Kandiah, M.; Nilsen, M. H.; Usseglio, S.; Jakobsen, S.; Olsbye, U.; Tilset, M.; Larabi, C.; Quadrelli, E. A.; Bonino, F.; Lillerud, K. P. Synthesis and Stability of Tagged UiO-66 Zr-MOFs. *Chem. Mater.* **2010**, 22(24), 6632-6640.

CHAPTER IV

4. CO₂ ADSORPTION

PROPERTIES OF THE M-BPZX MOFs

This chapter collects the textural and adsorption studies performed on the M-BPZX MOFs [M = Co, Ni, Cu, Zn; X = Me₂, NO₂, NH₂, (NH₂)₂]. The role of the different functionalization will be unveiled. Then, the adsorption performances will be comparatively analysed in relation to the nature of the functional groups and metal ions. A comparison with literature results is reported as well. A more detailed description of the experimental methods used can be found in Annex I.



4.1. Adsorption Properties of the M-BPZX MOFs

In the following sections, all the families of M-BPZX MOFs presented in chapter II will be evaluated for CO₂ capture [$X = \text{Me}_2, \text{NO}_2, (\text{NH}_2)_2$] or for CO₂ capture and utilization ($X = \text{NH}_2$). After a preliminary discussion on the textural characterization carried out through N₂ and CO₂ adsorption, the assessment of the influence of the functional group in CO₂ adsorption is reported, as a result of the application of different approaches for the different families, specifically:

- M-Me₂BPZ: N₂ and CO₂ adsorption, theoretical calculations;
- M-BPZNO₂: N₂ and CO₂ adsorption, *in situ* and *operando* high-resolution PXRD, theoretical calculations;
- M-BPZNH₂: N₂ and CO₂ adsorption, catalytic tests for CO₂ epoxidation;
- M-BPZ(NH₂)₂: N₂ and CO₂ adsorption.

All the experimental procedures are collected in Annex I.

4.2. M-Me₂BPZ

Adsorption isotherms. Specific surface area (SSA) and pore texture^{xi} of the M-Me₂BPZ and M-BPZ¹ (M = Co, Zn) MOFs were investigated by means of N₂ and CO₂ adsorption isotherms at 77 and 273 K, respectively, and compared. The N₂ adsorption isotherms are a mixture of type I and type II, typical for microporous and macroporous materials, Figure 4.1. The presence of mesoporosity is confirmed by the presence of hysteresis during the desorption process. The abrupt adsorption over $p/p_0 = 0.8$, can be ascribed to larger interparticle macropores and multilayer adsorption processes. The M-Me₂BPZ MOFs show BET areas of 434 m²/g for the Co(II) derivative and of 290 m²/g for the Zn(II) one. The Non-local Density Functional Theory (NLDFT)^{2,3} was used to calculate the pore size distribution (Figure 4.1): for all the compounds a sharper peak can be detected in the micropore region, and an additional maximum is present in the

^{xi} The textural characterization of the M-Me₂BPZ MOFs was carried out by Prof. F. J. Maldonado-Hódar, University of Granada, Spain.

mesopores range (except for Zn-BPZ), probably due to interparticle pores. The micropore diameters found for the M-Me₂BPZ MOFs are in good agreement with those obtained from the PXRD structural characterization. The micropore size of **Co-Me₂BPZ** is 0.79 nm, to be compared to the pore aperture of $0.76 \times 0.58 \text{ nm}^2$; similarly, **Zn-Me₂BPZ** has 1-D channels $0.72 \times 0.58 \text{ nm}^2$ wide and an average micropore size of 0.77 nm.

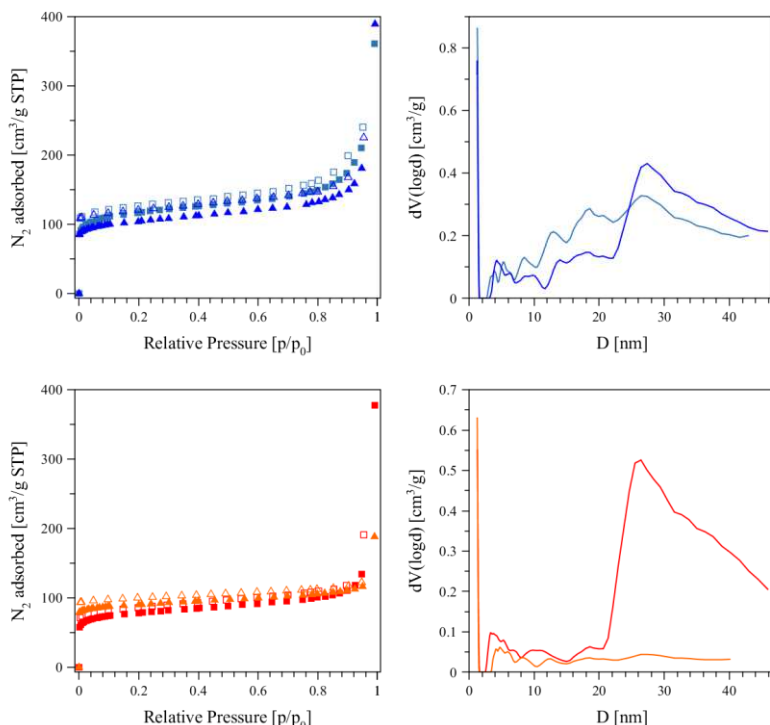


Figure 4.1 *Top*: N₂ adsorption isotherms at 77 K of **Co-BPZ** (blue triangle) and **Co-Me₂BPZ** (light blue square); empty symbols stand for desorption. Pore size distribution of **Co-BPZ** (blue trace) and **Co-Me₂BPZ** (light blue trace) obtained applying the NLDFT method on the N₂ adsorption isotherms. *Bottom*: N₂ adsorption isotherms at 77 K of **Zn-BPZ** (orange triangle) and **Zn-Me₂BPZ** (red square); empty symbols stand for desorption. Pore size distribution of **Zn-BPZ** (orange trace) and **Zn-Me₂BPZ** (red trace) obtained applying the NLDFT method on the N₂ adsorption isotherms.

CO₂ adsorption isotherms were acquired at 273 K in order to assess the role of the methyl group during adsorption; the resulting curves are collected in Figure 4.2. **Co-Me₂BPZ** and **Zn-Me₂BPZ**, at 273 K and 1 bar, adsorb 2.6 mmol g⁻¹ (11.5 wt. %) and 2.0 mmol g⁻¹ (8.8 wt. %), respectively, less than their untagged Co-BPZ and Zn-BPZ counterparts, 3.8 mmol g⁻¹ (16.7 wt. %) and 4.4 mmol g⁻¹ (19.3 wt. %), respectively.⁴

Despite the lower capacity in CO₂ adsorption, the two methylated M-Me₂BPZ compounds show a higher affinity to carbon dioxide and stronger host-guest interactions, with an associated Q_{st} of 26.2 kJ mol⁻¹ (**Co-Me₂BPZ**) and 24.8 (**Zn-Me₂BPZ**) kJ mol⁻¹, higher than those of the M-BPZ MOFs [24.2 kJ mol⁻¹ (M = Co) and 23.7 kJ mol⁻¹ (M = Zn)], confirming the positive role of the methyl group in CO₂ adsorption, as pointed out by theoretical studies.^{5,6} For all the compounds, only physisorption is at work, as revealed by the Q_{st} values. The higher amount of carbon dioxide adsorbed by the M-BPZ MOFs can be associated to their higher BET area. Indeed, in **Co-Me₂BPZ** and **Zn-Me₂BPZ** the steric hindrance of the methyl groups hampered their positive effect on affinity. The adsorption isotherms, except for **Co-Me₂BPZ**, were repeated in order to confirm the reproducibility of the measurements (Figure 4.2): the pristine capacity at 1 bar is recovered by degasifying the samples overnight at 383 K under vacuum.

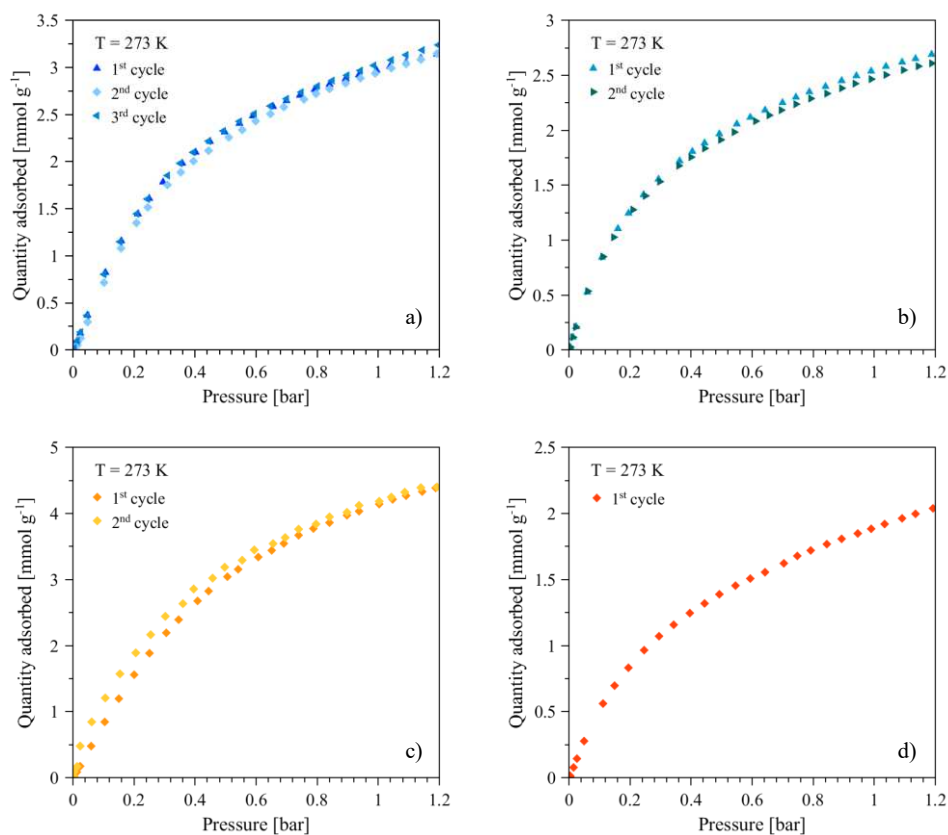


Figure 4.2 CO₂ adsorption isotherm of a) **Zn-BPZ**, b) **Zn-Me₂BPZ**, c) **Co-BPZ** and d) **Co-Me₂BPZ**.

A similar behaviour, *i.e.* higher affinity to CO₂ but lower uptake, can be found in the work by Liu *et al.*,⁷ in which the CO₂ adsorption performances of Zn(NDC)(DMBPY)_{0.5} and Zn(BDC)(DMBPY)_{0.5} (H₂NDC = 1,4-naphthalene-dicarboxylic acid; DMBPY = 2,2'-dimethyl-4,4'-bipyridine; H₂BDC = 1,4-benzene-dicarboxylic acid), were compared with that of the non-methylated counterparts Zn(NDC)(BPY)_{0.5} and Zn(BDC)(BPY)_{0.5} (BPY = 4,4'-bipyridine). In particular, the couple which contains NDC²⁻ shows the same trend of our materials. The performances of M-Me₂BPZ (M = Co, Zn) as CO₂ adsorbents were compared to those of other methylated MOFs under similar experimental conditions (273 K and 1 bar). The CO₂ adsorption capacity range of CH₃-containing MOFs is heterogeneous, starting from 4.0 wt. % for Zn(NDC)(DMBPY)_{0.5}·(DMF)₂ (H₂NDC = 2,6-naphthalenedicarboxylic acid, DMBPY=2,2'-dimethyl-4,4'-bipyridine) at 273 K and 1 bar,⁷ up to 17.3 wt. % for Cu₃(CMPEIP)₂ (H₃CMPEIP = 5-[(4-carboxy-2-methylphenyl)ethynyl]-isophthalic acid), at 273 K and 1 bar.⁸ The M-Me₂BPZ MOFs, with their adsorption capacities of 8.3-11.5 wt. %, ranks in the middle.

Ab initio simulations. As already pointed out, Torrisi *et al.*^{5,6} reported DFT calculations on the positive effect of the insertion of a -CH₃ group on a benzene ring for CO₂ affinity, increasing the strength of the interactions between the aromatic system and the molecular quadrupole of CO₂. Moreover, according to these calculations, the hydrogen atoms of the methyl group and CO₂ are involved in weak hydrogen bond-like interactions enhancing the stability of the CO₂-aromatic ring system. Starting from this evidences, the interactions of carbon dioxide with the M-Me₂BPZ (M = Co, Zn) MOFs and the parent Zn-BPZ compound were investigated. In order to unveil the nature and strength of the host-guest interactions in the M-Me₂BPZ MOFs, *ab initio* simulations^{xii} were performed by introducing an increasing number of CO₂ molecules within the channels (1–3 molecules *per cell*). The computational parameters adopted are detailed in Annex I. Preliminarily, the charge densities of the empty M-Me₂BPZ and Zn-BPZ MOFs were calculated, Figure 4.3: the positive regions (red) are located close to the metal ions, the negative ones near the nitrogen atoms. Then, an increasing amount of CO₂ molecules inside the MOF channels was introduced to evaluate the adsorption energy. Then, a

^{xii} *Ab initio* simulations were performed by Dr. S. Casassa, University of Turin, Italy.

geometry (*i.e.*, unit cell parameters and atomic positions) optimization was carried out and CO₂ adsorption was investigated a second time.

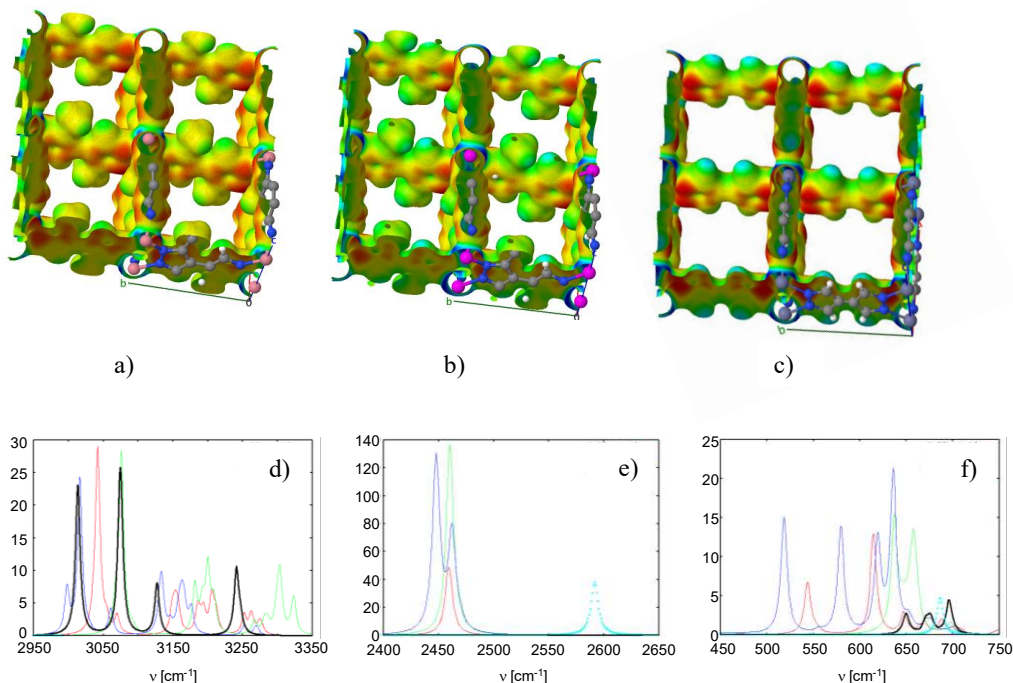


Figure 4.3 Calculated charge density of the M-Me₂BPZ and Zn-BPZ MOFs: a) Co-Me₂BPZ, b) Zn-Me₂BPZ and c) Zn-BPZ. Colour code: red (negative charges), blue (positive charges). Calculated IR spectra of: empty Zn-Me₂BPZ (black trace) and Zn-Me₂BPZ with $n = 1$ (red trace), 2 (green trace) and 3 (blue trace) CO₂ molecules *per cell*; carbon dioxide in the gas phase (dotted cyan trace). d): C-H stretching region of the methyl group; e) bending and f) asymmetric stretching regions of CO₂.

The optimized crystal structures of Co-Me₂BPZ, Zn-Me₂BPZ and Zn-BPZ were used to calculate the isosteric heats of adsorption, at 273 and 298 K, and the IR spectra of the three MOFs. The computational results confirm the experimental trend: $|Q_{st}(M-Me_2BPZ)| > |Q_{st}(Zn-BPZ)|$, and the values found (25-30 kJ mol⁻¹) are compatible with a physisorption process (see for comparison the values of the NO₂ derivatives reported in Table 4.1), as evinced by the textural characterization. The calculated IR spectra, Figure 4.3, confirm the interaction between the methyl groups and the carbon dioxide *via* quadrupolar- π electron density interactions: the comparison of the IR spectrum of empty Zn-Me₂BPZ with that of CO₂-loaded Zn-Me₂BPZ shows that the -CH₃ stretching

modes (at 3300 and 3000 cm^{-1}) are strongly perturbed by gas uptake. The bending and asymmetric stretching bands of CO_2 , at 686 and 2592 cm^{-1} in the gas phase, as well, are affected by the adsorption, resulting lowered and split in several bands. Hence, the driving forces during adsorption appear hydrogen bonds between the hydrogen atoms of the methyl groups and the oxygen atoms of CO_2 , together with weak multipolar interactions between CO_2 and the carbon and nitrogen atoms of the pyrazolate ring. The metal ions result inactive during carbon dioxide adsorption.

4.3. M-BPZNO₂

Adsorption isotherms. The textural properties^{xiii} of the M-BPZNO₂ (M = Co, Cu, Zn) MOFs were investigated through N₂ adsorption at 77 K (Figure 4.4). All the compounds are micro-mesoporous materials, as highlighted by their type IV isotherms. The recorded BET areas fall in the range 400-920 $\text{m}^2 \text{g}^{-1}$, Table 4.1, and are comparable to those of the other M-BPZX MOFs.^{1,4,9} Among them, the zinc(II) compound shows the highest BET area (916 $\text{m}^2 \text{g}^{-1}$), directly followed by the cobalt(II) (645 $\text{m}^2 \text{g}^{-1}$) and the copper(II) (408 $\text{m}^2 \text{g}^{-1}$) ones. As revealed by the *t*-plot analysis, the main contribution to the total surface area comes from micropores [77, 75, and 51% of the total specific surface area (SSA) for **Zn-BPZNO₂**, **Co-BPZNO₂** and **Cu-BPZNO₂**, respectively]. The existence of a small mesoporous component is witnessed by the presence of hysteresis loops at high relative pressure and by the appearance of adsorption at relative pressures higher than ~0.1. The micropore^{xiv} and mesopore^{xv} sizes fall in the ranges of 1.4-1.9 nm and 2.8-3.8 nm, respectively. The total pore volume is 1.03, 0.46 and 0.65 cm^3/g for **Zn-BPZNO₂**, **Co-BPZNO₂** and **Cu-BPZNO₂**, respectively. The micropore volume detected by N₂ adsorption at 77 K, except for **Zn-BPZNO₂**, cannot be compared with that estimated from the structural analysis. An explanation can be found in the partial collapse during the activation process, as revealed by the PXRD patterns collected after the activation.

At ambient conditions (298 K and 1 bar), see Figure 4.4 right, **Co-BPZNO₂**, **Cu-BPZNO₂** and **Zn-BPZNO₂** adsorb 13.2, 8.9 and 19.4 wt. % of CO_2 , respectively,

^{xiii} The textural characterization was performed by Dr. A. Rossin's group, ICCOM-CNR, Sesto Fiorentino, Italy.

^{xiv} NLDFT analysis for cylindrical pore shape of inorganic oxide materials.

^{xv} Estimated from the desorption branch of the isotherm through the BJH model.

showing a correlation between SSA and CO₂ adsorption capacity of the material. The value found for **Zn-BPZNO₂** (4.40 mmol g⁻¹ at 298 K and 1 bar) is remarkably high, falling among the best values for poly(pyrazolate)-containing MOFs under similar experimental conditions, see Table 4.2. Only the bis(pyrazolate) MOFs containing the longer H₂BPEB spacer [H₂BPEB = 1,4-bis(1*H*-pyrazol-4-ylethynyl)benzene] show higher CO₂ capacities (quantity adsorbed between 5.2 and 9.2 mmol g⁻¹).¹⁰ Comparing **Zn-BPZNO₂** to Zn-BPZ,⁴ the nitro-functionalized MOF shows a higher capacity in CO₂ adsorption at 273 K, suggesting a positive influence of the polar group in the ligand skeleton and the insurgence of interactions between the dipole of NO₂ and the quadrupole of CO₂.

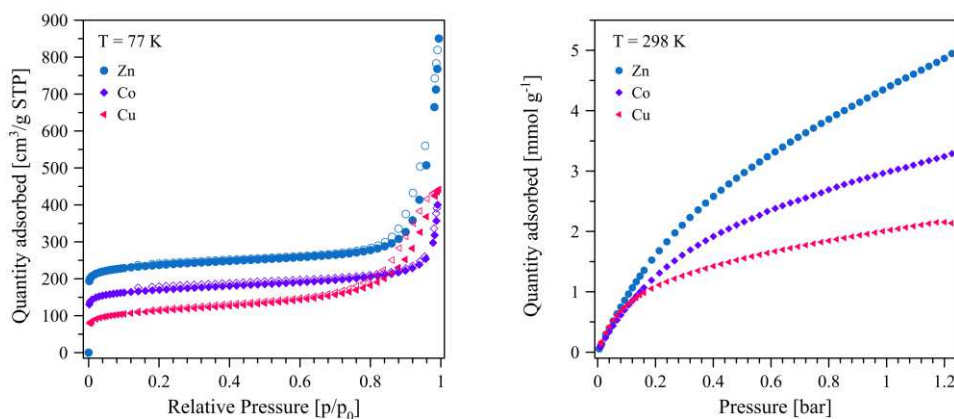


Figure 4.4 *Left*: N₂ adsorption isotherms at 77 K of **Co-BPZNO₂**, **Cu-BPZNO₂** and **Zn-BPZNO₂**; the desorption curves are plotted with empty markers. *Right*: CO₂ adsorption isotherms at 298 K of **Co-BPZNO₂**, **Cu-BPZNO₂** and **Zn-BPZNO₂**.

Table 4.1 Collection of the textural parameters of the M-BPZNO₂ MOFs, as retrieved from N₂ adsorption isotherms at 77 K.

Compound	BET SSA [m ² /g]	Micropore area ^a [m ² /g]	Total pore volume [cm ³ /g]	Mesopore size ^b [nm]	Micropore size ^c [nm]
Co-BPZNO₂	645	480 (74%)	0.46	3.8 / 3.1	1.4 / 1.7 / 1.9
Cu-BPZNO₂	408	207 (51%)	0.65	2.8	1.4 / 1.7
Zn-BPZNO₂	916	710 (77%)	1.03	2.9	1.4 / 1.7

^a From *t*-plot analysis; ^b From BJH; ^c From NLDFT.

Table 4.2 CO₂ uptake (at 1 bar and 273 and/or 298 K) and CO₂/N₂ selectivity at 298 K among the most representative bis(pyrazolate)-containing MOFs of the literature. When directly unavailable, the values were extrapolated from the published data.

Compound	CO ₂ uptake [mmol/g]		CO ₂ /N ₂ selectivity	Ref.
	273 K	298 K		
Zn-BPZNO₂	4.7	4.4	15 (Henry) / 17 (IAST)	11
Fe ₂ (BPEB) ₃	12	9.2	25 (IAST)	10
Ni(BPEB)	8.5	5.9	19 (IAST)	10
Zn(BPEB)	8.2	5.2	21 (IAST)	10
Zn(BDP)	9.1	---	---	12
Ni(BDP)	10	---	---	12
Zn(BDPNH ₂)	~2.5	---	---	12
Zn(BDPOH)	~4.5	---	---	12
Zn(BDPNO ₂)	~2.7	---	---	12
Co(bpdc)(BPZ)	5.5	3.1	12-28 (IAST)	13
NKU-108	4.6	2.2	27 (IAST)	14
NUS-5	---	1.8	35-46 (IAST)	15
Ni ₃ (BTTP) ₂	---	1.7	---	16
MAF-X9	2.2	1.3	12 (Henry)	17
Co ₂ (bpdc) ₂ (H ₂ BPZ)	1.9	1.0	---	18

Moreover, if compared to other MOFs bearing the -NO₂ group as unique tag, our zinc(II) and cobalt(II) MOFs show the highest uptake of CO₂ at mild conditions, see Table 4.3. With respect to the whole class of MOFs, **Zn-BPZNO₂**, with its 21.8 wt. CO₂% capacity at 298 K and 1.2 bar, ranks in the “top-ten” values, and is comparable to Co(DOBDC) [DOBDC²⁻ = 2,5-dioxoterephthalate; BET area = 1089 m²g⁻¹; wt. % CO₂ = 21.6]¹⁹ and ZIF-10 [Zn(imidazolate)₂, BET area = 1800 m²g⁻¹; wt. % CO₂ = 20.9],²⁰ despite the lower BET SSA. The CO₂ adsorption process in **Zn-BPZNO₂** is due to physisorption only, as highlighted by the Q_{st} of 20.5 kJ mol⁻¹ at zero coverage. Finally, **Zn-BPZNO₂** shows the CO₂/N₂ selectivity of 15^{xvi}/12^{xvii}.

^{xvi} The Henry CO₂/N₂ selectivity was estimated using the ratio of the initial slopes of the (CO₂ and N₂) adsorption isotherms at 298 K.

^{xvii} The IAST selectivity was estimated at 298 K for an equimolar mixture of the two gases at a total pressure of 1 bar, using a Henry and a BET model fitting for the N₂ and CO₂ isotherms, respectively.

Table 4.3 Comparison of the CO₂ uptake by NO₂-tagged MOFs at mild conditions. When directly unavailable from the publication, the values were extrapolated from the presented results.

Compound	T [K]	P [bar]	CO ₂ [mmol/g]	Ref.
Zn-BPZNO₂	298	1.0	4.40	11
NJU-Bai 14	298	1.0	4.04	21
Co-BPZNO₂	298	1.0	3.01	11
ZIF-78	298	1.2	2.91	22
UiO-66-NO ₂	296	1.0	2.64	23
Al-MIL-53-NO ₂	298	1.0	2.45	24
Cu-BPZNO₂	298	1.0	2.02	11
CAU-10-NO ₂	298	1.0	2.00	25
MIL-101Cr-NO ₂	293	1.0	1.79	26
MIL-101Cr-pNO ₂	293	1.0	1.63	26
Cu(azbpy)(2-ntp)	298	1.0	1.37	27
Cu(4-bpdb)(2-ntp)	298	1.0	0.40	27

High-resolution powder X-ray diffraction. In order to identify the primary CO₂ adsorption sites of **Zn-BPZNO₂** an *in situ* and *operando* experiment was performed at the high resolution PXRD (HR-PXRD) ID22 beamline of the European Synchrotron Radiation Facility (ESRF, Grenoble, France; experiment ch-5153) by using the gas handling system described by Brunelli *et al.*,²⁸ Figure 4.5. A capillary was filled with activated **Zn-BPZNO₂** powders (see Annex I for the experimental details). HR-PXRD data were collected at 298 K dosing CO₂ in the pressure range 0-5 bar, working at 27.5 keV (0.451 Å). The sample of **Zn-BPZNO₂** synthesised for the synchrotron experiment was an orthorhombic *Cccm* modification of the parent tetragonal framework described in chapter III. The reason can be found in the actual solvent distribution within the channels that modifies the section shape from square to rhombic. After activation, the sample maintained the orthorhombic symmetry. The data acquired at 0 bar of CO₂ were used to determine the orthorhombic structural model, as starting point for the localization of the CO₂ molecules at higher pressures. Comparing the HR-PXRD data at the different pressures, it appears that **Zn-BPZNO₂** does not lose crystallinity nor show any phase transition during CO₂ loading at 298 K.

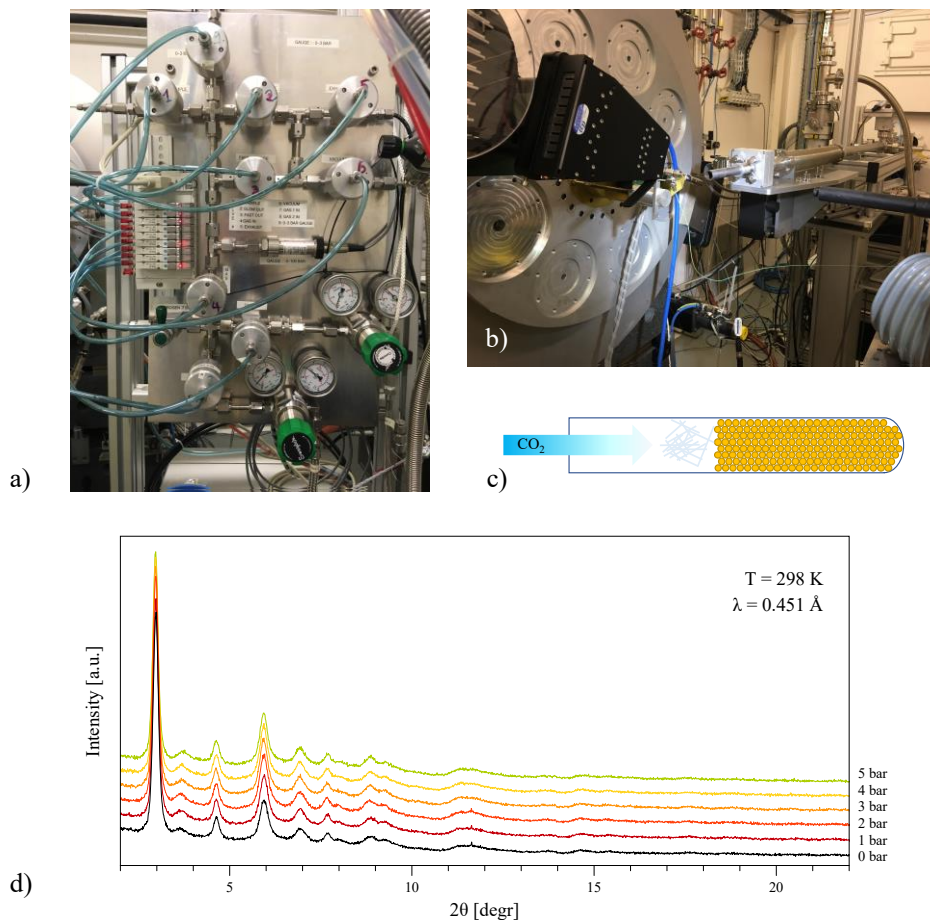


Figure 4.5 a-b) Experimental setup for the ch-5153 experiment on ID22, ESRF (France). c) Schematic representation of the sample environment during the experiment: yellow spheres, microcrystalline powders of **Zn-BPZNO₂**; light blue sticks, glass wool. d) HR-PXRD data collected at 298 K and CO₂ pressure in the 0-5 bar range.

To locate the primary CO₂ adsorption sites, the simulated annealing approach,¹⁵⁴ followed by Rietveld refinement (with TOPAS-Academic V6³⁰) were used. The CO₂ molecule was modelled as a rigid body. During simulated annealing, the position of the centre of mass, the orientation and the site occupancy factor of the CO₂ molecule, together with the torsion angle of the NO₂ group with respect to the plane of the ligand, were let free to vary. To improve the peak profile fitting, $\tan(\theta)$ -dependent fourth-order spherical harmonics were used. The background was described with a polynomial function of the Chebyshev type. A refined, isotropic thermal parameter was assigned to the metal atom, while isotropic thermal parameters 2.0 and 4.0 Å² higher were given to

the ligand and CO₂ atoms, respectively. During the final Rietveld refinement stages, ligand bond distances (except for the C-H distance) were refined in a restrained range of values. Table 4.4 collects the unit cell parameters, the CO₂ site occupation factor, the R_{wp} , R_p and R_{Bragg} figures of merit, and the number of refined parameters for all the Rietveld refinements.

The entrance of CO₂ molecules inside the MOF channels is accompanied by a progressive increase of the intensity of the $[h00]$ Bragg reflections. The adsorption process leads to an initial volume expansion (Table 4.4), in the range 0-2 bar, followed by a progressive restoring of the value observed at 0 bar. This cell volume shrinkage is one of the possible deformations to accommodate guest molecules.³¹ Moreover, the nitro group torsion with respect to the ligand plane increases by $\sim 60^\circ$ passing from 0 bar of CO₂ to 1-5 bar, Figure 4.6 b. The unit cell parameters modifications and the change in -NO₂ orientation suggest the insurgence and maintenance of host-guest interactions. As representatively illustrated in Figure 4.6 c, the guest carbon dioxide occupies a unique adsorption site, despite the different pressures applied, with an increasing site occupancy factor (Table 4.4-5). Only slight differences in the orientation of the CO₂ molecule at the different pressures were observed. Carbon dioxide, in contrast to what initially hypothesized and expected³² (*i.e.* a quadrupole-dipole interaction between CO₂ and -NO₂), is simultaneously involved in C_{host}/N_{host}...O_{guest} interactions in the range 2.5-3.4 Å, Figure 4.6 c. The C(3) carbon atom and the nitrogen atom N(3) of the NO₂ group interact with the O(31) atom of carbon dioxide. The quantity of CO₂ adsorbed, extrapolated from the Rietveld refinement, *i.e.* 14.3 wt. %, Figure 4.6 a, is lower than that observed at 298 K and 1 bar by adsorption isotherms, probably due to the different aperture of the 1-D channels of the studied orthorhombic phase. The interactions found by HR-PXRD confirm the physisorption nature of the process. To the best of our knowledge, this is the first time that the primary CO₂ adsorption sites in a nitro-functionalized MOF are revealed through X-ray diffraction. Moreover, the observed host-guest interactions between the C(3)-NO₂ moiety of the ligand and the nucleophilic oxygen atoms of CO₂ is in contrast with what has been found with amino-functionalized MOFs, where the preferential interaction is between the C atom of CO₂ and the nucleophilic N atom of the NH₂ tag.³³

Table 4.4 Unit cell parameters, CO₂ site occupation factor, R_{wp} , R_p and R_{Bragg} figures of merit and number of refined parameters for all the Rietveld refinements carried out on the HR-PXRD data of **Zn-BPZNO₂**.

p [bar]	a [Å]	b [Å]	c [Å]	V [Å³]	CO₂ s.o.f.	R_{wp}	R_p	R_{Bragg}	# ref. parameters
0	13.96(3)	11.11(2)	7.26(1)	1127(3)	n.a.	3.36	4.19	1.05	43
1	14.01(3)	11.09(1)	7.28(1)	1131(3)	0.229	2.97	3.63	0.51	48
2	14.02(2)	11.100(9)	7.297(7)	1136(2)	0.243	2.92	3.59	0.44	49
3	13.97(3)	11.15(2)	7.29(1)	1135(4)	0.249	2.90	3.54	0.35	49
4	13.93(3)	11.16(2)	7.28(1)	1132(4)	0.267	2.92	3.58	0.50	47
5	13.84(3)	11.22(1)	7.27(1)	1128(4)	0.270	2.93	3.58	0.43	47

Table 4.5. Fractional coordinates of the atoms of the independent CO₂ molecule at 298 K and different CO₂ pressures. The errors are present only for the O2 coordinates because it is the mass centre of the rigid body.

p [bar]	C			O1			O2		
	x	y	z	x	y	z	x	y	z
1	0.488	0.896	0.152	0.498	0.003	0.128	0.477(1)	0.789(5)	0.176(4)
2	0.488	0.897	0.153	0.491	0.005	0.141	0.478(2)	0.789(5)	0.165(12)
3	0.486	0.897	0.152	0.496	0.005	0.1422	0.476(2)	0.790(7)	0.162(9)
4	0.489	0.888	0.149	0.497	0.996	0.136	0.481(1)	0.781(5)	0.163(7)
5	0.492	0.890	0.151	0.501	0.997	0.144	0.482(3)	0.783(6)	0.158(10)

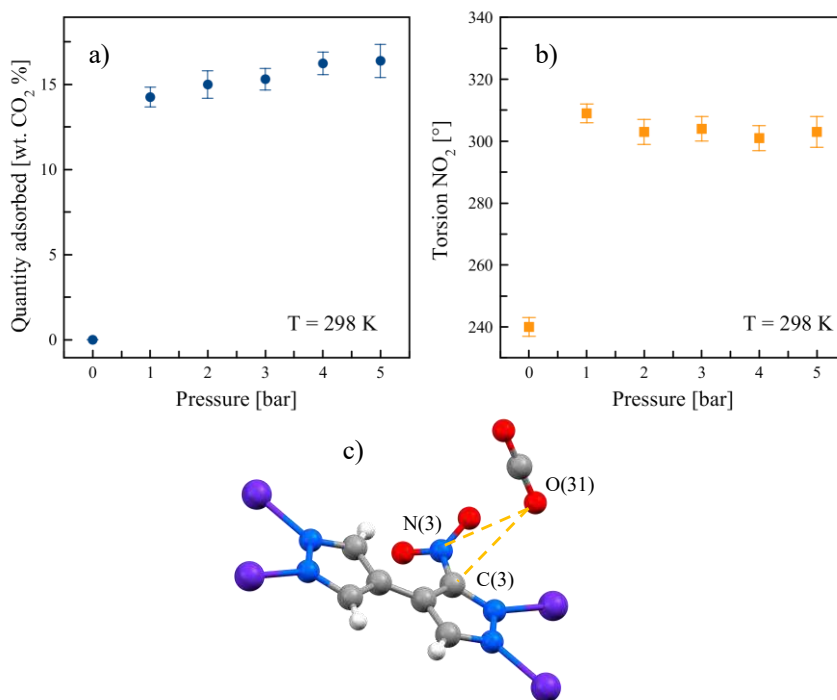


Figure 4.6 a) Quantity of CO₂ adsorbed at T = 298 K and pressure = 0-5 bar, as retrieved from Rietveld refinements on HR-PXRD data. b) Variation of the torsion angle between the nitro group and the ligand plane. c) Host-guest interactions (dashed orange lines) between CO₂ and **Zn-BPZNO₂**, at 1 bar of CO₂, as found from Rietveld refinement on HR-PXRD data. Atom colour code: carbon, grey; hydrogen, light grey; nitrogen, blue; oxygen, red; zinc, violet.

Grand Canonical Monte Carlo (GCMC) simulations. In order to confirm and verify the interactions evinced by HR-PXRD, GCMC simulations of the adsorption isotherms and of the primary CO₂ adsorption sites in **Zn-BPZNO₂** were performed both on an orthorhombic and on a tetragonal structural model, starting from the PXRD crystal structures and optimizing them.^{xviii} As a general trend, see Figure 4.7, the predicted N₂ adsorption isotherms underestimate the observed one; moreover the saturation loading for the tetragonal model is higher than that of the orthorhombic one. The difference, by ~30%, between simulated and observed curves could be ascribable to the presence of structural defects such as channel shape local deformations, as suggested by the anisotropic shape of specific classes of Bragg reflections in the PXRD patterns, or extra-

^{xviii} GCMC simulations were done by Prof. P. Moghadam's group, University of Cambridge, United Kingdom.

pore volume in the real sample; indeed, the adsorption isotherms simulated after the removal of the $-\text{NO}_2$ group are closer to the experimental ones (empty symbols in Figure 4.7). For CO_2 as well, the calculated adsorption isotherms underestimate the experimental ones over 0.4 bar of CO_2 . However, the calculated quantity of CO_2 adsorbed at 1 bar for the orthorhombic phase is comparable to the value found by the HR-PXRD experiment, green star in Figure 4.7 right. More importantly, the adsorption site found by HR-PXRD is in good agreement with that determined computationally. Figure 4.8 collects the snapshots of CO_2 molecules inside the channels. The $[\text{C}(3)_{\text{host}}/\text{N}_{\text{host}} \cdots \text{O}/\text{C}_{\text{guest}}]$ distances obtained by Radial Distribution Functions (RDFs) and atomic distance $[g(r) \text{ vs. } r]$ plots, Figure 4.8, fall around 4.0 \AA and are in good agreement with those obtained by Rietveld refinement on the HR-PXRD data ($r \sim 2.5\text{-}3.4 \text{ \AA}$).

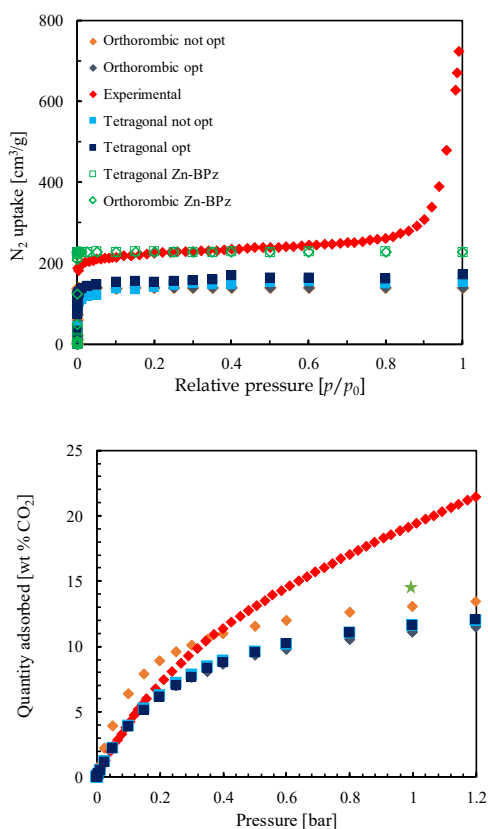


Figure 4.7 *Top*: Comparison between calculated and experimental N_2 adsorption isotherms for Zn-BPZNO_2 , 77 K. *Bottom*: Comparison between calculated and experimental CO_2 adsorption isotherms for Zn-BPZNO_2 , 298 K; green star, quantity of CO_2 adsorbed during the HR-PXRD experiment at 1 bar.

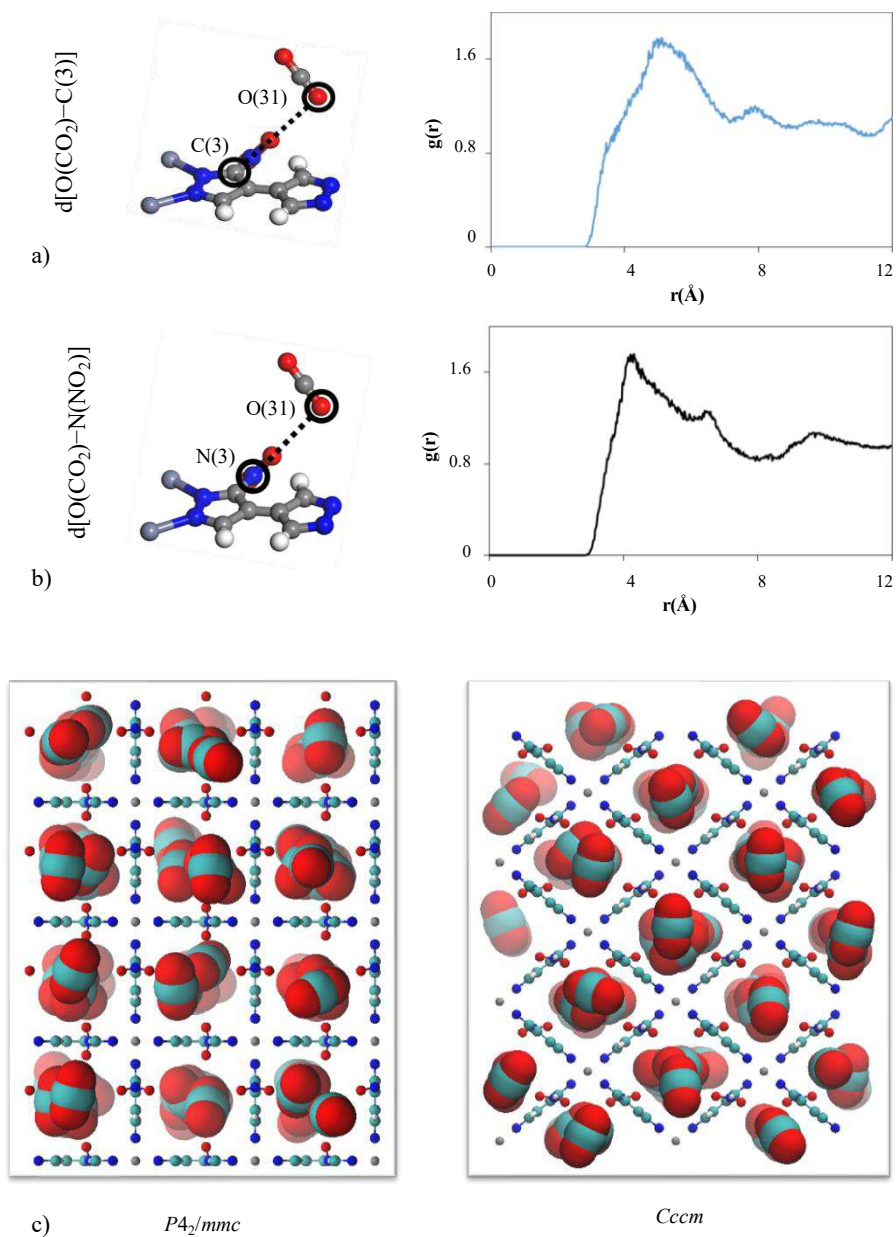


Figure 4.8 a-b) RDF plots for selected atomic distances for Zn-BPZNO₂ in the orthorhombic model. c) Snapshots of CO₂ molecules inside the 1-D channels in the tetragonal and orthorhombic structural models. Atom colour code: carbon light blue; nitrogen, blue; oxygen, red; zinc, grey.

4.4. M-BPZNH₂

Adsorption isotherms: The textural properties^{xix} of the M-BPZNH₂ (M = Ni, Cu, Zn) MOFs were investigated through N₂ adsorption at 77 K; the pertinent curves are reported in Figure 4.9 left, while the main results retrieved are collected in Table 4.6. All the samples show a type IV isotherm, related to the micro-mesoporous nature of these materials. BET areas range between 100 m² g⁻¹ [Cu(II)] and 395 m² g⁻¹ [Zn(II)], smaller, but comparable to those of other bis(pyrazolate) MOFs.^{4,9,11,34,35} The complete activation of all the compounds was confirmed by the thermogravimetric analysis on the activated samples, where no weight loss was observed before decomposition. The *t*-plot analysis revealed different contributions to the total surface area for **Zn-BPZNH₂**, mainly composed by micropores (69%), and for **Ni-BPZNH₂** and **Cu-BPZNH₂**, where the microporosity contribution is negligible (8.8 and 28.1% of the total area respectively). The adsorption at relative pressures (*p/p*₀) higher than ~0.1 and the hysteresis loop at high *p/p*₀ confirm the presence of mesopores in all the compounds. NLDFT analysis revealed two different micropore sizes in **Zn-BPZNH₂**, *i.e.* 1.4 and 1.7 nm, higher than those retrieved by the structural characterization. The BJH model, applied to the desorption branch, revealed mesopore sizes of 2.8/3.8, 3.4 and 3.9 nm for **Ni-BPZNH₂**, **Cu-BPZNH₂** and **Zn-BPZNH₂**, respectively. The total pore volume for **Ni-BPZNH₂**, **Cu-BPZNH₂** and **Zn-BPZNH₂** is 0.49, 0.46 and 0.57 cm³ g⁻¹, respectively.

Table 4.6 Collection of the textural parameters of the M-BPZNH₂ MOFs retrieved from the N₂ adsorption isotherms at 77 K.

	BET SSA [m ² /g]	Volume micro [cm ³ /g]	Total pore volume [cm ³ /g]	Mesopore size ^b [nm]	Micropore size ^c [nm]
Ni-BPZNH₂	192	0.02	0.49	2.8 / 3.8	-
Cu-BPZNH₂	100	0.01	0.46	3.4	-
Zn-BPZNH₂	395	0.11	0.57	3.9	1.4, 1.7

^{xix} The textural characterization, CO₂ adsorption isotherms and catalytic experiments were carried out by Dr. A. Rossin's group, ICCOM-CNR, Sesto Fiorentino, Italy.

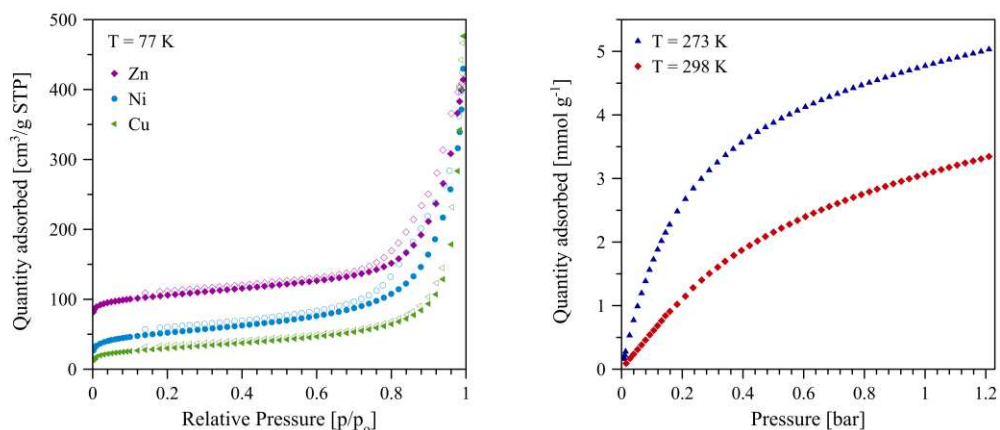


Figure 4.9 *Left:* N₂ adsorption isotherms of **Zn-BPZNH₂** (purple diamond), **Ni-BPZNH₂** (blue circle) and **Cu-BPZNH₂** (green triangle) at 77 K. The empty symbols stand for the desorption curves. *Right:* CO₂ adsorption isotherms of **Zn-BPZNH₂** at 273 K (blue triangle) and 298 K (red diamond).

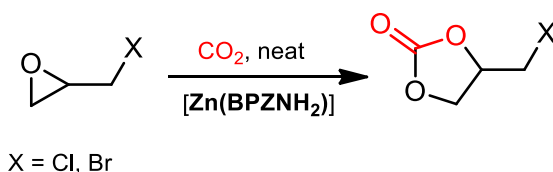
Due to the low BET SSA and microporosity of nickel(II) and copper(II) derivatives, only **Zn-BPZNH₂** was tested as carbon dioxide adsorbent, by collecting CO₂ adsorption isotherms at 273 and 298 K, Figure 4.9 right. At 273 K and 1 bar, **Zn-BPZNH₂** adsorbs 21.0 wt. % of CO₂, *i.e.* 4.8 mmol g⁻¹, outperforming the Zn-BPZ⁴ untagged parent (4.4 mmol g⁻¹). The introduction of the NH₂ group on the bis(pyrazolate) ligand, as expected, favours CO₂ adsorption. This result is in agreement with other literature works comparing the performance of isostructural MOFs containing the same metal ion and ligand skeleton except for the NH₂-functionalization.³⁶⁻⁴⁰ **Zn-BPZNH₂** performances are similar to those of other poly(pyrazolate) MOFs and rank well with other MOFs containing the -NH₂ group as unique tag, Table 4.7. Despite its lower SSA, at 273 K its CO₂ uptake can be compared to that of CPF-13 (BET SSA = 1008 m² g⁻¹),⁴¹ Ni(BDPNH₂) (BET SSA = 1305 m² g⁻¹),¹² and MIL-101Cr-(p)NH₂ (BET SSA = 2680 m² g⁻¹).²⁶ **Zn-BPZNH₂** becomes the best-adsorbent of the group when considering the amount of CO₂ adsorbed *per* SSA, Table 4.7.

Table 4.7 Comparison of CO₂ uptake (at 1 bar and 273 and/or 298 K) and Q_{st} among the most representative amino-functionalized MOFs of the state-of-the-art. When unavailable from the literature, the values were calculated from the results presented (if possible).

Compound	CO ₂ uptake [mmol/g]		BET SSA [m ² /g]	Uptake/SSA [mmol/m ²]		Q _{st} [kJ/mol]	Ref.
	273 K	298 K		273 K	298 K		
Zn(BPZNH₂)	4.8	3.1	395	0.012	0.008	35.6	42
MIL-53Al-NH ₂	1.5		1882	0.001		35.0	43
MIL-101Cr-NH ₂	3.2		1675	0.002		50.0	44
MIL-101Cr-(<i>p</i>)-NH ₂	4.5		2680	0.002		43.0	26
MOF-205-NH ₂	1.5		4330	0.0003		15.9	45
m ^{men} -CuBTTri		4.2	870		0.005	96.0	46
Zn ₂ (CN ₅ H ₂) ₃ (H ₂ O) ₃	2.4		341	0.007			47
m ^{men} -Mg-MOF-74		3.9	70		0.056	44.0	48
Bio-MOF-11	6.0		1040	0.006		45.0	49
CPF-13	5.2		1008	0.005		28.2	41
PEI-MIL-101		5.0	608		0.008		50
UiO-66-NH ₂		2.3	876		0.003		51
MIL-125-NH ₂	3.0		1302	0.002			52
MAF-66	6.3		1014	0.006		26.0	53
IRMOF-74-III-CH ₂ NH ₂		3.2	2310		0.001		54
d ^{men} -Mg-MOF-74		4.8	675		0.007	75.0	55
en-Mg ₂ (dondc)		2.6	40		0.065	83.0	56
(NiL _{ethylamine})(BPDC)	0.2	1.4				59.5	57
Zn(BDPNH ₂)	2.5		1345	0.002		28.1	12
Ni(BDPNH ₂)	4.5		1305	0.003		28.2	12
CAU-1-NH ₂		2.5	1530		0.002	-	58
TEPA-MIL-101		3.5	1553		0.002	-	59
CAU-10-NH ₂		1.7	940		0.002	-	25
[Me ₂ NH ₂][Zn ₂ (BDPP)(ATZ)]	5.5	3.2	1019	0.005	0.003	22.0	60
HHU-3	7.7		2354	0.003		24.6	61

The strong affinity of **Zn-BPZNH₂** for CO₂ is highlighted by its Q_{st} = 35.6 kJ mol⁻¹, higher than that of other M-BPZX MOFs (M = Co, Ni, Cu, Zn; X = H, NO₂, NH₂, Me₂),^{1,4,9,11} and that of other NH₂-tagged bis(pyrazolate) ones, *i.e.* Zn(BDPNH₂) or Ni(BDPNH₂),¹² Table 4.7. Finally, **Zn-BPZNH₂** has a good Henry CO₂/N₂ selectivity of 17, higher than its nitro-functionalized analogue (Henry CO₂/N₂ selectivity of 15).

Catalytic CO₂ epoxidation with Zn-BPZNH₂. **Zn-BPZNH₂**, was then tested for CCU, namely as heterogeneous catalyst for carbon dioxide epoxidation to cyclic carbonates under green conditions, *i.e.* without any solvent or co-catalysts. The presence of both a Lewis acid (*i.e.* the metal ion) and a basic site (*i.e.* a basic heteroatom in the ligand or a NH₂ group, as in this case) within the same material has a positive effect in CO₂ epoxidation. Indeed, the acid site activates the epoxide, while the basic one interacts with carbon dioxide. In **Zn-BPZNH₂**, epoxidation was found to work well with epoxides characterized by an electron-withdrawing group (-CH₂X, X = Cl, Br; Scheme 4.1). In particular, epichlorohydrin and epibromohydrin were used as substrates. T = 393 K and CO₂ pressure of 1 bar were found the best conditions for catalysis with a conversion of 41 and 47% for epichlorohydrin and epibromohydrin, respectively (TOF = 3.4 and 3.9).



Scheme 4.1 Scheme of the studied catalytic transformation of halogenated epoxides into cyclic carbonates.

Moreover, the possibility of recovery and reuse of the catalyst was tested. **Zn-BPZNH₂** maintains its catalytic activity at least for three epoxidation cycles, with a conversion of 94 (2nd cycle) and 92% (3rd cycle) with respect to the first use. The reduction of conversion rate can be imputed to a partial loss of the solid catalyst during the recycling procedure. Leaching of the metal into the reaction supernatant was investigated: a maximum ~0.003% of zinc(II) ions were detected, confirming the heterogeneous nature of the process.

The **Zn-BPZNH₂** performance as catalyst, though operating at lower CO₂ pressure and with smaller SSA, can be compared to those of ZIF-8-F (BET SSA = 1096 m² g⁻¹)⁶² or Zn(BDC)(DABCO)_{0.5} [BDC = terephthalate; DABCO = 1,4-diaza-bicyclo[2.2.2]-octane; BET SSA = 1725 m² g⁻¹] (Table 4.8).⁶³ The attempt of carrying out the epoxidation reaction with the nitro-functionalized counterpart, *i.e.* **Zn-BPZNO₂**,¹¹ lead to no reaction product, highlighting the central role of the amino group during the

catalysis. The strong dependence of the catalytic process under mild conditions on the substrate choice was confirmed by the unsatisfactory attempt of using non-activated epoxides or epoxides bearing electron-withdrawing groups other than halides.⁴² A possible mechanism of the process is reported in Figure 4.10.

Table 4.8 List of the catalytic results described (1-5) and comparison with the literature data for the epichlorohydrin epoxidation on zinc-based MOFs under similar reaction conditions (solvent- and co-catalyst-free), as reported in ref. ⁴².

Catalyst	P [bar]	T [K]	t [h]	Yield [%]	TOF ^a	Ref.
Zn(BPZ-NH₂)	1	393	24	41	3.4	42
Zn(BPZ-NH ₂)	1	373	24	14	1.2	42
Zn(BPZ-NH ₂)	5	393	24	32	2.6	42
Zn(BPZ-NH₂)	1	393	24	47	3.9	42
Zn(BPZ-NO ₂)	1	393	24	-	-	42
F-IRMOF-3	20	413	1.5	80	148	64
ZIF-8-F	7	373	4	73.1	7.5	62
BIT-103	30	433	8	90.8	27.4	65
[Zn ₆ (TATAB) ₄ (DABCO) ₃]	1	373	16	95	9.9	66
IL-ZIF-90	10	393	3	82.7	56	67
Zn(BDC)(DABCO) _{0.5}	8	373	12	99	7.5	63

Reaction conditions: mmol catalyst = 0.05; mmol epichlorohydrin = 10; ^a (mmol carbonate)·(mmol metal)⁻¹·h⁻¹; ^b epibromohydrin as substrate. H₃TATAB = 4,4',4''-s-triazine-1,3,5-triyl-tri-*p*-aminobenzoic acid, H₂BDC = terephthalic acid, DABCO = 1,4-diazabicyclo[2.2.2]-octane.

The ring opening of the initial epoxide can be due to its coordination to the metal node. Meantime, the amino group of the ligand activates the CO₂ molecule with the formation of a zwitterionic carbamate. The O-nucleophilic species contained into the carbamate triggers the metal-assisted epoxide ring opening. The closure of the catalytic cycle is due to an intramolecular addition–elimination on the carbamate intermediate, regenerating the active sites.

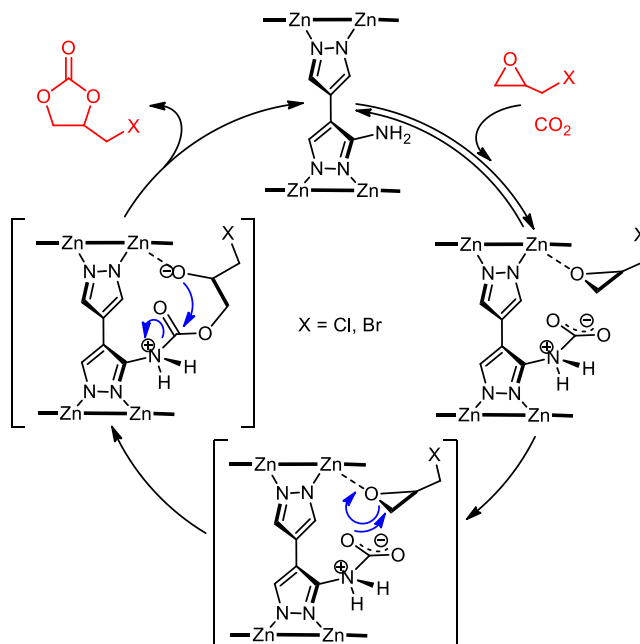


Figure 4.10 Proposed reaction mechanism between epoxides and CO₂ catalysed by **Zn-BPZ(NH₂)₂**, from ref. 42.

4.5. **Zn-BPZ(NH₂)₂**

The textural, adsorption, gas-chromatographic and theoretical simulation studies of **Zn-BPZ(NH₂)₂** were performed by the Ph. D. candidate at the University of Granada, under the supervision of Prof. J.A.R. Navarro, where she spent six months.

Textural characterization. In order to evaluate the porosity of the activated sample, **Zn-BPZ(NH₂)₂** was probed by N₂ adsorption at 77 K, Figure 4.11 a. **Zn-BPZ(NH₂)₂** shows a BET SSA of only 156 m² g⁻¹, lower with respect to that of **Zn-BPZ(NH₂)₂** (395 m² g⁻¹).⁴² The N₂ adsorption isotherm belongs to type IV, typical of a microporous/mesoporous material. The micropore area is equal to ~50%, as retrieved from the *t*-plot analysis. The Horvath-Kawazoe Differential Pore Volume Plot, obtained applying a cylinder pore geometry, shows a sharper peak at ~7.3 Å, in agreement with the value obtained from the structural analysis (~6.0 Å). The macropore component can be related to interparticle voids. At 1 bar of CO₂, **Zn-BPZ(NH₂)₂** adsorbs ~9.7 wt. % and

~6.1 wt. %, respectively, at 273 K and 298 K (Figure 4.11 b). The low capacity of this material can be related to the smaller accessible BET SSA.

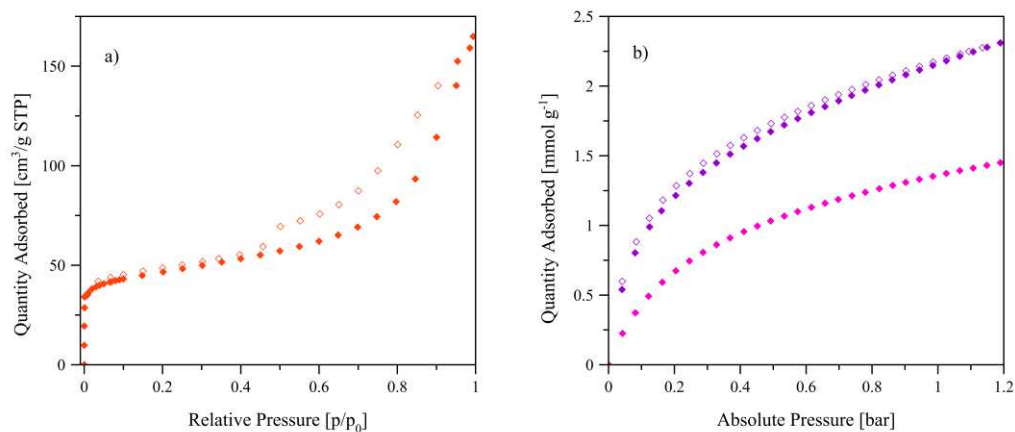


Figure 4.11 a) N₂ adsorption isotherms at 77 K on Zn-BPZ(NH₂)₂. b) CO₂ adsorption isotherms at 273 K (violet diamond) and 298 K (fuchsia diamond) on Zn-BPZ(NH₂)₂. Desorption curve in empty symbols.

Because of the unsatisfactory performances of Zn-BPZ(NH₂)₂ as CO₂ adsorbent and the limited accessible pore area, a different use is proposed in the following sections, namely in C₆H₁₄ isomers separation.

4.5.1. C₆H₁₄ Isomers Separation

The efficiency of internal combustion engines is related to the reactivity of the hydrocarbons comprised in the fuel. Linear hydrocarbons react faster than branched ones. If we consider the five C₆H₁₄ isomers, the research octane number (RON), which is directly related to the value of a specific component in gasoline, increases passing from 30 of the linear *n*-hexane up to 105 of the dibranched 2,3-dimethylbutane.⁶⁸⁻⁷⁰ As a consequence, for commercial purposes a mixture containing only C₆H₁₄ dibranched isomers is more appealing than one containing a mixture of the different isomers, due to its higher final RON.⁷¹ To date, low-RON molecules are recycled to an isomerization reactor to branch their carbon skeleton. However, the separation process, *i.e.* fractional distillation, is critically expensive. A cheaper alternative is the use of solid adsorbents,

namely zeolite 5A, which can separate linear from branched C₆H₁₄ isomers, followed by β -zeolite, for the further separation of monobranched and dibranched isomers.⁷¹⁻⁷³ Nonetheless, mono- from dibranched C₆ isomers separation is still a challenge. The similar polarizability and inert behaviour of C₆ isomers make the search for an efficient separation medium very challenging.⁷⁴ Metal-organic frameworks as well were tested for C₆ separation.⁷⁴⁻⁸⁰ According to Long and coworkers,⁷⁵ an efficient way to separate them is by using a “shape-controlled” adsorbent, which can interact differently with the five C₆H₁₄ isomers. Moreover, the addition of specific functional groups can improve the performance of the material.

In this context, the diamino-tagged **Zn-BPZ(NH₂)₂**, the untagged Zn-BPZ¹ and the dimethylated **Zn-Me₂BPZ⁴** were tested in C₆H₁₄ isomers separation and their performances compared. As described in chapter III, **Zn-BPZ(NH₂)₂·S**, Zn-BPZ·S¹ and Zn-Me₂BPZ·S⁴ are isorecticular⁸¹ and show a 3-D porous network characterized by square 1-D channels. Comparing the empty volume of the three MOFs, at ambient conditions the potential accessible solvent volume⁸² follows the trend: **Zn-BPZ(NH₂)₂** (43.8%) > Zn-BPZ¹ (42.0%) > **Zn-Me₂BPZ⁴** (38.0%). Moreover, the 1-D channel diameters^{xx} are in the 5.0 - 5.4 Å range, allowing all the hexane isomers to fit in.

4.5.2. Variable-temperature Pulse Gas Chromatography

Gas-chromatography was used to unveil the retention time of the three Zn(II)-based MOFs toward the five C₆H₁₄ isomers (2,2DMB = 2,2-dimethylbutane, 2,3DMB = 2,3-dimethylbutane, 2MP = 2-methylpentane, 3MP = 3-methylpentane, HEX = *n*-hexane) at three different temperatures (in the range 443-473 K). The introduction of functional tags was found beneficial in the separation of linear from monobranched and dibranched isomers. Indeed, Zn-BPZ traps all the alkanes within its pores in the range of temperatures relevant for industrial separation (373-473 K),⁸³ whereas **Zn-Me₂BPZ** and **Zn-BPZ(NH₂)₂** show the same trend in retention time, namely:

^{xx} The diameter of the circumference inscribed in the channel was calculated taking into account the van der Waals radii of the atoms decorating the channel walls.

2,2DMB<2,3DMB<3MP<2MP<HEX. The collected curves and the assessed thermodynamic values are gathered in Figures 4.12-4.13 and Tables 4.9-4.10.

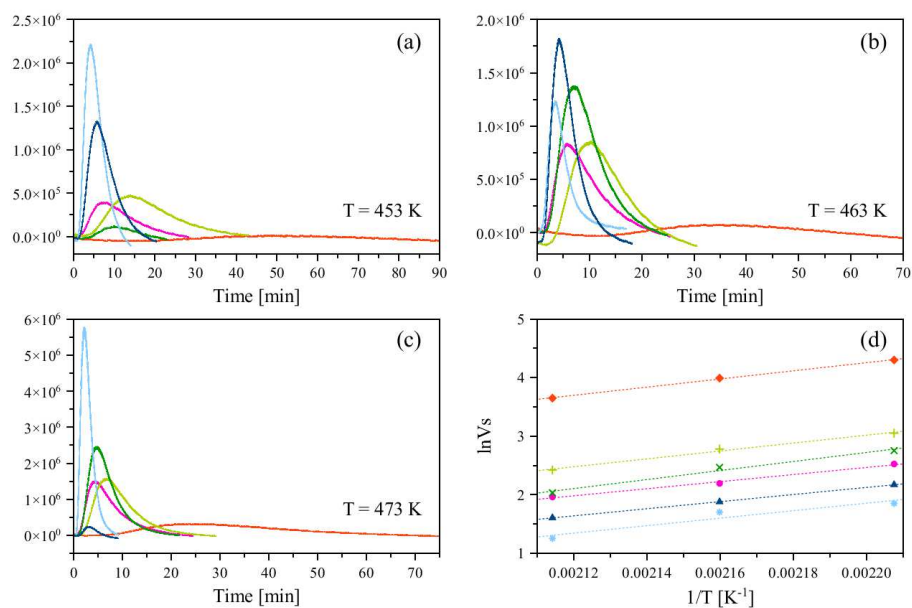


Figure 4.12 Variable temperature pulse gas chromatograms for C_6H_{14} isomers and pentane passed through a chromatographic column packed with $Zn-BPZ(NH_2)_2$, using a H_2 flow of 40 mL min^{-1} at a) 453 K, b) 463 K and c) 473 K. d) Fitting of the variation of the retention volume V_s (in $\text{cm}^3 \text{ g}^{-1}$) of $Zn-BPZ(NH_2)_2$ as a function of the adsorption temperature (453–473 K). Colour code: red, HEX; light green, 2MP; dark green, 3MP; light blue, 2,2DMB; blue, 2,3DMB; pink, pentane.

Table 4.9 $Zn-BPZ(NH_2)_2$: values of retention time, Henry coefficient (K_H), enthalpy (ΔH_{diff} = heat of adsorption; ΔH_{iso} = isosteric heat of adsorption), entropy (ΔS), Gibbs free energy (ΔG) and separation coefficient (α_{hex}) of the hexane isomers at 463 K. The Gibbs free energy was calculated using $\Delta G = \Delta H_{\text{iso}} - T_{\text{ave}} \Delta S$.

$Zn-BPZ(NH_2)_2$	Retention Time [min]	K_H	ΔH_{diff} [kJ mol ⁻¹]	ΔH_{iso} [kJ mol ⁻¹]	ΔS [J K ⁻¹ mol ⁻¹]	ΔG [kJ mol ⁻¹]	α_{hex}
HEX	33.98	53.30	-57.9	-61.7	-92.0	-19.2	1.00
2MP	10.15	15.59	-56.0	-59.9	-98.2	-14.4	3.38
3MP	7.43	11.16	-64.1	-67.9	-118.3	-13.1	4.94
2,2DMB	3.48	4.95	-53.1	-57.0	-101.4	-10.0	10.48
2,3DMB	4.14	6.97	-50.4	-54.2	-93.2	-11.1	7.79

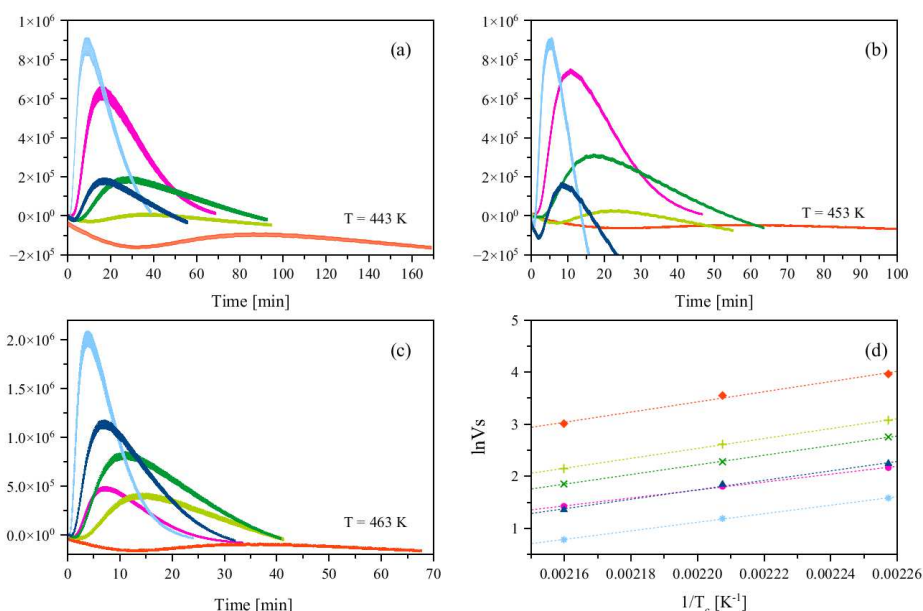


Figure 4.13 Variable-temperature pulse gas chromatograms for C₆H₁₄ isomers and pentane passed through a chromatographic column packed with **Zn-Me₂BPZ**, using a H₂ flow of 40 mL min⁻¹ at a) 443 K, b) 453 K and c) 463 K. d) Fitting of the variation of the retention volume V_s (in cm³ g⁻¹) of **Zn-Me₂BPZ** as a function of the adsorption temperature (443–463 K). Colour code: red, HEX; light green, 2MP; dark green, 3MP; light blue, 2,2DMB; blue, 2,3 DMB; pink, pentane.

Table 4.10 Zn-Me₂BPZ: Values of retention time, Henry coefficient (K_H), enthalpy (ΔH_{diff} = heat of adsorption; ΔH_{iso} = isosteric heat of adsorption), entropy (ΔS), Gibbs free energy (ΔG) and separation coefficient [α_{hex}] of the hexane isomers at 463 K. The Gibbs free energy was calculated using $\Delta G = \Delta H_{\text{iso}} - T_{\text{ave}} \Delta S$.

Zn-Me₂BPZ	Retention Time [min]	K_H	ΔH_{diff} [kJ mol ⁻¹]	ΔH_{iso} [kJ mol ⁻¹]	ΔS [J K ⁻¹ mol ⁻¹]	ΔG [kJ mol ⁻¹]	α_{hex}
HEX	34.71	20.82	-63.25	85.0	-150.2	-17.0	1.00
2MP	14.66	8.60	-81.22	82.9	-153.0	-13.6	2.42
3MP	10.92	6.34	-79.14	80.7	-150.7	-12.4	3.28
2,2DMB	3.76	2.20	-76.90	71.9	-140.7	-8.2	9.48
2,3DMB	6.67	3.95	-68.16	79.3	-151.7	-10.6	5.27

The adsorption enthalpies, calculated from the van't Hoff plot (Figures 4.12-4.13 d), follow the same trend (see Table 4.9-4.10); moreover, the branched isomers have a lower Henry constant than the linear one. Looking at the breakthrough curves, **Zn-Me₂BPZ** and **Zn-BPZ(NH₂)₂** can discern not only between dibranched, monobranched and linear hexanes, but also between 2,2DMB and 2,3DMB.

The separation capacity of **Zn-Me₂BPZ** and **Zn-BPZ(NH₂)₂** was evaluated by the “partition coefficient” α_{hex} .^{xxi} As shown by Tables 4.9 and 4.10, the values of the separation coefficient increase passing from the dibranched isomers to linear hexane, reflecting a shape selectivity of the two MOFs. Moreover, if compared to other MOFs of the literature (Table 4.11), both **Zn-Me₂BPZ** and **Zn-BPZ(NH₂)₂** show a better selectivity over *n*-hexane.

Table 4.11 Comparison of the separation coefficients of **Zn-Me₂BPZ** and **Zn-BPZ(NH₂)₂** with respect to other MOFs of the literature.

	T_a [K]	Separation coefficient α_{hex}						Ref
		PEN	HEX	2MP	3MP	2,2DMB	2,3DMB	
Zn-BPz	n.a.	n.a.	n.a.	n.a.	n.a.	n.a.	n.a.	
Zn-BPz(NH ₂) ₂	463	5.77	1.00	3.42	4.77	10.76	8.12	
Zn-Me ₂ BPz	463	4.98	1.00	2.42	3.28	9.48	5.27	
MIL-47	513	-	1.00	1.40	-	1.60	1.20	84
COK-18	423	3.44	1.00	1.29	1.20	1.47	1.32	74
HKUST-1	423	3.28	1.00	1.12	1.07	1.15	1.18	74
ZIF-8	398	-	1.00	-	3.7	11.9	-	85
IM-22	398	-	1.00	-	1.7	8.4	-	85
ZIF-76	398	-	1.00	-	0.8	0.7	-	85

4.5.3. Molecular Simulations

The alkanes adsorption sites of Zn-BPZ, **Zn-Me₂BPZ** and **Zn-BPZ(NH₂)₂** were localized by using the software Materials Studio.⁸⁶ Differently from what found by Finsy

^{xxi} The α_{hex} partition coefficients have been calculated from the ratio of V_N [V_N = net retention volume (mL)] for each gas at 463 K.

et al.,⁸⁶ all the isomers are located in the centre of the 1-D channels, without any preferred orientation (Figure 4.14). The host-guest distances are in the range 3.3-3.8 Å and do not follow any trend passing from linear to branched isomers. Probably, the narrow aperture of the 1-D channels prevents any preferred host-guest interactions.

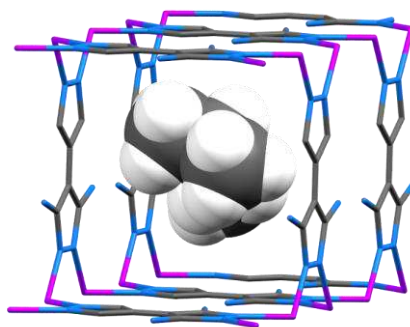


Figure 4.14 2MP adsorption site in **Zn-BPZ(NH₂)₂** simulated *via* the Adsorption Locator module in the Materials Studio 6.0 software.⁸⁷

The diffusivity coefficients of the different isomers were simulated using the molecular dynamic tools of Materials Studio,⁸⁷ Table 4.12. Comparing the diffusion values obtained for Zn-BPZ and **Zn-Me₂BPZ**, two different scenarios appear: on the one hand, the highly accessible pores of Zn-BPZ; on the other hand, the more constricted pores of **Zn-Me₂BPZ**.

Table 4.12 Diffusion coefficients of the C₆ isomers in Zn-BPZ and **Zn-Me₂BPZ** simulated using the molecular dynamic tools of Materials Studio.

	Diffusion coefficient at 453 K [cm ² s ⁻¹]			
	HEX	3MP	2,2DMB	2,3DMB
Zn-BPZ	4.4×10 ⁻⁵	3.0×10 ⁻⁴	1.2×10 ⁻⁴	5.5×10 ⁻⁵
Zn-Me₂BPZ	2.2×10 ⁻⁵	2.5×10 ⁻⁵	5.6×10 ⁻⁶	4.4×10 ⁻⁷

In the case of Zn-BPZ, all the isomers can diffuse inside the inner pore structure of the MOF: all the retrieved diffusivity coefficients are high (5.5×10⁻⁵ - 1.2×10⁻⁴ cm² s⁻¹) and the C₆ isomers probably remain trapped into the 1-D pores of this MOF. This

evidence could explain the difficulty in measuring the thermodynamic data of Zn-BPZ through gas-chromatography, see section 4.5.1. A clear difference of diffusivity coefficients between the dibranched (4.4×10^{-7} and 5.6×10^{-6} $\text{cm}^2 \text{s}^{-1}$, for 2,3DMB and 2,2DMB, respectively), monobranched (2.5×10^{-5} $\text{cm}^2 \text{s}^{-1}$, for 3MP) and linear (2.2×10^{-5} $\text{cm}^2 \text{s}^{-1}$, HEX) isomers is present in **Zn-Me₂BPZ**. This different behaviour is in good agreement with the results of gas-chromatography experiments. *n*-Hexane can diffuse inside and outside the porous system, while the branched and bulkier isomers probably diffuse only in the external particle surface and/or in the defective external pore surface. Unluckily, in the case of **Zn-BPZ(NH₂)₂** the diffusion coefficients are not consistent, avoiding a complete characterization.

4.6. Conclusions

In this chapter the performance of the M-BPZX MOFs were presented and discussed. N₂ adsorption isotherms at 77 K revealed BET SSA ranging from 100 $\text{m}^2 \text{g}^{-1}$ up to 916 $\text{m}^2 \text{g}^{-1}$. As a general trend among the same ligand family, the zinc(II) compounds, except for **Zn-Me₂BPZ**, show the highest BET SSA, with an associated higher CO₂ capacity. All the functional groups inserted on the BPZ²⁻ skeleton were confirmed to have a positive effect in carbon dioxide adsorption, enhancing the capacity and/or the affinity for CO₂ of the functionalized-MOFs with respect to the non-functionalized parents.

In the M-Me₂BPZ (M = Co, Zn) MOFs, despite the lower capacity in CO₂ adsorption, a higher affinity to carbon dioxide and stronger host-guest interactions were observed. *Ab initio* calculations confirmed the experimental results unveiling the mechanism. Two main adsorption driving forces were identified: *i*) hydrogen bonds between the hydrogen atoms of the methyl groups and the oxygen atoms of CO₂, *ii*) weak multipolar interactions between CO₂ and the carbon and nitrogen atoms of the pyrazolate ring. The metal ions are inactive during carbon dioxide adsorption and, at high concentration of CO₂ in the unit cell, additional guest-guest attractive interactions occur.

Among the M-BPZNO₂ (M = Co, Cu, Zn) MOFs, **Zn-BPZNO₂** showed an impressive capacity in CO₂ adsorption at mild conditions (1 bar and 298 K), falling among the best values for poly(pyrazolate)-containing MOFs and in the “top-ten” of all MOFs under

similar experimental conditions. A novel interaction, confirmed by GCMC simulations, between CO₂ and the nitro-group of the ligand was identified thanks to an *in situ* and *operando* HR-PXRD experiment performed at the European Synchrotron Radiation Facility (ESRF, Grenoble France).

The M-BPZNH₂ (M = Ni, Cu, Zn) MOFs show the highest affinity to CO₂ among the studied M-BPZX MOFs. Unfortunately, their limited SSA does not permit higher CO₂ uptake; nonetheless, when comparing the capacity *per* SSA, **Zn-BPZNH₂** has the best performance with respect to other MOFs containing the NH₂ group as unique tag. **Zn-BPZNH₂** was also tested as CCU material, namely as catalyst in CO₂ epoxidation under mild and green conditions.

Zn-BPZ(NH₂)₂ was found to have the lowest BET SSA among the studied Zn-BPZX MOFs and a limited capacity in carbon dioxide adsorption. However, it has been studied, together with Zn-BPZ and **Zn-Me₂BPZ**, as microporous material for the separation of linear, monobranched, and dibranched C₆ isomers. Both **Zn-BPZ(NH₂)₂** and **Zn-Me₂BPZ** show a good selectivity for dibranched C₆ isomers over the more linear ones.

Taking all the observations into account, among the studied MOFs **Zn-BPZNO₂** and **Zn-BPZNH₂** show the best performances, the first for CO₂ capacity, the latter for CO₂ affinity. Starting from these considerations, in the next chapter a series of mixed bis(pyrazolate) zinc(II)-MOFs will be presented in order to further elucidate the role of the -nitro and -amino functionalization with respect to carbon dioxide adsorption.

4.7. References

- (1) Pettinari, C.; Tăbăcaru, A.; Boldog, I.; Domasevitch, K. V.; Galli, S.; Masciocchi, N. Novel Coordination Frameworks Incorporating the 4,4'-Bipyrazolyl Ditopic Ligand. *Inorg. Chem.* **2012**, 51 (9), 5235.
- (2) Seaton, N. A.; Walton, J. A New Analysis Method for the Determination of the Pore Size Distribution of Porous Carbons from Nitrogen Adsorption Measurements. *Carbon N. Y.* **1989**, 27 (6), 853–861.
- (3) Landers, J.; Gor, G. Y.; Neimark, A. V. Density Functional Theory Methods for Characterization of Porous Materials. *Colloids Surfaces A Physicochem. Eng. Asp.* **2013**, 437, 3–32.
- (4) Mosca, N.; Vismara, R.; Fernandes, J. A.; Casassa, S.; Domasevitch, K. V.; Bailón-García, E.; Maldonado-Hódar, F. J.; Pettinari, C.; Galli, S. CH₃-Tagged Bis(Pyrazolato)-Based Coordination Polymers and Metal-Organic Frameworks: An Experimental and Theoretical Insight. *Cryst. Growth Des.* **2017**, 17 (7), 3854–3867.
- (5) Torrisi, A.; Mellot-Draznieks, C.; Bell, R. G. Impact of Ligands on CO₂ Adsorption in Metal-Organic Frameworks: First Principles Study of the Interaction of CO₂ with Functionalized Benzenes. I. Inductive Effects on the Aromatic Ring. *J. Chem. Phys.* **2009**, 130 (19), 194703.
- (6) Torrisi, A.; Bell, R. G.; Mellot-Draznieks, C. Functionalized MOFs for Enhanced CO₂ Capture. *Cryst. Growth Des.* **2010**, 10 (7), 2839–2841.
- (7) Liu, H.; Zhao, Y.; Zhang, Z.; Nijem, N.; Chabal, Y. J.; Zeng, H.; Li, J. The Effect of Methyl Functionalization on Microporous Metal-Organic Frameworks' Capacity and Binding Energy for Carbon Dioxide Adsorption. *Adv. Funct. Mater.* **2011**, 21 (24), 4754–4762.
- (8) Liu, H.; Zhao, Y.; Zhang, Z.; Nijem, N.; Chabal, Y. J.; Peng, X.; Zeng, H.; Li, J. Ligand Functionalization and Its Effect on CO₂ Adsorption in Microporous Metal-Organic Frameworks. *Chem. Asian J.* **2013**, 8 (4), 778–785.
- (9) Tăbăcaru, A.; Pettinari, C.; Timokhin, I.; Marchetti, F.; Carrasco-Marín, F.; Maldonado-Hódar, F. J.; Galli, S.; Masciocchi, N. Enlarging an Isorecticular Family: 3,3',5,5'-Tetramethyl-4,4'-Bipyrazolato-Based Porous Coordination Polymers. *Cryst. Growth Des.* **2013**, 13 (7), 3087–3097.
- (10) Galli, S.; Maspero, A.; Giacobbe, C.; Palmisano, G.; Nardo, L.; Comotti, A.; Bassanetti, I.; Sozzani, P.; Masciocchi, N. When Long Bis(Pyrazolates) Meet Late Transition Metals: Structure, Stability and Adsorption of Metal-Organic Frameworks Featuring Large Parallel Channels. *J. Mater. Chem. A* **2014**, 2 (31), 12208–12221.
- (11) Mosca, N.; Vismara, R.; Fernandes, J. A.; Tuci, G.; Di Nicola, C.; Domasevitch, K. V.; Giacobbe, C.; Giambastiani, G.; Pettinari, C.; Aragonés-Anglada, M.; et al. NO₂-Functionalized Bis(Pyrazolate) MOFs as CO₂ Capture Materials at Ambient Conditions. *Chem. - A Eur. J.* **2018**, 24 (50), 13170–13180.
- (12) Colombo, V.; Montoro, C.; Maspero, A.; Palmisano, G.; Masciocchi, N.; Galli, S.; Barea, E.; Navarro, J. A. R. Tuning the Adsorption Properties of Isorecticular Pyrazolate-Based Metal-Organic Frameworks through Ligand Modification. *J. Am. Chem. Soc.* **2012**.
- (13) Wang, H.-H.; Jia, L.-N.; Hou, L.; Shi, W.; Zhu, Z.; Wang, Y.-Y. A New Porous MOF

- with Two Uncommon Metal–Carboxylate–Pyrazolate Clusters and High CO₂/N₂ Selectivity. *Inorg. Chem.* **2015**, 54 (4), 1841–1846.
- (14) Jia, Y.-Y.; Liu, X.-T.; Feng, R.; Zhang, S.-Y.; Zhang, P.; He, Y.-B.; Zhang, Y.-H.; Bu, X.-H. Improving the Stability and Gas Adsorption Performance of Acylamide Group Functionalized Zinc Metal–Organic Frameworks through Coordination Group Optimization. *Cryst. Growth Des.* **2017**, 17 (5), 2584–2588.
- (15) Xu, G.; Peng, Y.; Hu, Z.; Yuan, D.; Donnadiou, B.; Zhao, D.; Cheng, H. A 2D Metal–Organic Framework Composed of a Bi-Functional Ligand with Ultra-Micropores for Post-Combustion CO₂ Capture. *RSC Adv.* **2015**, 5 (59), 47384–47389.
- (16) Tăbăcaru, A.; Galli, S.; Pettinari, C.; Masciocchi, N.; McDonald, T. M.; Long, J. R. Nickel(II) and Copper(I,II)-Based Metal–Organic Frameworks Incorporating an Extended Tris-Pyrazolate Linker. *CrystEngComm* **2015**, 17 (27), 4992–5001.
- (17) Chen, K.-J.; He, C.-T.; Liao, P.-Q.; Wei, Y.-S.; Zhang, P.-X.; Xue, W.; Zhang, W.-X.; Zhang, J.-P.; Chen, X.-M. A Flexible, Porous, Cluster-Based Zn–Pyrazolate–Dicarboxylate Framework Showing Selective Adsorption Properties. *New J. Chem.* **2014**, 38 (5), 2002–2007.
- (18) Jia, L.-N.; Zhao, Y.; Hou, L.; Cui, L.; Wang, H.-H.; Wang, Y.-Y. An Interpenetrated Pillared-Layer MOF: Synthesis, Structure, Sorption and Magnetic Properties. *J. Solid State Chem.* **2014**, 210 (1), 251–255.
- (19) Li, L.; Yang, J.; Li, J.; Chen, Y.; Li, J. Separation of CO₂/CH₄ and CH₄/N₂ Mixtures by M/DOBDC: A Detailed Dynamic Comparison with MIL-100(Cr) and Activated Carbon. *Microporous Mesoporous Mater.* **2014**, 198, 236–246.
- (20) Ding, L.; Yazaydin, A. O. The Effect of SO₂ on CO₂ Capture in Zeolitic Imidazolate Frameworks. *Phys. Chem. Chem. Phys.* **2013**, 15 (28), 11856–11861.
- (21) Zhang, M.; Wang, Q.; Lu, Z.; Liu, H.; Liu, W.; Bai, J. A Nitro-Decorated NbO-Type Metal–Organic Framework with a Highly Selective CO₂ Uptake and CH₄ Storage Capacity. *CrystEngComm* **2014**, 16 (28), 6287–6290.
- (22) Banerjee, R.; Furukawa, H.; Britt, D.; Knobler, C.; O’Keeffe, M.; Yaghi, O. M. Control of Pore Size and Functionality in Isoreticular Zeolitic Imidazolate Frameworks and Their Carbon Dioxide Selective Capture Properties. *J. Am. Chem. Soc.* **2009**, 131 (11), 3875–3877.
- (23) Rada, Z. H.; Abid, H. R.; Sun, H.; Wang, S. Bifunctionalized Metal Organic Frameworks, UiO-66-NO₂-N (N = -NH₂, -(OH)₂, -(COOH)₂), for Enhanced Adsorption and Selectivity of CO₂ and N₂. *J. Chem. Eng. Data* **2015**, 60 (7), 2152–2161.
- (24) Biswas, S.; Ahnfeldt, T.; Stock, N. New Functionalized Flexible Al-MIL-53-X (X = -Cl, -Br, -CH₃, -NO₂, -(OH)₂) Solids: Syntheses, Characterization, Sorption, and Breathing Behavior. *Inorg. Chem.* **2011**, 50 (19), 9518–9526.
- (25) Reinsch, H.; Waitschat, S.; Stock, N. Mixed-Linker MOFs with CAU-10 Structure: Synthesis and Gas Sorption Characteristics. *Dalt. Trans.* **2013**, 42 (14), 4840–4847.
- (26) Khutia, A.; Janiak, C. Programming MIL-101 Cr for Selective and Enhanced CO₂ Adsorption at Low Pressure by Postsynthetic Amine Functionalization. *Dalt. Trans.* **2014**, 43 (3), 1338–1347.
- (27) Maity, D. K.; Halder, A.; Bhattacharya, B.; Das, A.; Ghoshal, D. Selective CO₂

- Adsorption by Nitro Functionalized Metal Organic Frameworks. *Cryst. Growth Des.* **2016**, 16 (3), 1162–1167.
- (28) Brunelli, M.; Fitch, A. N. A Glass Capillary Cell for in Situ Powder X-Ray Diffraction of Condensed Volatile Compounds. Solid HCFC-123a and HCFC-124. *J. Synchrotron Radiat.* **2003**, 10 (4), 337–339.
- (29) Coelho, A. A. Whole-Profile Structure Solution from Powder Diffraction Data Using Simulated Annealing. *J. Appl. Crystallogr.* **2000**, 33 (3 II), 899–908.
- (30) Coelho, A. A. TOPAS-Academic V6. <http://www.topas-academic.net> 2016.
- (31) Férey, G.; Serre, C. Large Breathing Effects in Three-Dimensional Porous Hybrid Matter: Facts, Analyses, Rules and Consequences. *Chem. Soc. Rev.* **2009**, 38 (5), 1380–
- (32) Han, S. S.; Kim, D.; Jung, D. H.; Cho, S.; Choi, S.-H.; Jung, Y. Accurate Ab Initio-Based Force Field for Predictive CO₂ Uptake Simulations in MOFs and ZIFs: Development and Applications for MTV-MOFs. *J. Phys. Chem. C* **2012**, 116 (38), 20254–20261.
- (33) Vaidhyanathan, R.; Iremonger, S. S.; Shimizu, G. K. H.; Boyd, P. G.; Alavi, S.; Woo, T. K. Direct Observation and Quantification of CO₂ Binding within an Amine-Functionalized Nanoporous Solid. *Science*. **2010**, 330, 650–653.
- (34) Pettinari, C.; Tăbăcaru, A.; Galli, S. Coordination Polymers and Metal-Organic Frameworks Based on Poly(Pyrazole)-Containing Ligands. *Coord. Chem. Rev.* **2016**, 307, 1–31.
- (35) Galli, S.; Masciocchi, N.; Colombo, V.; Maspero, A.; Palmisano, G.; López-Garzón, F. J.; Domingo-Garcia, M.; Fernández-Morales, I.; Barea, E.; Navarro, J. A. R. Adsorption of Harmful Organic Vapors by Flexible Hydrophobic Bis-Pyrazolate Based MOFs. *Chem. Mater.* **2010**, 22 (5), 1664–1672.
- (36) Zhang, Y.; Su, W.; Sun, Y.; Liu, J.; Liu, X.; Wang, X. Adsorption Equilibrium of N₂, CH₂, and CO₂ on MIL-101. *J. Chem. Eng. Data* **2015**, 60 (10), 2951–2957.
- (37) Ko, N.; Hong, J.; Sung, S.; Cordova, K. E.; Park, H. J.; Yang, J. K.; Kim, J. A Significant Enhancement of Water Vapour Uptake at Low Pressure by Amine-Functionalization of UiO-67. *Dalt. Trans.* **2015**, 44 (5), 2047–2051.
- (38) Xydias, P.; Spanopoulos, I.; Klontzas, E.; Froudakis, G. E.; Trikalitis, P. N. Drastic Enhancement of the CO₂ Adsorption Properties in Sulfone-Functionalized Zr- and Hf-UiO-67 MOFs with Hierarchical Mesopores. *Inorg. Chem.* **2013**, 53 (2), 679–681.
- (39) Saha, D.; Bao, Z.; Jia, F.; Deng, S. Adsorption of CO₂, CH₄, N₂O, and N₂ on MOF-5, MOF-177, and Zeolite 5A. *Environ. Sci. Technol.* **2010**, 44 (5), 1820–1826.
- (40) Millward, A. R.; Yaghi, O. M. Metal-Organic Frameworks with Exceptionally High Capacity for Storage of Carbon Dioxide at Room Temperature. *J. Am. Chem. Soc.* **2005**, 127 (51), 17998–17999.
- (41) Zhai, Q. G.; Lin, Q.; Wu, T.; Wang, L.; Zheng, S. T.; Bu, X.; Feng, P. High CO₂ and H₂ Uptake in an Anionic Porous Framework with Amino-Decorated Polyhedral Cages. *Chem. Mater.* **2012**, 24 (14), 2624–2626.
- (42) Vismara, R.; Tuci, G.; Mosca, N.; Domasevitch, K. V.; Di Nicola, C.; Pettinari, C.; Giambastiani, G.; Galli, S.; Rossin, A. Amino-Decorated Bis(Pyrazolate) Metal–Organic Frameworks for Carbon Dioxide Capture and Green Conversion into Cyclic Carbonates. *Inorg. Chem. Front.* **2019**, 6 (2), 533–545.

- (43) Zhang, F.; Zou, X.; Gao, X.; Fan, S.; Sun, F.; Ren, H.; Zhu, G. Hydrogen Selective NH₂-MIL-53(Al) MOF Membranes with High Permeability. *Adv. Funct. Mater.* **2012**, 22 (17), 3583–3590.
- (44) Lin, Y.; Kong, C.; Chen, L. Direct Synthesis of Amine-Functionalized MIL-101(Cr) Nanoparticles and Application for CO₂ Capture. *RSC Adv.* **2012**, 2 (16), 6417–6419.
- (45) Sim, J.; Yim, H.; Ko, N.; Choi, S. B.; Oh, Y.; Park, H. J.; Park, S.; Kim, J. Gas Adsorption Properties of Highly Porous Metal–Organic Frameworks Containing Functionalized Naphthalene Dicarboxylate Linkers. *Dalt. Trans.* **2014**.
- (46) McDonald, T. M.; D’Alessandro, D. M.; Krishna, R.; Long, J. R. Enhanced Carbon Dioxide Capture upon Incorporation of N,N’- Dimethylethylenediamine in the Metal–Organic Framework CuBTTri. *Chem. Sci.* **2011**, 2, 2022–2028.
- (47) Yan, Q.; Lin, Y.; Wu, P.; Zhao, L.; Cao, L.; Peng, L.; Kong, C.; Chen, L. Designed Synthesis of Functionalized Two-Dimensional Metal–Organic Frameworks with Preferential CO₂ Capture. *Chempluschem* **2013**, 78 (1), 86–91.
- (48) McDonald, T. M.; Lee, W. R.; Mason, J. A.; Wiers, B. M.; Hong, C. S.; Long, J. R. Capture of Carbon Dioxide from Air and Flue Gas in the Alkylamine-Appended Metal–Organic Framework M_{men}-Mg₂ (Dobpdc). *J. Am. Chem. Soc.* **2012**, 134 (16), 7056–7065.
- (49) An, J.; Rosi, N. L. Tuning MOF CO₂ Adsorption Properties via Cation Exchange. *J. Am. Chem. Soc.* **2010**, 132 (16), 5578–5579.
- (50) Lin, Y.; Yan, Q.; Kong, C.; Chen, L. Polyethyleneimine Incorporated Metal–Organic Frameworks Adsorbent for Highly Selective CO₂ Capture. *Sci. Rep.* **2013**, 3, 14–16.
- (51) Luu, C. L.; Van Nguyen, T. T.; Nguyen, T.; Hoang, T. C. Synthesis, Characterization and Adsorption Ability of UiO-66-NH₂. *Adv. Nat. Sci. Nanosci. Nanotechnol.* **2015**, 6 (2), 25004.
- (52) Fu, Y.; Sun, D.; Chen, Y.; Huang, R.; Ding, Z.; Fu, X.; Li, Z. An Amine-functionalized Titanium Metal–Organic Framework Photocatalyst with Visible-light-induced Activity for CO₂ Reduction. *Angew. Chemie Int. Ed.* **2012**, 51 (14), 3364–3367.
- (53) Lin, R.-B.; Chen, D.; Lin, Y.-Y.; Zhang, J.-P.; Chen, X.-M. A Zeolite-like Zinc Triazolate Framework with High Gas Adsorption and Separation Performance. *Inorg. Chem.* **2012**, 51 (18), 9950–9955.
- (54) Fracaroli, A. M.; Furukawa, H.; Suzuki, M.; Dodd, M.; Okajima, S.; Gándara, F.; Reimer, J. A.; Yaghi, O. M. Metal–Organic Frameworks with Precisely Designed Interior for Carbon Dioxide Capture in the Presence of Water. *J. Am. Chem. Soc.* **2014**, 136 (25), 8863–8866.
- (55) Lee, W. R.; Jo, H.; Yang, L.-M.; Lee, H.; Ryu, D. W.; Lim, K. S.; Song, J. H.; Han, S. S.; Seo, J. G.; Park, Y. K. Exceptional CO₂ Working Capacity in a Heterodiamine-Grafted Metal–Organic Framework. *Chem. Sci.* **2015**, 6 (7), 3697–3705.
- (56) Yeon, J. S.; Lee, W. R.; Kim, N. W.; Jo, H.; Lee, H.; Song, J. H.; Lim, K. S.; Kang, D. W.; Seo, J. G.; Moon, D. Homodiamine-Functionalized Metal–Organic Frameworks with a MOF-74-Type Extended Structure for Superior Selectivity of CO₂ over N₂. *J. Mater. Chem. A* **2015**, 3 (37), 19177–19185.
- (57) Kim, Y. K.; Hyun, S.; Lee, J. H.; Kim, T. K.; Moon, D.; Moon, H. R. Crystal-Size Effects on Carbon Dioxide Capture of a Covalently Alkylamine-Tethered Metal–Organic

- Framework Constructed by a One-Step Self-Assembly. *Sci. Rep.* **2016**, 6, 19337.
- (58) Ahnfeldt, T.; Gunzelmann, D.; Wack, J.; Senker, J.; Stock, N. Controlled Modification of the Inorganic and Organic Bricks in an Al-Based MOF by Direct and Post-Synthetic Synthesis Routes. *CrystEngComm* **2012**, 14 (12), 4126–4136.
- (59) Wang, X.; Li, H.; Hou, X.-J. Amine-Functionalized Metal Organic Framework as a Highly Selective Adsorbent for CO₂ over CO. *J. Phys. Chem. C* **2012**, 116 (37), 19814–19821.
- (60) Liu, B.; Zhou, H. F.; Hou, L.; Wang, Y. Y. Functionalization of MOFs: Via a Mixed-Ligand Strategy: Enhanced CO₂ Uptake by Pore Surface Modification. *Dalt. Trans.* **2018**, 47 (15), 5298–5303.
- (61) Lu, Z.; Xing, Y.; Du, L.; He, H.; Zhang, J.; Hang, C. Isostructural Functionalization by–OH and –NH₂: Different Contributions to CO₂ Adsorption. *RSC Adv.* **2017**, 7 (75), 47219–47224.
- (62) Miralda, C. M.; MacÍas, E. E.; Zhu, M.; Ratnasamy, P.; Carreon, M. A. Zeolitic Imidazole Framework-8 Catalysts in the Conversion of CO₂ to Chloropropene Carbonate. *ACS Catal.* **2012**, 2 (1), 180–183.
- (63) Mousavi, B.; Chaemchuen, S.; Moosavi, B.; Zhou, K.; Yusubov, M.; Verpoort, F. CO₂ Cycloaddition to Epoxides by Using M-DABCO Metal–Organic Frameworks and the Influence of the Synthetic Method on Catalytic Reactivity. *ChemistryOpen* **2017**, 6 (5), 674–680.
- (64) Zhou, X.; Zhang, Y.; Yang, X.; Zhao, L.; Wang, G. Functionalized IRMOF-3 as Efficient Heterogeneous Catalyst for the Synthesis of Cyclic Carbonates. *J. Mol. Catal. A Chem.* **2012**, 361, 12–16.
- (65) Huang, X.; Chen, Y.; Lin, Z.; Ren, X.; Song, Y.; Xu, Z.; Dong, X.; Li, X.; Hu, C.; Wang, B. Zn-BTC MOFs with Active Metal Sites Synthesized via a Structure-Directing Approach for Highly Efficient Carbon Conversion. *Chem. Commun.* **2014**, 50 (20), 2624–2627.
- (66) Han, Y.-H.; Zhou, Z.-Y.; Tian, C.-B.; Du, S.-W. A Dual-Walled Cage MOF as an Efficient Heterogeneous Catalyst for the Conversion of CO₂ under Mild and Co-Catalyst Free Conditions. *Green Chem.* **2016**, 18 (14), 4086–4091.
- (67) Tharun, J.; Bhin, K.-M.; Roshan, R.; Kim, D. W.; Kathalikkattil, A. C.; Babu, R.; Ahn, H. Y.; Won, Y. S.; Park, D.-W. Ionic Liquid Tethered Post Functionalized ZIF-90 Framework for the Cycloaddition of Propylene Oxide and CO₂. *Green Chem.* **2016**, 18 (8), 2479–2487.
- (68) Herm, Z. R.; Bloch, E. D.; Long, J. R. Hydrocarbon Separations in Metal-Organic Frameworks. *Chem. Mater.* **2014**, 26 (1), 323–338.
- (69) Bao, Z.; Chang, G.; Xing, H.; Krishna, R.; Ren, Q.; Chen, B. Potential of Microporous Metal-Organic Frameworks for Separation of Hydrocarbon Mixtures. *Energy Environ. Sci.* **2016**, 9 (12), 3612–3641.
- (70) Schenk, M.; Vidal, S. L.; Vlugt, T. J. H.; Smit, B.; Krishna, R. Separation of Alkane Isomers by Exploiting Entropy Effects during Adsorption on Silicalite-1: A Configurational-Bias Monte Carlo Simulation Study. *Langmuir* **2001**, 17 (5), 1558–1570.
- (71) Bárcia, P. S.; Silva, J. A. C.; Rodrigues, A. E. Separation by Fixed-Bed Adsorption of

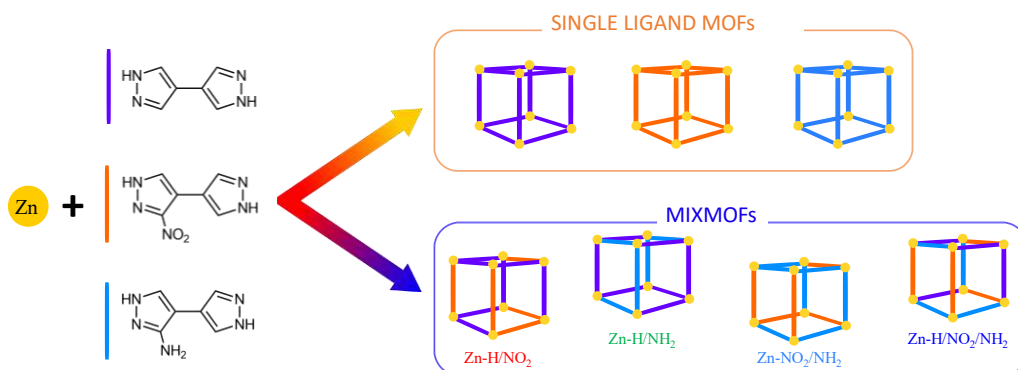
- Hexane Isomers in Zeolite BETA Pellets. *Ind. Eng. Chem. Res.* **2006**, 45 (12), 4316–4328.
- (72) Bárcia, P. S.; Silva, J. A. C.; Rodrigues, A. E. Adsorption Equilibrium and Kinetics of Branched Hexane Isomers in Pellets of BETA Zeolite. *Microporous Mesoporous Mater.* **2005**, 79 (1–3), 145–163.
- (73) Barcia, P. S.; Silva, J. A. C. Multicomponent Sorption of Hexane Isomers in Zeolite BETA. *American Institute of Chemical Engineers.* **2007**, pp 1970–1981.
- (74) Wee, L. H.; Meledina, M.; Turner, S.; Van Tendeloo, G.; Zhang, K.; Rodriguez-Abelo, L. M.; Masala, A.; Bordiga, S.; Jiang, J.; Navarro, J. A. R.; et al. 1D-2D-3D Transformation Synthesis of Hierarchical Metal-Organic Framework Adsorbent for Multicomponent Alkane Separation. *J. Am. Chem. Soc.* **2017**, 139 (2), 819–828.
- (75) Herm, Z. R.; Wiers, B. M.; Mason, J. A.; van Baten, J. M.; Hudson, M. R.; Zajdel, P.; Brown, C. M.; Masciocchi, N.; Krishna, R.; Long, J. R. Separation of Hexane Isomers in a Metal-Organic Framework with Triangular Channels. *Science* **2013**, 340, 960–964.
- (76) Chang, N.; Gu, Z. Y.; Yan, X. P. Zeolitic Imidazolate Framework-8 Nanocrystal Coated Capillary for Molecular Sieving of Branched Alkanes from Linear Alkanes along with High-Resolution Chromatographic Separation of Linear Alkanes. *J. Am. Chem. Soc.* **2010**.
- (77) Trung, T. K.; Ramsahye, N. A.; Trens, P.; Tanchoux, N.; Serre, C.; Fajula, F.; Férey, G. Adsorption of C5-C9 Hydrocarbons in Microporous MOFs MIL-100(Cr) and MIL-101(Cr): A Manometric Study. *Microporous Mesoporous Mater.* **2010**, 134 (1–3), 134–140.
- (78) Horcajada, P.; Mendes, P. A. P.; Rodrigues, A. E.; Eubank, J.; Silva, J. A. C.; Serre, C.; Devic, T. Separation of Hexane Isomers on Rigid Porous Metal Carboxylate-Based Metal–Organic Frameworks. *Adsorpt. Sci. Technol.* **2014**, 32 (6), 475–488.
- (79) Chang, N.; Yan, X. P. Exploring Reverse Shape Selectivity and Molecular Sieving Effect of Metal-Organic Framework UIO-66 Coated Capillary Column for Gas Chromatographic Separation. *J. Chromatogr. A* **2012**, 1257, 116–124.
- (80) Wang, H.; Dong, X.; Lin, J.; Teat, S. J.; Jensen, S.; Cure, J.; Alexandrov, E. V.; Xia, Q.; Tan, K.; Wang, Q.; et al. Topologically Guided Tuning of Zr-MOF Pore Structures for Highly Selective Separation of C6 Alkane Isomers. *Nat. Commun.* **2018**, 9 (1), 1–11.
- (81) Eddaoudi, M.; Kim, J.; Rosi, N.; Vodak, D.; Wachter, J.; Keeffe, M. O.; Yaghi, O. M.; Eddaoudi, M.; Kimrn, J.; Rosi, N.; et al. Systematic Design of Pore Size and Functionality in Isoreticular MOFs and Their Application in Methane Storage. *American Association for the Advancement of Science.* **2002**, 295 (5554), 469–472.
- (82) Spek, A. L. Structure Validation in Chemical Crystallography. *Acta Crystallogr. Sect. D* **2009**, 65 (2), 148–155.
- (83) Luebke, R.; Eubank, J. F.; Cairns, A. J.; Belmabkhout, Y.; Wojtas, L.; Eddaoudi, M. The Unique Rht-MOF Platform, Ideal for Pinpointing the Functionalization and CO₂ adsorption Relationship. *Chem. Commun.* **2012**, 48 (10), 1455–1457.
- (84) Finsy, V.; Calero, S.; García-Pérez, E.; Merklung, P. J.; Vedts, G.; De Vos, D. E.; Baron, G. V.; Denayer, J. F. M. Low-Coverage Adsorption Properties of the Metal-Organic Framework MIL-47 Studied by Pulse Chromatography and Monte Carlo Simulations. *Phys. Chem. Chem. Phys.* **2009**.
- (85) Peralta, D.; Chaplais, G.; Simon-Masseron, A.; Barthelet, K.; Pirngruber, G. D. Separation

- of C6 Paraffins Using Zeolitic Imidazolate Frameworks: Comparison with Zeolite 5A. *Ind. Eng. Chem. Res.* **2012**, *51* (12), 4692–4702
- (86) Finsy, V.; Calero, S.; García-Pérez, E.; Merklings, P. J.; Vedts, G.; De Vos, D. E.; Baron, G. V.; Denayer, J. F. Low-coverage adsorption properties of the metal–organic framework MIL-47 studied by pulse chromatography and Monte Carlo simulations. *Phys Chem Chem Phys*, **2008** *11*(18), 3515-3521.
- (87) Biovia Materials Studio 6.0. Dassault Systèmes BIOVIA, San Diego: Dassault Systèmes 2018.

CHAPTER V

5. ZN(II) MIXMOFs: SYNTHESIS, CRYSTAL STRUCTURE AND ADSORPTION PROPERTIES

This chapter collects the syntheses, solid state characterization and textural and adsorption studies carried out on the mixed-ligand MOFs (MIXMOFs). The role of the different functional groups in CO₂ adsorption in relation to their nature and stoichiometric ratio will be unveiled. Then, the adsorption performances of the studied MIXMOFs will be compared to those of their end-member parents Zn-BPZX (X = H, NO₂, NH₂). In the last part of the discussion, a comparison with literature results is reported as well. A more detailed description of the experimental methods used can be found in Annex I.



5.1. Zn(II) Mixed-ligand Bis(pyrazolate) MOFs

Multivariate MOFs¹⁻⁶ are an interesting sub-class of MOFs. Mixed-ligand MOFs (MIXMOFs) are solid solutions in which the metal ion/SBU coexists with two or more linkers. Generally speaking, the ligands are characterized by a common skeleton and different functional groups. Hence, the resulting MOF shows the same topology of the single-ligand parent together with pore heterogeneity.⁷⁻¹⁰ The possibility of inserting different ligands, in terms of both number and type of functional groups, in the same crystal structure has greatly increased the complexity and properties of MOFs, since the properties cannot be predicted by the simple combination of those belonging to the single-ligand analogues.

Concerning CO₂ capture and sequestration, the use of MIXMOFs can enhance the selectivity for CO₂ in gas mixtures.^{11,12} Moreover, it can influence the affinity and BET SSA of the resulting MOF. Starting from these observations, four new MIXMOFs were synthesized. The choice of the metal ion and the ligands was based on the performances of the MOFs presented in chapters II-IV, namely:

- Zn(II) based MOFs showed the highest chemical and physical stability;
- BPZNO₂²⁻ based MOFs showed the highest CO₂ adsorption capacity;
- BPZNH₂²⁻ based MOFs showed the best CO₂ affinity.

Together with BPZNO₂²⁻ and BPZNH₂²⁻, the untagged BPZ²⁻ ligand was used with the aim of tuning the selectivity and CO₂ capacity of the MIXMOFs in relation to the amount and type of functional groups.

The different sections of the current chapter aim at introducing the readers into the complete solid-state characterization and textural study of the MIXMOFs. In accordance to the scheme followed in chapters II-IV, first the syntheses methodology and preliminary characterization will be presented. Then, the structural and thermal properties will be analysed. Solid-state ¹³C CPMAS NMR spectroscopic studies follow this first part to allow the accurate quantification of the ligand stoichiometric ratio in the as-synthesized samples. Finally, the textural properties and capacities of the MIXMOFs will be

elucidated and compared with those of their single-ligand parents, *i.e.* Zn-BPZX (X = H, NO₂, NH₂),¹³⁻¹⁵ and of other zinc(II) poly(azolate) MOFs.

5.2. Synthesis and Preliminary Characterization of the MIXMOFs

Zn-(BPZ)_x(BPZNO₂)_{1-x}·S (**Zn-H/NO₂·S**), Zn-(BPZ)_x(BPZNH₂)_{1-x}·S (**Zn-H/NH₂·S**), Zn-(BPZNO₂)_x(BPZNH₂)_{1-x}·S (**Zn-NO₂/NH₂·S**) and Zn-(BPZ)_x(BPZNO₂)_y(BPZNH₂)_{1-x-y}·S (**Zn-H/NO₂/NH₂·S**) were obtained as microcrystalline samples in good yields (74-81%) following the same procedure reported for **Zn-BPZNO₂·S**¹⁴ and **Zn-BPZNH₂·S**,¹⁵ *i.e.* by reacting the proper ligands in equal proportion (50:50 or 33:33:33, depending on the number of the different linkers in the final MOF), and Zn(OAc)₂·2H₂O (OAc = acetate) in DMF under solvothermal conditions.^{xxii} The colour of the obtained MOFs is symptomatic of the used ligands, passing from the white of **Zn-H/NH₂·S** to a progressively brighter yellow in accordance with the increasing ratio of the BPZNO₂²⁻ ligand. IR spectroscopy,¹⁶ as reported in Figure 5.1, confirms:

i) the presence of the functionalized ligand(s): **Zn-H/NO₂·S**, **Zn-NO₂/NH₂·S** and **Zn-H/NO₂/NH₂·S** show the NO₂ symmetric stretching band centred at 1346, 1345 and 1347 cm⁻¹, respectively; **Zn-H/NH₂·S**, **Zn-NO₂/NH₂·S** and **Zn-H/NO₂/NH₂·S** show the NH₂ stretching bands in the range 3317-3390, 3314-3390 and 3316-3394 cm⁻¹, respectively;

ii) the absence of the N-H stretching band of the pyrazole ring ($\nu = 3175$ cm⁻¹),¹⁷ hence the complete ligand deprotonation;

iii) the presence of clathrated DMF molecules (C=O stretching band in the range 1656-1667 cm⁻¹).

Moreover, a trend in the intensity of the bands in the range ~3315-3390 cm⁻¹ passing from **Zn-H/NH₂·S** to **Zn-BPZNH₂·S** (Figure 5.1 b) and the bands at ~1345 cm⁻¹ passing from **Zn-H/NO₂·S** to **Zn-BPZNO₂·S** (Figure 5.1 a) can be ascribed to the increasing amount of the amino and nitro-functionalized ligands, respectively. However, this

^{xxii} The syntheses and preliminary analytical characterization of the MIXMOFs were performed by Prof. C. Pettinari's group, University of Camerino, Italy.

evidence cannot be extended to **Zn-NO₂/NH₂·S**, for which the N-H stretching bands are very weak and broad with respect to those of the other compounds. A first hypothesis on internal NO₂...H₂N hydrogen bond interactions was denied by ¹H CPMAS NMR. Indeed, all the MOFs containing the BPZNH₂²⁻ ligand show hydrogen bonds (see below). The confidence in having synthesised four different solid solutions instead of physic mixtures of the Zn-BPZX (X = H, NO₂, NH₂) parents is confirmed by multiple experimental evidences (PXRD, simultaneous thermal analysis) as described in the following sections.

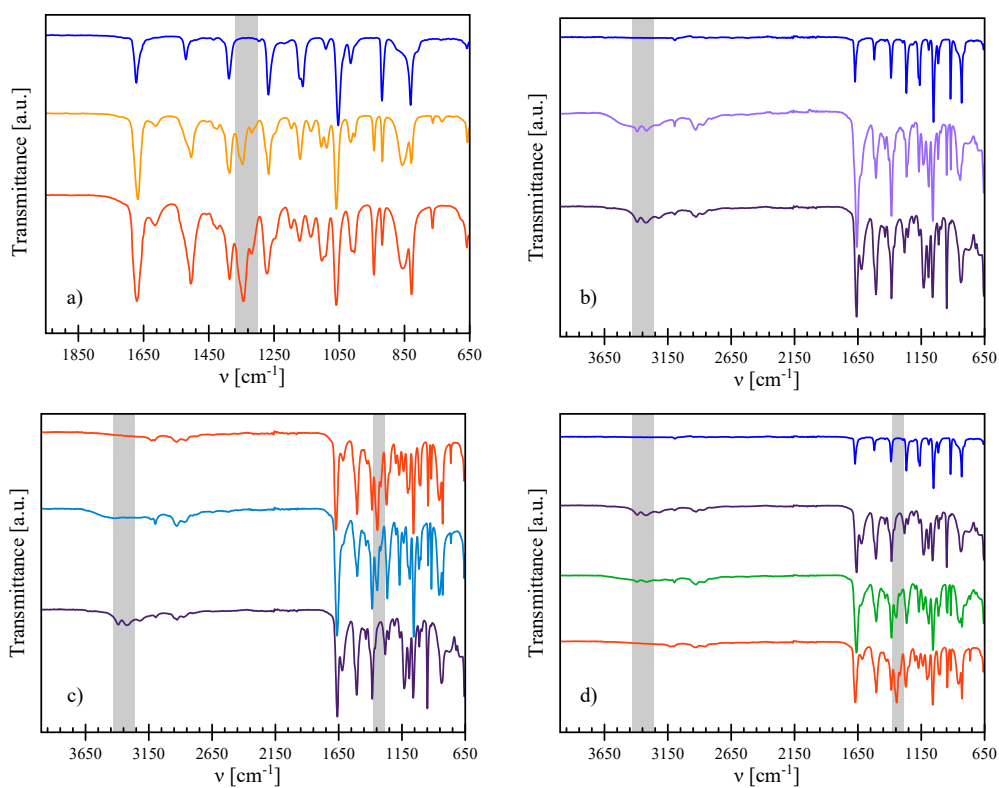


Figure 5.1 Comparison of the infrared spectra of: a) Zn-BPZ·S (blue trace), Zn-H/NO₂·S (orange trace) and Zn-BPZNO₂·S (red trace); b) Zn-BPZ·S (blue trace), Zn-H/NH₂·S (violet trace) and Zn-BPZNH₂·S (dark violet); c) Zn-BPZ·S (blue trace), Zn-BPZNH₂·S (dark violet), Zn-H/NO₂/NH₂·S (orange trace) and Zn-BPZNO₂·S (red trace). The regions of the symmetric NO₂ and NH₂ stretching bands are highlighted in grey.

5.3. Structural and Thermal Characterization of the MIXMOFs

As anticipated, PXRD was used to confirm the synthesis of single phases. Indeed, comparing the calculated PXRD patterns of the MIXMOFs to those of their end-members, the Bragg reflections are different in terms of position and/or number (Figure 5.2).

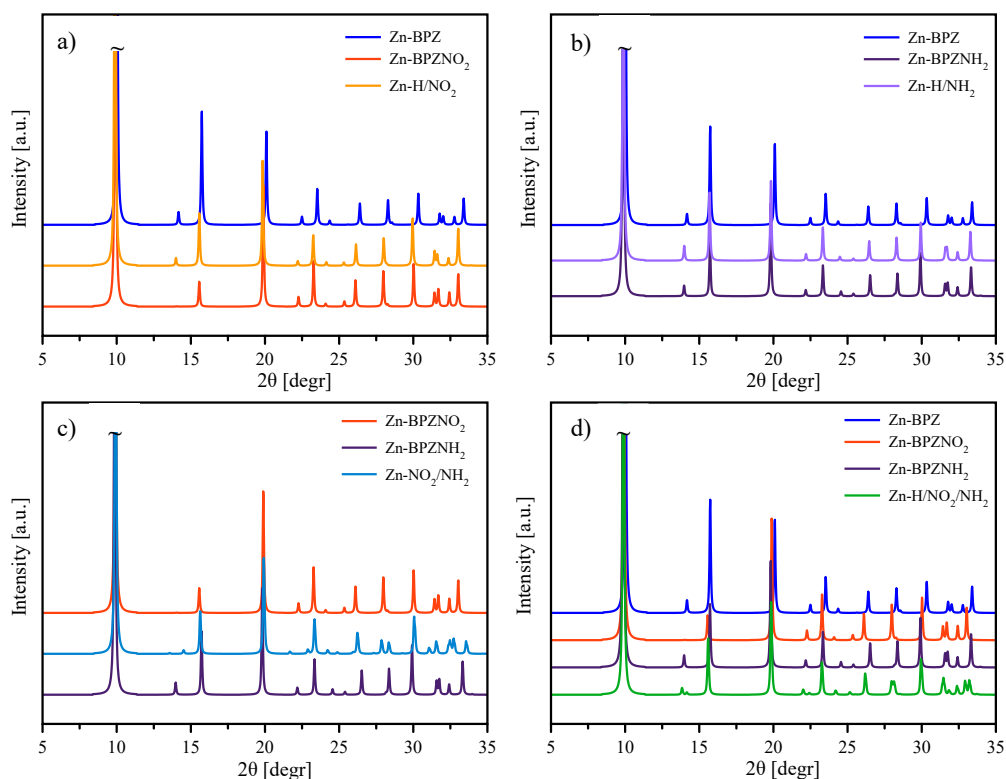


Figure 5.2 Low-angle region of the calculated PXRD patterns of a) Zn-BPZ, Zn-H/NO₂ and Zn-BPZNO₂; b) Zn-BPZ, Zn-H/NH₂ and Zn-BPZNH₂; c) Zn-BPZNO₂, Zn-NO₂/NH₂ and Zn-BPZNH₂; d) Zn-BPZ, Zn-BPZNO₂, Zn-BPZNH₂ and Zn-H/NO₂/NH₂.

A procedure analogous to that explained in chapter III was followed to structurally characterize the four MIXMOFs. The comparison of the PXRD patterns of the end members¹³⁻¹⁵ to those of the MIXMOFs suggested that the same structural motif, in either the orthorhombic or the tetragonal symmetry, was shared by all the compounds. Nonetheless, the correct space groups were assigned by the observation of the systematic extinctions after the approximate unit cell parameters were obtained through the Singular

Value Decomposition algorithm,¹⁸ as implemented in TOPAS-Academic V6.¹⁹ The crystal structure of the isostructural parents Zn-BPZX MOFs were used as starting point for the Rietveld refinements. As a preliminary approximation of the ligand stoichiometry, the ideal values derived from the reaction molar ratios were used and fixed. The crystallographically independent portion of the ligand was built as a rigid body with the z-matrix formalism, giving average values to bond distances and angles.^{xxiii} The position of the ligand and its orientation were refined when allowed by symmetry. Concerning the functional groups, the orientation of -NO₂ with respect to the skeleton of the ligand was let free to vary, whereas the amino-group was maintained co-planar to the ligand. As already noticed in **Zn-BPZNO₂** and **Zn-BPZNH₂**, the independent portion of the linker in tetragonal and orthorhombic symmetry is composed by a quarter of ligand, since its centre of mass lays on a *2/m* symmetry element. As a consequence, not only it is not possible to distinguish the different ligands in the unit cell (both are described by the same independent $\frac{1}{4}$ BPZX²⁻ portion), but also the same position can be occupied by the -NO₂, -NH₂ groups or H atom with proper probability of occupancy. As an example, in ideal **Zn(BPZ)_{0.5}(BPZNO₂)_{0.5}·S** the atom bonded to C3 (see Figure 5.3 for the labelling scheme) can be both the -NO₂ group with a 12.5% occupancy probability (0.5 out of 4 crystallographically equivalent positions) or a hydrogen atom with 87.5% occupancy probability (3.5 out of 4 crystallographically equivalent positions).

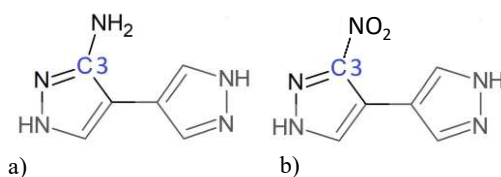


Figure 5.3 Scheme of the H₂BPZX (X = NO₂, NH₂) ligands, in black the portion of the ligand described in the asymmetric unit.

^{xxiii} Bond distances and angles for the rigid body describing the ligand: C-C and C-N of the pyrazole ring 1.36 Å; exocyclic C-C 1.40 Å; C-H 0.95 Å; C-N_{NO₂} 1.40 Å; N-O 1.23 Å; pyrazolate ring internal and external bond angles 108° and 126°, respectively; angles at the nitrogen atom of the nitro group 120°.

DMF, modelled as a rigid body,^{xxiv} was located by a combined Monte Carlo/Simulated Annealing approach²⁰ letting its position, orientation and site occupation factor free to vary. Finally, the site occupation factor of the ligands was refined. The obtained values were found in agreement with those assessed by ¹³C CPMAS NMR. Ligand bond distances (except the C/N-H distances) were refined as well in a restrained range of values during the last stages of Rietveld refinement.^{xxv} The background was described by a polynomial function of the Chebyshev type. A refined isotropic thermal factor was assigned to the metal centres, while a common 2 Å higher thermal factor was attributed to the other atoms. The Fundamental Parameters Approach²¹ was used to describe the peak profile. The anisotropic peak broadening of **Zn-H/NO₂·S**, **Zn-NO₂/NH₂·S** and **Zn-H/NO₂/NH₂·S** was successfully modelled using the Stephens approach.²² In **Zn-H/NH₂·S**, the convolution of two different tan(θ)-dependent spherical harmonics described the sharper $[h0l]$ and broader $[hkl]$ Bragg reflections. A Gaussian contribution further lowered the R_{wp} figure of merit of all the MIXMOFs. The final Rietveld refinement plots are shown in Figure 5.4.

As anticipated, the four MIXMOFs are isorecticular to their end-members. The dilution of the functionalization, respectively in **Zn-H/NO₂·S** and **Zn-H/NH₂·S**, lead to the preservation of the tetragonal $P4_2/mmc$ symmetry of their single-ligand parents. The 3-D (4,4)-connected porous network (Figure 5.5) is defined by the tetrahedral MN₄ nodes and the *exo*-tetradentate spacers; 1-D square channels run parallel to the [001] crystallographic direction. When the two different functional groups coexist in the same MOFs, *i.e.* in **Zn-NO₂/NH₂·S** and **Zn-H/NO₂/NH₂·S**, the lower orthorhombic $Cccm$ symmetry, which is a proper subgroup of $P4_2/mmc$, appears, implying rhombic 1-D channels (Figure 5.6). The topological analysis of the crystal lattice carried out on the four MIXMOFs taking both the Zn(II) ions and the ligands revealed a network topology belonging to the **sra**-type net.

^{xxiv} Bond distances and angles for the rigid body describing the solvent: C-N 1.45 Å; C-H 0.95 Å; C-O 1.25 Å; angles at the nitrogen and amidic carbon atoms 120°; angles at the carbon atoms of the methyl groups 109.5°.

^{xxv} Ranges of the refined bond distances in the Rietveld refinement: C-C 1.40-1.45 Å, C-C and C-N of the pyrazolate ring 1.32-1.38 Å. The ranges were identified after a preliminary bibliographic search in the CCDC database.

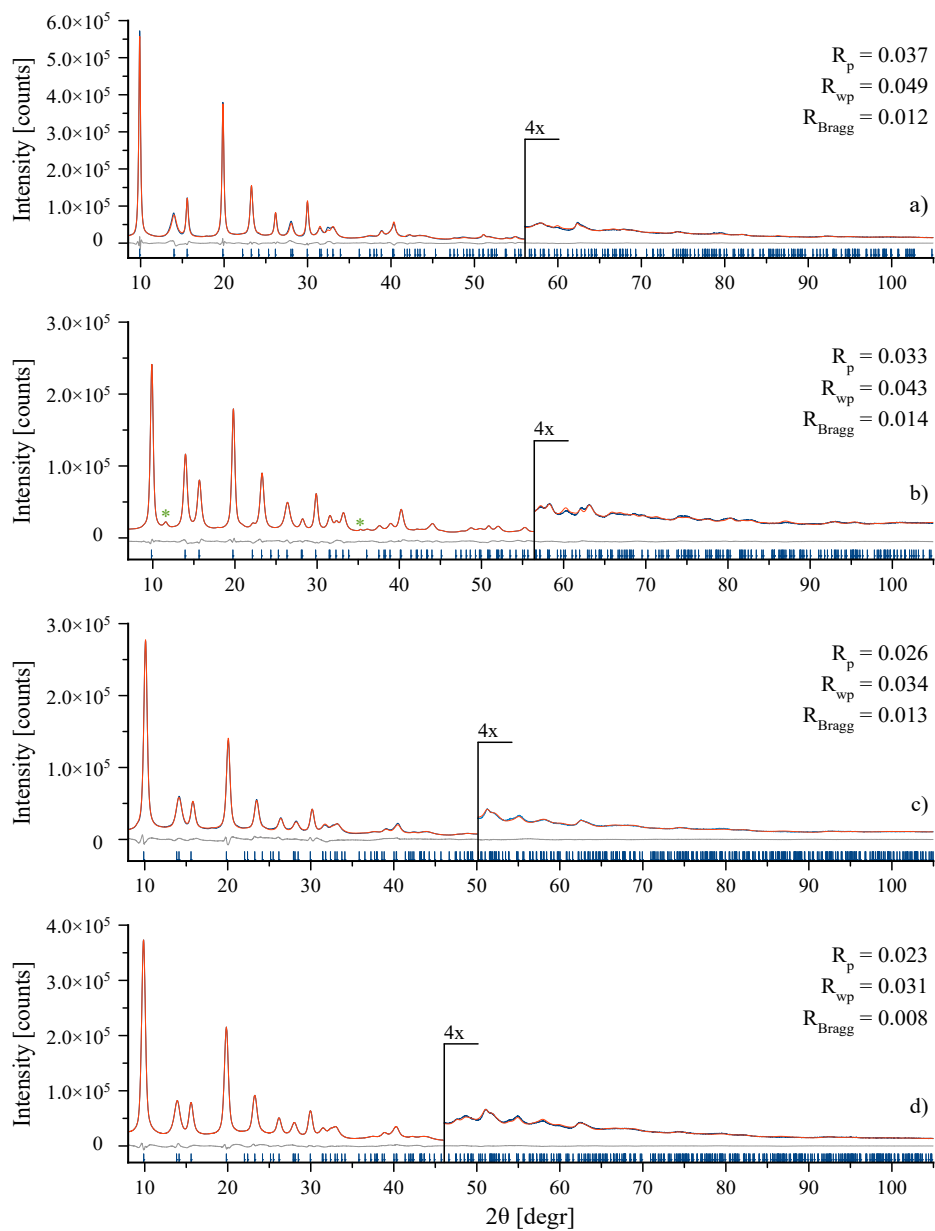


Figure 5.4 Graphical output of the final step of the Rietveld refinement on a) Zn-H/NO₂, b) Zn-H/NH₂, c) Zn-NO₂/NH₂ and d) Zn-H/NO₂/NH₂. Colour code: observed intensity, blue trace; calculated intensity, red trace; difference, grey trace; Bragg reflections, blue markers. The high-angle portion has been magnified for clarity. The green asterisks highlight an impurity.

The torsion angle of the nitro group with respect to the ligand plane, (Table 5.1), passes from nearly zero in **Zn-H/NO₂·S** to ~128° in **Zn-H/NO₂/NH₂·S** and ~81° in **Zn-NO₂/NH₂·S**. For the main distances and angles the readers are referred to the captions of Figures 5.4-5.5.

Table 5.1 Torsion angles of the nitro group with respect to the ligand plane in H₂BPZNO₂, MIXMOFs containing the -NO₂ group and **Zn-BPZNO₂**

Compound	NO ₂ Torsion [°]	Ref.
H ₂ BPZNO ₂ ,	~3°	14
Zn-NO₂/NH₂·S	~81°	24
Zn-H/NO₂/NH₂·S	~128°	24
Zn-H/NO₂·S	~0°	24
Zn-BPZNO₂	64°	14

The empty volume of the MIXMOFs ranges from ~41%^{xxvi} (~0.33 cm³ g⁻¹)^{xxvii} in **Zn-NO₂/NH₂** up to ~47% (~0.39 cm³ g⁻¹) in **Zn-H/NO₂/NH₂** at room temperature and pressure conditions, in accordance to what found for other bis(pyrazolate) MOFs.^{13,15-25} The readers are addressed to Table 5.2 for the comparison of the values of the four compounds and the end-members. The clathrated solvent, *i.e.* DMF, was found disordered within the channels in all the MIXMOFs.

^{xxvi} A The empty volume was estimated with the software PLATON³⁴ on an ordered model in *P1* for **Zn-H/NO₂**, **Zn-H/NH₂** and **Zn-NO₂/NH₂** after removal of the clathrated solvent, supposing that the nitro group protrudes into the channels. For **Zn-H/NO₂/NH₂** it was not possible to build an ordered model in *P1*, because of the discrepancy between the number of independent ligands of the asymmetric unit (four) and the number of different ligands of the formula unit (three). This is the reason why, for **Zn-H/NO₂/NH₂**, a range of porosity was estimated assigning as *minimum* the value obtained from a *P1* unit cell with one BPZ²⁻, two BPZNO₂²⁻ and one BPZNH₂²⁻ as ligands in the asymmetric unit, and as *maximum* the value obtained from a *P1* unit cell with two BPZ²⁻, one BPZNO₂²⁻ and one BPZNH₂²⁻ as ligands in the asymmetric unit.

^{xxvii} The empty volume calculated assuming that the nitro groups are coplanar to the 4,4'-bis(pyrazolate) skeleton.

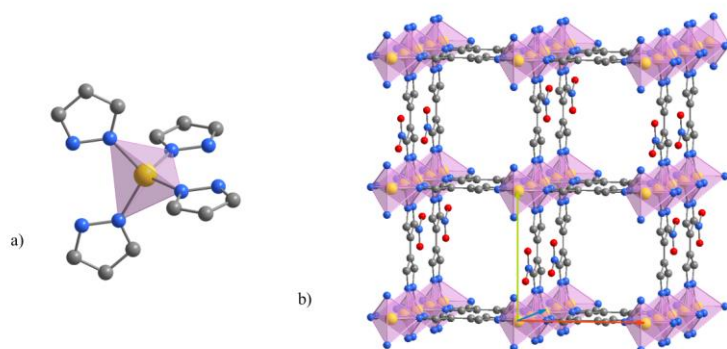


Figure 5.5 Representation of the crystal structure of **Zn-H/NO₂·S**: a) the tetrahedral node. b) Portion of the crystal packing, viewed, in perspective, along the [115] crystallographic direction. Atom colour code: carbon, grey; nitrogen, blue; oxygen, red; zinc, yellow. The DMF molecules and hydrogen atoms have been omitted for clarity. An ordered model has been adopted for the position of the NO₂ groups on the ligand skeleton for the sake of clarity, diminishing the symmetry down to *P1*. Except for the functional groups, the two images are representative also for **Zn-H/NH₂·S**. **Zn-H/NO₂·S** main bond distances and angles: Zn-N, 2.018(9) Å; Zn···Zn, 3.6833(2) and 8.9394(4) Å; N-Zn-N, 109.16(14)-110.1(3)°; **Zn-H/NH₂·S** main bond distances and angles: Zn-N, 2.062(4) Å; Zn···Zn, 3.6508(3) and 8.9808(4) Å; N-Zn-N, 108.23(6)-111.99(12)°.

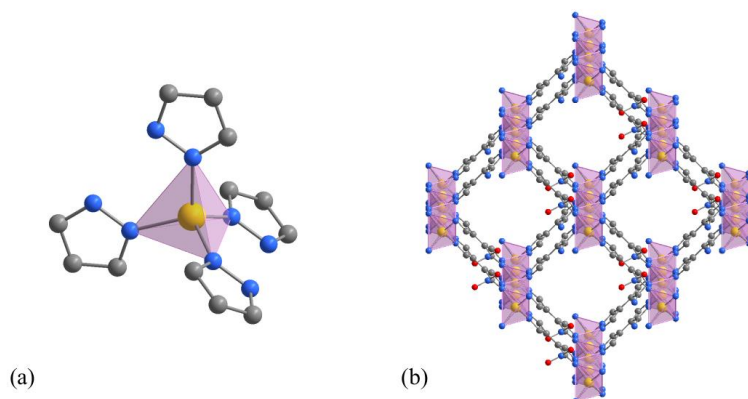


Figure 5.6 Representation of the crystal structure of **Zn-NO₂/NH₂·S**: a) the tetrahedral node. b) Portion of the crystal packing viewed, in perspective, along the [012] direction. The DMF molecules and hydrogen atoms have been omitted for clarity. An ordered model has been adopted for the position of the NO₂ groups on the ligand skeleton for the sake of clarity by diminishing the symmetry down to *P1*. Except for the orientation of the NO₂ groups with respect to the ligand plane and the ratio of the ligands, the crystal structure of **Zn-H/NO₂/NH₂·S** is similar at the drawing level. Atom colour code: carbon, grey; nitrogen, blue; oxygen, red; zinc, yellow. Main bond distances and angles at the Zn(II) ion: **Zn-NO₂/NH₂·S**: Zn-N, 2.031(6) Å; Zn···Zn, 3.6801(12) and 8.947(3) Å; N-Zn-N, 102.4(3)-113.17(17)°; **Zn-H/NO₂/NH₂·S**: Zn-N, 2.040(5) Å; Zn···Zn, 3.6767(9) and 8.947(3) Å; N-Zn-N, 106.4(2)-113.1(2)°.

Table 5.2 Comparison of the empty volume of **Zn-H/NO₂**, **Zn-H/NH₂**, **Zn-NO₂/NH₂** and **Zn-H/NO₂/NH₂** with respect to the end-members Zn-BPZ, Zn-BPZNO₂ and Zn-BPZNH₂.

Compound	Empty volume [%]	Empty volume [cm³/g]	Ref.
Zn-H/NO₂	46(46)	0.37(0.37)	24
Zn-H/NH₂	42	0.36	24
Zn-NO₂/NH₂	42(45)	0.33(0.35)	24
Zn-H/NO₂/NH₂	44(46)-46(47)	0.36(0.37)-0.38(0.39)	24
Zn-BPZ	42	0.37	13
Zn-BPZNO ₂	39(40)	0.29(0.29)	14
Zn-BPZNH ₂	46	0.38	15

The distribution of the ligands inside the MIXMOFs, *i.e.* random, clustered or ordered, cannot be obtained through PXRD alone.^{12,26} However the unit cell parameters^{xxviii} of the Zn-BPZ, **Zn-H/NO₂**, **Zn-BPZNO₂** and Zn-BPZ, **Zn-H/NH₂**, **Zn-BPZNH₂** series approximately follow the Vegard Law,²⁷ Figure 5.7 a-b. In the nitro-tagged series, the *c*-axis increases while the *a*- and *b*-axes shrink passing from Zn-BPZ to **Zn-BPZNO₂**, with an overall volume contraction of ~2.5% (Figures 5.7 a). Analogously, passing from Zn-BPZ to **Zn-BPZNH₂** the volume decreases by ~0.4%, thanks to the decrease of the *c*-axis and the increase of *a*- and *b*-axes (Figures 5.7 a). The apparently unexpected reduction of the unit cell volume with the increase of the tagged ligand inside a MIXMOFs was already reported in the literature, for example in the (MIX)MOF-535 and (MIX)UiO-66 couples.²⁸ The increase of the *c*-axis can be related to the higher steric hindrance of the functionalized ligand along the [001] crystallographic direction. As a consequence, to maintain the Zn-N bonds, the *a*- and *b*-axes shrink. The correlation between the *a*- and *c*-axis (*a/c*) and the ligand stoichiometric ratio confirms this relation (Figures 5.7).

^{xxviii} All the MOFs were activated before considering if their unit cell parameters satisfy the Vegard Law, since the different distribution of the solvent modifies their metrics.

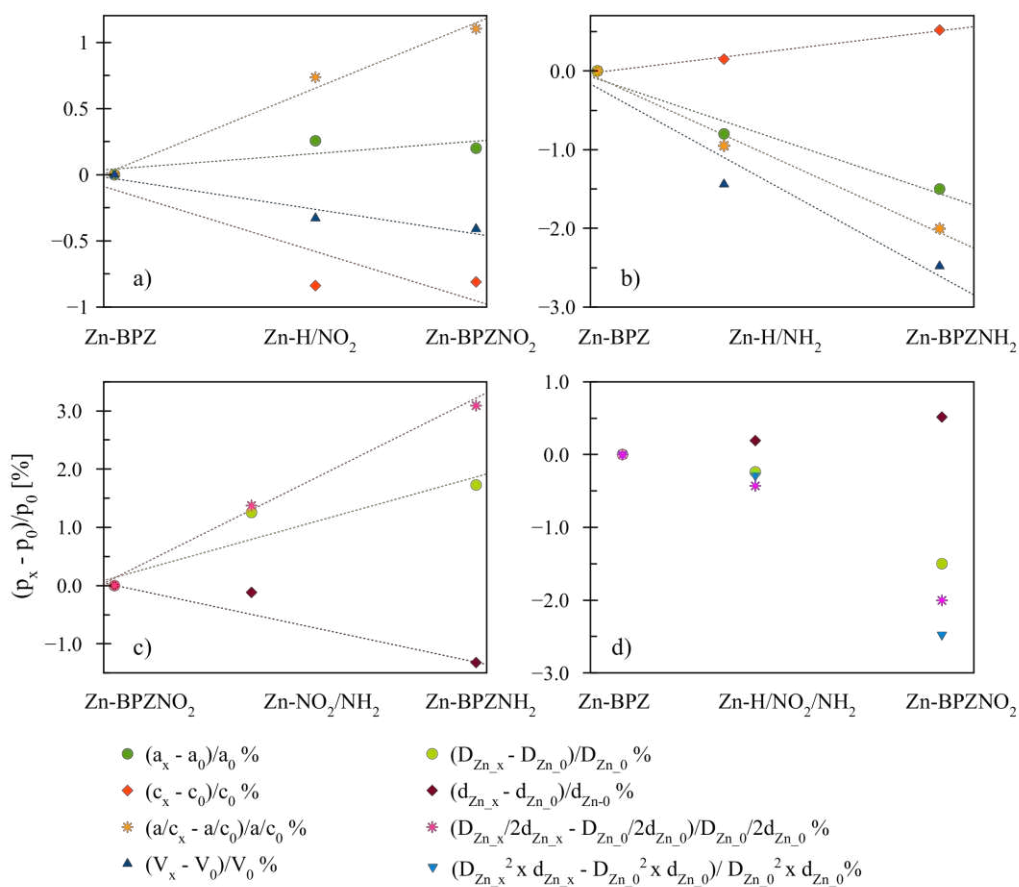


Figure 5.7 Percentage variation of the unit cell parameters (p_x) of a) Zn-BPZ, Zn-H/NO₂, and Zn-BPZNO₂, b) Zn-BPZ, Zn-H/NH₂, and Zn-BPZNH₂, c) Zn-BPZNO₂, Zn-NO₂/NH₂, and Zn-BPZNH₂ and d) Zn-BPZ, Zn-H/NO₂/NH₂, and Zn-BPZNO₂ as a function of the ligand stoichiometric ratio. The values reported for each compound have been normalized with respect to those of Zn-BPZ in a), b) and d) or to those of Zn-BPZNO₂ in c).

Zn-NO₂/NH₂ and Zn-H/NO₂/NH₂ show a different crystallographic symmetry with respect to their end-members. Hence, the correlation of the unit cell parameters, except for the c -axis, which runs parallel to the Zn(II) ion chains, cannot be directly made. Two different, but correlated, distances, namely the distance between consecutive Zn(II) ions of the same 1-D chain (d_{Zn} in Figure 5.8) and between two Zn(II) ions connected by a BPZX²⁻ ligand (D_{Zn} in Figure 5.8), were considered to overcome this symmetry-related obstacle. The obtained correlations are reported in Figure 5.7 c-d. Zn-H/NO₂/NH₂ has a

trend similar to that of **Zn-H/NO₂** and **Zn-H/NH₂** with an overall contraction of the unit cell volume and the growth of the d_{Zn} distance (corresponding to the c -axis) from Zn-BPZ to the functionalized compounds, Figure 5.7 d. **Zn-NO₂/NH₂** as well follows the empiric Vegard rule, Figure 5.7 c.

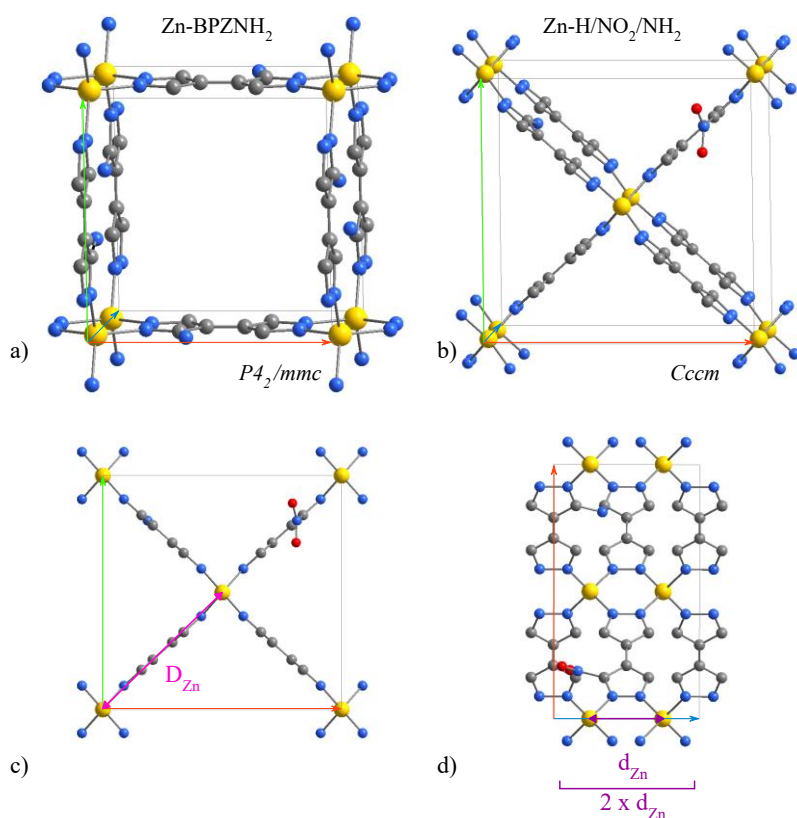


Figure 5.8 Comparison of the crystal structures of a) the tetragonal **Zn-BPZNH₂** and b) the orthorhombic **Zn-H/NO₂/NH₂**, along the [115] crystallographic direction. Unit cell axes: a (red), b (green), c (blue). c) and d), representation of the distances labelled D_{Zn} and d_{Zn} , respectively, used to compare the unit cell parameters of phases with different symmetry. The clathrated solvent and the hydrogen atoms have been omitted and an ordered model have been used for clarity. Atom colour code: carbon, grey; nitrogen, blue; oxygen, red; zinc, yellow.

The structural parameters are reproduced with permission from: “Vismara, R.; Tuci, G.; Tombesi, A.; Domasevitch, K.; Di Nicola, C.; Giambastiani, G.; Chierotti, M.; Bordignon, S.; Gobetto, R.; Pettinari, C.; Rossin, A. and Galli, S. Tuning carbon dioxide adsorption affinity of

zinc(II) MOFs by mixing bis(pyrazolate) ligands with N-containing tags. ACS Applied Materials & Interfaces, 2019, 11, 26956–26969.”

Crystal data for **Zn-H/NO₂·S**: Zn(BPZ)_{0.62}(BPZNO₂)_{0.38}·1.7(DMF), C_{11.1}H_{15.5}N_{6.1}O_{2.5}Zn, fw = 338.90 g mol⁻¹, *tetragonal*, *P4₂/mmc*, *a* = 8.9385(6) Å, *c* = 7.3662(6) Å, *V* = 588.53(9) Å³, *Z* = 16, *Z'* = 2, *F*(000) = 348.7, ρ = 1.854 g cm⁻³, *R*_{wp} = 0.049, *R*_p = 0.037 and *R*_{Bragg} = 0.012, 2 θ range = 8.0-105.0° for 4851 data and 34 parameters. CCDC No. 1912137.

Crystal data for **Zn-H/NH₂·S**: Zn(BPZ)_{0.56}(BPZNH₂)_{0.44}·1.2(DMF), C_{9.6}H_{12.8}N_{5.6}O_{1.2}Zn, fw = 291.85 g mol⁻¹, *tetragonal*, *P4₂/mmc*, *a* = 8.9805(4) Å, *c* = 7.3015(5) Å, *V* = 588.87(5) Å³, *Z* = 16, *Z'* = 2, *F*(000) = 299.0, ρ = 1.687 g cm⁻³, *R*_{wp} = 0.043, *R*_p = 0.033 and *R*_{Bragg} = 0.014, 2 θ range = 7.0-105.0° for 4901 data and 35 parameters. CCDC No. 1912135.

Crystal data for **Zn-NO₂/NH₂·S**: Zn(BPZNO₂)_{0.38}(BPZNH₂)_{0.62}·0.8(DMF), C_{8.4}H_{9.8}N_{5.8}O_{1.6}Zn, fw = 282.41 g mol⁻¹, *orthorhombic*, *Cccm*, *a* = 12.528(4) Å, *b* = 12.776(4) Å, *c* = 7.360(6) Å, *V* = 1178(5) Å³, *Z* = 16, *Z'* = 4, *F*(000) = 573.3, ρ = 1.597 g cm⁻³, *R*_{wp} = 0.034, *R*_p = 0.026 and *R*_{Bragg} = 0.013, 2 θ range = 8.0-105.0° for 4851 data and 37 parameters. CCDC No. 1912138.

Crystal data for **Zn-H/NO₂/NH₂·S**: Zn(BPZ)_{0.46}(BPZNO₂)_{0.33}(BPZNH₂)_{0.21}·1.2(DMF), C_{9.6}H_{12.3}N_{5.7}O_{1.9}Zn, fw = 303.25 g mol⁻¹, *orthorhombic*, *Cccm*, *a* = 12.791(3) Å, *b* = 12.516(3) Å, *c* = 7.3533(7) Å, *V* = 1177.2(4) Å³, *Z* = 16, *Z'* = 4, *F*(000) = 619.8, ρ = 1.710 g cm⁻³, *R*_{wp} = 0.031, *R*_p = 0.023 and *R*_{Bragg} = 0.008, 2 θ range = 8.0-105.0° for 4851 data and 37 parameters. CCDC No. 1912136.

5.4. Thermal Behaviour of the MIXMOFs

Simultaneous thermal analysis (STA, simultaneous thermogravimetric analysis and differential scanning calorimetry) was performed on the four MIXMOFs under a N₂ flow in the range 303-1173 K. In Figure 5.9, the differential scanning calorimetry (DSC) traces reveal that the decomposition processes are characterized by a single peak, confirming that the studied materials are a single phase.

Under N_2 , **Zn-H/NO₂**, **Zn-H/NH₂**, **Zn-NO₂/NH₂**, and **Zn-H/NO₂/NO₂** are highly stable with decomposition temperatures in the range of 708-726 K, as revealed by TGA (Figure 5.9). Table 5.3 collects the decomposition temperatures of the MIXMOFs and Zn-BPZX MOFs. As expected and already noticed for the M-BPZNO₂ MOFs,¹⁴ the presence of the nitro group affects the resulting thermal stability of the porous coordination polymers.²⁹ Hence, the decomposition temperatures of the MIXMOFs follow the trend: **Zn-H/NH₂** > **Zn-H/NO₂/NH₂** > **Zn-NO₂/NH₂** > **Zn-H/NO₂**. For all the compounds, dilution or mixing of the functional groups lead to a higher thermal stability with respect to the tagged end-members, *i.e.* **Zn-BPZNO₂** and **Zn-BPZNH₂**. After solvent loss, for temperatures above ~550 K, all the compounds are stable up to decomposition.

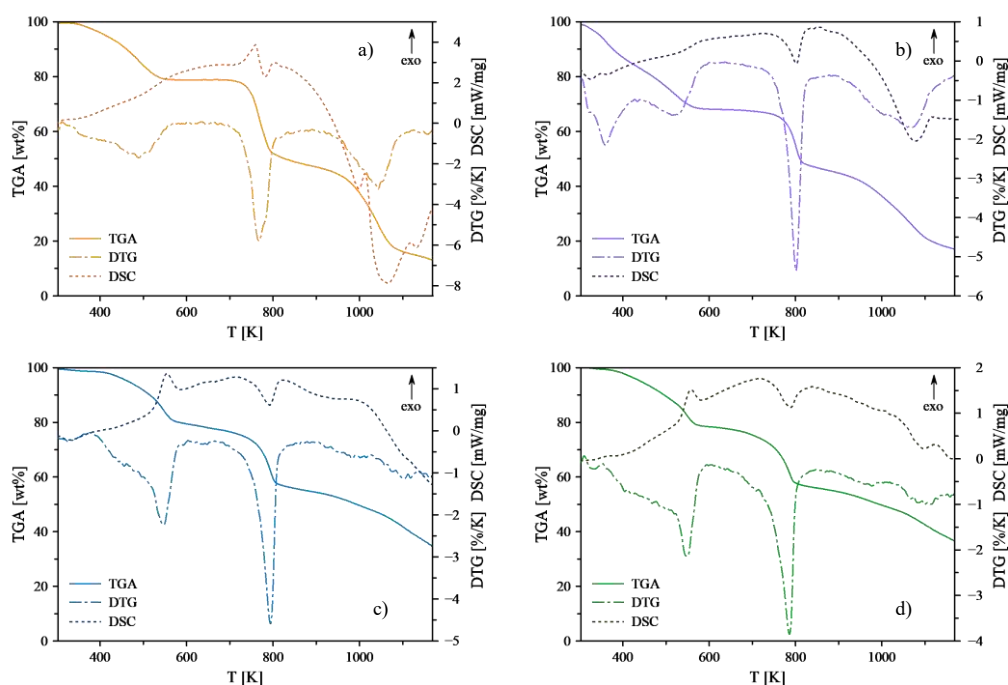


Figure 5.9 Simultaneous thermal analysis on: a) **Zn-H/NO₂**, TGA (orange trace), DTG (dash-dotted orange trace) and DSC (dotted dark orange trace); b) **Zn-H/NH₂**, TGA (violet trace), DTG (dash-dotted violet trace) and DSC (dotted dark violet trace); c) **Zn-NO₂/NH₂**, TGA (cyan trace), DTG (dash-dotted cyan trace) and DSC (dotted blue trace); d) **Zn-H/NO₂/NO₂**, TGA (green trace), DTG (dash-dotted green trace) and DSC (dotted dark green trace).

Table 5.3 Collection of the decomposition temperatures retrieved through TGA and DSC analyses of MIXMOFs and Zn-BPZX MOFs.

Compound	TGA Onset T_{dec} [K]	DSC Peak T_{dec} [K]	Ref.
Zn-H/NO₂	708	781	24
Zn-H/NH₂	726	801	24
Zn-NO₂/NH₂	718	792	24
Zn-H/NO₂/NH₂	721	789	24
Zn-BPZ	723	-	13
Zn-BPZNO₂	663	-	14
Zn-BPZNH₂	703	-	15

In situ VT-PXRD experiments were performed on all the compounds. Then, the collected data were refined through a parametric whole powder pattern refinement by the Le Bail method (Figures 5.10 a-f, Table 5.4). **Zn-H/NH₂·S**, **Zn-NO₂/NH₂·S** and **Zn-H/NO₂/NH₂·S** are stable upon heating and do not show any phase transition or loss of crystallinity before decomposition. The desolvation process is accompanied by a volume shrinkage in the range ~0.6-1.4%, due to the progressive shortening of the unit cell axes (*a*- and *c*-axes in **Zn-H/NH₂·S** and **Zn-NO₂/NH₂·S**, *b*- and *c*-axes in **Zn-H/NO₂/NH₂·S**). On the other hand, **Zn-H/NO₂·S** undergoes several phase transitions during the desolvation process (Figure 5.11). The pristine tetragonal $P4_2/mmc$ solvated form becomes first orthorhombic ($Cccm$, proper subgroup of $P4_2/mmc$, $T_0 = 363$ K), then monoclinic ($C2/c$, proper subgroup of $Cccm$, $T_0 = 403$ K) and orthorhombic again ($Cccm$, $T_0 = 483$ K), before turning into a tetragonal desolvated form ($P4_2/mmc$, $T_0 = 503$ K). Since the structural motif of the four phases is the same, **Zn-H/NO₂** retains its pristine porosity. The activated **Zn-H/NO₂** form shows a volume contraction of ~1% due to the decrease of the *a*- and *c*-axes by ~-0.3% and ~-0.5%, respectively (Figure 5.11).

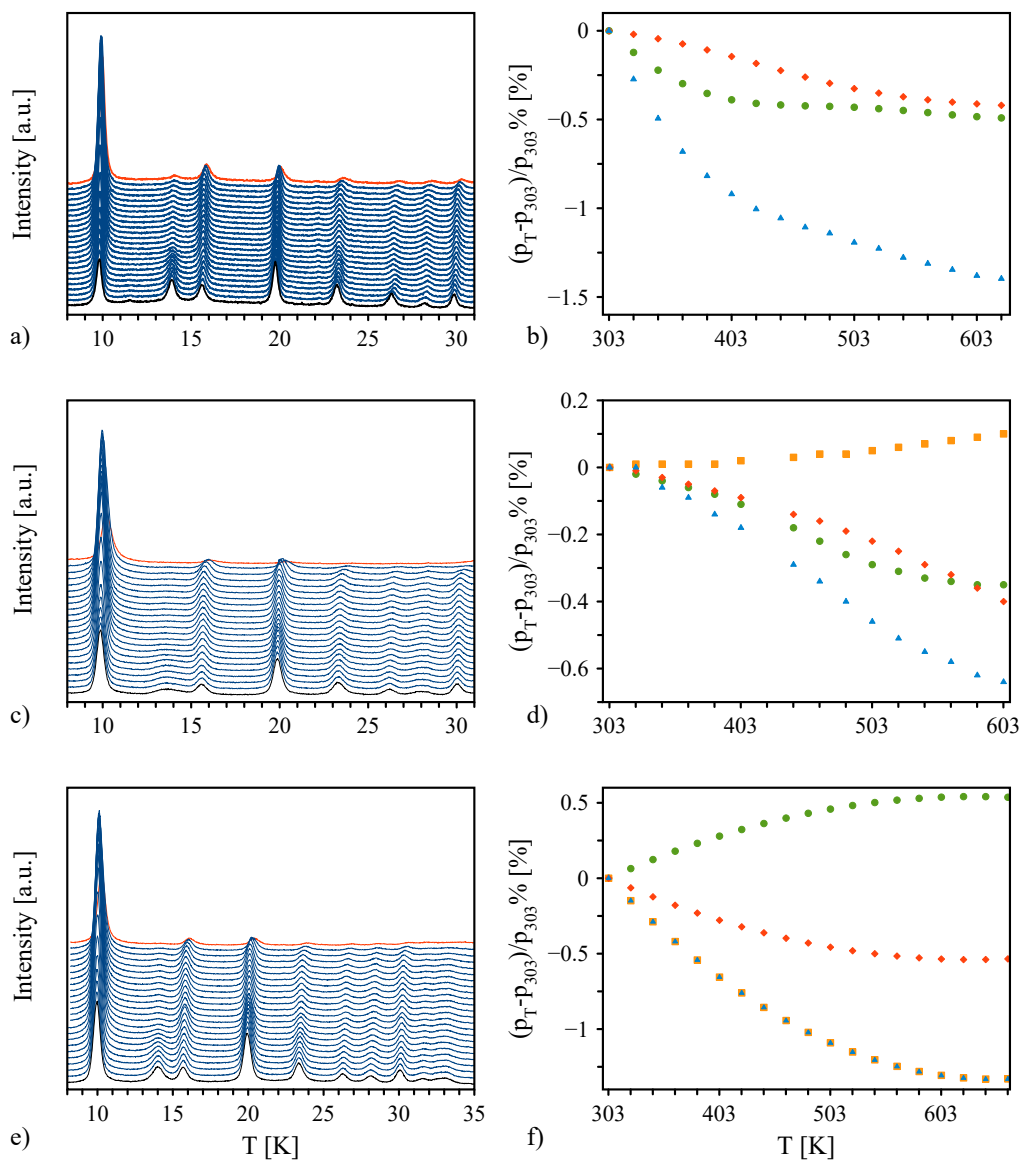


Figure 5.10 a) VT-PXRD patterns of **Zn-H/NH₂S**; b) result of the parametric whole powder pattern refinement on **Zn-H/NH₂S**; c) VT-PXRD patterns of **Zn-NO₂/NH₂S**; d) result of the parametric whole powder pattern refinement on **Zn-NO₂/NH₂S**; e) VT-PXRD patterns of **Zn-H/NO₂/NH₂S**; f) result of the parametric whole powder pattern refinement on **Zn-H/NO₂/NH₂S**.

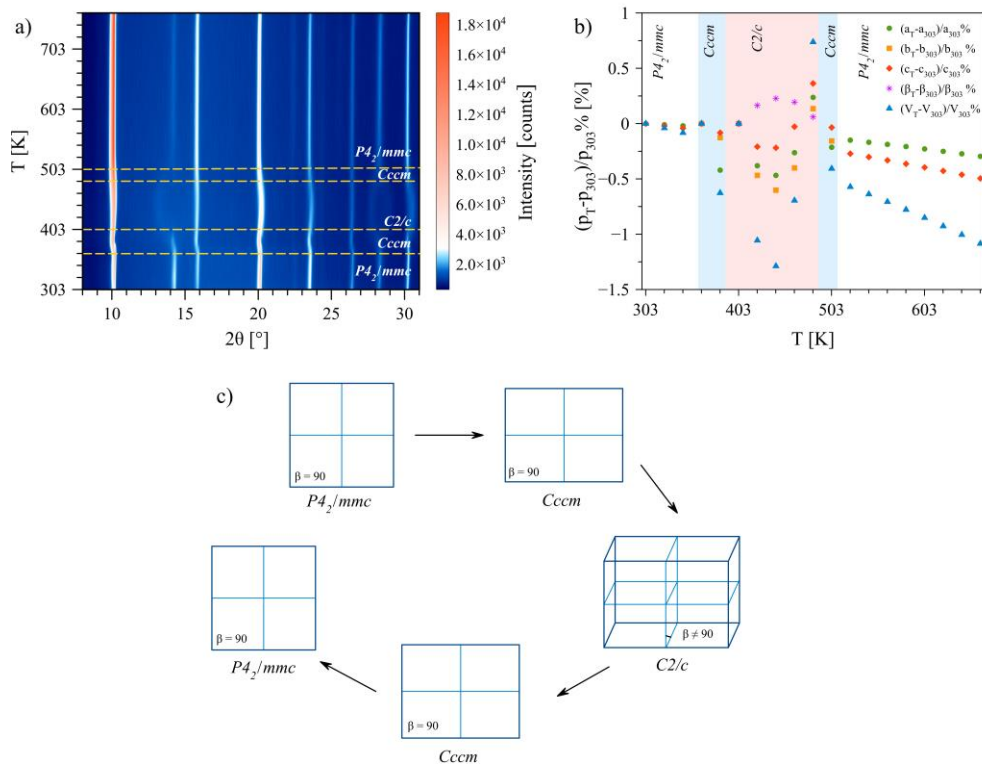


Figure 5.11 a) VT-PXRD 2-D plot of **Zn-H/NO₂·S**; b) result of the parametric whole powder pattern refinement; c) scheme of the phase transitions undergone by **Zn-H/NO₂·S** during the desolvation process ($P4_2/mmc$: $T_0 = 303$ K, $Cccm$: $T_0 = 363$ K, $C2/c$: $T_0 = 403$ K, $Cccm$: $T_0 = 483$ K, $P4_2/mmc$: $T_0 = 503$ K). Colour code: *a*, green circles; *b*, yellow squares; *c*, red diamonds; β , pink stars; *V*, blue triangles.

Table 5.4 Variation of the unit cell parameters of the Zn-MIXMOFs, obtained through the parametric whole powder pattern refinement of the VT-PXRD data.

Compound	T range [K]	Δa [%]	Δb [%]	Δc [%]	$\Delta \beta$ [%]	ΔV [%]
Zn-H/NO ₂	303-663 ($P4_2/mmc$)	-0.3		-0.5		-1.1
Zn-H/NO ₂	363-503 ($Cccm$)	-0.2	-0.2	-0.04		-0.4
Zn-H/NO ₂	403-483 ($C2/c$)	0.2	0.1	0.4	0.06	0.7
Zn-H/NH ₂	303-603	-0.5		-0.4		-1.4
Zn-NO ₂ /NH ₂	303-603	-0.4	0.1	-0.4		-0.6
Zn-H/NO ₂ /NH ₂	303-663	0.5	-1.3	-0.5		-1.3

5.5. Solid-state ^{13}C and ^{15}N CPMAS NMR Analysis of the MIXMOFs

To accurately determine the ligand composition in mixed-ligand MOFs, one of the most used techniques is ^1H NMR analysis of the liquid mixture obtained by sample digestion in acidic solutions, *i.e.* aqueous HCl, HF or H_2SO_4 .³⁰ However, this methodology did not lead to any results in the case of **Zn-MIXMOFs**, since the signals of the different linkers have nearly identical ^1H NMR chemical shift in solution, hampering signals assignment. Therefore, the semi-quantitative solid-state NMR approach,^{xxix} usually used for qualitative observations, was exploited for the first time, to the best of our knowledge, for ligands quantification in MIXMOFs. Thanks to the use of direct solid-state NMR analysis of the as-synthesized materials any possible contaminations, related to the digestion procedure, could be prevented. Moreover, the resonances were much better resolved in the solid-state NMR spectrum, thus overcoming the signal overlapping observed in solution. Considering that the ligands in the MIXMOFs are identical except for the functional group, nearly equal cross-polarization rates (*i.e.* T_{1S}) and ^1H $T_{1\rho}$ values were supposed, overcoming the quantitative limitations of the CPMAS experiment. As starting point, the ^{13}C CPMAS NMR spectra of the end-members Zn-BPZ, **Zn-BPZNO₂** and **Zn-BPZNH₂** were collected, Figure 5.12 b. The three spectra show distinctive features useful for linker identification in the MOFs:

- BPZNO₂²⁻: the C3 atom (see the labelling scheme in Figure 5.12) is deshielded with respect to Zn-BPZ, falling at $\delta_{\text{C}} \sim 150$ ppm. A signal at $\delta_{\text{C}} \sim 110$ ppm ascribable to the C4 and C4' atoms is present.
- BPZNH₂²⁻: the C3 atom is deshielded with respect to Zn-BPZ, falling at $\delta_{\text{C}} \sim 152$ ppm. A characteristic resonance is present for C4 at $\delta_{\text{C}} \sim 99$ ppm.
- BPZ²⁻: the C3 and C3' signals show the same chemical shift ($\delta_{\text{C}} \sim 135$ ppm). A signal at $\delta_{\text{C}} \sim 110$ ppm ascribable to the C4 and C4' atoms is present.

DMF is present in variable amounts in all the MOFs with a $\delta_{\text{C}} \sim 30$ ppm signal belonging to the methyl groups and $\delta_{\text{C}} \sim 160$ ppm resonance belonging to the C=O group.

^{xxix} The solid-state NMR spectra were collected and interpreted by Prof. Gobetto's group, University of Turin, Italy.

The well-resolved resonance signals of the C4/C4' atoms of the linkers allowed the quantitative estimation of ligand ratio in the MIXMOFs, Figure 5.13. In case of overlap, deconvolution was used to discriminate the different signals contribution; the obtained integrals were then used for ligand quantification. Worthy of note, only **Zn-H/NH₂·S** respects the predicted 50:50 ligand ratio (Table 5.5), while **Zn-H/NO₂·S** and **Zn-NO₂/NH₂·S** show a 64:36 and 66:34 ratio, respectively. In the case of **Zn-H/NO₂/NH₂·S** the untagged ligand is present as the majoritarian one (50%), BPZNO₂²⁻ and BPZNH₂²⁻ are almost equally present (27 and 23%, respectively). The resulting ligand ratios are in good agreement with those obtained from the structure refinements, as highlighted in Table 5.5.

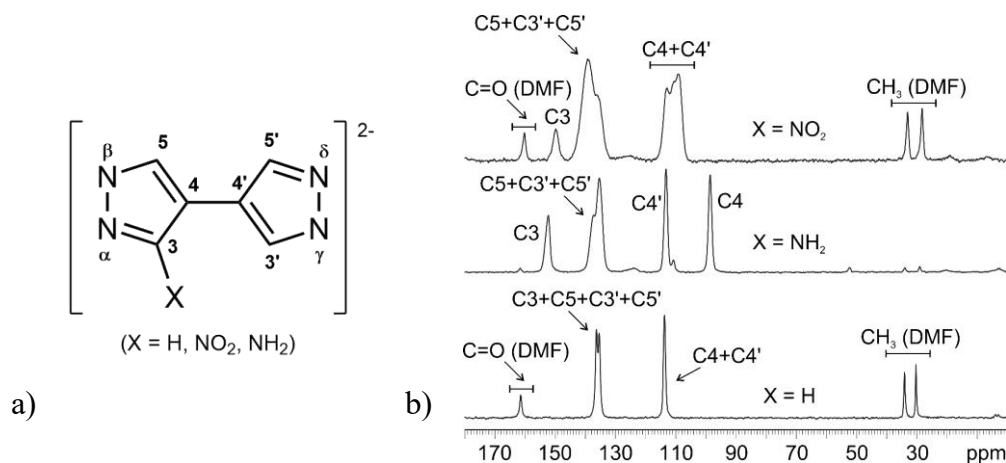


Figure 5.12 a) Scheme of the C- and N-atom labelling of the BPZX²⁻ ligands; b) ¹³C (150 MHz) CPMAS NMR spectra with signal assignment for Zn-BPZ, Zn-BPZNH₂ and Zn-BPZNO₂. The signals of DMF are highlighted for the sake of completeness. Images taken from Ref. ²⁴.

The ¹⁵N CPMAS NMR spectra of the end-members and MIXMOFs as well were collected. Unfortunately, they were characterized by a very low signal-to-noise ratio and were badly resolved, hampering the stoichiometric quantification. Thus, only the ¹³C spectra only were used.

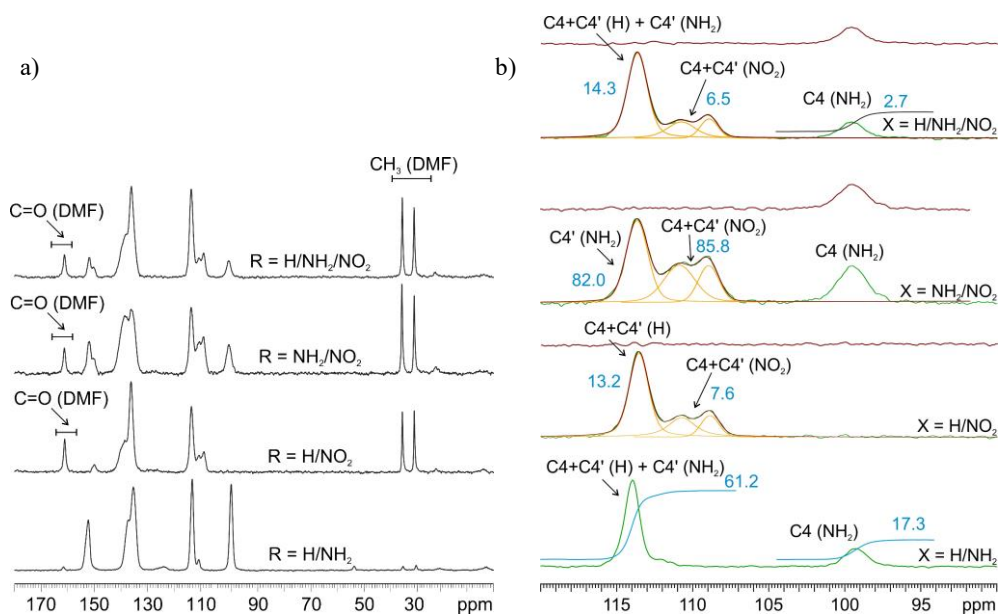


Figure 5.13 a) ^{13}C (150 MHz) CPMAS NMR spectra with signal assignment for $\text{Zn-H/NO}_2\cdot\text{S}$, $\text{Zn-H/NH}_2\cdot\text{S}$, $\text{Zn-NO}_2/\text{NH}_2\cdot\text{S}$ and $\text{Zn-H/NO}_2/\text{NH}_2\cdot\text{S}$. The signals of DMF are highlighted for the sake of completeness. b) Magnification of the ^{13}C CPMAS NMR spectra in the 90-120 ppm δ region. Colour code: experimental spectra, green; deconvolution of the signals between $\delta_{\text{C}} = 105$ and 120 ppm, yellow; sum of the deconvoluted peaks, dark red; difference between the experimental spectra and the sum of the deconvoluted resonances, red line above. Integrals for the corresponding signals are written in blue. Images taken from Ref. ²⁴.

Table 5.5 Relative percentage of the ligands in the studied MIXMOFs. In black the values obtained from the integration of the ^{13}C NMR spectra, in blue the values found by PXRD, in red those used for the syntheses.

Ligand	Zn-H/NO ₂	Zn-H/NH ₂	Zn-NO ₂ /NH ₂	Zn-H/NO ₂ /NH ₂
BPZ ²⁻	63.6 (62)	55.9 (56)	-	49.1 (46)
	50	50		33
BPZNH ₂ ²⁻	-	44.1 (44)	65.6 (62)	23.3 (21)
		50	50	33
BPZNO ₂ ²⁻	36.4 (38)	-	34.4 (38)	27.6 (33)
	50		50	33

As described in section 5.3, both the unambiguous assessment of the tag position on the ligand skeleton and the relative position of the different linkers cannot be determined through PXRD, since the ligand lays on a symmetry element ($2/m$). Thus, the presence of hydrogen bonds cannot be verified by PXRD. At variance, ^1H MAS NMR spectra

confirm the presence of hydrogen bonds in the end-member containing the -NH_2 group, as well as in all the MIXMOFs (Figure 5.14).

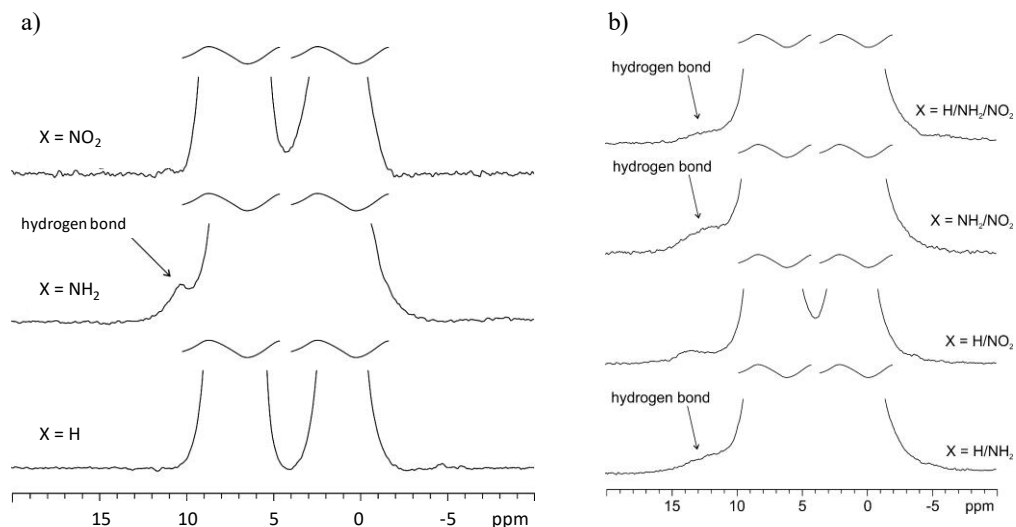


Figure 5.14 ^1H (400 MHz) MAS NMR spectra of: a) Zn-BPZNO_2 , Zn-BPZNH_2 and Zn-BPZ ; b) $\text{Zn-H/NO}_2/\text{NH}_2$, $\text{Zn-NO}_2/\text{NH}_2$, Zn-H/NO_2 and Zn-H/NH_2 .

5.6. Water Vapour Stability

The stability of the four MIXMOFs with respect to water vapour, one of the minor components of flue gases, was monitored for 11 days. The samples were introduced in an air-tight water-vapor saturated cell. Powder X-ray diffraction patterns were collected at different times and compared with that of a preliminary acquisition (black trace in Figure 5.15). None of the compounds show loss of the pristine crystallinity at least for 11 days of exposure. Figure 5.15 collects the mentioned PXRD patterns.

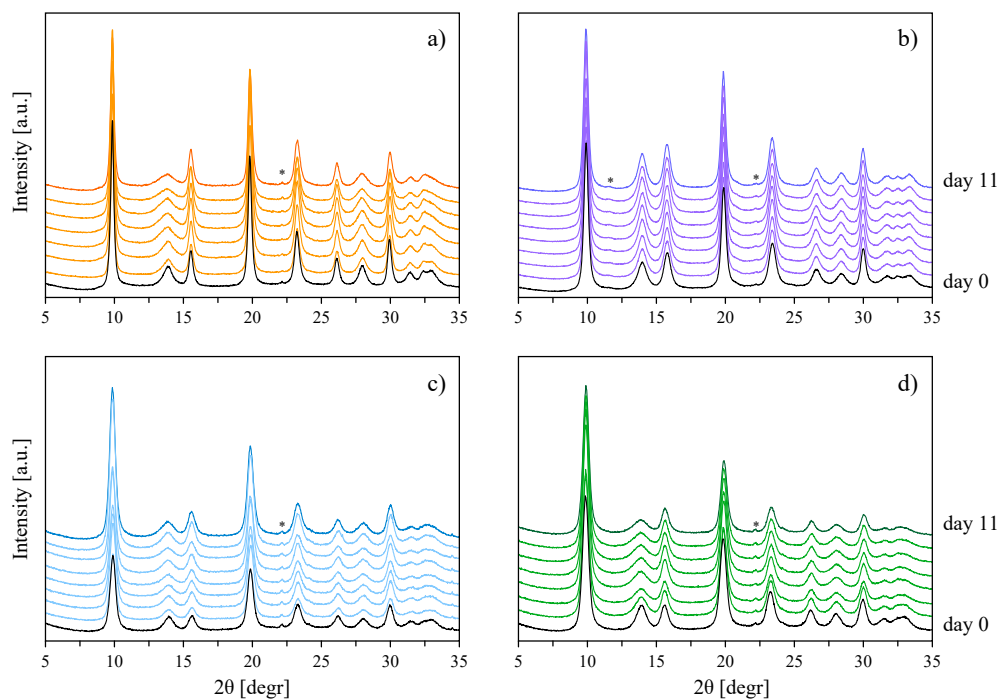


Figure 5.15 Powder X-ray diffraction patterns of a) **Zn-H/NO₂**, b) **Zn-H/NH₂**, c) **Zn-NO₂/NH₂** and d) **Zn-H/NO₂/NH₂**, before exposure to an atmosphere saturated of water vapour (black trace) and at different exposure times (orange, violet, light blue and green traces, respectively). The asterisk is an impurity of the sample.

5.7. Textural Properties and CO₂ Adsorption Ability of the MIXMOFs

N₂ adsorption isotherms: The textural properties^{xxx} of the Zn-mixed ligand MOFs were assessed through N₂ adsorption at 77 K (Figure 5.16). TGA was performed on the activated samples: none of them shows any loss of weight before decomposition confirming the complete desolvation. **Zn-H/NO₂**, **Zn-NO₂/NH₂** and **Zn-H/NO₂/NH₂** show a type I isotherm typical of microporous materials, while **Zn-H/NH₂·S** shows a type IV isotherm, typical of a micro-mesoporous sample. BET SSAs range between 400 (**Zn-H/NO₂**) and 600 m² g⁻¹ (**Zn-H/NO₂/NH₂**), smaller, as expected considering the functional groups decorating the pores, than that of Zn-BPZ (930 m² g⁻¹),³¹ and higher

^{xxx} The textural characterization and CO₂ adsorption isotherms were performed by Dr. A. Rossin's group, ICCOM-CNR Sesto Fiorentino, Italy.

than that of **Zn-BPZNH₂** (395 m² g⁻¹),¹⁵ confirming that the higher the amount of tags, the lower the surface area accessible.^{xxxi} Table 5.6 collects all the textural parameters retrieved by N₂ adsorption.

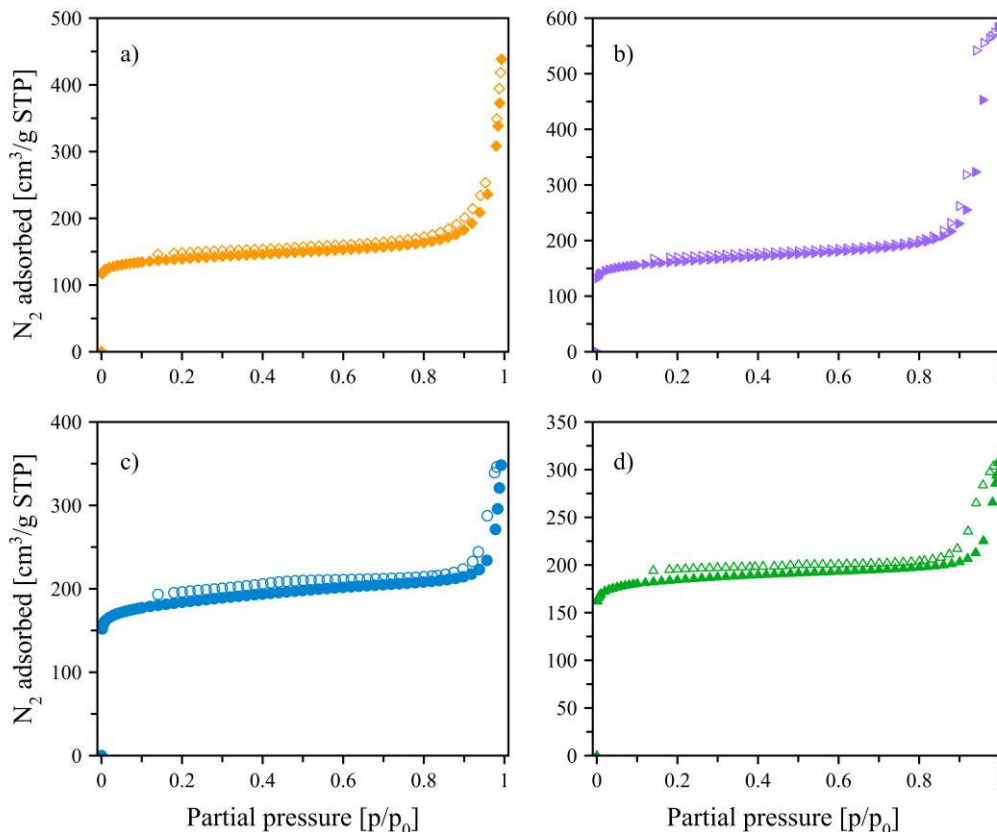


Figure 5.16 N₂ adsorption isotherms measured at 77 K on a) **Zn-H/NO₂**, b) **Zn-H/NH₂**, c) **Zn-NO₂/NH₂** and d) **Zn-H/NO₂/NH₂**. Empty symbols denote the desorption branches.

A narrow hysteresis loop is present in all the N₂ isotherms at high p/p_0 . The presence of interparticle macropores can explain the abrupt uptake at pressures close to condensation. As a matter of fact, SEM images, Figure 5.17, confirm the presence of macroporous cavities of the order of ~200 nm for **Zn-NO₂/NH₂** (Figure 5.17 a-b) and in

^{xxxi} **Zn-BPZNO₂** unexpectedly high BET area of 916 m² g⁻¹ can be ascribed to the presence of defects in the MOF crystal structure. Indeed, not only it does not follow the reported trend for the mixed-ligand series, but it is also higher than the theoretical upper limit of the BET area calculated through Grand Canonical Monte-Carlo simulations of the N₂ adsorption isotherm, as described in chapter IV.¹¹⁶

the 50-70 nm size range for **Zn-H/NO₂/NH₂** (Figure 5.17 c-d). As highlighted by the Dubinin-Astakhov analysis, the total pore volume is mainly composed by the micropore fraction (70-79%) for all the MIXMOFs except for **Zn-H/NH₂**.

Table 5.6 Collection of textural parameters retrieved from the N₂ adsorption isotherms at 77 K.

Compound	SSA BET [m ² /g]	V _{micro} (% of V _{tot}) [cm ³ /g]	V _{tot} [cm ³ /g]
Zn-H/NO ₂	431	0.27 (79%)	0.34
Zn-H/NH ₂	502	0.21 (32%)	0.66
Zn-NO ₂ /NH ₂	567	0.23 (70%)	0.33
Zn-H/NO ₂ /NH ₂	588	0.23 (70%)	0.33

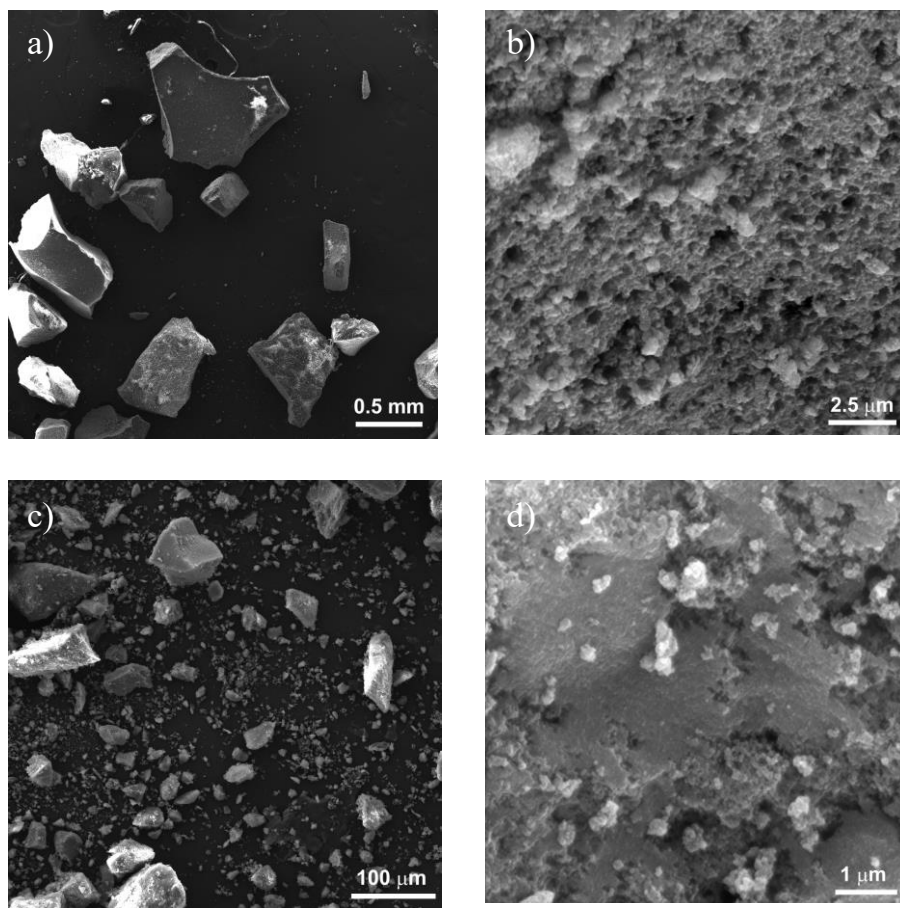


Figure 5.17 SEM images of **Zn-NO₂/NH₂** (a-b) and **Zn-H/NO₂/NH₂** (c-d).

CO₂ adsorption isotherms. To evaluate the CO₂ affinity and capacity of the MIXMOFs, CO₂ adsorption isotherms at 273 and 298 K up to 1.2 bar were collected. Then, their CO₂/N₂ (Henry and IAST) selectivity and Q_{st} were assessed. All the values found were compared to those of the Zn-BPX parents and of other Zn(II) azolates from the literature under similar experimental conditions, Table 5.7. At 273 K and 1 bar, **Zn-H/NO₂**, **Zn-H/NH₂**, **Zn-NO₂/NH₂** and **Zn-H/NO₂/NH₂** adsorb 3.0, 3.6, 3.2 and 3.6 mmol g⁻¹, respectively. The same trend, where **Zn-H/NH₂** has the higher CO₂ capacity and **Zn-H/NO₂** the lower one, can be observed at 298 K, with associated adsorption uptakes in the range from 2.4 (for **Zn-H/NO₂**) to 5.1 mmol g⁻¹ (for **Zn-H/NH₂**), Figure 5.18.

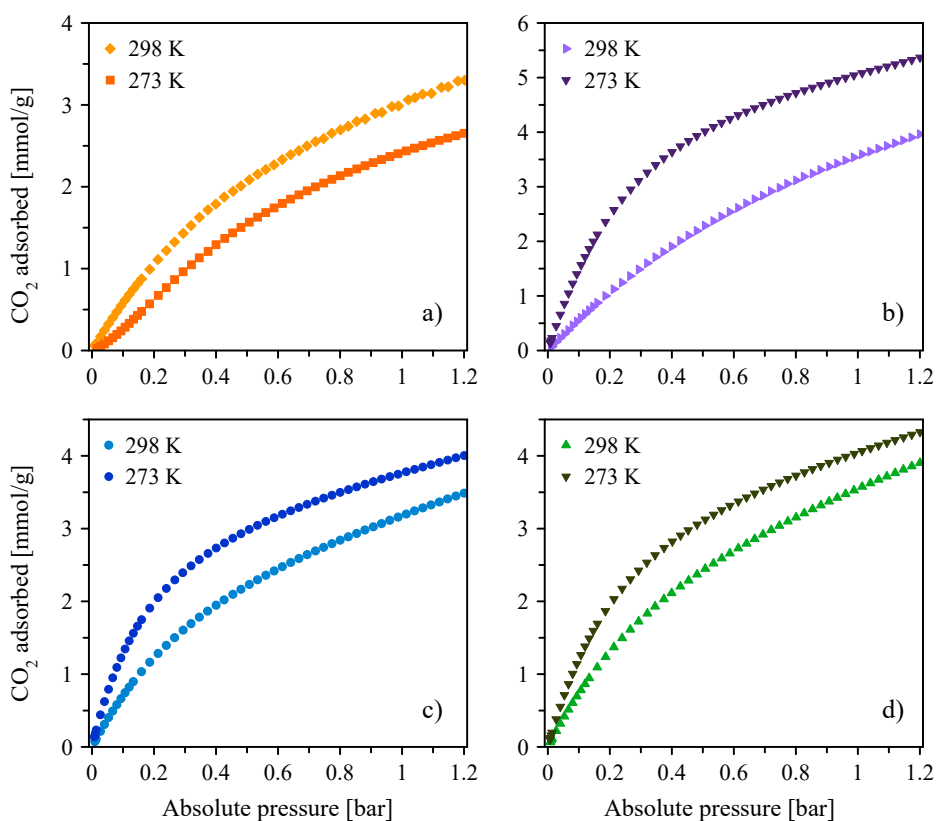


Figure 5.18 CO₂ adsorption isotherms measured at 298 K on a) **Zn-H/NO₂**, b) **Zn-H/NH₂**, c) **Zn-NO₂/NH₂** and d) **Zn-H/NO₂/NH₂**.

Concerning the CO₂ affinity, the MIXMOF bearing -NH₂ as unique functional group tag shows the highest $Q_{st} = 30.8 \text{ kJ mol}^{-1}$, directly followed by **Zn-H/NO₂** ($Q_{st} = 21.6 \text{ kJ mol}^{-1}$), **Zn-NO₂/NH₂** ($Q_{st} = 19.0 \text{ kJ mol}^{-1}$), and **Zn-H/NO₂/NH₂** ($Q_{st} = 16.1 \text{ kJ mol}^{-1}$).

Enlarging the comparison to the Zn-BPZX end-members, see Table 5.7:

- the higher capacity is retrieved by MOFs containing the amino group as functionalization, confirming the positive effect of this group in CO₂ adsorption.
- The MOFs containing the amino group show the higher Q_{st} values. As an example, in the **Zn-BPZ/Zn-BPZNH₂** series: **Zn-BPZNH₂** ($Q_{st} = 35.6 \text{ kJ mol}^{-1}$) > **Zn-H/NH₂** ($Q_{st} = 30.8 \text{ kJ mol}^{-1}$) > Zn-BPZ ($Q_{st} = 22.0 \text{ kJ mol}^{-1}$). On the other hand, the introduction of a -NO₂ group does not have a positive effect on the thermodynamic affinity (**Zn-H/NO₂**, $Q_{st} = 21.6 \text{ kJ mol}^{-1}$; **Zn-BPZNO₂**, $Q_{st} = 21.6 \text{ kJ mol}^{-1}$).
- The coexistence of the nitro and amino groups in the same MOF has a negative effect both on the affinity (**Zn-NO₂/NH₂**, $Q_{st} = 19.0 \text{ kJ mol}^{-1}$; **Zn-H/NO₂/NH₂**, $Q_{st} = 16.1 \text{ kJ mol}^{-1}$) and on the total capacity (see above).
- The dilution of the functional groups has a positive effect on the CO₂/N₂ selectivity, as demonstrated by **Zn-H/NO₂** and **Zn-H/NH₂**, if compared to **Zn-BPZNO₂** and **Zn-BPZNH₂**, respectively.

Summarizing, among the Zn-BPZX MOFs studied, **Zn-H/NH₂** show the best performances in terms of SSA, capacity, affinity and selectivity.

If compared to other Zn(II) azolate MOFs, the title MIXMOFs have a better performance in terms of both adsorption capacity (mmol g^{-1}) and CO₂ affinity (Q_{st}) with respect to other literature materials characterized by higher BET SSA, such as the Zn(BDPX) family,³² under the same experimental conditions.

Table 5.7 Comparison of the CO₂ adsorption properties of the title MIXMOFs with selected zinc(II) azolate MOFs from the literature. When not directly available in the article discussion, data were extrapolated from the presented graphs. Table reproduced from Ref. ²⁴⁰.

	BET area [m ² /g]	Q _{st} [kJ mol ⁻¹]	CO ₂ /N ₂ selectivity (Henry)	CO ₂ /N ₂ selectivity (IAST)	CO ₂ quantity adsorbed (p = 1 bar) [mmol/g]		Quantity adsorbed @ 298K/SSA [mmol/m ²]	Ref.
					T = 298 K	T = 273 K		
Zn-BPZ	930	22.0	15	15	3.7 (16.2 wt.%)	5.1 (22.5 wt.%)	0.0040	24,31
Zn-BPZNO ₂	916	20.5	15	12	4.4 (19.2 wt.%)	4.7 (20.6 wt.%)	0.0048	14
Zn-BPZNH ₂	395	35.6	17	14	3.1 (13.5 wt.%)	4.8 (20.9 wt.%)	0.0078	15
Zn-H/NH₂	502	30.8	18	17	3.6 (15.8 wt.%)	5.1 (22.3 wt.%)	0.0072	24
Zn-H/NO₂	431	21.6	20	20	3.0 (13.3 wt.%)	2.4 (10.6 wt.%)	0.0070	24
Zn-NO₂/NH₂	567	19.0	14	12	3.2 (14.0 wt.%)	3.3 (14.4 wt.%)	0.0056	24
Zn-H/NO₂/NH₂	588	16.1	11	11	3.6 (15.7 wt.%)	4.1 (17.9 wt.%)	0.0061	24
Zn(BDP)	2288	19.7				~ 3.0		32
Zn(BDPNO ₂)	1875	21.4				~ 2.9		32
Zn(BDPNH ₂)	1345	28.1				~ 2.8		32
Zn(BDPOH)	1170	22.9				~ 4.5		32
[Zn(SiF ₆ (pyz) ₂] _n (SIFSIX-3-Zn)	250	45.0		1818	2.5		0.0100	33
Zn-Me ₂ BPZ	290	24.8				2.0		31

5.8. Conclusions

The four MIXMOFs **Zn-H/NO₂**, **Zn-H/NH₂**, **Zn-NO₂/NH₂** and **Zn-H/NO₂/NH₂** were synthesised, starting from the most promising ligands and metal ion of the M-BPZX (M = Zn, X = NO₂, NH₂) MOFs presented in chapters II-IV, and fully characterized in the solid state. They are isorecticular to their end-members Zn-BPZ and Zn-BPZX (X = NO₂, NH₂) and, to the best of our knowledge, represent the first examples of isorecticular (pyr)azolate MIXMOFs. They show a 3-D open framework with 1-D square (**Zn-H/NO₂** and **Zn-H/NH₂**) or rhombic (**Zn-NO₂/NH₂** and **Zn-H/NO₂/NH₂**) channels, in which the functional groups decorate the walls. ¹³C CPMAS solid-state NMR spectra collected on the as-synthesized materials were used, for the first time on MIXMOFs, for accurate ligand stoichiometric quantification. The values extrapolated from the NMR spectra are in good agreement with those assessed by PXRD. These MIXMOFs show high thermal stability, with decomposition temperatures between 708 and 726 K under N₂. All of them are stable after desolvation and do not show any phase transition except for **Zn-H/NO₂**, which pass through multiple phase transitions to accommodate the desolvation process. They are micro-mesoporous materials with BET SSA in the range 400-600 m² g⁻¹, as highlighted by N₂ adsorption at 77 K. CO₂ adsorption capacity, CO₂ isosteric heat of adsorption (Q_{st}) and CO₂/N₂ selectivity were studied and compared to those of the end-member parents to unveil the role of functionalization during CO₂ adsorption. As a general trend, the amino-tagged derivatives show a better affinity and capacity with respect to the nitro-tagged counterparts. The dilution of the functional groups increases the CO₂/N₂ selectivity. The MIXMOFs in which NO₂ and NH₂ coexist show worst properties in terms of adsorption, selectivity and affinity. Among the MOFs studied, the best compromise is represented by **Zn-H/NH₂**.

5.9. References

- (1) Sue, A. C. H.; Mannige, R. V.; Deng, H.; Cao, D.; Wang, C.; Gándara, F.; Stoddart, J. F.; Whitlam, S.; Yaghi, O. M. Heterogeneity of Functional Groups in a Metal–Organic Framework Displays Magic Number Ratios. *Proc. Natl. Acad. Sci. U. S. A.* **2015**, 112 (18), 5591–5596.
- (2) Liu, B.; Zhou, H. F.; Hou, L.; Wang, Y. Y. Functionalization of MOFs: Via a Mixed-Ligand Strategy: Enhanced CO₂ Uptake by Pore Surface Modification. *Dalt. Trans.* **2018**, 47 (15), 5298–5303.
- (3) Burrows, A. D. Mixed-Component Metal–Organic Frameworks (MC-MOFs): Enhancing Functionality through Solid Solution Formation and Surface Modifications. *CrystEngComm* **2011**, 13 (11), 3623.
- (4) Pullen, S.; Clever, G. H. Mixed-Ligand Metal–Organic Frameworks and Heteroleptic Coordination Cages as Multifunctional Scaffolds - A Comparison. *Acc. Chem. Res.* **2018**, 51 (12), 3052–3064.
- (5) Helal, A.; Yamani, Z. H.; Cordova, K. E.; Yaghi, O. M. Multivariate Metal–Organic Frameworks. **2017**, 4 (3), 296–298.
- (6) Yuan, S.; Lu, W.; Chen, Y.-P.; Zhang, Q.; Liu, T.-F.; Feng, D.; Wang, X.; Qin, J.; Zhou, H.-C. Sequential Linker Installation: Precise Placement of Functional Groups in Multivariate Metal–Organic Frameworks. *J. Am. Chem. Soc.* **2015**, 137 (9), 3177–3180.
- (7) Gu, C.; Liu, J.; Hu, J.; Wang, W. Metal–Organic Frameworks Grafted by Univariate and Multivariate Heterocycles for Enhancing CO₂ Capture: A Molecular Simulation Study. *Ind. Eng. Chem. Res.* **2019**, 58 (6), 2195–2205.
- (8) Drummond, M. L.; Cundari, T. R.; Wilson, A. K. Cooperative Carbon Capture Capabilities in Multivariate MOFs Decorated with Amino Acid Side Chains: A Computational Study. *J. Phys. Chem. C* **2013**, 117 (28), 14717–14722.
- (9) Han, S. S.; Kim, D.; Jung, D. H.; Cho, S.; Choi, S.-H.; Jung, Y. Accurate Ab Initio-Based Force Field for Predictive CO₂ Uptake Simulations in MOFs and ZIFs: Development and Applications for MTV-MOFs. *J. Phys. Chem. C* **2012**, 116 (38), 20254–20261.
- (10) Li, S.; Chung, Y. G.; Simon, C. M.; Snurr, R. Q. High-Throughput Computational Screening of Multivariate Metal–Organic Frameworks (MTV-MOFs) for CO₂ Capture. *J. Phys. Chem. Lett.* **2017**, 8 (24), 6135–6141.
- (11) Deng, H.; Doonan, C. J.; Furukawa, H.; Ferreira, R. B.; Towne, J.; Knobler, C. B.; Wang, B.; Yaghi, O. M. Multiple Functional Groups of Varying Ratios in Metal–Organic Frameworks. *Science* **2010**, 327 (5967), 846–850.
- (12) Kong, X.; Deng, H.; Yan, F.; Kim, J.; Swisher, J. A.; Smit, B.; Yaghi, O. M.; Reimer, J. A. Mapping of Functional Groups in Metal–Organic Frameworks. *Science* **2013**, 341 (6148), 882–885.
- (13) Pettinari, C.; Tăbăcaru, A.; Boldog, I.; Domasevitch, K. V.; Galli, S.; Masciocchi, N. Novel Coordination Frameworks Incorporating the 4,4'-Bipyrazolyl Ditopic Ligand. *Inorg. Chem.* **2012**, 51 (9), 5235.
- (14) Mosca, N.; Vismara, R.; Fernandes, J. A.; Tuci, G.; Di Nicola, C.; Domasevitch, K. V.; Giacobbe, C.; Giambastiani, G.; Pettinari, C.; Aragonés-Anglada, M.; Moghadam, P.; Fairen-Jimenez, D.; Rossin, A.; Galli, S. NO₂-Functionalized Bis(Pyrazolate) MOFs as

- CO₂ Capture Materials at Ambient Conditions. *Chem. - A Eur. J.* **2018**, 24 (50), 13170–13180.
- (15) Vismara, R.; Tuci, G.; Mosca, N.; Domasevitch, K. V.; Di Nicola, C.; Pettinari, C.; Giambastiani, G.; Galli, S.; Rossin, A. Amino-Decorated Bis(Pyrazolate) Metal–Organic Frameworks for Carbon Dioxide Capture and Green Conversion into Cyclic Carbonates. *Inorg. Chem. Front.* **2019**, 6 (2), 533–545.
- (16) Nakamoto, K. *Infrared and Raman Spectra of Inorganic and Coordination Compounds*, 6th edn.; Wiley Press: NJ, **2009**.
- (17) Zerbi, G.; Alberti, C. Infrared Spectra of Pyrazoles-I: Pyrazoles Mono-Alkyl Substituted. *Spectrochim. Acta* **1962**, 18 (3), 407–423.
- (18) Coelho, A. A. Indexing of Powder Diffraction Patterns by Iterative Use of Singular Value Decomposition. *J. Appl. Crystallogr.* **2003**, 36 (1), 86–95.
- (19) Coelho, A. A. TOPAS-Academic V6. <http://www.topas-academic.net> 2016.
- (20) Coelho, A. A. Whole-Profile Structure Solution from Powder Diffraction Data Using Simulated Annealing. *J. Appl. Crystallogr.* **2000**, 33 (3 II), 899–908.
- (21) Cheary, R. W.; Coelho, A. Fundamental Parameters Approach to X-Ray Line-Profile Fitting. *J. Appl. Crystallogr.* **1992**, 25 (pt 2), 109–121.
- (22) Stephens, P. W. Phenomenological Model of Anisotropic Peak Broadening in Powder Diffraction. *J. Appl. Cryst.* **1999**, 32, 281–289.
- (23) Blatov, V. A.; Shevchenko, A. P.; Proserpio, D. M. Applied Topological Analysis of Crystal Structures with the Program Package Topospro. *Cryst. Growth Des.* **2014**, 14 (7), 3576–3586.
- (24) Vismara, R.; Tuci, G.; Tombesi, A.; Domasevitch, K. V.; Di Nicola, C.; Giambastiani, G.; Chierotti, M. R.; Bordignon, S.; Gobetto, R.; Pettinari, C.; Rossin, R.; Galli, S. Tuning Carbon Dioxide Adsorption Affinity of Zinc(II) MOFs by Mixing Bis(Pyrazolate) Ligands with N-Containing Tags. *ACS Appl. Mater. Interfaces* **2019**, 11 (30), 26956–26969.
- (25) Tăbăcaru, A.; Pettinari, C.; Timokhin, I.; Marchetti, F.; Carrasco-Marín, F.; Maldonado-Hódar, F. J.; Galli, S.; Masciocchi, N. Enlarging an Isorecticular Family: 3,3',5,5'-Tetramethyl-4,4'-Bipyrazolato-Based Porous Coordination Polymers. *Cryst. Growth Des.* **2013**, 13 (7), 3087–3097.
- (26) Taddei, M.; Tiana, D.; Casati, N.; Van Bokhoven, J. A.; Smit, B.; Ranocchiari, M. Mixed-Linker UiO-66: Structure–Property Relationships Revealed by a Combination of High-Resolution Powder X-Ray Diffraction and Density Functional Theory Calculations. *Phys. Chem. Chem. Phys.* **2017**, 19 (2), 1551–1559.
- (27) Vegard, L. Die Konstitution Der Mischkristalle Und Die Raumfüllung Der Atome. *Zeitschrift für Phys. A Hadron. Nucl.* **1921**, 5 (1), 17–26.
- (28) Chavan, S. M.; Shearer, G. C.; Svelle, S.; Olsbye, U.; Bonino, F.; Ethiraj, J.; Lillerud, K. P.; Bordiga, S. Synthesis and Characterization of Amine-Functionalized Mixed-Ligand Metal–Organic Frameworks of UiO-66 Topology. *Inorg. Chem.* **2014**, 53 (18), 9509–9515.
- (29) Kandiah, M.; Nilsen, M. H.; Usseglio, S.; Jakobsen, S.; Olsbye, U.; Tilset, M.; Larabi, C.; Quadrelli, E. A.; Bonino, F.; Lillerud, K. P. Synthesis and Stability of Tagged UiO-66 Zr-

- MOFs. *Chem. Mater.* **2010**, 22 (24), 6632–6640.
- (30) Tanabe, K. K.; Cohen, S. M. Postsynthetic Modification of Metal-Organic Frameworks - a Progress Report. *Chem. Soc. Rev.* **2011**, 40 (2), 498–519.
- (31) Mosca, N.; Vismara, R.; Fernandes, J. A.; Casassa, S.; Domasevitch, K. V.; Bailón-García, E.; Maldonado-Hódar, F. J.; Pettinari, C.; Galli, S. CH₃-Tagged Bis(Pyrazolato)-Based Coordination Polymers and Metal-Organic Frameworks: An Experimental and Theoretical Insight. *Cryst. Growth Des.* **2017**, 17 (7), 3854–3867.
- (32) Colombo, V.; Montoro, C.; Maspero, A.; Palmisano, G.; Masciocchi, N.; Galli, S.; Barea, E.; Navarro, J. A. R. Tuning the Adsorption Properties of Isoreticular Pyrazolate-Based Metal-Organic Frameworks through Ligand Modification. *J. Am. Chem. Soc.* **2012**.
- (33) Nugent, P.; Belmabkhout, Y.; Burd, S. D.; Cairns, A. J.; Luebke, R.; Forrest, K.; Pham, T.; Ma, S.; Space, B.; Wojtas, L. Porous Materials with Optimal Adsorption Thermodynamics and Kinetics for CO₂ Separation. *Nature* **2013**, 495 (7439), 80.
- (34) Spek, A. L. Structure Validation in Chemical Crystallography. *Acta Crystallogr. Sect. D* **2009**, 65 (2), 148–155.

CHAPTER VI

6. CONCLUSIONS

6.1. Conclusions

Among greenhouse gases, carbon dioxide gives a significant contribution to global warming. To date, the energy demand is very far from being completely satisfied by green sources. Therefore, the reduction of CO₂ emissions could be a transitional solution to limit its concentration into the atmosphere. Metal-organic frameworks (MOFs) are a class of finely tuneable organic/inorganic porous materials that can be employed as CO₂ adsorbents in post-combustion capture and sequestration. This Ph. D. thesis has been focused on the study of a series of bis(pyrazolate) MOFs to be used with this aim.

Firstly, a systematic study on the influence of both ligand functionalization [*i.e.* -(CH₃)₂, -NO₂, -NH₂, -(NH₂)₂] on the same ligand skeleton [H₂BPZ, 4,4'-bis(pyrazole)] and metal centre [M = Co, Ni, Cu, Zn] was carried out on single-ligand MOFs. Then, the building units granting the best performances in CO₂ adsorption were used to synthesize mixed-ligand MOFs.

After a preliminary overview on the motivations of investigating pyrazolate-based MOFs, chapter II briefly reports on the synthesis of the M-BPZX·S (M = Co, Ni, Cu, Zn; X = (CH₃)₂, NO₂, NH₂, (NH₂)₂; S = *N,N*-dimethylformamide) series. The feasibility of preparing different MOFs with good yields is demonstrated. All the materials proved to be stable under ambient conditions except for M-BPZNO₂ (M = Co, Cu), which start losing crystallinity after two weeks.

In chapter III, the structural and thermal characterization of the M-BPZX·S MOFs is reported. The crystal structures were determined and refined *via* powder X-ray diffraction (PXRD) on data acquired with laboratory instrumentation. The M-BPZX MOFs are isorecticular, showing a 3-D open-framework characterized by 1-D square or rhombic channels. The functional groups decorate the channel walls. At ambient conditions, the empty volume ranges between 35.6 and 45.7%. The thermal analysis performed by combining TGA and variable-temperature PXRD demonstrated that the M-BPZX MOFs are stable up to medium-high temperature (563-733 K). None of them undergoes phase transitions or collapse in response to heating. Comparing the different metal ions among the same ligand family, Zn(II)-based MOFs show the highest thermal stability.

Considering Zn(II) MOFs with different functionalization, the trend $T_{\text{dec}}(\text{BPZNH}_2) = T_{\text{dec}}(\text{BPZ}(\text{NH}_2)_2) > T_{\text{dec}}(\text{BPZNO}_2) > T_{\text{dec}}(\text{Me}_2\text{BPZ})$ is observed.

Chapter IV discusses the textural and adsorption properties of the M-BPZX MOFs. N_2 adsorption isotherms at 77 K revealed permanently porous materials with BET SSAs ranging from $100 \text{ m}^2 \text{ g}^{-1}$ up to $916 \text{ m}^2 \text{ g}^{-1}$. As a general trend among the same ligand family, the zinc(II) compounds, except for **Zn-Me₂BPZ**, show the highest BET SSA, with an associated higher CO_2 capacity. All the functional groups inserted on the BPZ^{2-} skeleton were confirmed to have a positive effect in carbon dioxide adsorption, enhancing the capacity and/or the affinity for CO_2 of the functionalized MOFs with respect to the non-functionalized parents. An unpredicted host-guest interaction, *i.e.* between the C- NO_2 moiety of the ligand in **Zn-BPZNO₂** and CO_2 , was discovered thanks to an *in situ* and *operando* high-resolution PXRD experiment and confirmed by Grand Canonical Monte Carlo simulations. Among the studied MOFs, **Zn-BPZNO₂** and **Zn-BPZNH₂** showed the best performances, the first for its impressive CO_2 capacity at ambient conditions (19.4 wt. % at 298 K and 1 bar), the latter for both CO_2 capacity and affinity (13.6 wt. % at 298 K and 1 bar, Henry CO_2/N_2 selectivity of 17, $Q_{\text{st}} = 35.6 \text{ mmol g}^{-1}$).

Starting from these considerations, as highlighted in chapter V, four mixed bis(pyrazolate) zinc(II) MOFs (MIXMOFs) were synthesized, namely: **Zn-H/NO₂**, **Zn-H/NH₂**, **Zn-NO₂/NH₂** and **Zn-H/NO₂/NH₂**, and fully characterized in the solid state, in order to further elucidate the role of the -nitro and -amino functionalization during carbon dioxide adsorption. These MIXMOFs are isorecticular to their end-members, *i.e.* Zn-BPZ and Zn-BPZX (X = NO_2 , NH_2), and, to the best of our knowledge, represent the first examples of isorecticular (pyr)azolate MIXMOFs. Likewise, ^{13}C CPMAS solid-state NMR was used, for the first time on MIXMOFs, for an accurate quantification of the ligand stoichiometry. All the MIXMOFs show high thermal stability ($T_{\text{dec}} = 708\text{-}726 \text{ K}$, under N_2) and permanent porosity after thermal activation, with BET SSAs in the range $400\text{-}600 \text{ m}^2 \text{ g}^{-1}$. Comparing the CO_2 adsorption capacity, the CO_2 isosteric heat of adsorption (Q_{st}) and the CO_2/N_2 selectivity of the MIXMOFs to those of the end-members, some observations can be done: *i*) the amino-tagged derivatives show a better affinity and capacity with respect to the nitro-tagged counterparts; *ii*) selectivity can be

enhanced through dilution of the functionalized ligand; *iii*) the coexistence of NO₂ and NH₂ groups has a negative effect on adsorption capacity, affinity and selectivity. Among the MOFs studied, the most promising material is the MIXMOF **Zn-H/NH₂**.

In summary, in this Ph. D. thesis we have demonstrated the exceptional performances of bis(pyrazolate) MOFs for post-combustion carbon capture and sequestration and carbon capture and utilization, including high CO₂ adsorption and selectivity, as well as high thermal stability. A novel host-guest interaction between the gaseous molecules and the framework has been proposed. Likewise, the beneficial effect of the dilution of the functionalized group in the MIXMOFs has been proved.

Future work will be addressed to test the performances of the most promising materials developed in this Ph. D. thesis as CO₂ adsorbents in simulated operating conditions, namely in the presence of water vapour and more complex mixture of gases. Moreover, given the strong correlation between CO₂ adsorption capacity and BET SSA, some efforts could be made in developing and characterizing novel Zn-MIXMOFs containing longer bis(pyrazolate) ligands and, therefore, expectedly showing higher surface area.

ANNEX I

7. MATERIALS AND METHODS

7.1. M-Me₂BPZ

Adapted with permission from “Mosca, N.; Vismara, R.; Fernandes, J. A.; Casassa, S.; Domasevitch, K. V.; Bailón-García, E.; Maldonado-Hódar, F. J.; Pettinari, C. and Galli, S. (2017). CH₃-Tagged Bis(pyrazolato)-Based Coordination Polymers and Metal–Organic Frameworks: An Experimental and Theoretical Insight. Crystal Growth & Design, 17(7), 3854–3867”. Copyright © (2017) American Chemical Society.

3,3'-Dimethyl-4,4'-bis(pyrazole) (H₂Me₂BPZ) was synthesized following the synthetic methodology previously published by Sharko *et al.*¹ All the chemicals and reagents employed were purchased from commercial suppliers and used as received without further purification. IR spectra were recorded as neat from 4000 to 600 cm⁻¹ with a PerkinElmer Spectrum One System instrument. Elemental analyses (C, H, N %) were performed with a Fisons Instruments 1108 CHNS-O elemental analyser. Thermogravimetric analyses were carried out under a N₂ flow with a Perkin Pyris 1 thermal analyser with heating rates in the range 5–10 K/min. Powder X-ray diffraction (PXRD) qualitative analyses were carried out with a Bruker D8 Advance diffractometer, acquiring data at room temperature in the 3–35° 2θ range, with steps of 0.02°, and time *per* step of 1 s (see section 7.1.2 for the instrument specifics). The nature and purity of all the batches employed for the functional characterization were assessed by elemental analysis, IR spectroscopy, and PXRD.

7.1.1. Synthesis and Preliminary Characterization

The synthesis and preliminary analytical characterization of the ligands were carried out by Prof. K. V. Domasevitch, University of Kyiv, Ukraine. The syntheses and preliminary analytical characterization of M-BPZ and **M-Me₂BPZ·S** (M = Co, Zn) were carried out by Prof. C. Pettinari's group, University of Camerino, Italy.

Co-Me₂BPZ·S. H₂Me₂BPZ (0.0324 g, 0.200 mmol) was dissolved in *N,N*-dimethylformamide (DMF) (8 mL). Then, Co(CH₃COO)₂·4H₂O (0.0498 g, 0.200 mmol) was added. The mixture was left under stirring in a high-pressure glass tube at 120 °C for 24 h, until a violet precipitate appeared. The precipitate was filtered off, washed with hot acetone (2 × 10 mL), and dried under vacuum. Yield: 86%. **Co-Me₂BPZ·S** is insoluble in dimethyl sulfoxide (DMSO), alcohols, acetone, acetonitrile (CH₃CN), chlorinated

solvents, and water. Elem. Anal. Calc. for $C_8H_8CoN_4 \cdot 0.9(C_3H_7NO)$ (fw = 284.89 g/mol): C, 44.97; H, 5.04; N, 24.01%. Found: C, 44.28; H, 4.68; N, 24.31%. IR (neat, cm^{-1}): 2920 (vw) [$\nu(C-H_{aliphatic})$], 1674 (vs) [$\nu(C=O)$], 1506 (m) [$\nu(C=C + C=N)$], 1443 (m), 1383 (w), 1345 (s), 1276 (m), 1097 (vs), 1060 (w), 994 (w), 969 (s), 824 (m). **Co-Me₂BPZ·S** may be isolated also by using $Co(NO_3)_2 \cdot 6H_2O$ in either solvothermal conditions or methanol at 100 °C for 1 day in the presence of aq. KOH (0.4 mmol).

Zn-Me₂BPZ·S. H_2Me_2BPZ (0.0324 g, 0.200 mmol) was dissolved in water (8 mL). Then, $Zn(CH_3COO)_2 \cdot 2H_2O$ (0.0438 g, 0.200 mmol) was added. The mixture was left under stirring at room temperature for 24 h. A white precipitate was obtained, filtered off, washed with hot DMF (2×10 mL), and dried under vacuum. Yield: 81%. **Zn-Me₂BPZ·S** is insoluble in DMSO, alcohols, acetone, CH_3CN , chlorinated solvents and water. Elem. Anal. Calc. for $C_8H_8N_4Zn \cdot 0.5(C_3H_7NO)$ (fw = 262.11 g/mol): C, 43.53; H, 4.42; N, 24.05%. Found: C, 43.57; H, 4.53; N, 23.56%. IR (neat, cm^{-1}): 2924 (vw) [$\nu(C-H_{aliphatic})$], 1675 (vs) [$\nu(C=O)$], 1506 (m) [$\nu(C=C + C=N)$], 1447 (m), 1382 (w), 1351 (s), 1108 (s), 1052 (w), 997 (w), 979 (s), 826 (m). **Zn-Me₂BPZ·S** may be isolated in the form of microcrystalline powders also by using other ZnX_2 salts ($X = NO_3^-$ or ClO_4^-).

7.1.2. Powder X-ray Diffraction Structural Characterization

Microcrystalline powders of **Co-Me₂BPZ·S** and **Zn-Me₂BPZ·S** were deposited in the hollow of a silicon zero-background plate 0.2 mm deep (supplied by Assing Srl, Monterotondo, Italy). Data acquisitions were performed on a vertical-scan Bruker AXS D8 Advance $\theta:\theta$ diffractometer, equipped with a Bruker Lynxeye linear position-sensitive detector, an X-ray tube (Cu $K\alpha$, $\lambda = 1.5418 \text{ \AA}$), primary beam Soller slits (2.5°), divergence slit (1 mm), antiscatter slit (8 mm), a filter of nickel in the diffracted beam. The generator was set at 40 kV and 40 mA. After preliminary acquisitions for qualitative analysis, performed in the $3\text{--}35^\circ$ 2θ range, diffraction data-sets for structure determination were collected up to 105° 2θ , with steps of 0.02° , with an overall scan time of approximately 12 h.

7.1.3. Variable-temperature Powder X-ray Diffraction (VT-PXRD)

To complement the thermogravimetric analyses, the thermal behaviour of **Co-Me₂BPZ·S** and **Zn-Me₂BPZ·S** was investigated *in situ* by variable-temperature powder X-ray diffraction. As a general procedure, using a custom-made sample heater (Officina Elettrotecnica di Tenno, Ponte Arche, Italy), 20-mg samples of as-synthesized compounds were heated in air from 303 K up to decomposition, with steps of 20 K; a PXRD pattern was acquired at each step, covering a sensible low-to-medium-angle 2 θ range. Treating the data acquired before loss of crystallinity by means of whole powder pattern parametric refinements with the Le Bail approach enabled us to disclose the behaviour of the unit cell parameters as a function of the temperature.

7.1.4. Textural Characterization

The textural characterization of M-BPZ and **M-Me₂BPZ·S** (M = Co, Zn) was carried out by Prof. F. J. Maldonado-Hodar's group, University of Granada, Spain.

Specific surface area and pore texture of the M-BPZ and **M-Me₂BPZ** (M = Co, Zn) MOFs were estimated by N₂ and CO₂ adsorption at 77 and 273 K, respectively. Adsorption isotherms were measured by the volumetric method with a Quantachrome Autosorb 1 instrument. Batches of ~50 mg of as-synthesized materials were introduced into pre-weighed analysis tubes and outgassed overnight at 110 °C under high vacuum (10⁻⁶ Torr) before running the adsorption experiments. The two probes we adopted are complementary and allow analysing different ranges of porosity:² CO₂ adsorption is used to assess the narrower microporosity (mean micropore width $L_0 < 0.7$ nm), where N₂ adsorption can be kinetically restricted.³ On the contrary, according to the Gurvitch rule,⁴ the volume of N₂ adsorbed at the relative pressure of 0.95 ($W_{0.95}$) is a measure of both the micro- and mesopore volumes, provided that there are no constrictions at the micropore entrance. Hence, $W_{0.95}$ is considered as the total pore volume, and the volume of N₂ adsorbed within the relative pressure range of 0.40–0.95 is considered as the mesopore volume.⁵ The non-local density functional theory method (NLDFT)^{6,7} was employed to determine the pore size distribution of M-BPZ and **M-Me₂BPZ**, as it was suggested to provide accurate results in MOFs textural characterization.^{8,9} The specific surface areas

were obtained through the BET method by fitting the N₂ adsorption data at low relative pressures ($p/p_0 < 0.35$).¹⁰ The Dubinin-Raduskevich equation^{11,12} (eq. 1) was used to fit both N₂ and CO₂ isotherms:

$$W = W_0 \exp \left[- \left(\frac{A}{\beta E_{ads}} \right)^n \right] \quad \text{eq. 1}$$

where W is the amount of gas absorbed at the relative pressure p/p_0 ; W_0 is the limiting amount filling the micropores; A is the differential molar work given by $A = RT \ln(p_0/p)$; β is the affinity coefficient (0.33 and 0.35 for N₂ and CO₂, respectively); E_{ads} is the characteristic adsorption energy. N₂ and CO₂ molar volumes were taken as 34.65 and 43.01 cm³/mol, respectively. Once E_{ads} was known, the mean micropore width, L_0 , was obtained by applying the Stoeckli equation¹³ (eq. 2):

$$L_0(nm) = \frac{10.8}{E_{ads}(kJ\ mol^{-1}) - 11.4} \quad \text{eq. 2}$$

which is valid for E_{ads} values between 42 and 20 kJ/mol, corresponding to pore widths between 0.35 and 1.3 nm.

7.1.5. Theoretical Calculations

The theoretical calculations were carried out by Dr. Silvia Casassa, University of Turin, Italy.

The Zn-BPZ¹⁴ and **M-Me₂BPZ** MOFs (M = Co, Zn) were characterized by means of *ab initio* calculations performed with the quantum-mechanics code CRYSTAL,^{15,16} which solves the Schrödinger equation for periodic systems in a basis set of localized atomic orbitals. Neglecting the clathrated solvent, the Becke–Lee–Yang–Parr^{17,18} (B3LYP) hybrid functional was adopted to perform the full geometry optimization of the crystal structure and calculate charge density. In the subsequent study of CO₂ diffusion into the channels, for a reliable estimate of the dispersive contributions to the binding energy the D3 a posteriori correction, originally proposed by Grimme¹⁹ and implemented in the CRYSTAL code²⁰ (B3LYP-D3), was exploited. The atoms were described with all electrons basis sets of 6-21* quality,²¹ and the counterpoise method²² was used to correct

the binding energy for the basis set superposition error.²³ The Pack-Monkhorst/Gilat shrinking factors for the k-point sampling of the reciprocal space were set to 4, corresponding to 24 points at which the Hamiltonian matrix was diagonalized. The accuracy of the integral calculations was increased by setting the five tolerances to 7, 7, 7, 10, and 20. The adsorption energy, E_{ads} , was calculated at the B3LYP-D3 level according to eq. 3:

$$E_{ads} = \left[\left(\frac{E(n\text{CO}_2@\text{MOF}) - E(\text{MOF}) - n \times E(\text{CO}_2)}{n} \right) \right] \quad \text{eq. 3}$$

where $E(n\text{CO}_2@\text{MOF})$, $E(\text{MOF})$, and $E(\text{CO}_2)$ are the total energies of the MOF with and without CO_2 , and of carbon dioxide in the gas phase, respectively, and n corresponds to the number of CO_2 molecules *per cell*.^{xxxii} Standard enthalpies, $H(T)$, at 0 and 298 K were calculated as follows:

$$H(T) = E + E_{ZPE} + E_T + P \times V \quad \text{eq. 4}$$

by adding at the pressure *per volume* term the zero-point (E_{ZPE}) and thermal (E_T) energy contributions arising from the analysis of the nuclear motion. The heat of adsorption, $H_{ads}(T)$, was then estimated with the same formula reported in eq. 3 by substituting $E(n\text{CO}_2@\text{MOF})$, $E(\text{MOF})$, $E(\text{CO}_2)$ with $H(n\text{CO}_2@\text{MOF})$, $H(\text{MOF})$, $H(\text{CO}_2)$, respectively. Complete phonon frequencies, at the $k = 0$ Γ point, were computed within the harmonic approximation by diagonalizing the mass-weighted Hessian matrix,²⁴ and the host-guest interactions were characterized by exploiting the potentiality of Bader topological analysis of the electron density,²⁵ as implemented in the TOPOND program²⁶ incorporated in CRYSTAL14.

7.2. M-BPZNO₂

Adapted with permission from “Mosca, N.; Vismara, R.; Fernandes, J. A.; Tuci, G.; Di Nicola, C.; Domasevitch, K. V.; Giacobbe, C.; Giambastiani, G.; Pettinari, C.; Aragonés-Anglada, M.; Moghadam, P. Z.; Fairen-Jimenez, D.; Rossin, A. and Galli, S. (2018). NO₂-Functionalized Bis(Pyrazolate) MOFs as CO₂ Capture Materials at Ambient Conditions. Chemistry - A European Journal. 24(50), 13170-13180.” Copyright © 2018 Wiley-CH Verlag GmbH & Co. KGaA,

^{xxxii} The cell used for the theoretical calculations is half of the crystallographic unit cell, hence it contains one 1-D channel, and is oriented in such a way, with respect to the crystallographic unit cell, that the *a*- and *b*-axes define the walls, not the diagonals, of the 1-D channel.

Weinheim.

All the chemicals and reagents employed were purchased from commercial suppliers and used as received without further purification. 4,4'-Bipyrazole was synthesized according to a previously published procedure.²⁷ IR spectra were recorded as neat from 4000 to 600 cm⁻¹ with a PerkinElmer Spectrum One System instrument. Elemental analyses (C, H, N %) were performed with a Fisons Instruments 1108 CHNS-O elemental analyser. Thermogravimetric analyses were carried out under a N₂ flow (20 mL/min) with a Perkin Pyris 1 thermal analyser with heating rates in the range 5–10 K/min. ¹H NMR spectra were recorded in DMSO-*d*₆ at 500 MHz and 296 K on a Bruker Ascend 500 instrument operating at room temperature. The chemical shifts are reported in ppm with respect to SiMe₄ as the internal standard. PXRD qualitative analyses were carried out with a Bruker D8 Advance diffractometer (see section 8.1.2 for the instrument specifics), acquiring data at room temperature in the 3–35° 2θ range, with steps of 0.02° and time *per* step of 1 s. The nature and purity of all the batches employed for the functional characterization were assessed by elemental analysis, IR spectroscopy and PXRD.

7.2.1. Synthesis and Preliminary Characterization

The synthesis and preliminary analytical characterization of the ligand were carried out by Prof. K. V. Domasevitch, University of Kyiv, Ukraine. The syntheses and preliminary analytical characterization of **M-BPZNO₂·S** were carried out by Prof. C. Pettinari's group, University of Camerino, Italy.

3-Nitro-4,4'-bipyrazole (H₂BPZNO₂). 4,4'-Bipyrazole (2.68 g, 20.0 mmol) was suspended in aqueous H₂SO₄ (90 mL, 91 wt. %, 1.820 g/cm³) and KNO₃ (2.73 g, 27.0 mmol) was added to the suspension, which was placed into an oil bath pre-heated at 368 K and left at that temperature under stirring for 1.5 h. Then, it was cooled down to r.t. and poured onto crushed ice (200 g). While cooling, the clear yellowish solution formed was brought to pH 6-7 with concentrated aqueous ammonia. The yellow precipitate was filtered off and then suspended under stirring in aqueous NaHCO₃ (100 mL, 5 wt. %) for 10-15 min to remove traces of the bis(nitrated) product (sufficiently acidic to react with HCO₃⁻) potentially present. The solid residue was filtered off and recrystallized from hot

water (3.66 g of product in 1 L of water), yielding bright-orange platelets of pure H_2BPZNO_2 . Yield: 68%. Mp = 287 °C. Elem. Anal. Calc. for $\text{C}_6\text{H}_5\text{N}_3\text{O}_2$ (fw = 179.14 g/mol): C, 40.22; H, 2.81; N, 39.10%. Found: C, 40.48; H, 2.90; N, 38.92%. IR (neat, cm^{-1}): 3232–2870 (m, br) [$\nu(\text{N-H}) + (\text{C-H})$], 1612–1540 (s) [$\nu(\text{C=C} + \text{C=N})$], 1513 (s) [$\nu_{\text{asym}}(\text{NO}_2)$], 1406 (s), 1337 (vs) [$\nu_{\text{sym}}(\text{NO}_2)$], 1298 (m), 1208 (w), 1162 (w), 1106 (m) [$\nu(\text{C-N})$], 1077 (m), 1034 (m), 944 (s), 877 (s). ^1H NMR (500 MHz, $\text{DMSO-}d_6$, 296 K, ppm): 7.61 (CH), 7.87 (CH), 8.08 (CH), 12.83 (NH), 13.80 (NH).

Co-BPZNO₂·S. H_2BPZNO_2 (0.0358 g, 0.200 mmol) was dissolved in DMF (8 mL). Then, $\text{Co}(\text{NO}_3)_2 \cdot 6\text{H}_2\text{O}$ (0.0582 g, 0.200 mmol) was added. The mixture was left under stirring in a high-pressure glass tube at 393 K for 48 h, until a brown precipitate was formed. The precipitate was filtered off, washed with hot DMF (2×10 mL) and hot dichloromethane (2×10 mL), and dried under vacuum. Yield: 80%. **Co-BPZNO₂·S** is insoluble in DMSO, alcohols, acetone, CH_3CN , chlorinated solvents and water. Elem. Anal. Calc. for $\text{C}_9\text{H}_{10}\text{CoN}_6\text{O}_3$ (fw = 309.15 g/mol): C, 34.97; H, 3.26; N, 27.18%. Found: C, 34.79; H, 3.44; N, 24.56%. IR (neat, cm^{-1}): 3126, 2928, 2857 (vw) [$\nu(\text{C-H}_{\text{aliphatic}})$], 1672 (vs) [$\nu(\text{C=O})$], 1494 (m) [$\nu(\text{C=C} + \text{C=N})$], 1383 (m), 1333 (s) [$\nu_{\text{symm}}(\text{NO}_2)$], 1259 (m), 1236 (w), 1164 (w), 1096 (s) [$\nu(\text{C-N})$], 1051 (s), 941 (s), 822 (s).

Cu-BPZNO₂·S. H_2BPZNO_2 (0.0358 g, 0.200 mmol) was dissolved in DMF (8 mL). Then, $\text{Cu}(\text{OAc})_2$ (0.0366 g, 0.200 mmol) was added. The mixture was left under stirring in a high-pressure glass tube at 393 K for 24 h, until a brown precipitate appeared. The precipitate was filtered off, washed with hot DMF (2×10 mL) and hot dichloromethane (2×10 mL), and dried under vacuum. Yield: 78%. **Cu-BPZNO₂·S** is insoluble in DMSO, alcohols, acetone, CH_3CN , chlorinated solvents and water. Elem. Anal. Calc. for $\text{C}_3\text{H}_3\text{CuN}_3\text{O}_3$ (fw = 313.76 g/mol): C, 34.45; H, 3.21; N, 26.78%. Found: C, 34.87; H, 3.20; N, 26.72%. IR (neat, cm^{-1}): 3138, 2928, 2864 (vw) [$\nu(\text{C-H}_{\text{aliphatic}})$], 1651 (vs) [$\nu(\text{C=O})$], 1490 (m) [$\nu(\text{C=C} + \text{C=N})$], 1386 (m), 1341 (s) [$\nu_{\text{symm}}(\text{NO}_2)$], 1270 (m), 1200 (w), 1174 (w), 1100 (s) [$\nu(\text{C-N})$], 1054 (s), 943 (s), 823 (s).

Zn-BPZNO₂·S. H_2BPZNO_2 (0.0358 g, 0.200 mmol) was dissolved in DMF (8 mL). Then, $\text{Zn}(\text{OAc})_2 \cdot 2\text{H}_2\text{O}$ (0.0439 g, 0.200 mmol) was added. The mixture was left under stirring in a high-pressure glass tube at 393 K for 24 h, until a yellow precipitate appeared.

The precipitate was filtered off, washed with hot acetone (2×10 mL) and dichloromethane (2×10 mL), and dried under vacuum. Yield: 68%. **Zn-BPZNO₂·S** is insoluble in DMSO, alcohols, acetone, CH₃CN, chlorinated solvents and water. Elem. Anal. Calc. for C₉H₁₀N₆O₃Zn (fw = 315.59 g/mol): C, 34.25; H, 3.19; N, 26.63%. Found: C, 34.67; H, 3.26; N, 26.41%. IR (neat, cm⁻¹): 3129, 2925, 2855 (vw) [ν (C-H_{aliphatic})], 1670 (vs) [ν (C=O)], 1503 (s) [ν (C=C + C=N)], 1385 (s), 1345 (s) [ν_{symm} (NO₂)], 1272 (s), 1196 (w), 1170 (w), 1104 (s) [ν (C-N)], 1060 (s), 943 (s), 829 (s).

7.2.2. Powder X-ray Diffraction Structural Characterization

Microcrystalline powders of **Co-BPZNO₂·S**, **Cu-BPZNO₂·S** and **Zn-BPZNO₂·S** were deposited in the hollow of a silicon zero- background plate 0.2 mm deep (supplied by Assing Srl, Monterotondo, Italy). Data acquisitions were performed on the vertical-scan Bruker AXS D8 Advance θ : θ diffractometer described in section 8.2.1. The generator was set at 40 kV and 40 mA. After preliminary acquisitions for qualitative analysis, performed in the 3–35° 2 θ range, diffraction data sets for a full structure characterization were collected from 5° up to 105° 2 θ with steps of 0.02°, with an overall scan time of approximately 12 hours.

7.2.3. Variable-temperature Powder X-ray Diffraction (VT-PXRD)

As a complement of the thermogravimetric analyses, the thermal behaviour of the three MOFs was investigated *in situ* by variable-temperature powder X-ray diffraction. As a general procedure, using a custom-made sample heater (Officina Elettrotecnica di Tenno, Ponte Arche, Italy), 20-mg samples of the as-synthesized compounds were heated in air from 303 K up to decomposition, with steps of 20 K; a PXRD pattern was acquired at each step, covering a sensible low-to-medium-angle 2 θ range. Whole powder pattern parametric refinements with the Le Bail approach on the data acquired before loss of crystallinity disclosed the behaviour of the unit cell parameters as a function of the temperature.

7.2.4. Textural Characterization

The textural characterization was carried out by Dr. A. Rossin's group, ICCOM-CNR, Sesto Fiorentino, Italy.

The Brunauer–Emmett–Teller (BET) specific surface area (SSA) and porosity were estimated by volumetric adsorption with an ASAP 2020 Micromeritics instrument, using N₂ as adsorbent at 77 K. The materials porosity was determined on the basis of the BJH method (Halsey thickness equation) for the mesopores and with the NLDFT (cylinder-like pore shape typical of inorganic oxide materials) for the micropores. The micropore area was evaluated through the *t*-plot method with the Harkins and Jura thickness equation. All the samples were activated at 403 K under high vacuum (10⁻⁶ Torr) for 24 h before each measurement. CO₂ adsorption isotherms were recorded at 195, 273 and 298 K at a maximum pressure of 1.2 bar, while the N₂ adsorption isotherm for the determination of the CO₂/N₂ selectivity was recorded at 298 K and up to 1.2 bar. The isosteric heat of adsorption (*Q*_{st}) of CO₂ on **Zn-BPZNO₂** was calculated as the arithmetic mean value of the three values coming from pairs of isotherm datasets (195 K / 273 K – 273 K / 298 K – 195 K / 298 K) applying, for each pair, a variant of the Clausius-Clapeyron equation (eq. 5):^{28,29}

$$\ln\left(\frac{P_1}{P_2}\right) = Q_{st} \times \frac{T_2 - T_1}{R \times T_1 \times T_2} \quad \text{eq. 5}$$

where P_n ($n = 1$ or 2) is the pressure value for isotherm n ; T_n ($n = 1$ or 2) is the temperature value for isotherm n ; R is the gas constant (8.314 J K⁻¹ mol⁻¹). The CO₂/N₂ selectivity at 298 K based on the Henry method was calculated as the ratio of the initial slopes of the adsorption isotherms. The IAST selectivity for an equimolar CO₂/N₂ mixture at a total pressure of 1 bar was determined as the ratio of the (adsorbed) molar fractions of the two gases³⁰ as derived from the application of the free software pyIAST (<https://github.com/CorySimon/pyIAST>) to the experimental N₂ and CO₂ isotherms of **Zn-BPZNO₂** collected at 298 K. A Henry (N₂) and a BET (CO₂) model were employed for the isotherm fitting, with RMS = 0.011 ($K_H = 0.624$) and 0.006 ($K_b = 0.199$; $K_a =$

2.312; $M = 4.722$) respectively. For a detailed explanation of these parameters, see the pyI^{AST} webpage and documentation.

7.2.5. High-resolution Powder X-ray Diffraction

HR-PXRD *in situ* and *operando* measurements were performed at the ID22 beamline of the European Synchrotron Radiation Facility (Grenoble, France) by using the gas handling system described in ref. 31. A sample of **Zn-BPZNO₂·S** was preliminarily activated at 403 K under vacuum (10^{-3} Torr) for 24 h. After light grinding with agate mortar and pestle, it was introduced into a 0.5 mm diameter borosilicate glass capillary and kept in place by glass wool. After alignment, the capillary was connected to the gas handling system and the sample was further activated at 403 K under high vacuum (10^{-6} Torr) for 1 h. HR-PXRD data were acquired at 298 K before and during CO₂ loading in the pressure range 1-5 bar, working at 27.5 keV (0.451 Å, calibrated with the Si NIST standard SRM 640c at room temperature), with a beam size of 1×1 mm² defined by water-cooled slits and monochromated by a cryogenically-cooled Si 111 channel-cut crystal. A bank of nine detectors, each preceded by a Si 111 analyser crystal, was scanned vertically to measure the diffracted intensity.

7.2.6. Computational Details

The Theoretical calculations were carried out by Dr. P. Moghadam's group, University of Cambridge, United Kingdom.

Grand Canonical Monte Carlo (GCMC) simulations were employed to obtain N₂ and CO₂ adsorption isotherms at 77 K and 298 K, respectively. The simulations were based on a model that includes Lennard-Jones (LJ) interactions for the guest-guest and guest-host interactions. The LJ potential parameters for the framework atoms were taken from the Universal Force Field (UFF).³² The interactions involving N₂ and CO₂ were described by the TraPPE force field.³³ An atomistic representation was used for the MOF, starting from its PXRD crystal structures. The simulation cell consisted of 24 (2×3×4) unit cells with a LJ cut-off radius of 12.8 Å and no tail corrections. For CO₂, the long-range electrostatic interactions were handled by the Ewald summation technique. Periodic

boundary conditions were applied in all three dimensions. For each state point, GCMC simulations consisted of 20,000 Monte Carlo cycles to guarantee equilibration, followed by 20,000 production cycles to calculate the ensemble averages. All simulations included insertion/deletion, translation and rotation moves with equal probabilities. Radial distribution functions were obtained by recording the distances between designated pair of atoms for every production cycle. GCMC simulations were run on two models, namely: the orthorhombic and tetragonal crystal structures obtained from PXRD; the unit cells were then subject to geometry optimization based on molecular mechanics, modifying the atomic coordinates but not the unit cell parameters. These calculations were performed with the Forcite module of Materials Studio, using an algorithm that is a cascade of the steepest descent, adjusted basis set Newton–Raphson, and quasi-Newton methods.³⁴⁻³⁶ The bonding and the short-range (van der Waals) interactions between atoms were modelled using UFF. A cut-off distance of 18.5 Å was used for the van der Waals interactions during the geometry optimization.

7.3. M-BPZNH₂

Reproduced and adapted with permission from “R. Vismara, G. Tuci, N. Mosca, K. V. Domasevitch, C. Di Nicola, C. Pettinari, G. Giambastiani, S. Galli and A. Rossin, Inorg. Chem. Front., 2019, 6, 533”. - Reproduced by permission of The Royal Society of Chemistry.

3-Nitro-4,4'-bipyrazole was synthesized as reported previously.³⁷ All the chemicals and reagents employed in the syntheses were purchased from commercial suppliers and used as received without further purification, while the epoxides used in the catalytic tests were distilled prior to use and stored over 4 Å molecular sieves under nitrogen. The RANEY® 2800 nickel (Ni-Re) slurry in 2-propanol was obtained by repeated decantation of the commercially available water slurry (Aldrich) after the addition of 2-propanol. IR spectra were recorded as neat from 4000 to 600 cm⁻¹ with a PerkinElmer Spectrum One System instrument. Elemental analyses (C, H, N %) were performed with a Fisons Instruments 1108 CHNS-O elemental analyser. The ¹H NMR spectrum of 3-amino-4,4'-bipyrazole was recorded in DMSO-*d*₆ on a Bruker Ascend 500 instrument operating at 500 MHz and 296 K. The chemical shifts are reported in parts *per* million and referred to SiMe₄ as internal standard. Thermogravimetric analyses were carried out

under a N₂ flow with a Perkin Pyris 1 thermal analyser or with a Mettler Toledo TGA 2 Star System with a heating rate of 5 or 10 K min⁻¹. Powder X-ray diffraction (PXRD) qualitative analysis was carried out with a Bruker AXS D8 Advance diffractometer (see section 8.2.1 for the instrument specifics), acquiring data at room temperature in the 4–35° 2θ range, with steps of 0.02°, and time *per* step of 1 s. The nature and purity of all the batches employed for the functional characterization were assessed by elemental analysis, IR spectroscopy and PXRD. GC/MS analyses of the reaction mixtures after the catalytic runs were performed on a Shimadzu QP2010S apparatus equipped with a flame ionization detector and a Supelco SPB-1 fused-silica capillary column (30 m length, 0.25 mm internal diameter, 0.25 μm film thickness).

7.3.1. Synthesis and Preliminary Characterization

The synthesis and preliminary analytical characterization of the ligand were carried out by Prof. K. V. Domasevitch, University of Kyiv, Ukraine. The syntheses and preliminary analytical characterization of **M-BPZNH₂·S** were carried out by Prof. C. Pettinari's group, University of Camerino, Italy.

3-Amino-4,4'-bipyrazole (H₂BPZNH₂). 3-Nitro-4,4'-bipyrazole (6.00 g, 33.5 mmol) was suspended in 2-propanol (400 mL) and heated at 333 K. A Ni-Re slurry in 2-propanol (2 mL) was added. Then, a solution of hydrazine hydrate (14.5 mL, 300 mmol) in 2-propanol (55 mL) was added dropwise over 14 h at 333 K under vigorous stirring. Every 2 h, a new aliquot (2 mL) of the Ni-Re slurry was added. After 7 h, complete dissolution of the starting nitro-functionalized ligand occurred, followed by a gradual colour fading of the reaction mixture during the next 7 h. After the reaction completion, the mixture was filtered hot to remove the catalyst and the solid was thoroughly washed with boiling 2-propanol (400 mL) to recover product traces. The colourless mother liquor and washing solvent were combined and evaporated under reduced pressure to a volume of 80–100 mL and cooled to 273 K. Colourless crystals of 3-amino-4,4'-bipyrazole were formed. The crystals were filtered and washed with cold 2-propanol (5 mL). The single-crystal X-ray diffraction data acquisition and treatment as well as the crystal and molecular structure of H₂BPZNH₂ are described in detail in the Electronic Supplementary

Information of ref. 37. Pure bulk H_2BPZNH_2 was obtained by recrystallization from hot water, yielding a white powder. Yield: 88%. H_2BPZNH_2 sublimes above 503 K; $\text{Mp} = 560$ K. Elem. Anal. Calc. for $\text{C}_6\text{H}_7\text{N}_5$ (fw = 149.15 g mol⁻¹): C, 48.31; H, 4.73; N, 46.96%. Found: C, 48.07; H, 4.67; N, 47.22%. IR (neat, cm⁻¹): 3404–2920 (m, br) [$\nu(\text{N-H}) + (\text{C-H})$], 1619–1594 (m) [$\nu(\text{C=C} + \text{C=N})$], 1512 (m), 1474 (vs), 1393 (w), 1371 (vs), 1349 (s), 1294 (w), 1212 (m), 1153 (s), 1115 (w) [$\nu(\text{C-N})$], 1057 (m), 1035 (m), 948 (s), 860 (vs). ¹H NMR (500 MHz, DMSO-*d*₆, 296 K, ppm): 4.56 s (2H, NH₂), 7.52 s (1H, CH), 7.74 s (2H, CH), 12.08 s br (2H, NH).

Ni-BPZNH₂·S. H_2BPZNH_2 (0.0298 g, 0.200 mmol) was dissolved in DMF (8 mL) at 333 K. Then, $\text{Ni}(\text{CH}_3\text{COO})_2 \cdot 4\text{H}_2\text{O}$ (0.0496 g, 0.200 mmol) was added. The mixture was reacted at reflux for 5 h. After cooling the mixture to room temperature, the brick-red solid was collected by filtration, washed with methanol (3 × 10 mL) and dried under vacuum. Yield: 81%. **Ni-BPZNH₂·S** is insoluble in DMSO, alcohols, acetone, CH_3CN , chlorinated solvents, and water. Elem. Anal. Calc. for $\text{C}_9\text{H}_{12}\text{NiN}_6\text{O}$ (fw = 278.92 g mol⁻¹): C, 38.75; H, 4.34; N, 30.13%. Found: C, 38.63; H, 4.36; N, 30.18%. IR (neat, cm⁻¹): 3313–3208 (m) [$\nu(\text{N-H})$], 2925 (w) [$\nu(\text{C-H}_{\text{aromatic}}) + (\text{C-H}_{\text{aliphatic}})$], 1657 (s) [$\nu(\text{C=O})$], 1513 (s) [$\nu(\text{C=C} + \text{C=N})$], 1387 (s), 1292 (m), 1211 (vw), 1140 (s), 1097 (m), 1065 (s), 951 (vs), 819 (vs). **Ni-BPZNH₂·S** can also be isolated in the form of a brick-red powder through a solvothermal synthesis in DMF at 393 K for 48 h, starting from $\text{Ni}(\text{CH}_3\text{COO})_2 \cdot 4\text{H}_2\text{O}$.

Cu-BPZNH₂·S. H_2BPZNH_2 (0.0298 g, 0.200 mmol) was dissolved in DMF (8 mL). Then, $\text{Cu}(\text{CH}_3\text{COO})_2$ (0.0366 g, 0.200 mmol) was added. The mixture was left under stirring in a high-pressure glass tube at 393 K for 48 h, until a brown precipitate appeared. The precipitate was filtered off, washed with hot acetone (2 × 10 mL) and dried under vacuum. Yield: 78%. **Cu-BPZNH₂·S** is insoluble in DMSO, alcohols, acetone, CH_3CN , chlorinated solvents and water. Elem. Anal. Calc. for $\text{C}_9\text{H}_{12}\text{CuN}_6\text{O}$ (fw = 283.76 g mol⁻¹): C, 38.09; H, 4.26; N, 29.61%. Found: C, 37.95; H, 4.24; N, 29.70%. IR (neat, cm⁻¹): 3320 (m) [$\nu(\text{N-H})$], 2927–2858 (w) [$\nu(\text{C-H}_{\text{aromatic}}) + (\text{C-H}_{\text{aliphatic}})$], 1647 (vs) [$\nu(\text{C=O})$], 1497 (s) [$\nu(\text{C=C} + \text{C=N})$], 1433 (w), 1385 (s), 1279 (m), 1252 (w), 1200 (vw), 1126 (s), 1093 (s), 1056 (s), 947 (s), 827 (s).

Zn-BPZNH₂·S. H₂BPZNH₂ (0.0298 g, 0.200 mmol) was dissolved in water (8 mL). Then, Zn(CH₃COO)₂·2H₂O (0.0438 g, 0.200 mmol) was added. The mixture was left under stirring at room temperature for 24 h. After that time, the white precipitate formed was filtered off, washed with hot DMF (2 × 10 mL) and dried under vacuum. Yield: 86%. **Zn-BPZNH₂·S** is insoluble in DMSO, alcohols, acetone, CH₃CN, chlorinated solvents and water. Elem. Anal. Calc. for C₉H₁₂N₆OZn (fw = 285.61 g mol⁻¹): C, 37.85; H, 4.23; N, 29.42%. Found: C, 37.71; H, 4.21; N, 29.55%. IR (neat, cm⁻¹): 3330 (m) [ν(N-H)], 3095–2927 (w) [ν(C-H_{aromatic}) + (C-H_{aliphatic})], 1662 (vs) [ν(C=O)], 1622 (m), 1508 (s) [ν(C=C + C=N)], 1436 (m), 1385 (s), 1282 (m), 1255 (w), 1209 (w), 1133 (s), 1092 (m), 1014 (m), 976 (vs), 830 (s). **Zn-BPZNH₂·S** can also be obtained in the form of a white powder through a solvothermal synthesis (in a Teflon-lined stainless steel autoclave under autogenous pressure) in DMF at 393 K for 48 h, starting from Zn(CH₃COO)₂·2H₂O.

7.3.2. Powder X-ray Diffraction Structural Characterization

Microcrystalline powders of **Ni-BPZNH₂·S**, **Cu-BPZNH₂·S** and **Zn-BPZNH₂·S** were deposited in the hollow of a silicon zero-background plate 0.2 mm deep (Assing Srl, Monterotondo, Italy). Data acquisitions were performed on the vertical-scan Bruker AXS D8 Advance θ : θ diffractometer described in section 8.2.1. The generator was set at 40 kV and 40 mA. After preliminary acquisitions for qualitative analysis, performed in the 4–35° 2 θ range, diffraction data sets for a full structure characterization were collected from 5° up to 105° 2 θ , with steps of 0.02°, with an overall scan time of approximately 12 hours.

7.3.3. Water Vapour Stability

To monitor the stability of **Zn-BPZNH₂·S** towards water vapour, 15 mg of sample were deposited in the hollow of an aluminium sample-holder. Preliminary PXRD data were acquired in the 9–34° (2 θ) range. Then, the sample holder was introduced into an air-tight water-vapor saturated cell. At different time points, the sample was checked by PXRD, adopting the same conditions employed for the preliminary acquisition.

7.3.4. Textural Characterization

The textural characterization was carried out by Dr. A. Rossin's group, ICCOM-CNR, Sesto Fiorentino, Italy.

All the samples were activated at 403 K under high vacuum (10^{-6} Torr) for 24 h before each measurement. The BET SSAs and porosity were estimated by volumetric adsorption with an ASAP 2020 Micromeritics instrument, using N_2 as an adsorbent at 77 K. The material porosity was determined based on the BJH method (Halsey thickness equation) for the mesopores and on the NLDFT (cylinder-like pore shape typical of inorganic oxide materials) for the micropores. The micropore area was evaluated through the t -plot method with the Harkins and Jura thickness equation. CO_2 adsorption isotherms were recorded at 273 and 298 K at a maximum pressure of 1.2 bar, while the N_2 adsorption isotherm for the determination of the CO_2/N_2 selectivity was recorded at 298 K and up to 1.2 bar. The isosteric heat of adsorption (Q_{st}) was calculated from the CO_2 isotherms measured at 273 and 298 K according to a variant of the Clausius–Clapeyron equation (see eq. 5). The CO_2/N_2 selectivity at 298 K was calculated based on the Henry method as the ratio of the initial slopes of the adsorption isotherms. The IAST selectivity for an equimolar CO_2/N_2 mixture at a total pressure of 1 bar was determined as the ratio of the (adsorbed) molar fractions of the two gases,³¹ as derived from the application of the free software pyIAST to the experimental N_2 and CO_2 isotherms of **Zn-BPZNH₂** collected at 298 K. A quadratic (CO_2) and a Henry (N_2) model were employed for the isotherm fitting, with root mean square deviation = 0.017 ($K_a = 2.59$; $K_b = 2.29$; $M = 2.51$) and 0.004 ($K_H = 0.371$), respectively.

7.3.5. Catalytic CO_2 Epoxidation with **Zn-BPZNH₂**

The catalytic tests were carried out by Dr. A. Rossin's group, ICCOM-CNR, Sesto Fiorentino, Italy.

Before the catalytic trials, **Zn-BPZNH₂** was activated at 403 K under high vacuum (10^{-6} Torr) for 24 h and then stored under an inert atmosphere. The MOF catalyst (0.05 mmol) and the epoxide substrate (10 mmol) were placed in a Teflon sample holder inside a stainless-steel reactor under an inert atmosphere. The reactor was then pressurized with

CO₂ and kept at the chosen temperature for 24 h under stirring. CO₂ was continuously fed to maintain the reactor pressure constant. At the end of the reaction, the reactor was cooled in an ice/water bath and bis(2-chloroethyl)ether (10 mmol) was added to the mixture as internal standard. The as-obtained suspension was finally filtered over a Celite pad and analysed by gas chromatography. For the recycling tests, after the first catalytic run the supernatant liquid was carefully removed under an inert atmosphere. The solid catalyst was washed with dry and degassed acetone (3 × 5 mL) and it was then dried under vacuum for 1 h to remove all volatile compounds before re-using it for further catalytic cycles.

7.4. Zn-BPZ(NH₂)₂

All the chemicals and reagents employed were purchased from commercial suppliers and used as received without further purification. IR spectra were recorded as neat from 4000 to 600 cm⁻¹ with a PerkinElmer Spectrum One System instrument. Elemental analyses (C, H, N %) were performed with a Fisons Instruments 1108 CHNS-O elemental analyser. The nature and purity of all the batches employed for the functional characterization were assessed by elemental analysis, IR spectroscopy and PXRD.

7.4.1. Synthesis and Preliminary Characterization

The synthesis and preliminary analytical characterization of the ligand were carried out by Prof. K. V. Domasevitch, University of Kyiv, Ukraine. The syntheses and preliminary analytical characterization of **Zn-BPZ(NH₂)₂·S** were carried out by Prof. C. Pettinari's group, University of Camerino, Italy.

Zn-BPZ(NH₂)₂·S. H₂BPZ(NH₂)₂ (0.0328 g, 0.200 mmol) was dissolved in DMF (15 mL). Then, Zn(CH₃COO)₂·2H₂O (0.0438 g, 0.200 mmol) was added. The mixture was left under stirring at 120 °C for 8 h, until a white precipitate was formed. The white precipitate was filtered off, washed with hot DMF (2 × 10 mL) and dried under vacuum. Yield: 83%. **Zn-BPZ(NH₂)₂·S** is insoluble in DMSO, alcohols, acetone, CH₃CN, chlorinated solvents and water. Elem. Anal. Calc. for C₉H₁₃N₇OZn (fw = 300.63 g mol⁻¹): C, 35.96; H, 4.36; N, 32.61%. Found: C, 35.92; H, 4.34; N, 32.60%. IR (neat, cm⁻¹):

3330 (m) [$\nu(\text{N-H})$], 3095–2927 (w) [$\nu(\text{C-H}_{\text{aromatic}}) + (\text{C-H}_{\text{aliphatic}})$], 1662 (vs), 1657 (s) [$\nu(\text{C=O})$], 1508 (s) [$\nu(\text{C=C} + \text{C=N})$], 1436 (m), 1385 (s), 1282 (m), 1255 (w), 1209 (w), 1133 (s), 1092 (m), 1014 (m), 976 (vs), 830 (s).

7.4.2. Powder X-ray Diffraction Structural Characterization

Microcrystalline powders of **Zn-BPZ(NH₂)₂·S** were deposited in the hollow of a silicon zero-background plate 0.2 mm deep (Assing Srl, Monterotondo, Italy). Data acquisitions were performed on the vertical-scan Bruker AXS D8 Advance θ : θ diffractometer described in section 8.2.1. The generator was set at 40 kV and 40 mA. After a preliminary acquisition for qualitative analysis, performed in the 4–35° 2θ range, diffraction data for a full structure characterization were collected from 5° up to 105° 2θ , with steps of 0.02°, with an overall scan time of approximately 12 hours.

7.4.3. Variable-temperature Powder X-ray Diffraction

The thermal behaviour of **Zn-BPZ(NH₂)₂·S** was investigated *in situ* by variable-temperature powder X-ray diffraction. As a general procedure, using a custom-made sample heater (Officina Elettrotecnica di Tenno, Ponte Arche, Italy), 20 mg samples of the as-synthesized compounds were heated in air from 303 K until decomposition, with steps of 20 K; a PXRD pattern was acquired at each step, covering a sensible low-to-medium-angle 2θ range. Whole powder pattern parametric refinements with the Le Bail approach on the data acquired before loss of crystallinity disclosed the behaviour of the unit cell parameters as a function of temperature.

7.4.4. Gas-chromatography

These experiments were performed by the Ph. D. candidate at the University of Granada, Spain, under the supervision of Prof. J. A. R. Navarro.

C₆H₁₄ adsorption at zero coverage was studied using the pulse chromatographic technique, with Varian 450-gc fid gas chromatograph (Bruker) and steel column (length ~15 cm, $\varnothing_{\text{int}} = 0.4$ cm) packed with ~400 mg of **Zn-BPZ(NH₂)₂**. Prior to measurement, the material was activated overnight at 443 K in a He flow (20 mL min⁻¹). Reactivation

was also performed after each gas pulse. The different C₆H₁₄ isomers were injected separately in order to unveil their retention time. The zero-coverage thermodynamic parameters of the adsorption process were calculated using a van't Hoff type analysis employing isothermal chromatographic measurements.³⁸ The volume expansion of the gas entering the capillary at the different temperatures was taken into account and, consequently, the retention volumes corrected according to eq. 6:

$$V_N = (t_R - t_m) \times F_a \times \left(\frac{T}{T_a}\right) \times j \quad \text{eq. 6}$$

Where V_N is the net retention volume (mL); t_R is the retention time (min); t_m is the dead time (min); F_a are the volumetric flow-rate measures at ambient temperature (mL min⁻¹); T is the column temperature (K); T_a is ambient temperature (K); the James–Martin gas compressibility correction³⁹ j is defined as in eq. 7:

$$j = \frac{3\left(\frac{p_i}{p_0}\right)^2 - 1}{2\left(\frac{p_i}{p_0}\right)^3 - 1} \quad \text{eq. 7}$$

where p_i is the inlet pressure of gas and p_0 is the pressure of gas at the outlet. Once these corrections were applied, the van't Hoff plot of the volume equation, eq. 8:

$$V_N = \ln(RTn_s) + \frac{\Delta S}{R} - \frac{\Delta H_{diff}}{RT} \quad \text{eq. 8}$$

was used to calculate the thermodynamic parameters of each analyte, taking into account that the term $\ln(RTn_s)$ is usually small and can be neglected in the determination of ΔS . In addition to the ΔH_{diff} value obtained from the van't Hoff plot, the isosteric heat of adsorption (ΔH_{iso}) was also determined according to the relation $|\Delta H_{iso}| = |\Delta H_{diff}| + RT_{average}$. The α_{hex} partition coefficients were calculated from the ratios of V_N for each gas at 423 K.

7.4.5. Molecular Simulations

These calculations were performed by the Ph. D. candidate at the University of Granada, Spain, under the supervision of Prof. J. A. R. Navarro.

In order to localize the position of the alkane isomers within the MOF porosity, the Adsorption Locator module in the Materials Studio 6.0 software³⁴ was employed to perform MC simulations. The used forcefield was COMPASS, the charge was forcefield assigned and the summation methods were group- and atom-based. Monte Carlo simulations yielded the most stable conformation of the C₆H₁₄ within **Zn-BPZ(NH₂)₂**.

7.5. Zn-MIXMOFs

Adapted with permission from “Vismara, R.; Tuci, G.; Tombesi, A.; Domasevitch, K.; Di Nicola, C.; Giambastiani, G.; Chierotti, M.; Bordignon, S.; Gobetto, R.; Pettinari, C.; Rossin, A. and Galli, S. Tuning carbon dioxide adsorption affinity of zinc(II) MOFs by mixing bis(pyrazolate) ligands with N-containing tags. ACS Applied Materials & Interfaces, 2019, 11, 26956–26969.”. Copyright © (2019) American Chemical Society.

All the chemicals and reagents employed were purchased from commercial suppliers and used as received without further purification. 4,4'-Bipyrazole,²⁷ 3-nitro-4,4'-bipyrazole,³⁷ 3-amino-4,4'-bipyrazole,⁴⁰ Zn-BPZ,¹⁵ **Zn-BPZNO₂**³⁷ and **Zn-BPZNH₂**⁴⁰ were synthesized according to previously published procedures. IR spectra were recorded as neat from 4000 to 600 cm⁻¹ with a PerkinElmer Spectrum One System instrument. Elemental analyses (C, H, N %) were performed with a Fisons Instruments 1108 CHNS-O elemental analyser. Thermogravimetric analysis and differential scanning calorimetry were carried out simultaneously using a NETZSCH STA 409 PC instrument. 10 mg of as-synthesised samples were placed in alumina crucibles; the temperature programme ranged from 303 to 1173 K with a heating rate of 10 K min⁻¹ and under a N₂ flow (40 mL min⁻¹). Raw data from TGA and DSC were corrected based on a background curve. PXRD qualitative analyses were carried out with a Bruker AXS D8 Advance diffractometer (see section 8.2.1 for the instrument specifics), acquiring data at room temperature in the 4.0–35.0° 2θ range, with steps of 0.02°, and time *per* step of 1 s. The nature and purity of all the batches employed for the thermal, NMR and functional characterization were assessed by elemental analysis, IR spectroscopy and PXRD. FIB-

SEM (Focused Ion Beam-Scanning Electron Microscope) analysis was carried out with a Gaia 3 microscope (Tescan s.r.o, Brno, Czech Republic) on samples previously coated with gold. The electron beam used for SEM imaging had a voltage of 20 kV, operated in high-vacuum mode and with secondary electron (SE) detector.

7.5.1. Synthesis and Preliminary Characterization

The synthesis and preliminary analytical characterization of the ligands were carried out by Prof. K. V. Domasevitch, University of Kyiv, Ukraine. The syntheses and preliminary analytical characterization (but the simultaneous thermal analyses) of the MIXMOFs were carried out by Prof. C. Pettinari's group, University of Camerino, Italy.

Zn-H/NO₂·S [**Zn(BPZ)_x(BPZNO₂)_{1-x}·S**]. H₂BPZNO₂ (0.036 g, 0.20 mmol) and H₂BPZ (0.027 g, 0.20 mmol) were dissolved in DMF (10 mL). Then, Zn(OAc)₂·2H₂O (0.088 g, 0.40 mmol) (OAc = acetate) was added and the mixture was left under stirring in a high-pressure glass tube at 393 K for 24 h, until a yellow precipitate appeared. The precipitate was filtered off, washed with hot acetone (2 × 10 mL) and dichloromethane (2 × 10 mL), and dried under vacuum. Yield: 74%. **Zn-H/NO₂·S** is insoluble in DMSO, alcohols, acetone, CH₃CN, chlorinated solvents and water. Elemental analysis calculated for Zn(BPZ)_{0.64}(BPZNO₂)_{0.36}·0.75(DMF) (fw = 268.5 g/mol): C, 36.90; H, 3.34; N, 26.66%. Found: C, 36.79; H, 3.51; N, 26.29%. IR (neat, cm⁻¹): 3130, 3098 (vw) [ν(C-H)], 2927 (vw) [ν(C-H)_{DMF}], 1667 (s) [ν(C=O)_{DMF}], 1504 (s) [ν(C=C + C=N)], 1386 (s), 1346 (s) [ν_{sym}(NO₂)], 1267 (s), 1196 (w), 1170 (w), 1104 (s) [ν(C-N)], 1059 (s), 943 (s), 918 (s), 856 (s), 829 (s), 637 (s).

Zn-H/NH₂·S [**Zn(BPZ)_x(BPZNH₂)_{1-x}·S**]. H₂BPZNH₂ (0.074 g, 0.50 mmol) and H₂BPZ (0.067 g, 0.50 mmol) were dissolved in DMF (10 mL). Then, Zn(OAc)₂·2H₂O (0.219 g, 1.00 mmol) was added and the mixture was left under stirring in a high-pressure glass tube at 393 K for 3 h, until a white precipitate appeared. The precipitate was filtered off, washed with hot acetone (2 × 10 mL) and dichloromethane (2 × 10 mL), and dried under vacuum. Yield: 81%. **Zn-H/NH₂·S** is insoluble in DMSO, alcohols, acetone, CH₃CN, chlorinated solvents and water. Elemental analysis calculated for Zn(BPZ)_{0.56}(BPZNH₂)_{0.44}·(DMF) (fw = 277.2 g/mol): C, 38.99; H, 4.16; N, 27.49%.

Found: C, 38.87; H, 4.17; N, 27.70%. IR (neat, cm^{-1}): 3390 (m), 3317 (m) [$\nu(\text{N-H})$], 3095 (vw) [$\nu(\text{C-H})$], 2930 (vw) [$\nu(\text{C-H})_{\text{DMF}}$], 1658 (vs) [$\nu(\text{C=O})_{\text{DMF}}$], 1507 (s) [$\nu(\text{C=C} + \text{C=N})$], 1435 (m), 1385 (s), 1265 (s), 1168 (m), 1133 (m), 1091 (s) [$\nu(\text{C-N})$], 1058 (s), 1016 (m), 949 (s), 917 (s), 842 (m).

Zn-NO₂/NH₂·S [Zn(BPZNO₂)_x(BPZNH₂)_{1-x}·S]. H₂BPZNH₂ (0.075 g, 0.50 mmol) and H₂BPZNO₂ (0.089 g, 0.50 mmol) were dissolved in DMF (20 mL). Then, Zn(OAc)₂·2H₂O (0.219 g, 1.00 mmol) was added and the mixture was left under stirring in a high-pressure glass tube at 393 K for 3 h, until a yellow precipitate appeared. The precipitate was filtered off, washed with DMF (2 × 10 mL) and dried under vacuum. Yield: 78%. **Zn-NO₂/NH₂·S** is insoluble in DMSO, alcohols, acetone, CH₃CN, chlorinated solvents and water. Elemental analysis calculated for Zn(BPZNO₂)_{0.34}(BPZNH₂)_{0.66}·0.85(DMF) (fw = 284.9 g/mol): C, 36.04; H, 3.64; N, 28.77%. Found: C, 36.10; H, 3.74; N, 28.82%. IR (neat, cm^{-1}): 3390 (w), 3314 (w) [$\nu(\text{N-H})$], 3098 (w) [$\nu(\text{C-H})$], 2927 (w) [$\nu(\text{C-H})_{\text{DMF}}$], 2871 (w), 1656 (vs) [$\nu(\text{C=O})_{\text{DMF}}$], 1505 (s) [$\nu(\text{C=C} + \text{C=N})$], 1434 (m), 1384 (s), 1346 (s) [$\nu_{\text{sym}}(\text{NO}_2)$], 1273 (s), 1169 (m), 1132 (m), 1091 (s) [$\nu(\text{C-N})$], 1058 (s), 1012 (m), 943 (s), 917 (m), 842 (m), 827 (m), 657 (m).

Zn-H/NO₂/NH₂·S [Zn-(BPZ)_x(BPZNO₂)_y(BPZNH₂)_{1-x-y}·S]. H₂BPZ (0.045 g, 0.33 mmol), H₂BPZNH₂ (0.050 g, 0.33 mmol) and H₂BPZNO₂ (0.060 g, 0.33 mmol) were dissolved in DMF (20 mL). Then, Zn(OAc)₂·2H₂O (0.219 g, 1.00 mmol) was added and the mixture was left under stirring in a high-pressure glass tube at 393 K for 3 h, until a yellow precipitate appeared. The precipitate was filtered off, washed with DMF (2 × 10 mL) and dried under vacuum. Yield: 75%. **Zn-H/NO₂/NH₂·S** is insoluble in DMSO, alcohols, acetone, CH₃CN, chlorinated solvents and water. Elemental analysis calculated for Zn(BPZ)_{0.49}(BPZNO₂)_{0.28}(BPZNH₂)_{0.23}·0.75(DMF) (FW = 268.4 g/mol): C, 36.92; H, 3.46; N, 27.46%. Found: C, 36.98; H, 3.85; N, 27.23%. IR (neat, cm^{-1}): 3394 (w), 3316 (w) [$\nu(\text{N-H})$], 3098 (w) [$\nu(\text{C-H})$], 2928 (w) [$\nu(\text{C-H})_{\text{DMF}}$], 2868 (w), 1656 (vs) [$\nu(\text{C=O})_{\text{DMF}}$], 1505 (s) [$\nu(\text{C=C} + \text{C=N})$], 1434 (m), 1384 (s), 1346 (m) [$\nu_{\text{sym}}(\text{NO}_2)$], 1265 (m), 1168 (m), 1133 (m), 1090 (m) [$\nu(\text{C-N})$], 1056 (s), 1013 (m), 943 (m), 917 (m), 845 (m), 828 (m), 657 (m).

7.5.2. Powder X-ray Diffraction Structural Characterization

Microcrystalline powders of the four MIXMOFs were deposited in the hollow of a silicon zero-background plate 0.2 mm deep (supplied by Assing Srl, Monterotondo, Italy). Data acquisitions of **Zn-H/NO₂·S** and **Zn-H/NO₂/NH₂·S** were performed on the vertical-scan Bruker AXS D8 Advance θ : θ diffractometer described in section 8.2.1. The generator was set at 40 kV and 40 mA. Data acquisitions of **Zn-H/NH₂·S** and **Zn-NO₂/NH₂·S** were performed on a vertical-scan Rigaku Miniflex θ : 2θ diffractometer, equipped with a Dtex linear position-sensitive detector, an X-ray tube (Cu K α , $\lambda = 1.5418$ Å), a filter of nickel in the diffracted beam and the following optical components: primary beam Soller slits (2.5°), fixed divergence slit (1.25°), antiscatter slit (4 mm). The generator was set at 30 kV and 10 mA. After preliminary acquisitions for fingerprinting analysis, typically performed in the 4–35° 2θ range, diffraction data sets for a full structure determination were collected from 5° up to 105° 2θ , with steps of 0.02°, with an overall scan time of approximately 12 hours.

7.5.3. Solid-state NMR Characterization

The NMR characterization was carried out by Prof. R. Gobetto's group, University of Turin, Italy.

The ¹³C and ¹⁵N CPMAS NMR spectra of all compounds were acquired with a Jeol ECZR 600 instrument, operating at 600.17, 150.91 and 60.81 MHz for ¹H, ¹³C and ¹⁵N nuclei, respectively. The powder samples were packed into a cylindrical zirconia rotor with a 3.2 mm external diameter and a 60 μ L volume. 50 mg of as-synthesized sample were used without further manipulations to fill the rotor. The ¹³C and ¹⁵N CPMAS NMR spectra were acquired at room temperature, at a spinning speed of 20 (¹³C) and 12 (¹⁵N) kHz, using a ramp cross-polarization pulse sequence with a 90° ¹H pulse of 2.1 μ s, and a contact time of 3.5 (¹³C) and 4.0 (¹⁵N) ms. An optimized recycle delay between 1.0 and 2.5 s was used, for a number of scans in the range 160-2600 (¹³C) and 29000-164000 (¹⁵N), depending on the sample. For each spectrum, a two-pulse phase modulation (TPPM) decoupling scheme was used, with a radiofrequency field of 108.5 kHz. The ¹³C and ¹⁵N chemical shift scales were calibrated against proper signals of the external

standard glycine (^{13}C methylenic signal at $\delta_{\text{C}} = 43.7$ ppm and ^{15}N signal at $\delta_{\text{N}} = 33.4$ ppm with respect to NH_3). The stoichiometric coefficients x and y in the molecular formulae $\text{Zn}(\text{BPZX})_x(\text{BPZY})_{1-x}$ and $\text{Zn}(\text{BPZ})_x(\text{BPZNO}_2)_y(\text{BPZNH}_2)_{1-x-y}$ were calculated from the ^{13}C NMR signal integrals of C4 and C4': the integral values (extracted directly from the signals or after deconvolution) were used to build systems of equations with x and y as variables. The stoichiometric coefficients were then transformed into percentage amounts (%) through simple proportions. The ^1H MAS spectra of all compounds were acquired with a Bruker Avance II 400 Ultra Shield instrument, operating at 400.23 MHz for the ^1H nuclei. Powder samples were packed into cylindrical zirconia rotors with a 2.5 mm o.d. and a 14 μL volume. 50 mg of sample were used without further preparations to fill the rotor. The spectra were acquired at room temperature at a spinning speed of 32 kHz using a depth sequence, with a 90° ^1H pulse of 2.5 μs , optimized recycle delays of ca. 0.4-1.6 s and 16 scans. The ^1H chemical shift scale was calibrated through the ^1H signal of the external standard adamantane (at 1.87 ppm).

7.5.4. Variable-temperature Powder X-ray Diffraction

To complement the simultaneous thermal analysis, the thermal behaviour of the four MIXMOFs was investigated *in situ* by variable-temperature powder X-ray diffraction. Using a custom-made sample heater (Officina Elettrotecnica di Tenno, Ponte Arche, Italy), 20-mg samples of the as-synthesized compounds were heated in air from 303 K up to 763 K (the highest temperature reached by the instrument), with steps of 20 K; a PXRD pattern was acquired at each step, covering a sensible low-to-medium-angle 2θ range. Whole powder pattern parametric refinements with the Le Bail method on the data acquired before loss of crystallinity enabled us to disclose the behaviour of the unit cell parameters as a function of the temperature.

7.5.5. Water Vapor Stability

To monitor the stability of the MIXMOF samples towards water vapor, 15 mg of sample were deposited in the hollow of an aluminium sample-holder. Preliminary PXRD data were acquired in $5\text{-}35^\circ$ (2θ) range. Then, the sample holder was introduced into an

air-tight water-vapor saturated cell. At different time points from day one up to 11 days, the sample was checked by PXRD, adopting the same conditions employed for the preliminary acquisition.

7.5.6. Textural Characterization

The textural characterization was carried out by Dr. A. Rossin's group, ICCOM-CNR, Italy.

All the samples were activated at 393 K under high vacuum (10^{-6} Torr) for 24 h before any measurement. The Brunauer–Emmett–Teller (BET) specific surface area and porosity were estimated by volumetric adsorption with an ASAP 2020 Micromeritics instrument, using N_2 as adsorbate at 77 K. A typical measurement used 40 mg of sample. For the BET specific surface area calculation, the 0.01-0.1 p/p_0 pressure range was used to fit the data. Within this range, all the Rouquerol consistency criteria⁴¹ are satisfied. The micropore area was evaluated through the t -plot method with the Harkins and Jura thickness equation, while the micropore volume was estimated through the application of the Dubinin-Astakhov model to the N_2 isotherm in the $0 \leq p/p_0 \leq 0.02$ range.⁴² CO_2 adsorption isotherms were recorded at 273 and 298 K at a maximum pressure of 1.2 bar. The N_2 adsorption isotherms for the determination of the CO_2/N_2 selectivity were acquired at 298 K and up to 1.2 bar. The isosteric heat of adsorption (Q_{st}) was calculated from the CO_2 isotherms measured at 273 and 298 K according to a variant of the Clausius-Clapeyron equation (eq. 5). The CO_2/N_2 selectivity at 298 K was calculated based on the Henry method as the ratio of the initial slopes of the adsorption isotherms. The IAST selectivity for an equimolar CO_2/N_2 mixture at a total pressure of 1 bar was determined as the ratio of the (adsorbed) molar fractions of the two gases³⁰ as derived from the application of the free software pyIAST to the experimental N_2 and CO_2 isotherms collected at 298 K. A BET (CO_2) and a Henry (N_2) model were employed for the isotherm fitting.

7.6. References

- (1) Sharko, A. V.; Senchyk, G. A.; Rusanov, E. B.; Domasevitch, K. V. Preparative Synthesis of 3(5),3'(5')-Dimethyl-4,4'-Bipyrazole. *Tetrahedron Lett.* **2015**, 56 (44), 6089–6092.
- (2) Garrido, J.; Linares-Solano, A.; Martin-Martinez, J. M.; Molina-Sabio, M.; Rodriguez-Reinoso, F.; Torregrosa, R. Use of Nitrogen vs. Carbon Dioxide in the Characterization of Activated Carbons. *Langmuir* **1987**, 3 (1), 76–81.
- (3) Cazorla-Amorós, D.; Alcaniz-Monge, J.; De la Casa-Lillo, M. A.; Linares-Solano, A. CO₂ as an Adsorptive to Characterize Carbon Molecular Sieves and Activated Carbons. *Langmuir* **1998**, 14 (16), 4589–4596.
- (4) Rouquerol, J.; Rouquerol, F.; Llewellyn, P.; Maurin, G.; Sing, K. S. W. Adsorption by Powders and Porous Solids: Principles, Methodology and Applications; Academic press, **2013**.
- (5) Fairén-Jiménez, D.; Carrasco-Marín, F.; Moreno-Castilla, C. Adsorption of Benzene, Toluene, and Xylenes on Monolithic Carbon Aerogels from Dry Air Flows. *Langmuir* **2007**, 23 (20), 10095–10101.
- (6) Seaton, N. A.; Walton, J. A New Analysis Method for the Determination of the Pore Size Distribution of Porous Carbons from Nitrogen Adsorption Measurements. *Carbon N. Y.* **1989**, 27 (6), 853–861.
- (7) Landers, J.; Gor, G. Y.; Neimark, A. V. Density Functional Theory Methods for Characterization of Porous Materials. *Colloids Surfaces A Physicochem. Eng. Asp.* **2013**, 437, 3–32.
- (8) Fernández, B.; Beobide, G.; Sánchez, I.; Carrasco-Marín, F.; Seco, J. M.; Calahorra, A. J.; Cepeda, J.; Rodríguez-Diéguez, A. Controlling Interpenetration for Tuning Porosity and Luminescence Properties of Flexible MOFs Based on Biphenyl-4, 4'-Dicarboxylic Acid. *CrystEngComm* **2016**, 18 (8), 1282–1294.
- (9) Ojeda, M. L.; Esparza, J. M.; Campero, A.; Cordero, S.; Kornhauser, I.; Rojas, F. On Comparing BJH and NLDFT Pore-Size Distributions Determined from N₂ Sorption on SBA-15 Substrata. *Phys. Chem. Chem. Phys.* **2003**, 5 (9), 1859–1866.
- (10) Brunauer, S.; Emmett, P. H.; Teller, E. Adsorption of Gases in Multimolecular Layers. *J. Am. Chem. Soc.* **1938**, 60 (2), 309–319.
- (11) Dubinin, Mm. The Potential Theory of Adsorption of Gases and Vapors for Adsorbents with Energetically Nonuniform Surfaces. *Chem. Rev.* **1960**, 60 (2), 235–241.
- (12) Gregg, S. J.; Sing, K. S. W. Adsorption, Surface Area and Porosity. London Acad. Press **1982**, 195–197.
- (13) Stoeckli, F.; Patrick, J. Porosity in Carbons: Characterization and Applications. Arnold, London **1995**, 67.
- (14) Pettinari, C.; Tăbăcaru, A.; Boldog, I.; Domasevitch, K. V.; Galli, S.; Masciocchi, N. Novel Coordination Frameworks Incorporating the 4,4'-Bipyrazolyl Ditopic Ligand. *Inorg. Chem.* **2012**, 51 (9), 5235.
- (15) Zhang, J.-P.; Kitagawa, S. Supramolecular Isomerism, Framework Flexibility, Unsaturated Metal Center, and Porous Property of Ag (I)/Cu (I) 3,3',5,5'-Tetramethyl-4,4'-Bipyrazolate. *J. Am. Chem. Soc.* **2008**, 130 (3), 907–917.

- (16) Dovesi, R.; Orlando, R.; Erba, A.; Zicovich-Wilson, C. M.; Civalieri, B.; Casassa, S.; Maschio, L.; Ferrabone, M.; De La Pierre, M.; d'Arco, P. CRYSTAL14: A Program for the Ab Initio Investigation of Crystalline Solids. *Int. J. Quantum Chem.* **2014**, 114 (19), 1287–1317.
- (17) Vosko, S. H.; Wilk, L.; Nusair, M. Accurate Spin-Dependent Electron Liquid Correlation Energies for Local Spin Density Calculations: A Critical Analysis. *Can. J. Phys.* **1980**, 58 (8), 1200–1211.
- (18) Becke, A. D. Becke's Three Parameter Hybrid Method Using the LYP Correlation Functional. *J. Chem. Phys.* **1993**, 98, 5648–5652.
- (19) Grimme, S.; Antony, J.; Ehrlich, S.; Krieg, H. A Consistent and Accurate Ab Initio Parametrization of Density Functional Dispersion Correction (DFT-D) for the 94 Elements H-Pu. *J. Chem. Phys.* **2010**, 132 (15), 154104.
- (20) Civalieri, B.; Zicovich-Wilson, C. M.; Valenzano, L.; Ugliengo, P. B3LYP Augmented with an Empirical Dispersion Term (B3LYP-D*) as Applied to Molecular Crystals. *CrystEngComm* **2008**, 10 (4), 405–410.
- (21) <http://www.crystal.unito.it/basis-sets.php>, 2014.
- (22) Davidson, E. R.; Feller, D. Basis Set Selection for Molecular Calculations. *Chem. Rev.* **1986**, 86 (4), 681–696.
- (23) Boys, S. F.; Bernardi, F. de. The Calculation of Small Molecular Interactions by the Differences of Separate Total Energies. Some Procedures with Reduced Errors. *Mol. Phys.* **1970**, 19 (4), 553–566.
- (24) Zicovich-Wilson, C. M.; Pascale, F.; Roetti, C.; Saunders, V. R.; Orlando, R.; Dovesi, R. Calculation of the Vibration Frequencies of A-quartz: The Effect of Hamiltonian and Basis Set. *J. Comput. Chem.* **2004**, 25 (15), 1873–1881.
- (25) Gatti, C.; Saunders, V. R.; Roetti, C. Crystal Field Effects on the Topological Properties of the Electron Density in Molecular Crystals: The Case of Urea. *J. Chem. Phys.* **1994**, 101 (12), 10686–10696.
- (26) Gatti, C.; Casassa, S. M. TOPOND14 User's Manual. **2013**.
- (27) Boldog, I.; Sieler, J.; Chernega, A. N.; Domasevitch, K. V. 4,4'-Bipyrazolyl: New Bitopic Connector for Construction of Coordination Networks. *Inorganica Chim. Acta* **2002**, 338 (v), 69–77.
- (28) Zhu, X.; Mahurin, S. M.; An, S.-H.; Do-Thanh, C.-L.; Tian, C.; Li, Y.; Gill, L. W.; Hagaman, E. W.; Bian, Z.; Zhou, J.-H. Efficient CO₂ Capture by a Task-Specific Porous Organic Polymer Bifunctionalized with Carbazole and Triazine Groups. *Chem. Commun.* **2014**, 50 (59), 7933–7936.
- (29) Zhu, X.; Tian, C.; Veith, G. M.; Abney, C. W.; Dehaut, J.; Dai, S. In Situ Doping Strategy for the Preparation of Conjugated Triazine Frameworks Displaying Efficient CO₂ Capture Performance. *J. Am. Chem. Soc.* **2016**, 138 (36), 11497–11500.
- (30) Schell, J.; Casas, N.; Pini, R.; Mazzotti, M. Pure and Binary Adsorption of CO₂, H₂, and N₂ on Activated Carbon. *Adsorption* **2012**, 18 (1), 49–65.
- (31) Brunelli, M.; Fitch, A. N. A Glass Capillary Cell for in Situ Powder X-Ray Diffraction of Condensed Volatile Compounds. Solid HCFC-123a and HCFC-124. *J. Synchrotron Radiat.* **2003**, 10 (4), 337–339.

- (32) Rappé, A. K.; Casewit, C. J.; Colwell, K. S.; Goddard III, W. A.; Skiff, W. M. UFF, a Full Periodic Table Force Field for Molecular Mechanics and Molecular Dynamics Simulations. *J. Am. Chem. Soc.* **1992**, 114 (25), 10024–10035.
- (33) Potoff, J. J.; Siepmann, J. I. Vapor–Liquid Equilibria of Mixtures Containing Alkanes, Carbon Dioxide, and Nitrogen. *AIChE J.* **2001**, 47 (7), 1676–1682.
- (34) Biovia Materials Studio 6.0. Dassault Systèmes BIOVIA, San Diego: Dassault Systèmes **2018**.
- (35) Fairen-Jimenez, D.; Colón, Y. J.; Farha, O. K.; Bae, Y.-S.; Hupp, J. T.; Snurr, R. Q. Understanding Excess Uptake Maxima for Hydrogen Adsorption Isotherms in Frameworks with *Rht* Topology. *Chem. Commun.* **2012**, 48 (85), 10496–10498.
- (36) Bury, W.; Fairen-Jimenez, D.; Lalonde, M. B.; Snurr, R. Q.; Farha, O. K.; Hupp, J. T. Control over Catenation in Pillared Paddlewheel Metal–Organic Framework Materials via Solvent-Assisted Linker Exchange. *Chem. Mater.* **2013**, 25 (5), 739–744.
- (37) Mosca, N.; Vismara, R.; Fernandes, J. A.; Tuci, G.; Di Nicola, C.; Domasevitch, K. V.; Giacobbe, C.; Giambastiani, G.; Pettinari, C.; Aragones-Anglada, M.; Fairen-Jimenez, D.; Rossin, A.; Galli, S. NO₂-Functionalized Bis(Pyrazolate) MOFs as CO₂ Capture Materials at Ambient Conditions. *Chem. - A Eur. J.* **2018**, 24 (50), 13170–13180.
- (38) Münch, A. S.; Seidel, J.; Obst, A.; Weber, E.; Mertens, F. O. R. L. High-Separation Performance of Chromatographic Capillaries Coated with MOF-5 by the Controlled SBU Approach. *Chem. - A Eur. J.* **2011**, 17 (39), 10958–10964.
- (39) James, A. T.; Martin, A. J. P. Gas-Liquid Partition Chromatography: The Separation and Micro-Estimation of Volatile Fatty Acids from Formic Acid to. Dodecanoic Acid BY. *Biochem. J.* **1952**, 50, 679–690.
- (40) Vismara, R.; Tuci, G.; Mosca, N.; Domasevitch, K. V.; Di Nicola, C.; Pettinari, C.; Giambastiani, G.; Galli, S.; Rossin, A. Amino-Decorated Bis(Pyrazolate) Metal–Organic Frameworks for Carbon Dioxide Capture and Green Conversion into Cyclic Carbonates. *Inorg. Chem. Front.* **2019**, 6 (2), 533–545.
- (41) Roquerol, F.; Roquerol, J.; Sing, K. Adsorption by Powders & Porous Solids. Principles, Methodology and Applications; **1999**.
- (42) Saeidi, N.; Parvini, M. Accuracy of Dubinin-Astakhov and Dubinin-Radushkevich Adsorption Isotherm Models in Evaluating Micropore Volume of Bentonite. *Period. Polytech. Chem. Eng.* **2016**, 60 (2), 123–129.

LIST OF PUBLICATIONS

1. Mosca, N.; **Vismara, R.**; Fernandes, J. A.; Casassa, S.; Domasevitch, K. V.; Bailon-Garcia, E.; Maldonado-Hódar, F. J.; Pettinari, C. and Galli, S. CH₃-tagged Bis(pyrazolato)-based CPs and MOFs: An Experimental and Theoretical Insight. *Crystal Growth & Design*, **2017**, 17, 3854-3867.
2. Mosca, N.; **Vismara, R.**; Fernandes, J. A.; Pettinari, C. and Galli, S. The Hg (3,3'-dimethyl-1H,1H'-4,4'-bipyrazolate) Coordination Polymer: Synthesis, Crystal Structure and Thermal Behavior. *Inorganica Chimica Acta*, **2018**, 470, 423-427.
3. Mosca, N.; **Vismara, R.**; Fernandes, J. A.; Tuci, G.; Di Nicola, C.; Domasevitch, K. V.; Giacobbe, C.; Giambastiani, G.; Pettinari, C.; Aragonés-Anglada, M.; Moghadam, P. Z.; Fairen-Jimenez, D.; Rossin, A. and Galli, S. Nitro-functionalized bis(pyrazolate) metal-organic frameworks as carbon dioxide capture materials under ambient conditions. *Chemistry - A European Journal*, **2018**, 24, 13170-13180.
4. **Vismara, R.**; Tuci, G.; Mosca, N.; Domasevitch, K. V.; Di Nicola, C.; Pettinari, C.; Giambastiani, G.; Galli, S. and Rossin, A. Amino-decorated bis(pyrazolate) metal-organic frameworks for carbon dioxide capture and green conversion into cyclic carbonates. *Inorganic Chemistry Frontiers*, **2019**, 6, 533-545.
5. **Vismara, R.**; Tuci, G.; Tombesi, A.; Domasevitch, K.; Di Nicola, C.; Giambastiani, G.; Chierotti, M.; Bordignon, S.; Gobetto, R.; Pettinari, C.; Rossin, A. and Galli, S. Tuning carbon dioxide adsorption affinity of zinc(II) MOFs by mixing bis(pyrazolate) ligands with N-containing tags. *ACS Applied Materials & Interfaces*, **2019**, 11, 26956-26969.
6. Galli, S.; Cimino, A.; Ivy, J. F.; Giacobbe, C.; Arvapally, R. K.; **Vismara, R.**; Checchia, S.; Rawshdeh, M. A.; Cardenas, C. T.; Yaseen, W. K.; Maspero, A. and Omary M. A. Fluorous metal-organic frameworks and non-porous coordination

polymers as low- κ dielectrics. *Advanced Functional Materials*, **2019**, 29(40), 1904707.

7. Nowacka, A.; **Vismara, R.**; Mercuri, G.; Moroni, M.; Palomino, M.; Domasevitch, K.V.; Di Nicola, C.; Pettinari, C.; Giambastiani, G.; Llabrés i Xamena, F. X.; Galli, S.; and Rossin, A. “Cobalt(II) bis(pyrazolate) metal-organic frameworks as heterogeneous catalysts in cumene aerobic oxidation: a tag-dependent selectivity”, *manuscript in preparation*.
8. Di Nicola, C.; Tombesi, A.; Moroni, M.; **Vismara, R.**; Marchetti, F.; Pettinari, R.; Nardo, L.; Visco, G.; Galli, S.; Casassa, S.; Pandolfo, L.; and Pettinari, C. “Solvochromic behaviour of copper(II) pyrazolate coordination polymers interconverting from DMF solvated to unsolvated forms”, *submitted*.

ACKNOWLEDGEMENTS

First, I would like to acknowledge my supervisor Prof. Simona Galli for the opportunity of being part of this amazing project, for her permanent support and for trusting in my work since the first step of my Ph.D. I would like to thank all the people who contributed to this work: Prof. Claudio Pettinari's group (University of Camerino), Dr. Andrea Rossin's group (CNR of Sesto Fiorentino), Dr Konstantin V. Domasevitch's (University of Kiev) and all the collaborations that have made it possible.

A special thanks goes to Prof. Jorge Andrés Rodríguez Navarro and to all the group of Inorganic Chemistry in University of Granada for welcoming me in their laboratories, sharing their knowledge and making me feel like home.

I would like also to thank Prof. Norberto Masciocchi and Dr. Antonella Guagliardi for the fruitful discussions and pleasant conversations during the last three years. I would like to express my very special thanks to all the people who have been in the Third floor of the Cubo: Kiko, Gregorio, Dani, Fede, Anna e Marco, together with Silvia, Lizeth, Clemence, Valentina and Jenny. Thanks all guys for the lunches, the laughs, the post-work drinks and the outdoor trips! A special thanks goes to Alice, for our hiking, swimming and conversations and to the whole GNAS group.

I would like to thank Prof. Monica Dapiaggi and Prof. Giacomo Diego Gatta from University of Milan for trusting in me since my master studies and encouraging me to start a Ph.D.

Finally, I want to dedicate this work to my family and to Kiko for the constant support, the words of encouragement and the patience of the last months.

